Applications of Droplet Interface Bilayers: Specific Capacitance Measurements and Membrane Protein Corralling

Linda Claire Margret Gross

A thesis submitted in partial fulfilment of
the requirements for the degree of
Doctor of Philosophy at the University of Oxford

St John's College
University of Oxford
Trinity Term 2011

Abstract

Applications of Droplet Interface Bilayers:
Specific Capacitance Measurements and Membrane Protein Corralling

Linda C M Gross - St John's College - University of Oxford

Submitted for the degree of Doctor of Philosophy in Trinity Term 2011

Droplet Interface Bilayers (DIBs) have a number of attributes that distinguish them from conventional artificial lipid bilayers. In particular, the ability to manipulate bilayers mechanically is explored in this thesis. Directed bilayer area changes in particular are used to make precise measurements of the specific capacitance of DIBs and to control the two dimensional concentration of a membrane protein reconstituted in the bilayer.

Chapter 1 provides a general introduction to the role of the lipid membrane environment in the function of biological membranes and their integral proteins. An overview of model lipid bilayer systems is given.

Chapter 2 introduces work carried out in this laboratory previously and illustrates the experimental setup of DIBs. Some important bilayer biophysical concepts are covered to provide the theoretical background to experiments in this and in later chapters. Results from the characterisation of DIBs are reported, and an account of the development of methods to manipulate the bilayer by mechanical means is given.

Chapter 3 describes experiments that apply bilayer area manipulation in DIBs to achieve precise measurement of specific capacitance in a range of lipid systems.

Chapter 4 reports results from experiments investigating the response of bilayer specific capacitance to an applied potential.

Chapter 5 covers the background and experimental setup for total internal fluorescence microscopy experiments in DIBs and describes the expression, purification and characterisation of the bacterial β-barrel membrane protein pore α-Hemolysin.

Chapter 6 describes experiments that apply the mechanical manipulation of bilayer area in DIBs to the corralling and control of the surface density of α-Hemolysin.

Declaration

The work described in this thesis was carried out between January 2008 and August 2011, in the laboratory of Dr. Mark Wallace at the Chemistry Research Laboratory of the University of Oxford. All the work described within this thesis is entirely my own, unless expressly attributed to my co-workers. This work has not been submitted previously for any other degree at the University of Oxford or any other university. Publications stemming from this work are detailed in Appendix A.

Linda C M Gross

September 2011

Acknowledgements

I would firstly like to thank Dr. Mark Wallace for the opportunity to carry out this research in his lab, and for the constantly open door, for the hours spent aligning lasers when I was still a newbie, and for life lessons in efficiency. Thank you also to Dr. James Thompson for fielding the majority of my questions about, well, everything, and making sure that I could stand on my own two feet in next to no time.

I am very much indebted to Dr. Bríd Cronin, Dr. Sebastian Leptihn, Dr. Lydia Harriss, Lauriane Angue, Mathew Horrocks, acting biochemistry guru David Marshall and especially Dr. Andrew Heron and Dr. Oliver Castell for insightful comments and in-depth discussions. You have made the lab a pleasant place to be in, and I owe you for absorbing some of my rants when another day of invariably bursting bubbles had come to an end.

My thanks also go to Dr. Grant Ritchie for giving me the opportunity to inflict droplets on his laboratory's optical tweezing setup, and to Dr. Mike Summers and especially Lee Moore for proving that constant banter and good science do coexist quite happily.

I am extremely grateful to Prof. Martin Stokes and Dr. Jason Schnell for their time and supportive words, and to St John's College for a financial lifeline.

My most sincere thanks have to go to Prof. David Gavaghan and Prof. Elspeth Garman for their invaluable support, advice and kind words, without which I doubt I would be here now. Thank you also to all the rest of the team at the Life Science Interface Doctoral Training Centre, especially to Maureen York for making everything work in the first year, and to Dr. Eoin Malins, Sam Miles, Lisa Bligh, and Kirsten Yost for making my forced part-time change of scenery a very pleasant experience.

Thank you to Rob, Bartu, Loukas, and 'honorary member' Jochen for absolutely brilliant fun during the first year at the DTC; to Sylvie, Lema, Isabel, Carly and Vanessa for wonderful girly times; to Tim for spiffing companionship; and to everyone at the Yacht Club for making sure that a sense of adventure could not be smothered among all the lab work.

Not quite last, but furthest from least, thank you to Benjamin, for your amazing proofreading marathons, for the the invaluable wisdom of someone who has been there, but most of all, for your unfailing love and understanding.

Finally, thank you to Mum and Dad for providing me with an education that has got me this far, and to all my family for your constant love, support, and encouragement – throughout the sometimes rather unpredictable path that I have followed. Let's see where it goes next!

Für
Omi und Opi

Contents

List of Tables

List of Figures

Abbreviations

α-HL	α-Hemolysin
γ-CD	γ-cyclodextrin
AC	alternating current
AFM	atomic force microscopy
BFP	barrier free path
BLM	black lipid membrane
BSA	bovine serum albumin
DC	direct current
DIB	Droplet Interface Bilayer
DIC	difference interference contrast
DOC	deoxycholate
DOE	diffractive optical element
DOPC	1,2-dioleoyl-*sn*-glycero-3-phosphocholine
DOPG	1,2-dioleoyl-*sn*-glycero-3-phospho-(1'-rac-glycerol)
DPhPC	1,2-diphytanoyl-*sn*-glycero-3-phosphocholine
DPI	dual polarisation interferometry
DPPC	1,2-dipalmitoyl-*sn*-glycero-3-phosphocholine
DPPE	1,2-dipalmitoyl-*sn*-glycero-3-phosphoethanolamine
DPTL	2,3-di-O-phytanyl-*sn*-glycerol-1-tetraethylene glycol-DL-α-lipoic acid ester lipid
E. coli	*Escherichia coli*
EDTA	ethylenediaminetetraacetic acid
eggPC	egg phosphatitdyl choline (egg lethicin)
EIS	electron impedance spectroscopy
EM	electron microscopy
emCCD	electron-multiplying charge-coupled device
EPR	electron paramagnetic resonance
EWOD	electrowetting on dielectric
FPLC	fast protein liquid chromatography
FRAP	fluorescence recovery after photobleaching
GMO	glyceryl mono-olein
GPCR	G-protein coupled receptor
GUV	giant unilamellar vesicle
hβ-CD	heptakis(2,3,6-tri-O-methyl)-β -cyclodextrin
HEPES	4-(2-hydroxyethyl)-1-piperazineethanesulfonic acid
HILO	highly inclined laminated optical sheet
IMAC	immobilised metal-affinity chromatography

IPTG	isopropyl-β -D-1-thiogalactopyranoside
IVTT	coupled *in vitro* transcription and translation
LB	Luria-Bertani
Luk	leukocidin protein
MBP	maltose binding protein
MD	molecular dynamics
MSD	mean-squared displacement
NA	numerical aperture
NCAM	neural cell adhesion molecule
Ni-NTA	nickel-nitrilotriacetic acid
NMR	nuclear magnetic resonance
OMP	outer membrane protein
PC	phosphatidylcholine
PDMS	polydimethyl siloxane
PE	phosphatidylethanolamine
PEG	polyethylene glycol
PFT	pore forming toxin
PHMS	polyhydroxymethyl siloxane
PMMA	polymethyl methacrylate
POPC	1-palmitoyl-2-oleoyl-*sn*-glycero-3-phosphocholine
POPE	1-palmitoyl-2-oleoyl-*sn*-glycero-3-phosphoethanolamine
POPG	1-palmitoyl-2-oleoyl-*sn*-glycero-3-phospho-(1'-rac-glycerol)
PTFE	polytetrafluoroethylene
QCM	quartz crystal microbalance
S. aureus	*Staphylococcus aureus*
SCCaFIT	single-channel calcium fluorescence intransient
SCCaFT	single-channel calcium fluorescence transient
SCR	single channel recording
SDS	sodium dodecyl sulfate
SiO_2	silicon dioxide
SLB	supported lipid bilayer
SLM	spatial light modulator
SMF	single molecule fluorescence
SPR	surface plasmon resonance
SPT	single-particle tracking
TEO	tetraethyleneoxy
TIRF	total internal reflection fluorescence
TRIS	tris(hydroxymethyl)aminomethane

Symbols

A_{M}	bilayer area
a	interfacial area per molecule
C	capacitance
C	molar concentration
C_{dl}	double layer capacitance
C_{g}	geometric capacitance
C_{m}	specific capacitance
$C_{\mathrm{m,0}}$	specific capacitance at zero applied potential
C_0	background capacitance
C'_{T}	total membrane capacitance
C_{T}	total measured capacitance
D_{lat}	lateral diffusion coefficient
d_{m}	thickness of the bilayer hydrocarbon core
d_0	blayer thickness at zero applied potential
F_{grad}	gradient force
F_{scat}	scattering force
F	Faraday constant
I_{C}	capacitve current
I_{M}	measured current
I_{R}	resistive current
k_B	Boltzmann constant
K_{A}	isotropic area compressibility modulus
K_{t}	isothermal thickness compressibility modulus
ℓ	topological charge
m_0	0th moment of particle intensity
m_2	2nd moment of particle intensity
Π	surface pressure
R	universal gas constant
R_{tm}	radius of the protein transmembrane domain
R_{d}	droplet radius
R_ℓ	radius of a Laguerre-Gaussian beam
r_{m}	radius of the bilayer membrane
T_{misc}	miscibility transition temperature
T	absolute temperature
V_{a}	applied potential
w	particle radius
γ_{do}	surface tension of the droplet–oil interface

γ_{ho}	surface tension of the hydrogel–oil interface
γ_{i}	interfacial free energy per unit area, or surface tension
γ_{m}	bilayer membrane surface tension
ε_{m}	dielectric coefficient of hydrocarbon
ε_0	dielectric permittivity of free space
ε_{w}	dielectric coefficient of water
η	expected particle percentile
θ	droplet contact angle
ν_m	viscosity of the bilayer liquid crystalline phase
ξ	trajectory linking parameter
ϕ_{c}	critical angle of incidence for total internal reflection
$\Delta\Psi$	membrane potential
$\Delta\Psi_m$	potential drop across the membrane
$\Delta\Psi_s$	surface potential
φ	osmotic coefficient
σ_ℓ	line tension
σ_{t}	uniform normal stress (force per unit area)
σ	charge density
Υ	osmolarity
χ	particle discrimination parameter
ω	radius of a Gaussian beam

Chapter 1

Introduction

The following paragraphs examine our present understanding of the effect that biophysical parameters such as membrane fluidity, thickness and curvature have on the function of biological membranes and the proteins embedded within them, aiming to put the experiments in this thesis on the characterisation and manipulation of these membrane parameters into context. The fundamental properties of lipid membranes and their constituents are summarised, followed by an overview of model membrane systems that form the basis of the Droplet Interface Bilayer (DIB) system employed here.

1.1 Lipid-Protein Interactions

Our understanding of the complex environment of the cell membrane is constantly being refined by new experiments that reveal the influence of a large number of biological and biophysical parameters on membrane function (Engelman, 2005; Lundbæk, 2008; Phillips et al., 2009). The membrane can store energy through conformational flexibility (Hamill and Martinac, 2001; Mouritsen and Bloom, 1993), lateral tension can provide a driving force that impacts on the open probability of ion channels (Beyder et al., 2010; Cantor, 1999; Marsh, 1996), and membrane electrostatics and hydrophobic thickness matching of membrane components affect the dynamic assembly of membrane protein oligomers and the mechanisms they mediate (Aguilella and Bezrukov, 2001; Jensen and Mouritsen, 2004; Lee, 2003; Petrache et al., 2002; Tieleman et al., 1998; Williamson et al., 2002). Specific lipids are essential for maintaining

the function of some membrane proteins (Cheng et al., 2011; van der Does et al., 2000). The required diverse environment is sustained by dynamic, genetically encoded variations in lipid composition (Wenk and De Camilli, 2004). Domains of varying order, diffusional properties and thickness, stabilised by cholesterol for example, are now known to provide structural variability (Andersen and Koeppe, 2007; Maxfield and Tabas, 2005). All these elements highlight that cell membranes are far more than an inert envelope surrounding the cytoplasm. They represent a crowded medium of lipid and protein components that can modulate both structure and function of individual membrane proteins, and it is increasingly evident that the role of membrane proteins existing in this complex environment cannot be fully understood when studied in isolation.

Many membrane proteins undergo dynamic conformational transitions between discrete structural states that dictate function. Structural studies, centred on the ability to isolate proteins, have provided invaluable insights into the nature of these discrete states (Stahlberg et al., 2001). Techniques have improved and can now access high resolution structural data on features such as inter-subunit interactions, lipidation, glycosylation and structural water molecules. Both specific and non-specific strongly bound lipids have been found in recent high resolution structures (Engelman, 2005; Lee, 2003) and are thought to not only have structural, stabilising roles, but also functional effects by imposing restraints on protein dynamics (Cramer et al., 2006). It is unclear to what degree lipid binding itself is dynamic, but the removal of bound cardiolipin in ADP/ATP carrier, for example, results in a 20 % decrease in activity (Nury et al., 2006). These are tantalising clues to the possibilities of membrane protein regulation by the membrane environment, but such single, averaged protein structures can only ever give an incomplete picture of true mechanisms. When visualising transitional states as points on an energy landscape, it becomes clear that a very large number of transitional paths between conformational states are possible (Sachs and Engelman, 2006). Nothing we know so far precludes the possibility that the numerous biophysical parameters of the membrane are controlled by the cell to effect the dynamic alteration of the energy landscape between conformational states. In the case of mechanosensitive channels, it is already apparent that changes

in bilayer thickness and curvature can profoundly influence activation energy by stabilising conformational intermediates (Perozo et al., 2002), illustrating that the forces involved are of a magnitude that could play a role in conformational changes in other membrane proteins. Indeed, it has been shown that voltage gated ion channels also respond to mechanical stress in the bilayer (Drew, 2011; Morris and Juranka, 2007). The limitation of available paths between intermediate states, by means of physical constraints placed on the protein by the membrane environment, would provide a further mechanism for the cell to use the lipid bilayer as a controlling and tuning instrument for membrane protein function (Sachs and Engelman, 2006). To progress in the understanding of the complexity that results from the combinatorial possibilities of the multitude of parameters influencing a membrane protein in a membrane, it is now vital to find simplifications of its molecular environment that remain true to biology but can be investigated experimentally. This thesis focuses on the possibilities offered in this respect by Droplet Interface Bilayers (DIBs), a novel artificial bilayer system that enables the manipulation of lipid membranes while allowing for the simultaneous investigation of reconstituted membrane proteins by single channel recording (SCR) and single molecule fluorescence (SMF) methods (Bayley et al., 2008; Heron et al., 2007).

1.2 Lipid Membranes

Lipid membranes mediate the compartmentalisation that is essential for the existence of living organisms. They form upon the spontaneous non-covalent assembly of lipids into bimolecular leaflets that serve as a permeability barrier around aqueous volumes such as cells and organelles. From an evolutionary perspective, it is immediately clear that the primary function of a permeability barrier has to be modified by macromolecules to enable nutrient uptake and disposal of waste. Selective permeability for small molecules is conferred by membrane proteins embedded in the lipid bilayer. These have further evolved to add the capability for energy storage and also to mediate the passing of information between the cell and its immediate surroundings by establishing gradients of ions and proteins.

1.2.1 Re-examining the Fluid Mosaic Model

An important and insightful development in the study of the cell envelope was the formulation of the 'fluid mosaic model' by Singer and Nicholson in 1972 (Singer and Nicolson, 1972). Despite many recent developments that will be discussed below, the model has until very recently been the dominant conceptual framework for membrane architecture. Also termed the two-dimensional continuum fluid model, it describes proteins that match the hydrophobic thickness of an unperturbed bilayer, diffusing freely in a fluid medium of lipid that is mostly exposed to the aqueous environment. However, since then it has become clear that the model cannot account for the fact that macroscopic diffusion coefficients of proteins and lipids in biological membranes are $5-50$ times smaller than those observed for proteins reconstituted in artificial membranes (Kusumi et al., 2005). Neither can it explain why diffusion rates sometimes drop dramatically upon oligomerisation of membrane proteins or artificial cross-linking of lipids (Murase et al., 2004). The generalisations of the fluid mosaic model have only recently been examined in more detail and refined to represent what is known about biological membranes (Engelman, 2005; Jacobson et al., 1995; Kusumi et al., 2005).

It is now clear that membranes are far more 'patchy' than the model suggests. Engelman (2005) points out that the random two-dimensional liquid of lipid and protein molecules of the Singer-Nicholson model would require that all pairwise interaction energies between species in the membrane be within the range of the thermal energy ($\sim$0.6 kcal mol^{-1} at room temperature). When taking into consideration interactions such as hydrogen bonds, electrostatics, the hydrophobic effect and packing effects due of the large number of species present in the membrane (the *Escherichia coli* (*E. coli*) genome for example codes for more than 1000 helical transmembrane proteins (Liu et al., 2002)), a non-random distribution should be expected, characterised by complexes, transient associations and regions of varying lipid composition. Furthermore, the large ectodomains of many proteins and protein complexes that can cover multiple times the area of their transmembrane regions (Iverson et al., 1999; Stock et al., 1999) result in additional interactions out-of-plane of the membrane with lipid head groups.

When taken together with estimates of proteinaceous content in many membranes of 50-70 % (w/w) (Mitra et al., 2004; Szalontai et al., 2000), it is likely that the area of lipid exposed to the aqueous environment is in fact far smaller than implied by the often seen schematic of a membrane as described by the Singer-Nicholson model.

Membrane thickness is also likely to be far from uniform. Known structures of membrane proteins show that the length of the hydrophobic surface area varies, not only between proteins but also around the circumference of a single protein. The exposure of such hydrophobic regions to the aqueous phase is unfavourable by about 25 $Å^{-2}$ (Engelman, 2005) and so either the protein or the lipid bilayer has to distort to ensure matching of hydrophobic regions. The relative stiffness of protein transmembrane regions (Zaccai, 2000) compared to the bilayer (Lundbæk and Andersen, 1999) suggests that it is the lipid bilayer that expands or compresses (Mitra et al., 2004; Petrache et al., 2002). Such local distortion and, if asymmetric, any resulting membrane curvature would be expected to play a role in lateral protein interactions, encouraging the formation of complexes that minimise the area of hydrophobic mismatch.

1.2.2 Lateral Diffusion in Biological Membranes

Advances in single-particle tracking techniques have revealed a diverse set of characteristic lateral protein mobilities. Far from the uniform fluidity of the Singer-Nicholson model, biological membranes are characterised by a distribution of diffusion coefficients (Saxton, 1997) that suggest that directed motion, confined motion and anomalous diffusion all take place (Kusumi et al., 2005; Saxton and Jacobson, 1997). Aside from the lipid-protein interactions, membrane protein oligomerisation and the variability of membrane thickness discussed above, transmembrane interactions, adhesion sites, ectodomain collisions in crowded membranes, and cytoskeletal structure are also responsible for variable degrees of motional freedom of membrane proteins. Single-particle tracking (SPT) and fluorescence recovery after photobleaching (FRAP) experiments in cells have shown that a substantial fraction of proteins can be transiently confined to small domains in apparently undifferentiated regions of membrane, while others undergo rapid directional movement (Jacobson et al., 1995). Edidin et al. (1991) investigated the distance that a membrane protein conjugated

to an optically trapped bead could be moved in the plane of the membrane. This distance, termed the barrier free path (BFP), almost trebled for lipid-linked isoforms of major histocompatibility antigens relative to transmembrane types, and increased with temperature. These experiments support the concept of a 'membrane-skeleton fence' formed by cytoskeletal components (Kusumi et al., 1993). Cytoskeletal corrals formed by this fence are thought to be around 100 – 600 nm^2 in area, but it remains unclear whether they interfere with protein motion dynamically or form static corrals (Brown et al., 2000). What is apparent, however, is that confinement is not only limited to those transmembrane components that could be directly impeded by the cytoskeleton. A lipid-linked isoform of a neural cell adhesion molecule (NCAM) was found to persist in confined domains for up to eight seconds and SPT analysis showed that proteins in these domains appear to be diffusing through a dense region of obstacles (Simson et al., 1998). More recently, it has become clear that diffusion is not only impeded by physical constraints outside of the bilayer plane, but that heterogeneity in the lipid organisation and composition within the bilayer results in varying diffusional properties, as will be described in more detail below.

1.2.3 Lipids

Lipids consist of a wide range of amphiphilic compounds containing a non-polar and a polar region. Biological membranes contain primarily the complex lipids such as phospholipids, sphingolipids, glycolipids and lipopolysaccharides. A single membrane typically contains over 100 different lipid species (Hauser and Poupart, 2005). Lipid composition, along with the asymmetric distribution of lipids between the inner and outer bilayer leaflets, is important for biological functions from membrane trafficking to signal transduction (Holowka et al., 2005; Mukherjee and Maxfield, 2004; Simons and Vaz, 2004). The outer leaflet of the eukaryotic cell membrane contains a large proportion of glycolipids, and the extracellular leaflet of the outer membrane of *E. coli* is composed exclusively of lipopolysaccharides. The major lipid components in eukaryotic and prokaryotic membranes however are the glycerophospholipids, namely phosphatidylcholine (PC) and phosphatidylethanolamine (PE). The *E. coli* inner membrane, for example, can contain as much as 70 – 80 % phos-

phatidylethanolamine (Dowhan, 1997). Glycerophospholipids, such as the examples illustrated in Figure 1.1, are derivatives of *sn*-glycero-3-phosphoric acid and usually have two fatty acids esterified in the *sn*-1 and *sn*-2 positions that form the hydrophobic acyl chains of the molecule. Acyl chains of lipids found in biological membranes have an even number of C-atoms, ranging from $C_{14}-C_{22}$, but they predominantly have $16-18$ C-atoms. The degree of unsaturation of the acyl chains varies considerably and $1-4$ double bonds are common. Phospholipids usually have one unsaturated chain in the *sn*-2 position as exemplified by POPE and POPG in Figure 1.1. The polar head group, which usually consists of choline, ethanolamine, glycerol or serine is attached to the *sn*-3 position of the glycerol moiety via a phosphoric acid group by ester bonds. Phosphocholine and phosphoethanolamine are zwitterionic and therefore are effectively neutral (Figure 1.1 A). Charged lipids (Figure 1.1 B) such as those with phosphoglycerol and phosphoserine head groups are present in biological membranes at a fraction of around $10-20\,\%$ (Hauser and Poupart, 2005) .

1.2.4 Non-Lamellar Phases

The structural forms assumed by biomembrane lipids when mixed with water are a function of their shape and charge and can differ significantly from the bimolecular leaflet typically found in cell membranes. Clearly, the type of structure that is formed depends both on the temperature (thermotropic mesomorphism) and the degree of hydration of the lipid (lyotropic mesomorphism) (Caffrey and Cherezov, 2009; Chapman, 1993). Below a characteristic melting temperature, different phases are distinguished by the relative position of essentially rigid molecules. Above the melting temperature of the lipid however, liquid-crystalline phases are characterised by changes in the shape of the lipid-water interface (Gruner, 2005). Broadly, the type of aggregate that an amphiphile is likely to form can be predicted from the geometry of the molecule (Hamai et al., 2006; Lichtenberg, 1993). Lipids with a cylindrical volume governed by a polar head group of similar lateral dimensions as the hydrophobic tail will preferentially assemble into planar lamellar structures. Molecules with bulky acyl chains will tend to enclose aqueous volumes with their head groups pointing inwards, an arrangement that can result in the formation of cylindrical structures of indefinite

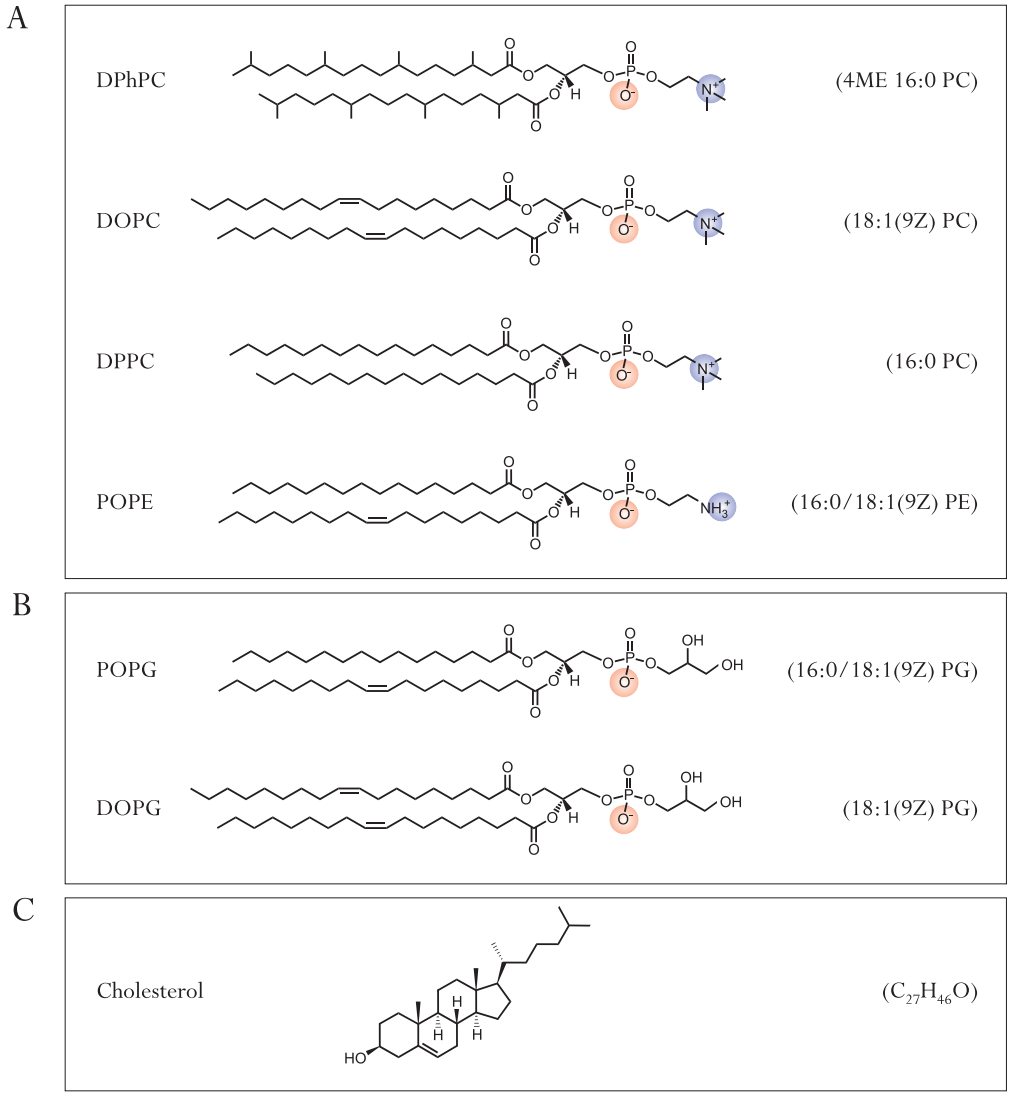

Figure 1.1: Lipids mentioned in this work. **(A)** Neutral (zwitterionic) diacylglycerophospholipids: 1,2-diphytanoyl-*sn*-glycero-3-phosphocholine (DPhPC); 1,2-dioleoyl-*sn*-glycero-3-phosphocholine (DOPC); 1,2-dipalmitoyl-*sn*-glycero-3-phosphocholine (DPPC) and 1-palmitoyl-2-oleoyl-*sn*-glycero-3-phosphoethanolamine (POPE). **(B)** Charged diacylglycerophospholipids: 1-palmitoyl-2-oleoyl-*sn*-glycero-3-phospho-(1'-rac-glycerol) (POPG) and 1,2-dioleoyl-*sn*-glycero-3-phospho-(1'-rac-glycerol) (DOPG) **(C)**The structure of cholesterol.

Figure 1.2: Phase diagram for monoolein. Clockwise from right the illustrations show the pseudo-crystalline state, the lamellar liquid crystalline phase, the fluid isotropic phase, the inverse hexagonal phase, the micellar (diamond) cubic phase and the gyroid cubic phase. *Figure reprinted from Cherezov et al. (2006) with permission from Elsevier.*

length that stack in a hexagonal lattice, termed an inverse hexagonal phase (H_{II}).

Conversely, detergents and lipids with large head groups and small, single acyl chains form micelles or a hexagonal phase where the acyl chains are directed into the interior of the cylindrical structures, which are surrounded by a continuous aqueous phase (H_I). The radius of the sphere along which an amphiphile molecule preferentially aggregates is also known as the spontaneous radius of curvature. Every biological bilayer membrane contains at least one non-bilayer forming lipid (Dowhan, 1997). The diacylglycerophospholipids shown in Figure 1.1 are examples of lamellar lipids, although even subtle differences such as the three methyl groups in PE vs. PC can be apparent in the preferred radius of curvature (Hamai et al., 2006). At low hydration, a number of more complex structures known as cubic phases can also be observed. They are characterised by three-dimensional networks of aqueous channels and a lipidic phase that is either formed by a continuous bilayer that extends and branches in three dimensions, or by packed connected micelles arranged in a cubic lattice (Cribier et al., 1993; Landau and Rosenbusch, 1996). These phases are macroscopically stable and highly viscous, and have therefore been used as an artificial membrane

environment to achieve membrane protein crystallisation (Landau and Rosenbusch, 1996) as will be described in more detail below.

1.2.5 Lamellar Phases

Lamellar lipids studied in pure synthetic systems at low (<50 %) hydration, where lipid bilayers are stacked on top of each other, have revealed a number of mesomorphic transitions that depend on temperature and hydration (Chapman, 1993; Luzzati et al., 1968). At low temperature, the hydrocarbon chains arrange into an orderly crystalline lattice with slightly tilted, tightly packed hydrocarbon chains (pseudo-crystalline state L'_c). With increasing temperature, a transition to a 'gel' or L'_β phase occurs, where the chains are still packed in an orderly lattice, but are more tilted and have limited rotational freedom and the head groups are more hydrated. As temperature increases further, disorder increases and the bilayer goes through a ripple phase (P'_β) which differs from the gel phase in that lipids are rotationally symmetric and are displaced along the long axis, resulting in a bilayer that is not planar but contains a series of periodic waves (Lewis and McElhaney, 2005). At the gel to liquid-crystalline transition temperature, which depends on the nature of the lipid chains and the amount of water present, the chains melt, resulting in a fluid L_α phase with marked increase in the cross-sectional area of the lipids accompanied by effective shortening of the hydrocarbon chains (Lewis and McElhaney, 2005; Maxfield and Tabas, 2005) mediated by their dynamic rotation and flexing into kinks (Casal and McElhaney, 1990). The lipids now pack in a loose hexagonal lattice, and the increased area available to the headgroup permits fast rotation on the nuclear magnetic resonance (NMR) time scale (Lewis and McElhaney, 2005).

1.2.6 Domains and Rafts in Biological Membranes

First proposed by Jain and White 3rd (1977) and refined by Karnovsky et al. (1982), the idea that segregated domains with different lipid phase characteristics and functional roles can co-exist in biological membranes has engendered much discussion, with many questioning not only the size and persistence of these domains (Edidin,

2001, 2003), but also their very existence (Munro, 2003). Based on observations of inhomogeneous mixing of lipids in artificial membrane systems and polarity observed in epithelial cells, Simons and Ikonen (1997) described lipid 'rafts', a particular class of domain consisting of dynamic assemblies of cholesterol and sphingolipids, in what became known as the 'lipid raft hypothesis'. Rafts were subsequently defined as "small (10-200 nm), heterogeneous, highly dynamic, sterol-and sphingolipid-enriched domains that compartmentalise cellular processes" (Pike, 2006). It is now widely accepted that inhomogeneities in this form exist and that they play important roles in cellular function (Allen et al., 2007; Goñi and Alonso, 2009; Mongrand et al., 2010; Pike, 2009; Sharma et al., 2004).

Heterogeneous mixtures of lipids found in biological membranes exist predominantly in the fluid L_α phase. At physiological temperature, lipid bilayers are therefore fluid and far more disordered than commonly depicted in schematic illustrations. The L_α phase, often also referred to as the liquid disordered phase (L_d), is characterised by fast diffusion rates. Bending and tilting of the acyl chains results in terminal methyl groups widely distributed over the hydrophobic core (Gawrisch, 2005; Nagle and Tristram-Nagle, 2000). Lipids with unsaturated and therefore naturally kinked acyl chains promote a lipid disordered organisation. A more ordered but still fluid phase, the liquid-ordered phase (L_o), is observed only in bilayers of mixed composition, usually in the presence of cholesterol. Eukaryotic membranes contain significant amounts of cholesterol, which has a very different structure to the common membrane lipids (Figure 1.1 C). As well as mediating a lipid-ordered membrane structure, cholesterol is thought to stabilise boundaries between coexisting domains in biological membranes (Feigenson, 2009; Goñi and Alonso, 2009). The position of cholesterol in the bilayer is determined by the polar hydroxyl group, which aligns with phospholipid headgroups while the rest of the molecule lies parallel with the acyl chains in the core of the bilayer. The increase in order is thought to be imparted by the rigidity of the planar ring system in the hydrophobic part of the molecule, which restricts the space available to lipid acyl chains to bend and kink. The resulting lipid organisation is characterised by increased packing of the atoms in the hydrophobic core and elongation of the acyl chains with a concomitant increase in bilayer thickness (Maxfield and

Tabas, 2005). Diffusion occurs almost as rapidly as in the L_o phase, but this type of organisation is less permeable to small molecules than the L_d phase (Maxfield and Tabas, 2005; Quinn and Wolf, 2009). Other molecules with small headgroups, such as simple sphingolipids (Wang and Silvius, 2003) and ceramide (Megha and London, 2004), can rigidify the membrane even further, resulting in gel-like domains (Goñi and Alonso, 2009).

1.3 Membrane Proteins

Membrane proteins typically make up around 30 % of the open reading frames in sequenced genomes (Dowhan and Bogdanov, 2009; Stahlberg et al., 2001). The majority are integrated into the membrane by a variable number of hydrophobic α-helices that span the membrane (Type I-III integral membrane proteins). Type IV integral membranes may also contain α-helices, but this type is defined by an aqueous channel surrounded by a variable number of homologous domains within a single polypeptide chain, or by independent subunits. (See Singer (1990) for a comprehensive review of membrane protein types and subtypes) In both eukaryotes and prokaryotes, polytopic α-helical membrane proteins, i.e. those with several transmembrane helices, are inserted into the membrane co-translationally by direct association of the ribosome with another membrane complex, the Sec translocon (Renthal, 2009). The precise mechanism of lateral exit of newly formed helices from the translocon is unclear, but subsequent helices tend to be anti-parallel and the N terminus tends to remain on the cytoplasmic side of the membrane (Dowhan and Bogdanov, 2009). Transmembrane helices in larger (Type III and IV) proteins are connected by flexible loops, which affords the ability to vary the position of helices with respect to each other. Large-scale movements of the protein backbone are the basis of function in many ion channels, enabling reversible opening and closing (gating) of aqueous channels through the interior of the protein (Ashcroft, 2006). G-protein coupled receptors (GPCRs), the largest family of membrane proteins involved in cell signalling at the cell surface, of which around 800 human unique full-length variants are known, are another common example (Lagerstrom and Schioth, 2008). Due to their common

topology they are also referred to as seven-transmembrane helix receptors, and most mediate transmembrane signalling by a conformational change upon binding of small signalling molecules on their extracellular side (Palczewski, 2006).

In other membrane proteins (Type IVb), the transmembrane domain consists of an anti-parallel β-pleated sheet in a barrel conformation, with hydrophobic side chains on the outside in contact with the hydrophobic core of the membrane, and hydrophilic side chains pointing into the interior of a rigid aqueous pore that allows indiscriminate passive diffusion of hydrophilic molecules. This motif is commonly found in the outer membranes of bacteria, mitochondria and chloroplasts (Wimley, 2003). The insertion mechanism of porins is not fully understood, but since individual insertion of β-strands would be highly unfavourable, it is likely that some type of post-translational cooperative mechanism must exist. Other outer membrane proteins appear to be necessary for insertion of porins (Singer, 1990), while β-barrel cytolytic toxins are thought to insert spontaneously into the membrane through inter-domain cooperativity between monomers bound to the membrane in a prepore complex. The exact mechanism of the concerted conformational change leading to membrane insertion of the β-barrel is still poorly understood. (Dang et al., 2005; Heuck et al., 2000, 2010; Iacovache et al., 2008).

Given the pivotal role that membrane proteins play in cellular functions from adhesion to cell proliferation, signal transduction, nerve and muscle excitation and energy storage, it is unsurprising that about 60-70 % of drug targets are membrane proteins (Ashcroft, 2006; Dowhan and Bogdanov, 2009; Stahlberg et al., 2001). However, due to the difficulty of isolating these proteins from the membrane without destroying their physiological environment and thus their integrity (Cramer et al., 2006), membrane proteins are far less well studied than their soluble counterparts. Nevertheless, membrane protein structure determination is now progressing more rapidly, as evidenced by the growing collection in the database[†] compiled by White (2009). It is becoming clear that oligomerisation is a highly common motif in membrane proteins (Engelman, 2005) but many hurdles remain to be overcome before the oligomeric state detected by biophysical methods that involve removal or substitution of the

[†] Membrane Proteins of Known 3D Structure: http://blanco.biomol.uci.edu/mpstruc (White, 2009)

natural membrane environment can be verified (Marianayagam et al., 2004; Nury et al., 2006), and before distinguishing between dimers and higher order oligomers will become trivial (Sachs and Engelman, 2006). The continuing debate around the functional importance of GPCR dimerisation is a case in point (Bouvier, 2001; Casado et al., 2009; Chabre and le Maire, 2005; Gurevich and Gurevich, 2008; Palczewski, 2006; Salahpour and Masri, 2007; Smith and Milligan, 2010).

1.3.1 Frontiers in Membrane Protein Structure Determination

The first atomic-resolution structure of a membrane protein was that of the *Rhodopseudomonas viridis* photosynthetic reaction centre solved by Deisenhofer et al. in 1985, showing that X-ray crystallography of membrane proteins was possible. Despite the immense difficulties of this technique, more than 180 unique structures have now been solved (White, 2009). This is a major achievement, but does not compare to the number of unique crystal structures of soluble proteins, of which there are now far more than 10000 (Stahlberg et al., 2001). Problems encountered in the determination of membrane protein structures with X-ray crystallography include low abundance in cells (Ford and Holzenburg, 2008) and the need to maintain an environment that at the very least mimics the membrane sufficiently to maintain the protein in its native conformation. Instability of especially mammalian membrane proteins can be circumvented by studying more stable bacterial homologues (Bayley, 2007) and advances in methods for overexpression in bacteria and eukaryotes go some way towards addressing these problems for other membrane proteins such as GPCRs (Mancia and Hendrickson, 2007).

Electron microscopy provides an alternative way to obtain three dimensional data. In an approach known as tomography, projections from transmission electron micrographs of different orientations of a sample relative to an incident beam are used to calculate 3D structures. The different orientations can be random, as was the case in the 7.5 Å resolution structure of the *E. coli* large ribosomal subunit that was obtained by cryo-electron microscopy from single molecules resting on a support film (Matadeen et al., 1999). Alternatively, and of far more relevance to membrane proteins, orientations can be imposed by tilting a specimen of uniformly oriented molecules, such

as two dimensional crystals. If crystals are large enough and well ordered, data from the recorded image can be combined with that from a diffraction pattern in the back focal plane of the objective lens (Ford and Holzenburg, 2008). This latter approach, referred to as electron crystallography, is particularly of interest for membrane proteins as it promises the study of the proteins in a near physiological environment. The technique has two major advantages. Less protein is needed than for three dimensional crystals, and since images as well as diffraction patterns of the 2D crystals can be recorded, both amplitude and phase information can be obtained, which avoids the phase problem encountered in X-ray crystallography (Ford and Holzenburg, 2008; Yin et al., 2005). Careful specimen preparation has enabled high resolution structure determination from naturally occurring 2D crystals, such as those formed by bacteriorhodopsin (Henderson et al., 1990), or from 2D crystals formed spontaneously by some proteins upon detergent solubilisation, such as the light harvesting complex-II (LHC-II) (Kuhlbrandt et al., 1994). The formation of 2D crystals from other membrane proteins in artificial bilayers, however, is still very much a trial and error process (Yin et al., 2005). For proteins that can be recombinantly overexpressed, histidine tags can be used to encourage crystallisation on lipid membranes with nickel-coupled lipids (Lebeau et al., 2001; Lévy et al., 2001, 1999). With few exceptions, the achievable resolution with this method is still limited to about 5-8 Å (Ford and Holzenburg, 2008). One reason for this is that the specimen cannot usually be tilted by more than 60°, resulting in a 'missing cone' of information. However, with improvements in sample preparation and image processing, resolution can even surpass that of X-ray crystallography, as highlighted by the 1.9 Å structure of Aquaporin (Gonen et al., 2005).

1.3.2 Membrane Protein Crowding

It is widely recognised that the crowded environment experienced by proteins in the cytosol has important implications for the biophysical investigation of many biological processes (Ellis, 2001; Ellis and Minton, 2003; Hong and Gierasch, 2010; Zhou et al., 2008). There are many experimental studies and theoretical models of the effects of 'macromolecular crowding', or the excluded volume effect, on cytosolic proteins (Dong

et al., 2010; Elcock, 2010; Hong and Gierasch, 2010; McGuffee and Elcock, 2010). Two-dimensional macromolecular crowding of membrane proteins (Zhou, 2009) is far less well studied, but given the high surface density of membrane proteins in biological membranes (Alberts et al., 2002; Dupuy and Engelman, 2008) it is clear that it must play a key role in membrane protein oligomerisation (Woolf and Linderman, 2003) and clustering (Sieber et al., 2007). These mechanisms are instrumental in neurotransmission (Stollberg and Fraser, 1990), immune regulation (Liew et al., 2005; Paul, 2008), chemotaxis (Sourjik, 2004), cell adhesion (Arnold et al., 2004) and many other membrane-associated biological processes (Bethani et al., 2010). Experimental approaches capable of measuring and dynamically controlling the surface density of membrane proteins are needed to verify theoretical predictions and to enable the rigorous characterisation of lateral membrane protein interactions. The experiments described in Chapter 6 take the first steps towards this goal with Droplet Interface Bilayers (DIBs).

1.4 Model Membrane Systems

Advances in the design of experimental membrane models continue to address the challenge of providing a physiologically relevant environment for the study of membrane biophysics and membrane protein function in a simplified system (Arumugam et al., 2011). Made from either natural or synthetic lipids, these systems exist a large variety of configurations: Bilayers in the form of free or tethered vesicles (liposomes), depending on their size either referred to as small unilamellar vesicles (tens of nanometers) or giant unilamellar vesicles (GUVs, tens of microns in diameter); lipid nanodiscs stabilised by membrane scaffolding protein; supported lipid bilayers in direct contact with a solid substrate or spaced from it in a number of ways; free standing bilayers formed across apertures or nanopatterned surfaces; lipid nanotubes which can be pulled from vesicles; coated beads; and aqueous droplets that form bilayers in a surrounding oil phase. The most closely relevant systems to the DIBs used in this thesis are described in more detail below in the context of the techniques used to interrogate the bilayer, along with highlights of a few of the most recent devel-

opments in model membrane systems. For more details of other model systems, the reader is referred to excellent reviews by Castellana and Cremer (2006), Chan and Boxer (2007) and Loose and Schwille (2009).

1.4.1 Membrane Protein Reconstitution

Model membrane systems have been used extensively for the study of classes of membrane protein that insert spontaneously into bilayers by the cooperative action of monomers. These include β-barrel bacterial pore forming toxins (PFTs) such as α-Hemolysin (α-HL), α-toxins such as the actinoporins produced by sea anemones (Kristan et al., 2009) and antimicrobial peptides, a highly diverse set of soluble amphipathic molecules present in many multicellular organisms, such as alamethicin and magainin to name but a few (Huang, 2006; Zasloff, 2002). The introduction, or reconstitution, of other membrane proteins into planar bilayers is far from trivial (Miller, 1986). Pre-formed β-barrel protein pore oligomers such as α-HL heptamer or bacterial and mitochondrial outer membrane proteins (OMPs) can be stabilised by a low level of detergent such as sodium dodecyl sulfate (SDS) or deoxycholate (DOC) and added to the aqueous solution to spontaneously insert into bilayers. Such spontaneous insertion can be sufficient, as only a small number of functional pores are needed for single molecule measurements. For non-spontaneously inserting classes such as ion channels, reconstitution of purified membrane protein into vesicles before addition to the aqueous solution – an entire subject area of its own, thoroughly reviewed by Rigaud and Lévy (2003) – can facilitate insertion by fusion of the resulting proteoliposomes with the planar bilayer. Fusion can be encouraged by salt gradients or the inclusion of fusogenic peptides such as nystatin (Woodbury and Miller, 1990). In a different approach, α-HL, the potassium channel KcsA and Leukocidin pore protein (Luk) have been inserted mechanically in a controlled manner by touching an agarose-tipped probe containing purified protein directly to the bilayer (Holden and Bayley, 2005). To circumvent the need for laborious and expensive protein purification of protein expressed either by cell free synthesis (coupled *in vitro* transcription and translation, IVTT) or by overexpression of recombinant protein in *E. coli*, the authors developed this technique further to permit the direct transfer of both polytopic

α-helical and β-barrel membrane proteins from overexpressing bacterial colonies to the artificial membrane by using a sharp glass probe (Holden et al., 2006).

1.4.2 Planar Lipid Bilayers for Single Channel Recording

In a method first developed by Mueller et al. (1962), planar bilayers for the electrical interrogation of membrane proteins are formed across an approximately 100 μm diameter aperture pierced through a plastic film between two aqueous chambers. The separating plastic is often referred to as a septum and now usually consists of 20 μm thick polytetrafluoroethylene (PTFE, or Teflon) (Maglia et al., 2010). In the so-called Müller-Rudin method, a solution of a lipid in a mixture of hydrocarbon solvents is painted across the aperture in the septum with a small brush before filling the chambers with aqueous solution to immerse the aperture. The lipid molecules in the solution at the aperture form monolayers at the hydrocarbon-water interface, and the solvent begins to drain to the edge of the aperture, aided by gravity. Eventually, the two monolayers on either side of the septum contact to form a bilayer, a process accompanied by optical blackening of the film suspended across the aperture. Hence, the resulting planar bilayer is also known as a black lipid membrane (BLM). Montal and Mueller (1972) developed this method further to shorten the time to bilayer formation, in a technique also referred to as the apposition of monolayers, or the Montal-Müller method. To achieve fast bilayer formation, the edge of the aperture is pretreated with a mixture of a non-volatile n-alkane such as decane or hexadecane (but no lipid) in a solvent such as pentane or hexane before the chambers are filled to a level below that of the aperture. A drop of lipid dissolved in a volatile solvent such as pentane or hexane is then added to the aqueous solution. As the solvent evaporates, a monolayer of lipid forms at the air-water interface on the surface of the solution in the chamber, essentially creating a Langmuir-Blodgett trough. Upon raising the level of the aqueous solution in one chamber past the aperture, the lipid monolayer in this region bends so that the hydrocarbon tails interface with the pretreated septum, resulting in a vertically oriented monolayer across the aperture. Repeating this procedure with the solution in the other chamber results in the apposition of the two monolayers and a bilayer is formed more or less immediately, surrounded by a ring of

the pretreatment alkane, referred to as an annulus or torus (White et al., 1976).

1.4.3 Supported Lipid Bilayers

A major limitation of the planar bilayers described above is that they are difficult to image and are therefore outside of the reach of powerful characterisation methods, including single molecule fluorescence (SMF), surface characterisation methods such as quartz crystal microbalance (QCM), surface plasmon resonance (SPR), SPR excited fluorescence, ellipsometry, optical waveguide methods such as dual polarisation interferometry (DPI) and surface scanning techniques such as atomic force microscopy (AFM) (Alessandrini and Facci, 2011). This has led to the development of many types of horizontal bilayers on solid substrates, collectively referred to as supported lipid bilayers (SLBs).

SLBs can be formed on a large variety of substrates including metals such as gold (required for SMF and SPR), semiconductor oxides, mica, quartz and borosilicate glass. Composite substrates can also be used and serve a number of functions. As an example, gold surfaces, which can be too rough for sensitive surface characterisation techniques, can be smoothed by the deposition of a thin layer of silicon dioxide (SiO_2) by exposing a layer of polyhydroxymethyl siloxane (PHMS) to oxygen plasma (Satriano et al., 2010, 2008). Nanofabricated substrates can provide patterned surfaces to induce membrane curvature and anomalous diffusion (Jung et al., 2011; Tero et al., 2011; Yu and Groves, 2010), or can act as zero mode waveguides in advanced SMF techniques (Samiee et al., 2006).

1.4.3.1 Solid Supported Lipid Bilayers

Deposition of bilayers on planar substrates can be achieved in a number of ways, a subset of which are illustrated in Figure 1.3 A. In a method known as Langmuir-Blodgett deposition, the substrate is raised through the surface of a Langmuir-Blodgett trough, resulting in the transfer of a monolayer as illustrated in Figure 1.3 A-1. By subsequently lowering the substrate through the surface, the monolayer is folded back on itself, creating a bilayer. Alternatively, the monolayer on the substrate can simply

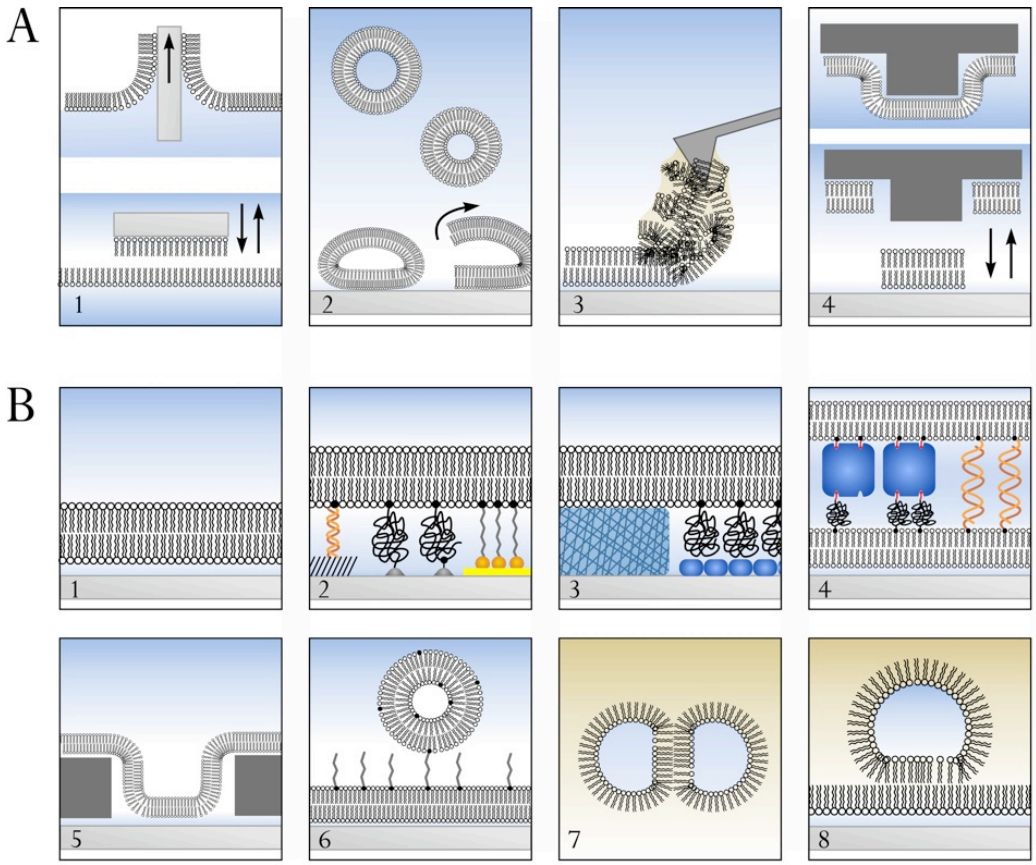

Figure 1.3: Model bilayer systems. **(A)** Methods for the deposition of supported lipid bilayers (SLBs). For details see main text. *(A-1)* Langmuir-Blodgett deposition. *(A-2)* Vesicle rupture. *(A-3)* Dip-pen nanolithography. *(A-4)* Microcontact printing. **(B)** Common types of model bilayer systems. For details and references, see main text. *(B-1)* Solid supported lipid bilayer (s-SLB). *(B-2)* Tethered lipid bilayers (t-SLB). Tethers can consist of spacers such as DNA (left), functionalised lipopolymers (centre) or thiolipids interfacing with a gold surface (right). *(B-3)* Cushioned bilayers. A hydrogel cushioned bilayer (left) and a double cushioned bilayer containing non-functionalised lipopolymers resting on a BSA layer. *(B-4)* Double bilayer systems, spaced by modular large components such as Streptavidin linked to both membranes via biotinylated lipids or lipopolymers (left) or by complementary DNA strands. *(B-5)* A bilayer on a nanostructured substrate such as a zero mode waveguide. *(B-6)* A tethered vesicle. *(B-7)* A Droplet Interface Bilayer (DIB). *(B-8)* An alternative configuration of a DIB.

be brought into contact with the surface of the Langmuir-Blodgett trough a second time, resulting in the transfer to the second leaflet to the substrate (Moraille and Badia, 2003). Vesicle rupture on substrates with high surface energy that drives flattening and bursting of the vesicles can also be used to form a coherent bilayer (Gözen et al., 2010; McConnell et al., 1986) (Figure 1.3 A-2). On SiO_2-based substrates, this process occurs in three phases. At first, intact vesicles populate the surface. Vesicle rupture then occurs spontaneously at a critical coverage of vesicles . Finally, patches of bilayer coalesce to form a contiguous bilayer sheet that covers the whole surface (Reimhult et al., 2006; Richter et al., 2006). The key parameters that drive vesicle rupture at the substrate are lipid composition and surface charge density (Dimitrievski and Kasemo, 2009; Gromelski et al., 2009; Oleson and Sahai, 2008). Divalent or trivalent cations such as Ca^{2+} or Eu^{3+} are often used to screen charges between the head groups and the substrate and thus promote adhesion of the bilayer to the surface (Kim et al., 2006; Lobovkina et al., 2010). On other substrates where SLBs do not spontaneously form, vesicle rupture can be induced by a critical concentration of these ions (Gözen et al., 2010). Negatively charged surfaces can improve homogeneous coverage (Gromelski et al., 2009), but positively charged surfaces can encourage rupture. Tuning cholesterol content, cationic lipid content and temperature can result in a number of different 'spreading modes' (Nissen et al., 1999; Sackmann, 1996). On SiO_2 substrates, multilamellar vesicles spread spontaneously until a single bilayer remains on the substrate. Conversely, patches of deposited bilayer stemming from ruptured unilamellar vesicles generally coalesce to form a contiguous sheet. With sufficiently optimised conditions, even cells can be induced to spread and rupture on substrates such as SiO_2, resulting in 'inside-out' biological membrane sheets that are fully accessible to the techniques mentioned above (Danelon et al., 2006; Perez et al., 2006). Methods that afford greater control over the position and shape of the deposited bilayer include dip pen lithography (Sekula et al., 2008) (Figure 1.3 A-3) and microcontact printing using raised plasma-oxidised polydimethyl siloxane (PDMS) surfaces, for example (Hovis and Boxer, 2001; Jung et al., 2005; Majd and Mayer, 2005) (Figure 1.3 A-4). These methods have been used to create arrays of bilayer patches for high throughput screening applications (Majd and Mayer, 2005).

In systems where bilayers are directly deposited onto substrates, a thin water layer of $\sim 10-20$ Å exists between the lipid and the surface, which suffices to maintain membrane fluidity (Castellana and Cremer, 2006; Xing and Faller, 2008; Zwang et al., 2010). However, this layer is often too thin to provide the requisite space for membrane proteins with any ectodomains to insert into the bilayer and diffuse freely (Tanaka and Sackmann, 2005; Wagner and Tamm, 2000). In addition, it provides only a small ionic reservoir for electrochemical characterisation of membrane proteins. Langmuir-Blodgett deposition on solid substrates also tends to result in incomplete coverage and a large amount of defects in the SLB, making it extremely difficult to obtain reproducible results (Czolkos et al., 2011; Mashaghi et al., 2008).

1.4.3.2 Tethered and Cushioned SLBs

To mitigate these problems, bilayers can also be tethered to the surface by a covalently linked spacer molecule, or be made to rest on nonspecific polymer, protein, or hydrogel cushions (Tanaka and Sackmann, 2005; Wong et al., 1999; Yuan et al., 1996). These systems provide a larger intermediate water layer with a thickness that can be tuned, greatly improving the conditions for the incorporation and diffusion of functional membrane proteins (Wagner and Tamm, 2000). Tethering requires the incorporation of modified lipids such as thiolipids, functional lipopolymers or biotinylated lipids in the bilayer. The spacing from the substrate is provided by a linker between the functional group and the lipid, such as, for example, a tetraethyleneoxy (TEO) chain in the case of thiolipids (Becucci et al., 2010; Schiller et al., 2003), a polymer chain such as polyethylene glycol (PEG), or by modular spacers such as DNA or protein. Glass can by modified with silanol groups (Chung and Park, 2009) or other covalent modifications resulting in functionalised amine surfaces (Rossi et al., 2007), or covalently linked biotinylated bovine serum albumin (BSA) to provide attachment sites for tethers (Taylor et al., 2007). Silane-polyethyleneglycol lipid is an example of a functional lipopolymer used as a common tether for glass surfaces (Wagner and Tamm, 2000), and thiolipids such as the archaea lipid analogue DPTL result in tethered bilayers with good resistive properties on gold surfaces (Figure 1.3 B-2) (Naumann et al., 2003; Schiller et al., 2003). Cushioned bilayers on the other hand

are not covalently attached to the substrate. However, cushioning can still be provided by PEG chains of modified lipid, either resting directly on the surface or on a layer of BSA in a 'double cushion' configuration (Diaz et al., 2008). Alternatively, nonspecific spacers such as hydrogels or other polymers can be used. Finally, double membrane systems provide a good model for systems such as the mitochondrial intermembrane space (Murray et al., 2009). Figure 1.3 B shows schematic illustrations of some common model membrane systems.

1.4.3.3 Confined and Suspended SLBs

In most implementations of SLBs, single channel recording is problematic. It is difficult to achieve a suitable electrical seal between the the two sides of the bilayer, as a deposited membrane has open edges and often also contains defects that occur during deposition (Richter et al., 2003). Electrochemical characterisation of functionally incorporated membrane proteins is therefore in many cases still limited to macroscopic measurements such as electron impedance spectroscopy (EIS) (Naumann et al., 2003; Vockenroth et al., 2007). Danelon et al. (2006) report a seal of >1 GΩ using lithographically confined gold electrodes, but point out that macroscopic membrane resistance differences measured with different methods without specific and reproducible dose response character should not be taken as proof of channel activity, as membrane defects cannot at present be ruled out. A number of methods of have suspended planar bilayers over small apertures or porous substrates to create suitable aqueous volumes on both sides of the bilayer to enable SCR in SLBs, a method referred to as planar patch clamping. Bilayer suspension can be achieved, for example, by using glass nanopores, (White et al., 2007) or porous silicon nitride diaphragms (Kresák et al., 2009). A major advantage is that suspended bilayers tend to be more stable than the conventional planar Black Lipid Membranes (BLMs) described in section 1.4.2 (Bayley, 2007).

1.4.4 Droplet Interface Bilayers

Droplet Interface Bilayer systems address the problem of ensuring a tight electrical seal by completely enclosing the aqueous volumes on either side of the bilayer in an oil

phase. The formation of DIB is straightforwardly achieved by pipetting small aqueous volumes into a solution of lipid in an alkane such as hexadecane, and allowing a monolayer to assemble at the oil-water interface. Upon bringing droplets into contact, the oil in the contact region is displaced and lipid bilayers form spontaneously (Figure 1.3 B-7). By piercing the droplets with an electrode, essentially a similar configuration to a Montal-Müller bilayer as described in section 1.4.2 is achieved, with the additional advantage of far greater stability (Bayley et al., 2008). In marked contrast to other SLBs, droplet integrity provides a straightforward diagnostic of a defect-free bilayer.

In an alternative configuration, a single droplet can be interfaced with a planar supporting hydrogel on a solid substrate such as a glass coverslip (Figure 1.3 B-8). This method essentially takes advantage of the benefits of SLBs with respect to the accessibility of the bilayer to imaging methods, while retaining the ability to carry out electrical recordings. This arrangement is the basis of the experiments described in this thesis and will be described in full detail in Chapter 2.

1.5 Summary

There is constant demand for model systems that allow us to gain a deeper understanding of lipid membrane structure, dynamics and function, and how these properties impact on membrane proteins. DIBs have the prerequisites to become an invaluable tool in this respect. In the next chapters, their potential for the physical manipulation of lipid membranes is explored, followed by a demonstration of their use in the characterisation of bilayer thickness. Finally, the first steps are taken towards using physical bilayer manipulation in DIBs to control the surface density of integral membrane proteins, with the aim of beginning to address the questions posed by our recent improved understanding of the degree of crowding that is prevalent in biological membranes.

Bibliography

Aguilella, V. M. and S. M. Bezrukov (2001). Alamethicin channel conductance modified by lipid charge. *European Biophysics Journal 30*(4), 233–241.

Alberts, B., A. Johnson, J. Lewis, M. Raff, K. Roberts, and P. Walter (2002). *Molecular Biology of the Cell* (4th ed.). Garland Science, New York.

Alessandrini, A. and P. Facci (2011). Unraveling lipid/protein interaction in model lipid bilayers by atomic force microscopy. *Journal of Molecular Recognition 24*(3), 387–396.

Allen, J. A., R. A. Halverson-Tamboli, and M. M. Rasenick (2007). Lipid raft microdomains and neurotransmitter signalling. *Nature Reviews Neuroscience 8*(2), 128–140.

Andersen, O. S. and R. E. Koeppe (2007). Bilayer thickness and membrane protein function: An energetic perspective. *Annual Review of Biophysics and Biomolecular Structure 36*(1), 107–130.

Arnold, M., E. A. Cavalcanti-Adam, R. Glass, J. Blümmel, W. Eck, M. Kantlehner, H. Kessler, and J. P. Spatz (2004). Activation of integrin function by nanopatterned adhesive interfaces. *ChemPhysChem 5*(3), 383–388.

Arumugam, S., G. Chwastek, and P. Schwille (2011). Protein–membrane interactions: The virtue of minimal systems in systems biology. *Wiley Interdisciplinary Reviews: Systems Biology and Medicine 3*(3), 269–280.

Ashcroft, F. M. (2006). From molecule to malady. *Nature 440*(7083), 440–447.

Bayley, H. (2007). Understanding and manipulating channels and pores. *Molecular BioSystems 3*(10), 645–647.

Bayley, H., B. Cronin, A. Heron, M. A. Holden, W. L. Hwang, R. Syeda, J. Thompson, and M. Wallace (2008). Droplet Interface Bilayers. *Molecular BioSystems 4*(12), 1191.

Becucci, L., M. D'Amico, S. Daniele, M. Olivotto, A. Pozzi, and R. Guidelli (2010). A metal-supported biomimetic micromembrane allowing the recording of single-channel activity and of impedance spectra of membrane proteins. *Bioelectrochemistry 78*(2), 176–180.

Bethani, I., S. S. Skanland, I. Dikic, and A. Acker-Palmer (2010). Spatial organization of transmembrane receptor signalling. *EMBO Journal 29*(16), 2677–2688.

Beyder, A., J. L. Rae, C. Bernard, P. R. Strege, F. Sachs, and G. Farrugia (2010). Mechanosensitivity of Nav1.5, a voltage-sensitive sodium channel. *The Journal of Physiology 588*(24), 4969–4985.

Bouvier, M. (2001). Oligomerization of G-protein-coupled transmitter receptors. *Nature Reviews Neuroscience 2*(4), 274–286.

Brown, F. L., D. M. Leitner, J. A. McCammon, and K. R. Wilson (2000). Lateral diffusion of membrane proteins in the presence of static and dynamic corrals: Suggestions for appropriate observables. *Biophysical Journal 78*(5), 2257–2269.

Caffrey, M. and V. Cherezov (2009). Crystallizing membrane proteins using lipidic mesophases. *Nature Protocols 4*(5), 706–731.

Cantor, R. S. (1999). The influence of membrane lateral pressures on simple geometric models of protein conformational equilibria. *Chemistry and Physics of Lipids 101*(1), 45–56.

Casado, V., A. Cortes, J. Mallol, K. Perez-Capote, S. Ferre, C. Lluis, R. Franco, and E. Canela (2009). GPCR homomers and heteromers: A better choice as targets for drug development

than GPCR monomers? *Pharmacology & Therapeutics 124*(2), 248–257.

Casal, H. L. and R. N. McElhaney (1990). Quantitative determination of hydrocarbon chain conformational order in bilayers of saturated phosphatidylcholines of various chain lengths by fourier transform infrared spectroscopy. *Biochemistry 29*(23), 5423–5427.

Castellana, E. T. and P. S. Cremer (2006). Solid supported lipid bilayers: From biophysical studies to sensor design. *Surface Science Reports 61*(10), 429–444.

Chabre, M. and M. le Maire (2005). Monomeric G-protein-coupled receptor as a functional unit. *Biochemistry 44*(27), 9395–9403.

Chan, Y.-H. M. and S. G. Boxer (2007). Model membrane systems and their applications. *Current Opinion in Chemical Biology 11*(6), 581–587.

Chapman, D. (1993). Lipid phase transitions. *In:* M. Shinitzky (Ed.), *Biomembranes: Physical Aspects*, pp. 29–61. VCH: Weinheim.

Cheng, J. T., J. D. Hale, M. Elliott, R. E. Hancock, and S. K. Straus (2011). The importance of bacterial membrane composition in the structure and function of aurein 2.2 and selected variants. *Biochimica et Biophysica Acta (BBA) - Biomembranes 1808*(3), 622–633.

Cherezov, V., J. Clogston, M. Z. Papiz, and M. Caffrey (2006). Room to move: Crystallizing membrane proteins in swollen lipidic mesophases. *Journal of Molecular Biology 357*(5), 1605–1618.

Chung, H. J. and T. G. Park (2009). Self-assembled and nanostructured hydrogels for drug delivery and tissue engineering. *Nano Today 4*(5), 429–437.

Cramer, W. A., H. Zhang, J. Yan, G. Kurisu, and J. L. Smith (2006). Transmembrane traffic in the cytochrome b_6f complex. *Annual Review of Biochemistry 75*(1), 769–790.

Cribier, S., A. Gulik, P. Fellmann, R. Vargas, P. F. Devaux, and V. Luzzati (1993). Cubic phase of lipid-containing systems : A translational diffusion study by fluorescence recovery after photobleaching. *Journal of Molecular Biology 229*(2), 517–525.

Czolkos, I., A. Jesorka, and O. Orwar (2011). Molecular phospholipid films on solid supports. *Soft Matter 7*(10), 4562.

Danelon, C., J. Perez, C. Santschi, J. Brugger, and H. Vogel (2006). Cell membranes suspended across nanoaperture arrays. *Langmuir 22*(1), 22–25.

Dang, T. X., E. M. Hotze, I. Rouiller, R. K. Tweten, and E. M. Wilson-Kubalek (2005). Prepore to pore transition of a cholesterol-dependent cytolysin visualized by electron microscopy. *Journal of Structural Biology 150*(1), 100–108.

Deisenhofer, J., O. Epp, K. Miki, R. Huber, and H. Michel (1985). Structure of the protein subunits in the photosynthetic reaction centre of *Rhodopseudomonas viridis* at 3 Å resolution. *Nature 318*(6047), 618–624.

Diaz, A. J., F. Albertorio, S. Daniel, and P. S. Cremer (2008). Double cushions preserve transmembrane protein mobility in supported bilayer systems. *Langmuir 24*(13), 6820–6826.

Dimitrievski, K. and B. Kasemo (2009). Influence of lipid vesicle composition and surface charge density on vesicle adsorption events: A kinetic phase diagram. *Langmuir 25*(16), 8865–8869.

Dong, H., S. Qin, and H. Zhou (2010). Effects of macromolecular crowding on protein conformational changes. *PLoS Computational Biology 6*, e1000833.

Dowhan, W. (1997). Molecular basis for membrane phospholipid diversity: Why are there so many lipids? *Annual Review of Biochemistry 66*(1), 199–232.

Dowhan, W. and M. Bogdanov (2009). Lipid-dependent membrane protein topogenesis. *Annual Review of Biochemistry 78*(1), 515–540.

Drew, L. J. (2011). Sodium channel mechanosensitivity: Pay a-tension to voltage sensor movement. *The Journal of Physiology 589*(5), 1003–1004.

Dupuy, A. D. and D. M. Engelman (2008). Protein area occupancy at the center of the red blood cell membrane. *Proceedings of the National Academy of Sciences of the United States of America 105*(8), 2848–2852.

Edidin, M. (2001). Shrinking patches and slippery rafts: Scales of domains in the plasma membrane. *Trends in Cell Biology 11*(12), 492–496.

Edidin, M. (2003). The state of lipid rafts: From model membranes to cells. *Annual Review of Biophysics and Biomolecular Structure 32*(1), 257–283.

Edidin, M., S. Kuo, and M. Sheetz (1991). Lateral movements of membrane glycoproteins restricted by dynamic cytoplasmic barriers. *Science 254*(5036), 1379 –1382.

Elcock, A. H. (2010). Models of macromolecular crowding effects and the need for quantitative comparisons with experiment. *Current Opinion in Structural Biology 20*(2), 196–206.

Ellis, R. J. (2001). Macromolecular crowding: obvious but underappreciated. *Trends in Biochemical Sciences 26*(10), 597–604.

Ellis, R. J. and A. P. Minton (2003). Cell biology: Join the crowd. *Nature 425*(6953), 27–28.

Engelman, D. M. (2005). Membranes are more mosaic than fluid. *Nature 438*(7068), 578–580.

Feigenson, G. W. (2009). Phase diagrams and lipid domains in multicomponent lipid bilayer mixtures. *Biochimica et Biophysica Acta (BBA) - Biomembranes 1788*(1), 47–52.

Ford, R. C. and A. Holzenburg (2008). Electron crystallography of biomolecules: mysterious membranes and missing cones. *Trends in Biochemical Sciences 33*(1), 38–43.

Gawrisch, K. (2005). The dynamics of membrane lipids. *In:* P. Yeagle (Ed.), *The Structure of Biological Membranes*, pp. 147–171. CRC Press: Boca Raton, FL.

Gonen, T., Y. Cheng, P. Sliz, Y. Hiroaki, Y. Fujiyoshi, S. C. Harrison, and T. Walz (2005). Lipid-protein interactions in double-layered two-dimensional AQP0 crystals. *Nature 438*(7068), 633–638.

Goñi, F. M. and A. Alonso (2009). Effects of ceramide and other simple sphingolipids on membrane lateral structure. *Biochimica et Biophysica Acta (BBA) - Biomembranes 1788*(1), 169–177.

Gözen, I., P. Dommersnes, I. Czolkos, A. Jesorka, T. Lobovkina, and O. Orwar (2010). Fractal avalanche ruptures in biological membranes. *Nat Mater 9*(11), 908–912.

Gromelski, S., A. M. Saraiva, R. Krastev, and G. Brezesinski (2009). The formation of lipid bilayers on surfaces. *Colloids and Surfaces B: Biointerfaces 74*(2), 477–483.

Gruner, S. M. (2005). Nonlamellar lipid phases. *In:* P. Yeagle (Ed.), *The Structure of Biological Membranes*, pp. 173–199. CRC Press: Boca Raton, FL.

Gurevich, V. V. and E. V. Gurevich (2008). GPCR monomers and oligomers: It takes all kinds. *Trends in Neurosciences 31*(2), 74–81.

Hamai, C., T. Yang, S. Kataoka, P. S. Cremer, and S. M. Musser (2006). Effect of average phospholipid curvature on supported bilayer formation on glass by vesicle fusion. *Biophysical Journal 90*(4), 1241–1248.

Hamill, O. P. and B. Martinac (2001). Molecular basis of mechanotransduction in living cells. *Physiological Reviews 81*(2), 685–740.

Hauser, H. and G. Poupart (2005). Lipid structure. *In:* P. Yeagle (Ed.), *The Structure of Biological Membranes*, pp. 1–51. CRC Press: Boca Raton, FL.

Henderson, R., J. Baldwin, T. Ceska, F. Zemlin, E. Beckmann, and K. Downing (1990). Model for the structure of bacteriorhodopsin based on high-resolution electron cryo-microscopy. *Journal of Molecular Biology 213*(4), 899–929.

Heron, A. J., J. R. Thompson, A. E. Mason, and M. I. Wallace (2007). Direct detection of membrane channels from gels using water-in-oil droplet bilayers. *Journal of the American Chemical Society 129*(51), 16042–16047.

Heuck, A. P., E. M. Hotze, R. K. Tweten, and A. E. Johnson (2000). Mechanism of membrane insertion of a multimeric β-barrel protein: Perfringolysin O creates a pore using ordered and coupled conformational changes. *Molecular Cell 6*(5), 1233–1242.

Heuck, A. P., P. C. Moe, and B. B. Johnson (2010). The cholesterol-dependent cytolysin family of gram-positive bacterial toxins. *Sub-Cellular Biochemistry 51*, 551–577.

Holden, M. A. and H. Bayley (2005). Direct introduction of single protein channels and pores into lipid bilayers. *Journal of the American Chemical Society 127*(18), 6502–6503.

Holden, M. A., L. Jayasinghe, O. Daltrop, A. Mason, and H. Bayley (2006). Direct transfer of membrane proteins from bacteria to planar bilayers for rapid screening by single-channel recording. *Nature Chemical Biology 2*(6), 314–318.

Holowka, D., J. A. Gosse, A. T. Hammond, X. Han, P. Sengupta, N. L. Smith, A. Wagenknecht-Wiesner, M. Wu, R. M. Young, and B. Baird (2005). Lipid segregation and IgE receptor signaling: A decade of progress. *Biochimica et Biophysica Acta (BBA) - Molecular Cell Research 1746*(3), 252–259.

Hong, J. and L. M. Gierasch (2010). Macromolecular crowding remodels the energy landscape of a protein by favoring a more compact unfolded state. *Journal of the American Chemical Society 132*(30), 10445–10452.

Hovis, J. S. and S. G. Boxer (2001). Patterning and composition arrays of supported lipid bilayers by microcontact printing. *Langmuir 17*(11), 3400–3405.

Huang, H. W. (2006). Molecular mechanism of antimicrobial peptides: The origin of cooperativity. *Biochimica et Biophysica Acta (BBA) - Biomembranes 1758*(9), 1292–1302.

Iacovache, I., F. G. van der Goot, and L. Pernot (2008). Pore formation: An ancient yet complex form of attack. *Biochimica et Biophysica Acta (BBA) - Biomembranes 1778*(7-8), 1611–1623.

Iverson, T. M., C. Luna-Chavez, G. Cecchini, and D. C. Rees (1999). Structure of the *Escherichia coli* fumarate reductase respiratory complex. *Science 284*(5422), 1961 –1966.

Jacobson, K., E. D. Sheets, and R. Simson (1995). Revisiting the fluid mosaic model of membranes. *Science 268*(5216), pp. 1441–1442.

Jain, M. K. and H. B. White 3rd (1977). Long-range order in biomembranes. *Advances in Lipid Research 15*, 1–60.

Jensen, M. Ø. and O. G. Mouritsen (2004). Lipids do influence protein function – the hydrophobic matching hypothesis revisited. *Biochimica et Biophysica Acta (BBA) - Biomembranes 1666*(1-2), 205–226.

Jung, M., N. Vogel, and I. Köper (2011). Nanoscale patterning of solid-supported membranes by integrated diffusion barriers. *Langmuir 27*(11), 7008–7015.

Jung, S., M. A. Holden, P. S. Cremer, and C. P. Collier (2005). Two-component membrane lithography via lipid backfilling. *ChemPhysChem 6*(3), 423–426.

Karnovsky, M. J., A. M. Kleinfeld, R. L. Hoover, E. A. Dawidowicz, D. E. McIntyre, E. A. Salzman, and R. D. Klausner (1982). Lipid domains in membranes. *Annals of the New York Academy of Sciences 401*, 61–75.

Kim, Y., M. M. Rahman, Z. Zhang, N. Misawa, R. Tero, and T. Urisu (2006). Supported lipid bilayer formation by the giant vesicle fusion induced by vesicle-surface electrostatic attractive interaction. *Chemical Physics Letters 420*(4-6), 569–573.

Kresák, S., T. Hianik, and R. L. C. Naumann (2009). Giga-seal solvent-free bilayer lipid membranes: from single nanopores to nanopore arrays. *Soft Matter 5*(20), 4021.

Kristan, K. C., G. Viero, M. Dalla Serra, P. Macek, and G. Anderluh (2009). Molecular mechanism of pore formation by actinoporins. *Toxicon 54*(8), 1125–1134.

Kuhlbrandt, W., D. N. Wang, and Y. Fujiyoshi (1994). Atomic model of plant light-harvesting complex by electron crystallography. *Nature 367*(6464), 614–621.

Kusumi, A., C. Nakada, K. Ritchie, K. Murase, K. Suzuki, H. Murakoshi, R. S. Kasai, J. Kondo, and T. Fujiwara (2005). Paradigm shift of the plasma membrane concept from the two-dimensional continuum fluid to the partitioned fluid: High-speed single-molecule tracking of membrane molecules. *Annual Review of Biophysics and Biomolecular Structure 34*(1), 351–378.

Kusumi, A., Y. Sako, and M. Yamamoto (1993). Confined lateral diffusion of membrane receptors as studied by single particle tracking (nanovid microscopy). Effects of calcium-induced differentiation in cultured epithelial cells. *Biophysical Journal 65*(5), 2021–2040.

Lagerstrom, M. C. and H. B. Schioth (2008). Structural diversity of G-protein-coupled receptors and significance for drug discovery. *Nature Reviews Drug Discovery 7*(4), 339–357.

Landau, E. M. and J. P. Rosenbusch (1996). Lipidic cubic phases: A novel concept for the crystallization of membrane proteins. *Proceedings of the National Academy of Sciences of the United States of America 93*(25), 14532–14535.

Lebeau, L., F. Lach, C. Vénien-Bryan, A. Renault, J. Dietrich, T. Jahn, M. G. Palmgren, W. Kühlbrandt, and C. Mioskowski (2001). Two-dimensional crystallization of a membrane protein on a detergent-resistant lipid monolayer. *Journal of Molecular Biology 308*(4), 639–647.

Lee, A. G. (2003). Lipid-protein interactions in biological membranes: A structural perspective. *Biochimica et Biophysica Acta (BBA) - Biomembranes 1612*(1), 1–40.

Lévy, D., M. Chami, and J. Rigaud (2001). Two-dimensional crystallization of membrane proteins: The lipid layer strategy. *FEBS Letters 504*(3), 187–193.

Lévy, D., G. Mosser, O. Lambert, G. S. Moeck, D. Bald, and J. Rigaud (1999). Two-Dimensional crystallization on lipid layer: A successful approach for membrane proteins. *Journal of Structural Biology 127*(1), 44–52.

Lewis, R. N. A. H. and R. N. McElhaney (2005). The mesomorphic behavior of lipid bilayers. *In:* P. Yeagle (Ed.), *The Structure of Biological Membranes*, pp. 53–120. CRC Press: Boca Raton, FL.

Lichtenberg, D. (1993). Micelles and liposomes. *In:* M. Shinitzky (Ed.), *Biomembranes: Physical Aspects*, pp. 63–95. VCH: Weinheim.

Liew, F. Y., D. Xu, E. K. Brint, and L. A. J. O'Neill (2005). Negative regulation of toll-like receptor-mediated immune responses. *Nat Rev Immunol 5*(6), 446–458.

Liu, Y., D. Engelman, and M. Gerstein (2002). Genomic analysis of membrane protein families: abundance and conserved motifs. *Genome Biology 3*(10), research0054.1–research0054.12.

Lobovkina, T., I. Gözen, Y. Erkan, J. Olofsson, S. G. Weber, and O. Orwar (2010). Protrusive growth and periodic contractile motion in surface-adhered vesicles induced by Ca^{2+}-gradients. *Soft Matter 6*(2), 268.

Loose, M. and P. Schwille (2009). Biomimetic membrane systems to study cellular organization. *Journal of Structural Biology 168*(1), 143–151.

Lundbæk, J. A. (2008). Lipid bilayer–mediated regulation of ion channel function by amphiphilic drugs. *The Journal of General Physiology 131*(5), 421–429.

Lundbæk, J. A. and O. S. Andersen (1999). Spring constants for channel-induced lipid bilayer deformations estimates using gramicidin channels. *Biophysical Journal 76*(2), 889–895.

Luzzati, V., T. Gulik-Krzywicki, and A. Tardieu (1968). Polymorphism of lecithins. *Nature 218*(5146), 1031–1034.

Maglia, G., A. J. Heron, D. Stoddart, D. Japrung, H. Bayley, and N. G. Walter (2010). Analysis of single nucleic acid molecules with protein nanopores. In *Single Molecule Tools, Part B: Super-Resolution, Particle Tracking, Multiparameter, and Force Based Methods*, Volume 475, pp. 591–623. Academic Press.

Majd, S. and M. Mayer (2005). Hydrogel stamping of arrays of supported lipid bilayers with various lipid compositions for the screening of Drug–Membrane and Protein–Membrane interactions. *Angewandte Chemie International Edition 44*(41), 6697–6700.

Mancia, F. and W. A. Hendrickson (2007). Expression of recombinant G-Protein coupled receptors for structural biology. *Molecular BioSystems 3*(10), 723.

Marianayagam, N. J., M. Sunde, and J. M. Matthews (2004). The power of two: protein dimerization in biology. *Trends in Biochemical Sciences 29*(11), 618–625.

Marsh, D. (1996). Lateral pressure in membranes. *Biochimica et Biophysica Acta (BBA) - Reviews on Biomembranes 1286*(3), 183–223.

Mashaghi, A., M. Swann, J. Popplewell, M. Textor, and E. Reimhult (2008). Optical anisotropy of supported lipid structures probed by waveguide spectroscopy and its application to study of supported lipid bilayer formation kinetics. *Analytical Chemistry 80*(10), 3666–3676.

Matadeen, R., A. Patwardhan, B. Gowen, E. V. Orlova, T. Pape, M. Cuff, F. Mueller, R. Brimacombe, and M. van Heel (1999). The *Escherichia coli* large ribosomal subunit at 7.5 Å resolution. *Structure 7*(12), 1575–1583.

Maxfield, F. R. and I. Tabas (2005). Role of cholesterol and lipid organization in disease. *Nature 438*(7068), 612–621.

McConnell, H., T. Watts, R. Weis, and A. Brian (1986). Supported planar membranes in studies of cell-cell recognition in the immune system. *Biochimica et Biophysica Acta (BBA) - Reviews on Biomembranes 864*(1), 95–106.

McGuffee, S. R. and A. H. Elcock (2010). Diffusion, crowding & protein stability in a dynamic molecular model of the bacterial cytoplasm. *PLoS Comput Biol 6*(3), e1000694.

Megha and E. London (2004). Ceramide selectively displaces cholesterol from ordered lipid domains (Rafts). *Journal of Biological Chemistry 279*(11), 9997–10004.

Miller, C. (1986). *Ion Channel Reconstitution*. Plenum Press: New York.

Mitra, K., I. Ubarretxena-Belandia, T. Taguchi, G. Warren, and D. M. Engelman (2004). Modulation of the bilayer thickness of exocytic pathway membranes by membrane proteins rather than cholesterol. *Proceedings of the National Academy of Sciences of the United States of America 101*(12), 4083–4088.

Mongrand, S., T. Stanislas, E. M. Bayer, J. Lherminier, and F. Simon-Plas (2010). Membrane rafts in plant cells. *Trends in Plant Science 15*(12), 656–663.

Montal, M. and P. Mueller (1972). Formation of bimolecular membranes from lipid monolayers and a study of their electrical properties. *Proceedings of the National Academy of Sciences of the United States of America 69*(12), 3561–3566.

Moraille, P. and A. Badia (2003). Nanoscale stripe patterns in phospholipid bilayers formed by the Langmuir-Blodgett technique. *Langmuir 19*(19), 8041–8049.

Morris, C. E. and P. F. Juranka (2007). Nav channel mechanosensitivity: Activation and inactivation accelerate reversibly with stretch. *Biophysical Journal 93*(3), 822–833.

Mouritsen, O. G. and M. Bloom (1993). Models of lipid-protein interactions in membranes. *Annual Review of Biophysics and Biomolecular Structure 22*(1), 145–171.

Mueller, P., D. O. Rudin, H. Ti Tien, and W. C. Wescott (1962). Reconstitution of cell membrane structure *in vitro* and its transformation into an excitable system. *Nature 194*(4832), 979–980.

Mukherjee, S. and F. R. Maxfield (2004). Membrane domains. *Annual Review of Cell and Developmental Biology 20*(1), 839–866.

Munro, S. (2003). Lipid rafts: Elusive or illusive? *Cell 115*(4), 377–388.

Murase, K., T. Fujiwara, Y. Umemura, K. Suzuki, R. Iino, H. Yamashita, M. Saito, H. Murakoshi, K. Ritchie, and A. Kusumi (2004). Ultrafine membrane compartments for molecular diffusion as revealed by single molecule techniques. *Biophysical Journal 86*(6), 4075–4093.

Murray, D., L. Tamm, and V. Kiessling (2009). Supported double membranes. *Journal of Structural Biology 168*(1), 183–189.

Nagle, J. F. and S. Tristram-Nagle (2000). Structure of lipid bilayers. *Biochimica et Biophysica Acta (BBA) - Reviews on Biomembranes 1469*(3), 159–195.

Naumann, R., D. Walz, S. Schiller, and W. Knoll (2003). Kinetics of valinomycin-mediated K+ ion transport through tethered bilayer lipid membranes. *Journal of Electroanalytical Chemistry 550-551*, 241–252.

Nissen, J., S. Gritsch, G. Wiegand, and J. Rädler (1999). Wetting of phospholipid membranes on hydrophilic surfaces - concepts towards self-healing membranes. *The European Physical Journal B 10*(2), 335–344.

Nury, H., C. Dahout-Gonzalez, V. Trézéguet, G. Lauquin, G. Brandolin, and E. Pebay-Peyroula (2006). Relations between structure and function of the mitochondrial ADP/ATP carrier. *Annual Review of Biochemistry 75*(1), 713–741.

Oleson, T. A. and N. Sahai (2008). Oxide-dependent adsorption of a model membrane phospholipid, dipalmitoylphosphatidylcholine: Bulk adsorption isotherms. *Langmuir 24*(9), 4865–4873.

Palczewski, K. (2006). G Protein–Coupled receptor rhodopsin. *Annual Review of Biochemistry 75*(1), 743–767.

Paul, W. E. (2008). *Fundamental Immunology*. Lippincott Williams & Wilkins.

Perez, J. B., K. L. Martinez, J. M. Segura, and H. Vogel (2006). Supported Cell-Membrane sheets for functional fluorescence imaging of membrane proteins. *Advanced Functional Materials 16*(2), 306–312.

Perozo, E., A. Kloda, D. M. Cortes, and B. Martinac (2002). Physical principles underlying the transduction of bilayer deformation forces during mechanosensitive channel gating. *Nature Structural Biology 9*(9), 696–703.

Petrache, H. I., D. M. Zuckerman, J. N. Sachs, J. A. Killian, R. E. Koeppe, and T. B. Woolf (2002). Hydrophobic matching mechanism investigated by molecular dynamics simulations. *Langmuir 18*(4), 1340–1351.

Phillips, R., T. Ursell, P. Wiggins, and P. Sens (2009). Emerging roles for lipids in shaping membrane-protein function. *Nature 459*(7245), 379–385.

Pike, L. J. (2006). Rafts defined: A report on the keystone symposium on lipid rafts and cell function. *Journal of Lipid Research 47*(7), 1597–1598.

Pike, L. J. (2009). The challenge of lipid rafts. *Journal of Lipid Research 50*(Supplement), S323–328.

Quinn, P. J. and C. Wolf (2009). The liquid-ordered phase in membranes. *Biochimica et Biophysica Acta (BBA) - Biomembranes 1788*(1), 33–46.

Reimhult, E., M. Zäch, F. Höök, and B. Kasemo (2006). A multitechnique study of liposome adsorption on Au and lipid bilayer formation on SiO_2. *Langmuir 22*(7), 3313–3319.

Renthal, R. (2009). Helix insertion into bilayers and the evolution of membrane proteins. *Cellular and Molecular Life Sciences 67*(7), 1077–1088.

Richter, R., A. Mukhopadhyay, and A. Brisson (2003). Pathways of lipid vesicle deposition on solid surfaces: a combined QCM-D and AFM study. *Biophys. J. 85*(5), 3035–3047.

Richter, R. P., R. Bérat, and A. R. Brisson (2006). Formation of solid-supported lipid bilayers: An integrated view. *Langmuir 22*, 3497–3505.

Rigaud, J. and D. Lévy (2003). Reconstitution of membrane proteins into liposomes. *Methods in Enzymology 372*, 65–86.

Rossi, C., E. Briand, P. Parot, M. Odorico, and J. Chopineau (2007). Surface response methodology for the study of supported membrane formation. *The Journal of Physical Chemistry B 111*(26), 7567–7576.

Sachs, J. N. and D. M. Engelman (2006). Introduction to the membrane protein reviews: The interplay of structure, dynamics, and environment in membrane protein function. *Annual Review of Biochemistry 75*(1), 707–712.

Sackmann, E. (1996). Supported membranes: Scientific and practical applications. *Science 271*(5245), 43–48.

Salahpour, A. and B. Masri (2007). Experimental challenge to a 'rigorous'BRET analysis of GPCR oligomerization. *Nature Methods 4*(8), 599–600.

Samiee, K., J. Moran-Mirabal, Y. Cheung, and H. Craighead (2006). Zero mode waveguides for single-molecule spectroscopy on lipid membranes. *Biophysical Journal 90*(9), 3288–3299.

Satriano, C., M. Edvardsson, G. Ohlsson, G. Wang, S. Svedhem, and B. Kasemo (2010). Plasma oxidized Polyhydroxymethylsiloxane – A new smooth surface for supported lipid bilayer formation. *Langmuir 26*(8), 5715–5725.

Satriano, C., G. Marletta, and B. Kasemo (2008). Oxygen plasma-induced conversion of polysiloxane into hydrophilic and smooth SiOx surfaces. *Surface and Interface Analysis 40*(3-4), 649–656.

Saxton, M. J. (1997). Single-particle tracking: the distribution of diffusion coefficients. *Biophysical Journal 72*(4), 1744–1753.

Saxton, M. J. and K. Jacobson (1997). Single-particle tracking: Applications to membrane dynamics. *Annual Review of Biophysics and Biomolecular Structure 26*(1), 373–399.

Schiller, S. M., R. Naumann, K. Lovejoy, H. Kunz, and W. Knoll (2003). Archaea analogue thiolipids for tethered bilayer lipid membranes on ultrasmooth gold surfaces. *Angewandte Chemie International Edition 42*(2), 208–211.

Sekula, S., J. Fuchs, S. Weg-Remers, P. Nagel, S. Schuppler, J. Fragala, N. Theilacker, M. Franzreb, C. Wingren, P. Ellmark, C. A. K. Borrebaeck, C. A. Mirkin, H. Fuchs, and S. Lenhert (2008). Multiplexed lipid Dip-Pen nanolithography on subcellular scales for the templating of functional proteins and cell culture. *Small 4*(10), 1785–1793.

Sharma, P., R. Varma, R. Sarasij, Ira, K. Gousset, G. Krishnamoorthy, M. Rao, and S. Mayor (2004). Nanoscale organization of multiple GPI-anchored proteins in living cell membranes. *Cell 116*(4), 577–589.

Sieber, J. J., K. I. Willig, C. Kutzner, C. Gerding-Reimers, B. Harke, G. Donnert, B. Rammner, C. Eggeling, S. W. Hell, H. Grubmüller, and T. Lang (2007). Anatomy and dynamics of a supramolecular membrane protein cluster. *Science 317*(5841), 1072–1076.

Simons, K. and E. Ikonen (1997). Functional rafts in cell membranes. *Nature 387*(6633), 569–572.

Simons, K. and W. L. Vaz (2004). Model systems, lipid rafts, and cell membranes. *Annual Review of Biophysics and Biomolecular Structure 33*(1), 269–295.

Simson, R., B. Yang, S. E. Moore, P. Doherty, F. S. Walsh, and K. A. Jacobson (1998). Structural mosaicism on the submicron scale in the plasma membrane. *Biophysical Journal 74*(1), 297–308.

Singer, S. J. (1990). The structure and insertion of integral proteins in membranes. *Annual Review of Cell Biology 6*(1), 247–296.

Singer, S. J. and G. L. Nicolson (1972). The fluid mosaic model of the structure of cell membranes. *Science 175*(4023), 720–731.

Smith, N. J. and G. Milligan (2010). Allostery at G-protein-coupled receptor homo- and heteromers: Uncharted pharmacological landscapes. *Pharmacological Reviews 62*(4), 701

–725.

Sourjik, V. (2004). Receptor clustering and signal processing in *E. coli* chemotaxis. *Trends in Microbiology 12*(12), 569–576.

Stahlberg, H., D. Fotiadis, S. Scheuring, H. Rémigy, T. Braun, K. Mitsuoka, Y. Fujiyoshi, and A. Engel (2001). Two-dimensional crystals: A powerful approach to assess structure, function and dynamics of membrane proteins. *FEBS Letters 504*(3), 166–172.

Stock, D., A. G. W. Leslie, and J. E. Walker (1999). Molecular architecture of the rotary motor in ATP synthase. *Science 286*(5445), 1700–1705.

Stollberg, J. and S. E. Fraser (1990). Acetylcholine receptor clustering is triggered by a change in the density of a nonreceptor molecule. *The Journal of Cell Biology 111*(5), 2029–2039.

Szalontai, B., Y. Nishiyama, Z. Gombos, and N. Murata (2000). Membrane dynamics as seen by fourier transform infrared spectroscopy in a cyanobacterium, synechocystis PCC 6803: The effects of lipid unsaturation and the protein-to-lipid ratio. *Biochimica et Biophysica Acta (BBA) - Biomembranes 1509*(1-2), 409–419.

Tanaka, M. and E. Sackmann (2005). Polymer-supported membranes as models of the cell surface. *Nature 437*(7059), 656663.

Taylor, J. D., K. S. Phillips, and Q. Cheng (2007). Microfluidic fabrication of addressable tethered lipid bilayer arrays and optimization using SPR with silane-derivatized nanoglassy substrates. *Lab on a Chip 7*(7), 927.

Tero, R., G. Sazaki, T. Ujihara, and T. Urisu (2011). Anomalous diffusion in supported lipid bilayers induced by oxide surface nanostructures. *Langmuir 27*(16), 9662–9665.

Tieleman, D. P., L. R. Forrest, M. S. P. Sansom, and H. J. C. Berendsen (1998). Lipid properties and the orientation of aromatic residues in OmpF, influenza M2, and alamethicin systems: Molecular dynamics simulations. *Biochemistry 37*(50), 17554–17561.

van der Does, C., J. Swaving, W. van Klompenburg, and A. J. M. Driessen (2000). Non-bilayer lipids stimulate the activity of the reconstituted bacterial protein translocase. *Journal of Biological Chemistry 275*(4), 2472–2478.

Vockenroth, I. K., P. P. Atanasova, J. R. Long, A. T. A. Jenkins, W. Knoll, and I. Koper (2007). Functional incorporation of the pore forming segment of AChR m2 into tethered bilayer lipid membranes. *Biochim. Biophys. Acta 1768*(5), 1114–1120.

Wagner, M. L. and L. K. Tamm (2000). Tethered polymer-supported planar lipid bilayers for reconstitution of integral membrane proteins: Silane-Polyethyleneglycol-Lipid as a cushion and covalent linker. *Biophysical Journal 79*(3), 1400–1414.

Wang, T. and J. R. Silvius (2003). Sphingolipid partitioning into ordered domains in cholesterol-free and cholesterol-containing lipid bilayers. *Biophysical Journal 84*(1), 367–378.

Wenk, M. R. and P. De Camilli (2004). Protein-lipid interactions and phosphoinositide metabolism in membrane traffic: Insights from vesicle recycling in nerve terminals. *Proceedings of the National Academy of Sciences of the United States of America 101*(22), 8262–8269.

White, R. J., E. N. Ervin, T. Yang, X. Chen, S. Daniel, P. S. Cremer, and H. S. White (2007). Single ion-channel recordings using glass nanopore membranes. *Journal of the American Chemical Society 129*(38), 11766–11775.

White, S. H. (2009). Biophysical dissection of membrane proteins. *Nature 459*(7245), 344–346.

White, S. H., D. C. Petersen, S. Simon, and M. Yafuso (1976). Formation of planar bilayer membranes from lipid monolayers. a critique. *Biophys. J. 16*(5), 481489.

Williamson, I. M., S. J. Alvis, J. M. East, and A. G. Lee (2002). Interactions of phospholipids with the potassium channel KcsA. *Biophysical Journal 83*(4), 2026–2038.

Wimley, W. C. (2003). The versatile β-barrel membrane protein. *Current Opinion in Structural Biology 13*(4), 404–411.

Wong, J. Y., J. Majewski, M. Seitz, C. K. Park, J. N. Israelachvili, and G. S. Smith (1999). Polymer-cushioned bilayers. i. a structural study of various preparation methods using neutron reflectometry. *Biophysical Journal 77*(3), 1445–1457.

Woodbury, D. and C. Miller (1990). Nystatin-induced liposome fusion. A versatile approach to ion channel reconstitution into planar bilayers. *Biophysical Journal 58*(4), 833–839.

Woolf, P. J. and J. J. Linderman (2003). Self organization of membrane proteins via dimerization. *Biophysical Chemistry 104*(1), 217–227.

Xing, C. and R. Faller (2008). Interactions of lipid bilayers with supports: A Coarse-Grained molecular simulation study. *The Journal of Physical Chemistry B 112*(23), 7086–7094.

Yin, C., H. Han, R. Wei, and F. A. Lai (2005). Two-dimensional crystallization of the ryanodine receptor Ca^{2+} release channel on lipid membranes. *Journal of Structural Biology 149*(2), 219–224.

Yu, C.-h. and J. T. Groves (2010). Engineering supported membranes for cell biology. *Medical & Biological Engineering & Computing 48*(10), 955–963.

Yuan, H., A. Leitmannova-Ottova, and H. T. Tien (1996). An agarose-stabilized BLM: a new method for forming bilayer lipid membranes. *Materials Science and Engineering: C 4*(1), 35–38.

Zaccai, G. (2000). How soft is a protein? A protein dynamics force constant measured by neutron scattering. *Science 288*(5471), 1604–1607.

Zasloff, M. (2002). Antimicrobial peptides of multicellular organisms. *Nature 415*(6870), 389–395.

Zhou, H. (2009). Crowding effects of membrane proteins. *The Journal of Physical Chemistry B 113*(23), 7995–8005.

Zhou, H., G. Rivas, and A. P. Minton (2008). Macromolecular crowding and confinement: Biochemical, biophysical, and potential physiological consequences. *Annual Review of Biophysics 37*(1), 375–397.

Zwang, T. J., W. R. Fletcher, T. J. Lane, and M. S. Johal (2010). Quantification of the layer of hydration of a supported lipid bilayer. *Langmuir 26*(7), 4598–4601.

Chapter 2

Characterisation and Manipulation of Droplet Interface Bilayers

This chapter provides the background to some of the biophysical characteristics of lipid bilayers that later chapters will draw on and describes the experimental procedures used in the preparation of Droplet Interface Bilayers (DIBs). It then examines the stability, viscosity and morphological characteristics of DIBs formed in a number of different lipid-oil systems as a function of parameters such as preparation method, humidity and temperature. Finally, an account of the development of methods to manipulate bilayers using an inserted electrode, an applied potential, patterned surfaces and optical tweezers is given.

2.1 Introduction

Droplet Interface Bilayer (DIB) model membrane systems rest on the concept of slowly bringing aqueous volumes into contact in a medium consisting of lipid dissolved in an alkane oil. Upon contact, self-assembled monolayers at the oil-water interfaces of the volumes 'zip' together to form a bilayer. This idea was first tested by Tsofina et al. in 1966, but its potential was not fully explored until 2005, when David Needham[†]

[†] Present address: Center for Biomolecular and Tissue Engineering, Duke University, Durham, NC

suggested at a conference that two droplets brought together in a solution of GMO in squalene would form bilayers (Bayley et al., 2008). In quick succession, authors in Japan (Funakoshi et al., 2006), California (Malmstadt et al., 2006) and Oxford (Heron et al., 2007; Holden et al., 2007; Thompson et al., 2007) published reports of bilayers between aqueous volumes in a bulk oil phase. The approaches by Funakoshi et al. and Malmstadt et al. relied on microfluidics or PDMS chambers to encase the aqueous volumes and provide pressure to ensure contact between them, while Holden et al. pipetted free aqueous droplets into an oil reservoir, bringing them into contact with the aid of an 'egg-box'-moulded substrate or by piercing the droplets with Ag/AgCl electrodes and using these to manoeuvre the droplets. All three groups obtained single-channel recordings of the staphylococcal β-barrel protein pore α-Hemolysin (α-HL) in the novel systems.

The experiments described in this thesis centre on DIBs formed between a single droplet and a supporting hydrogel. In this configuration, the droplet is simply pipetted into a lipid-oil reservoir above an aqueous planar substrate and gravity ensures contact between the two aqueous volumes. The droplet and supporting hydrogel can then be pierced with electrodes to provide electrical access (Figure 2.2). As already indicated in Chapter 1, one major advantage of DIBs in the on-hydrogel configuration is that they unite the versatility of SLBs in terms of accessibility for a multitude of surface characterisation techniques with the ability to carry out high quality electrical recordings of channels reconstituted in the membrane. This was exemplified by the recent achievement of simultaneous single channel recording and single molecule imaging by total internal reflection fluorescence (TIRF) microscopy of individual α-HL pores by Heron et al. (2009).

This thesis explores a further major advantage that arises from the unique geometry of DIBs in the on-hydrogel configuration, namely the ability to mechanically manipulate the bilayer by translating or deforming the droplet. As DIBs are more stable than planar BLM (Heron et al., 2007), manipulations with an inserted electrode do not generally break the bilayer. On a well hydrated support, the bilayer can thus be moved laterally by dragging the droplet at speeds up to 1 $\mathrm{mm\,s^{-1}}$ (Heron et al., 2007). By raising the electrode, the bilayer size decreases and the two bilayer leaflets

can be disconnected without impacting on droplet integrity. Upon subsequently allowing the droplet to come into contact with the substrate, the bilayer reforms. This process can be repeated without any noticeable loss in efficiency of bilayer formation or droplet stability.

The ability to translate a bilayer across a gel substrate has already been exploited in the direct detection of electrophoretically separated ion channels and protein pores in polyacrylamide gels (Heron et al., 2007). Upon translation of a DIB across the bands in a conventional SDS-PAGE gel, the viral potassium channel Kcv and α-HL were shown to spontaneously insert into the bilayer, as detected by characteristic single-channel current traces. In an alternative approach, the analytes γ-cyclodextrin (γ-CD) and heptakis(2,3,6-tri-O-methyl)-β-cyclodextrin (hβ-CD) doped into separate regions of a gel support were detected by the difference in the degree of blocking of current through α-HL pores present in the bilayer (Heron et al., 2007). These experiments also showed that the translation of the bilayer does not destroy α-HL pores in the bilayer. Conversely, upon disconnection of the two bilayer leaflets, pores disappear, presumably by denaturation of the protein, as they do not return when the bilayer is reformed in the absence of fresh protein in either the droplet or the hydrogel support (Heron et al., 2007).

The ability to manipulate bilayers in this way promises a series of new avenues in the study of the effect of forces exerted by the lipid bilayer on membrane proteins. β-barrel pores such as α-HL are extremely robust, but the stresses that can be imposed in a controlled manner by lateral bilayer translation or size changes could prove invaluable in the study of mechanosensitive ion channels for example. It is highly likely that other membrane proteins with functions that rely on finely tuned gating mechanisms or conformational changes would also be affected by such manipulations, which could provide unprecedented insight into their function. The voltage gated ion channels mentioned in Chapter 1, for example, which have already been shown to respond to mechanical stress in the bilayer, could be prime candidates for further investigation in DIBs (Drew, 2011; Morris and Juranka, 2007).

2.2 Background and Theory

2.2.1 Electrical Properties of Bilayers

Capacitance Since lipid membranes consist of a hydrophobic layer of low conductance in between two polar layers, they can be likened to parallel plate capacitors. That is, for a given voltage drop across the membrane, charge separation occurs in the membrane and the amount of charge that builds up on both sides of the bilayer is directly proportional to the capacitance, a characteristic quantity that depends on the total area of the capacitor, the separation between the polar plates and the dielectric constant of the insulating medium. Bilayer capacitance is thus an important diagnostic of bilayer thickness, composition, and integrity, and will be covered in full detail in Chapter 3 and 4.

Membrane Potential Biological membranes maintain a resting potential ($\Delta\Psi$) by means of their selective permeability to ions in conjunction with ion pumps that transfer ions across the membrane against their electrical or chemical potential gradient. It should be noted here that in artificial systems of pure lipid bilayers, the effective impermeability of the bilayer means that any potential has to be applied externally.

Surface Potential As a result of the separation of charges in the presence of a potential, and due to a number of charging mechanisms such as the dissociation of surface groups or the adsorption of ions from solution, the distribution of ions in an electrolyte solution bordering the membrane is affected (Israelachvili, 2011). The surface charge is balanced by an equal and opposite charged region of counterions. Some of these ions are transiently bound, forming the 'Stern' or 'Helmholtz' layer, while others form an atmosphere in rapid thermal motion close to the surface, known as the diffuse electric double-layer. A set of equations known as Gouy-Chapman theory (Loew, 1993) first described the profile of this diffuse double layer at the beginning of the century (see Grahame (1947) for a review). Guoy and Chapman described the electrical potentials associated with the surface charge and the opposing aqueous

ions using Poisson's equation, and combined it with the Boltzmann relation, which accounts for the statistical distribution of the ions over distances x from the surface. The model states that the difference between the potential in the bulk electrolyte ($x = \infty$) and that at the surface ($x = 0$), $\Delta\Psi_s(0)$, is determined by the surface charge density (σ) and the concentration of the electrolyte in the bulk solution (Israelachvili, 2011; Loew, 1993). The original equations refer to simple symmetrical 1:1 electrolytes such as NaCl. The model was extended to asymmetrical electrolytes such as $CaCl_2$ by Grahame (1953) with a set of complex equations. At low potentials however, below about 25 mV, the model in both cases simplifies to (Israelachvili, 2011; Loew, 1993):

$$\Delta\Psi_s(0) = \frac{\sigma}{\varepsilon_w \varepsilon_0 \, \kappa} \qquad ; \qquad \kappa = \left(\sum_j c_{\infty j} \, z_j^2 F^2 / \varepsilon_w \varepsilon_0 \, RT \right)^{1/2} m^{-1} \tag{2.1}$$

where $c_{\infty j}$ is the concentration (moles per cubic meter) of a charged species j of valency z_j at infinite distance from the surface (i.e. in the bulk solution), ε_w and ε_0 are the dielectric coefficient of water and the dielectric permittivity of free space, respectively, R is the gas constant, F is the Faraday constant and T is the absolute temperature.

The surface potential thus becomes directly proportional to the surface charge density. It is also worth noting that at a constant surface charge density, the surface potential is inversely proportional to electrolyte concentration. Equation 2.1 is the same as that for a parallel plate capacitor whose plates are separated by a distance $1/\kappa$, have charges of $\pm\sigma$, at a potential difference of $\Delta\Psi_s(0)$. It is this analogy with a charged capacitor that gave rise to the term 'double layer' for describing the ionic atmosphere near a charged surface. The characteristic 'thickness' $1/\kappa$ of this capacitor is known as the Debye-Hückel length, which defines the decay length of the potential near a surface, in what is known as the Debye-Hückel equation (Israelachvili, 2011):

$$\Delta\Psi_s(x) = \Delta\Psi_s(0) \, e^{-\kappa x}. \tag{2.2}$$

As illustrated in Figure 2.1 A, the potential drop within the membrane is the same as the difference in potential between the bulk electrolyte solutions. This is only the case for symmetric membranes, where the charge density is equal on both sides of the

membrane. For asymmetric membranes, the difference in surface potentials means that the potential drop across the membrane ($\Delta\Psi_m$) can be larger than the potential difference between the bulk electrolyte solutions ($\Delta\Psi$), as shown in Figure 2.1 B. It is important to note that any transmembrane channels and pores experience $\Delta\Psi_m$, and that any alterations in surface potential of the membrane could therefore have significant effects on protein function (Loew, 1993).

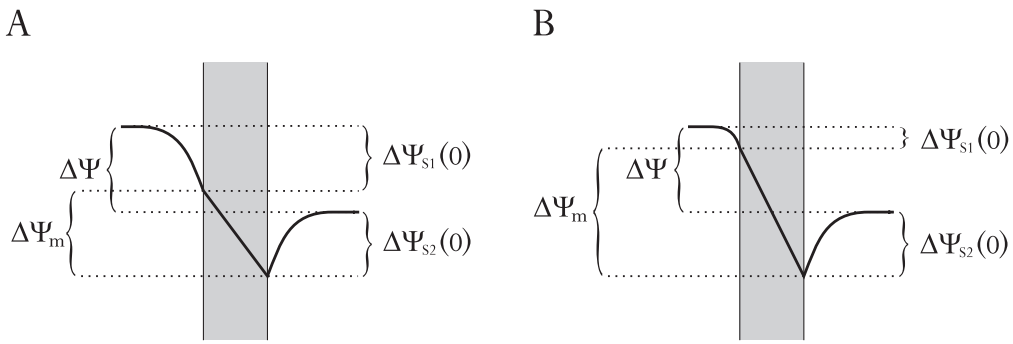

Figure 2.1: Simplified schematic illustration of the potential profile across a lipid bilayer, illustrating that an asymmetric membrane surface potential ($\Delta\Psi_s$) can result in a potential drop across the membrane ($\Delta\Psi_m$) that is significantly greater than the potential difference between the bulk phases ($\Delta\Psi$). **(A)** Symmetric membrane surface potential. **(B)** Asymmetric surface potential, arising, for example, from a difference in lipid composition between the two bilayer leaflets, with charged lipids concentrated on one side.

2.2.2 Lateral Forces in a Bilayer

The forces that drive the self-assembly of lipids into macromolecular structures of defined shape such as bilayers or the nonlamellar structures described in Chapter 1 are the result of attractive or interfacial tension forces arising between hydrophobic parts of the amphiphile, and ionic or steric repulsion between the hydrophilic head groups (Tanford, 1974). Collectively, these two opposing forces act mainly at the hydrocarbon-water interface to minimise the interfacial free energy per molecule (μ_N^o) by increasing or decreasing the interfacial area per molecule (a) that is exposed to the aqueous phase. The hydrophobic attraction is described by a positive interfacial free energy per unit area, or surface tension ($\gamma_{\rm i}$), and thus its contribution to μ_N^o is $\gamma_{\rm i} a$. The repulsive contribution from steric effects, hydration force, and electrostatics between the head groups is inversely proportional to the surface area occupied per

head group (Israelachvili, 2011), and thus the total interfacial free energy per molecule in an aggregate can be approximated by

$$\mu_N^o = \gamma_\mathrm{i} a + K/a \tag{2.3}$$

where K is a constant. Under the assumption that the attractive and repulsive terms act in the same plane at the hydrocarbon-water interface, the minimised interfacial free energy occurs at $\mathrm{d}\mu_N^0/\,\mathrm{d}a = 0$, which gives

$$\mu_N^o(min) = 2\gamma_\mathrm{i} a_0, \qquad a_0 = \sqrt{K/\gamma_\mathrm{i}}. \tag{2.4}$$

The constant K can now be eliminated in equation 2.3, and the interfacial free energy per molecule can be described in terms of the optimal area per head group, a_0, and the surface tension, γ_i:

$$\mu_N^o = 2\gamma_\mathrm{i} a_0 + \frac{\gamma_\mathrm{i}}{a}(a - a_0)^2. \tag{2.5}$$

The characteristic γ_i for a hydrocarbon interface in the presence of a lipid monolayer is $\gamma_\mathrm{i} \approx 20 - 50\ \mathrm{mJ\,m^{-2}}$ (Israelachvili, 2011). While the approximations above do not account for specific head group interactions, the effects of surface curvature, or acyl chain packing that is not perfectly fluid, they do highlight that the opposing forces in a bilayer lead to an optimal area per head group, a_0, which for fluid membranes does not depend to a great extent on the acyl chain length or the number of chains (Lewis and Engelman, 1983).

2.2.3 Bilayer Elasticity

A bilayer expands elastically when stretched (Israelachvili, 2011; Rawicz et al., 2000). For fluid bilayers, the isotropic area compressibility modulus (K_A) can be estimated from equation 2.5, since by definition:

$$\text{Elastic energy} = \frac{1}{2} K_\mathrm{A} (a - a_0)^2/a \tag{2.6}$$

which by comparison with equation 2.5 gives:

$$K_A \approx 2\gamma_{\mathrm{i}} \text{ per Monolayer, and } K_{\mathrm{A}} \approx 4\gamma_{\mathrm{i}} \text{ per bilayer.} \tag{2.7}$$

Given that the surface energy of a monolayer is $\sim 20 - 50\ \mathrm{mJ\,m^{-2}}$, the expected K_{A} for bilayers would therefore be $K_{\mathrm{A}} \approx 4\gamma_{\mathrm{i}} \approx 80 - 200\ \mathrm{mJ\,m^{-2}}$. This value compares reasonably well with that measured experimentally (Rawicz et al., 2000). Naturally, the equations above only hold for a limited range (Israelachvili, 2011). On stretching the bilayer beyond a certain point, pores form that rapidly lead to bilayer rupture, unless sufficient time is allowed for the tensile stress to be relaxed by the diffusion of lipids from the bulk solution into the bilayer. Upon compression, the bilayer can fold so that changes in the area per molecule can be minimised.

2.2.4 Bilayer Surface Tension

It is extremely difficult to measure bilayer surface tension, as direct measurements are complicated by thermal fluctuations in the membrane, which means that any stretching is associated with flattening the bilayer and thus changing only its projected area, not its surface area (Brandt et al., 2011; Fournier and Barbetta, 2008; Rawicz et al., 2000). As a result, there has been considerable debate as to its magnitude, with many proponents of the idea that bilayer surface tension must in fact be zero (Brandt et al., 2011; Jähnig, 1996; Tanford, 1979). This argument is based on a bilayer of, for example, a vesicle in water with a sufficiently large radius to exclude any curvature effects. Since the vesicle is permeable to water (Paula et al., 1996), the assumption can be made that the pressure inside (P_i) and outside (P_o) the vesicle is equal (Tanford, 1979). The Young-Laplace equation, on the other hand, requires the existence of a pressure differential for a finite interfacial surface tension γ_{i}

$$P_i - P_o = 2\gamma_{\mathrm{i}}/R_s \tag{2.8}$$

where γ_{i} is the interfacial surface tension and R_s is the radius of curvature of the surface. The opposing forces model of the bilayer detailed in section 2.2.2 can also

lead to the conclusion that the surface tension must be zero (Jähnig, 1996; Tanford, 1979). Given the permeability of the surface, the surface energy (F) can be minimised by the contraction of the vesicle until the opposing forces arising from the repulsion of the head groups exactly opposes the contractile forces. At this point:

$$\gamma_{\mathrm{i}} = \mathrm{d}F/\,\mathrm{d}A = 0 \tag{2.9}$$

where F is the free energy of the surface and A is the surface area. Finally, simulations of membrane thermal fluctuations and undulations also point to surface tensions that are at least very small (Brandt et al., 2011). However, as White (1980) points out, there are several factors that need to be considered, namely that the Young-Laplace equation was derived for the interface in a pure liquid system, whereas the bilayer has a defined thickness and volume and should therefore be considered like a thin bulk phase (White (1980) and references therein). For the same reason, White questions the conjecture that minimisation of the surface tension is sufficient to attain equilibrium. In considering the free energy of the surface, the bulk properties of the volume in the bilayer (V^{σ}) need to be taken into account. The Helmholtz surface free energy (F^{σ}), distinct from the surface tension, considers a number of other parameters as contributors to the thermodynamics of the 'surface' (White, 1980). At constant temperature,

$$\mathrm{d}F^{\sigma} = -P\,\mathrm{d}V^{\sigma} + \gamma_{\mathrm{i}}\,\mathrm{d}A + \sum_{i} \mu_i^{\sigma}\,\mathrm{d}n_i^{\sigma} \tag{2.10}$$

where P is the pressure within the bilayer, μ_i^{σ} is the chemical potential and n_i^{σ} is the number of molecules of each species i in the bilayer. The last term thus accounts for the chemical potential of the lipid molecules (l) and associated water (w), $i = \{l, w\}$. At equilibrium, $\mathrm{d}F^{\sigma} = 0$. This relationship suggests that a number of interrelated variables play a role in minimising $\mathrm{d}F^{\sigma}$, with the important conclusion that equation 2.9 cannot be a statement of equilibrium, and γ_{i} can therefore take values other than zero (White, 1980).

2.2.5 Surface Tension and Contact Angle of DIBs

Figure 2.2 illustrates the surface forces in a droplet in contact with a planar hydrogel, assuming a nonzero bilayer surface tension, γ_{m}, as discussed in more detail in later parts of this chapter. At equilibrium, the balance of forces acting on the three phase contact line in our system is given by the modified Young equation, which includes a term for the line tension (σ_ℓ) (Wallace and Schürch, 1990; Widom, 1995):

$$\gamma_{\mathrm{m}} = \gamma_{\mathrm{ho}} - \gamma_{\mathrm{do}} \cos\theta - \sigma_\ell / r_{\mathrm{m}} \tag{2.11}$$

where γ_{m} is the interfacial surface tension of the bilayer, γ_{ho} and γ_{do} are the interfacial surface tensions of the lipid monolayers at the hydrogel-oil interface and droplet-oil interface respectively, θ is the contact angle between the droplet and hydrogel, σ_ℓ is the line tension, and r_{m} is the radius of the bilayer (Figure 2.2). If the bilayer is large, the line tension term becomes insignificant, resulting in the classic Young equation:

$$\gamma_{\mathrm{m}} = \gamma_{\mathrm{ho}} - \gamma_{\mathrm{do}} \cos\theta. \tag{2.12}$$

For a DIB on a flat hydrogel surface, θ can be calculated from the radius of the bilayer membrane (r_{m}) and the droplet radius (R_{d}). For a DIB on a flat hydrogel surface (for which $r_{\mathrm{m}} < R_{\mathrm{d}}$):

$$\theta = \pi - \sin^{-1}\left(\frac{r_{\mathrm{m}}}{R_{\mathrm{d}}}\right). \tag{2.13}$$

2.2.6 Electrowetting on Dielectric (EWOD)

The geometry of a DIB in the on-hydrogel configuration is reminiscent of electrowetting on dielectric (EWOD) systems, used in microfluidics and other chip-based technologies to effect movement of liquid drops on dielectric surfaces. Movement is induced by changes in the contact angle of the liquid that are dependent on the magnitude of a voltage applied across the dielectric (Chung et al., 2010; Mugele and Baret, 2005). The relationship between the observed contact angle and the applied voltage is parabolic, as will be shown in the equations in the next section. The parabolic relationship,

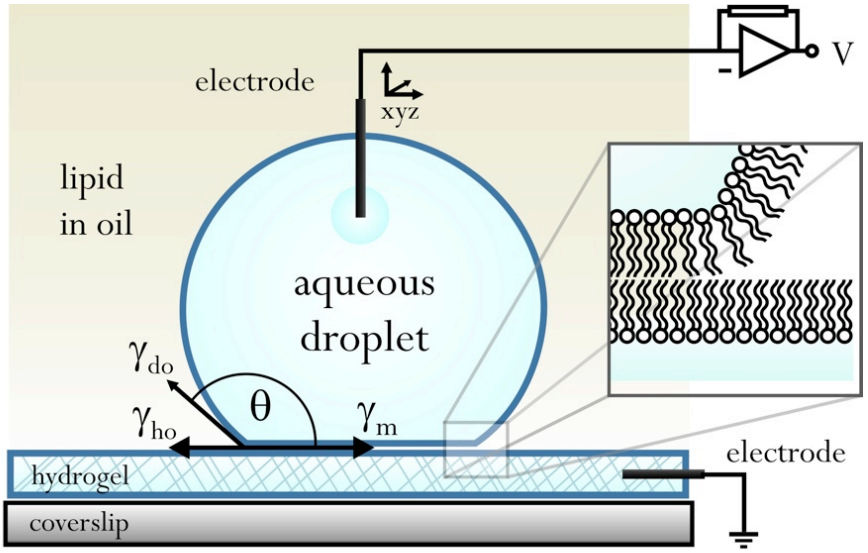

Figure 2.2: Schematic of a droplet forming a Droplet Interface Bilayer (DIB) with a hydrogel substrate, accessible to simultaneous optical and electrical measurements. The DIB forms spontaneously when an aqueous droplet that is pipetted into a well containing a lipid/oil solution settles on the substrate. The droplet is pierced with a 100 μm diameter micromanipulator-mounted Ag/AgCl electrode. A corresponding ground electrode in the agarose permits electrical recording across the bilayer. Schematic illustrations of the surface tensions of the bilayer membrane (γ_m), the droplet-oil interface (γ_{do}) and of the hydrogel-oil interface (γ_{do}) are shown. θ is the droplet contact angle. *Adapted with permission from Gross et al. (2011a). Copyright (2011) American Chemical Society.*

however, only holds at low voltages; at high voltages, contact angle saturation occurs. No transition to complete wetting has been observed in any of a number of different EWOD systems. The reasons for this saturation are not clear, and have been attributed to factors such as screening of the applied field by a charge build up in the dielectric, or finite conductivity of the liquid (Mugele and Baret, 2005). As will be shown in experiments described later, DIBs do indeed behave like EWOD systems, as the bilayer has the dielectric properties of a capacitor that essentially forms the support of the aqueous droplet.

2.2.6.1 The Young-Lippmann Equation for a Droplet on a Surface

Contact angle changes of a droplet on a dielectric surface with an applied potential are described by the Young-Lippmann Equation. The Lippmann relation states that the surface tension of an interface (γ_m in a DIB, see Figure 2.2) depends on the charge density (σ) and thus changes with applied potential (V_a) (see also the translation of Lippmann's original work from 1875 in the appendix of Mugele and Baret, 2005):

$$\frac{d\gamma_m}{dV_a} = -\sigma = -C_m V_a \tag{2.14}$$

where C_m is the capacitance of the interface. This is a simple differential with the solution:

$$\gamma_m(V_a) = \gamma_m(0) - \frac{1}{2} C_m {V_a}^2. \tag{2.15}$$

Substituting the Young relation 2.12 into equation 2.15 and assuming that the surface tension of the droplet-oil and hydrogel-oil interfaces remain unchanged, we obtain the Young-Lippmann equation:

$$\cos\theta_V = \cos\theta_0 + \frac{C_m}{2\gamma_{do}} {V_a}^2 \tag{2.16}$$

Essentially, the stored electrical energy in the parallel plate capacitor modifies the surface energy, which results in changes of contact angle with applied voltage. In our system, the decrease in θ leads to a concomitant increase in bilayer area as monolayers at the water-lipid-oil interface 'zip' together to form new bilayer at the edges.

2.2.7 Background to Optical Tweezing Experiments

Optical tweezing is a technique that takes advantage of attractive and repulsive forces that arise in a focussed laser beam at interfaces with a refractive index mismatch. Microscopic objects with refractive index higher than the surrounding medium can be trapped by a single focussed beam and their position can be controlled on a nanometre scale (Ashkin et al., 1986). An object in a beam will experience two types of force exerted on it. The scattering force (F_{scat}) points in the direction of the incident light and is proportional to the optical intensity. The gradient force (F_{grad}) is proportional to the intensity gradient and points in the direction of increasing intensity. In a Gaussian beam focussed to a point, F_{grad} will therefore point towards the focal point. For optical trapping to work, the intensity gradient has to be steep enough for F_{grad} to dominate, as the total force experienced by the particle is given by:

$$F = F_{\text{scat}} + F_{\text{grad}}. \tag{2.17}$$

Focussing the trapping beam with a high numerical aperture (NA) objective (NA = 1.2 – 1.4) increases F_{grad} outside of the plane normal to the incident beam and enables the trapping of particles in three dimensions.

Since conventional optical trapping requires a particle with a refractive index higher than the surrounding medium, it is of little interest in the context of aqueous droplets in an oil phase. However, two derivatives of optical tweezing, namely optical trap arrays and trapping with a Laguerre-Gaussian beam (LG beam) can take advantage of the scattering force to trap low-index particles.

2.2.7.1 Optical Trap Arrays

A diffractive optical element (DOE) can split a trapping beam into multiple components, each of which can subsequently be focussed into an independent optical trap. A DOE essentially modulates the phase of the incident beam and causes a simple Fourier transform of the beam between the plane of the DOE and the corresponding focal plane on the far side of a lens. A spatial light modulator (SLM) is an array

of liquid crystals able to impart a phase modulation of $0-2\,\pi$ on a laser beam in a series of discreet levels, which can be used to generate a DOE by interpreting a computer generated hologram (kinoform) such as that shown on the bottom left of Figure 2.3. It is possible to compute a series of kinoforms that can be applied by the SLM sequentially to produce and control a series of independent optical traps in an arrangement known as Dynamic Holographic Optical Tweezers (Curtis et al., 2002). The advantage of creating optical trap arrays in this way is that elements can be added to the kinoform that displace the focal point of a trap in the axial direction, enabling the formation of three dimensional trapping arrays (Curtis et al., 2002).

2.2.7.2 Laguerre-Gaussian Beams

Modulating the phase of a Gaussian beam to create a helical wavefront results in a beam that can no longer be focussed to a point. Instead, destructive interference in the centre of the beam will create a dark region at the image plane, surrounded by a region of constructive interference in the shape of a ring with a radius R_ℓ. In such a beam, also known as a Laguerre-Gaussian beam (LG beam), R_ℓ can theoretically be predicted by (Padgett and Allen, 1995):

$$R_\ell = \omega\sqrt{\frac{\ell}{2}} \tag{2.18}$$

where ω is the radius of the Gaussian beam and ℓ is an integer known as the topological charge. A beam modulated in this way carries $\ell\hbar$ units of orbital angular momentum per photon and is therefore also referred to as an optical vortex (Curtis and Grier, 2003). In practice, the radius of the vortex beam profile scales linearly with ℓ, not $\sqrt{\ell}$, which is due to the superposition of higher-order Laguerre-Gaussian modes (Curtis and Grier, 2003). The top half of Figure 2.3 shows a kinoform with a topological charge of $\ell = 10$ and the corresponding beam profile of the optical vortex at the image plane of the objective. Optical vortices have been used to trap particles with a radius much smaller than R_ℓ and with a refractive index higher than the surrounding medium. These particles are held in the ring of high intensity, and revolve around it driven by the angular momentum transferred to them by the beam.

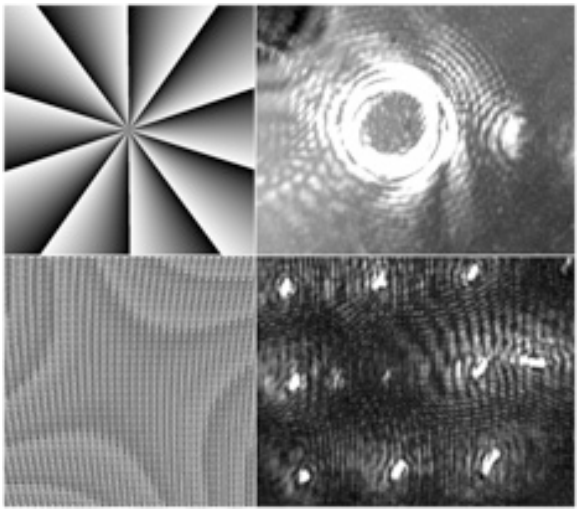

Figure 2.3: Kinoforms applied by a spatial light modulator (SLM) and the resulting trapping beam configuration. Top: a kinoform to generate an $\ell = 10$ LG beam and an image of the beam profile at the image plane. Bottom: a kinoform to generate an array of traps in a square formation and an image of an 8-trap array at the image plane. The displaced zero order beam can be seen on the right of the image.

2.3 Materials and Methods

2.3.1 Materials

1,2-Diphytanoyl-*sn*-glycero-3-phosphocholine (DPhPC, Avanti Polar Lipids, Alabaster, AL), hexadecane (H6703 or 296317 (anhydrous), Sigma-Aldrich, St. Louis, MO) and low melt agarose (A9414, Sigma-Aldrich) were used without further purification. Agarose was prepared fresh when required by dissolving in water (1 % w/v) or buffer (2.5 % w/v) at 90 °C. Sodium chloride, calcium chloride (both Sigma-Aldrich) and potassium chloride (TraceSelect, Fluka, Buchs, Switzerland) solutions were buffered with 10 mM tris(hydroxymethyl)aminomethane (TRIS)-HCl (Trizma base, T6066) or HEPES (H3375, both Sigma-Aldrich), adjusted with hydrochloric acid (Sigma-Aldrich), and filtered prior to use by a 0.22 μm Steriflip disposable filtration system (Millipore Corporation, Billerica, MA). 0.22 μm filtered, doubly-deionised 18 mΩ cm^{-1} water was used throughout (Milli-Q Synthesis or Direct-Q, Millipore Corporation). Quest™ Fluo-8 (pentapotassium salt, Invitrogen, UK) and ethylenediaminetetraacetic acid (EDTA) (Sigma-Aldrich) were used without further purification. 1 μm silica beads were from Fluka and Sephadex beads (G-100, 40 – 120 μm) were from Sigma-Aldrich. Coverslips were Menzel #1, 25 × 40 × 0.13 – 1.16 mm (VWR International, Radnor, PA). Polymethyl methacrylate (PMMA) and polyoxymethylene (Delrin) were from RS Components (Electrocomponents, Oxford, UK) and were machined on a Roland Modela MDX40 CNC machine using 0.5 – 2 mm ball or slot drills (Electrocomponents).

2.3.2 Alkane Lipid Solutions

Dry lipids are extremely hygroscopic, and often arrive from the supplier in a 'gummy' form that contains a limited amount of water. Lipid solutions were prepared by a number of methods, the merits of which are discussed later.

2.3.2.1 Pentane stocks

The content of a dry lipid vial as purchased was dissolved in pentane to give a known lipid concentration of 20 mg/mL and aliquoted into 200 μL volumes in 2 mL glass vials

with screw caps and a PTFE liner (Supelco), layered with nitrogen and sealed with parafilm. The vials were stored at -20 ℃. When needed, the pentane was evaporated by streaming dry nitrogen into the vial for around 5 minutes until a waxy film of lipid was visible in the bottom of the vial. Evaporative cooling was counteracted by holding and warming the sample in the hand. Hexadecane or other alkane as required was then added to make a final concentration of 5 mg/mL (5.9 mM) and the film was dissolved by vortexing for 3 – 5 minutes.

2.3.2.2 Dissolving Lipid in Alkane via Chloroform

A small amount of dry lipid was taken from the container as purchased and added to a previously weighed 2 mL glass vial. The lipid was then dissolved by vortexing in a small amount (~100 μL) of chloroform that was added with a glass pipette. Subsequently, the chloroform was carefully evaporated using a stream of nitrogen until a waxy film was visible. the vial was then placed under vacuum for 30 minutes to ensure complete evaporation of chloroform. The sample was then weighed and hexadecane or other alkane as required was added to the desired final concentration. The waxy film was dissolved by vortexing for 2 hours or by briefly heating the solution (~50 ℃ for 5-10 minutes) followed by vortexing for 3 – 5 minutes. The sample was used immediately and was kept at room temperature.

2.3.2.3 Hexadecane Solutions

As above, a small amount of dry lipid was taken and added to a weighed 2 mL glass vial. The sample was weighed directly, and dissolved in hexadecane by heating and vortexing as above to a final concentration of 10 mg/mL and stored at room temperature. When needed, aliquots of this stock were dissolved with anhydrous hexadecane (kept in a sealed container and removed with a syringe) to the desired final concentration.

2.3.3 DIB Device Assembly

2.3.3.1 Devices Suitable for TIRF Microscopy

DIBs were formed in devices designed to rest on glass coverslips and provide oil reservoirs above a thin hydrogel. Coverslips were prepared by exposing them to an O_2 plasma (3 minutes, PT 7100 Radio Frequency Plasma Barrel Etcher, Bio-Rad Laboratories Ltd, Hemel-Hempstead, UK; or 7 minutes, Plasma Cleaner System Femto, Diener Electronic, Germany). To form the supporting hydrogel, 5 μL of 1 % (w/v) low melt agarose in MQ water heated to 90 °C was pipetted onto a coverslip, and spread by placing a second coverslip on top and then quickly swiping it off. The resulting thin film was then left to dry. Alternatively, an agarose film can be deposited by spin coating with 175 μL of 0.75 % agarose heated to 90 °Cat 4000 – 7000 rpm for 30 seconds (WS-400-6NPP-LITE, Laurell Technologies) which resulted in a dry (invisible) film. A PMMA or Delrin microchannel device, fabricated as described below and extensively washed with water and dried with N_2 gas before each use, was then placed on the dried coverslip, and ~200 μL of 2.5 % (w/v) agarose in buffer was carefully pipetted into one of the filling holes. The molten agarose travels along the channels in the device in contact with the coverslip, rehydrating the dried thin film (Figure 2.4 C). Careful pipetting ensures that surface tension prevents the rehydrating agarose from encroaching into the wells, leaving the thin hydrogel exposed (Figure 2.4 A). Previous work in this lab suggests that the rehydrated hydrogel is at most 200 nm thick as it is possible to excite fluorophores on lipid bilayers above the hydrogel in an evanescent field generated by a beam totally internally reflecting from the underside of the coverslip (see also Chapter 5).

The wells in the device are filled with the appropriate lipid in alkane solution (see below) and the filling holes on top of the device are sealed with laboratory adhesive labels (Toughtags, Sigma) to prevent drying out of the agarose. If needed, a ground electrode, prepared as described below, can be inserted into a designated hole to make electrical contact with the supporting hydrogel. The device is ideally left for 15 minutes before the addition of any droplets to allow a lipid monolayer to form at the interface of the hydrogel with the lipid solution.

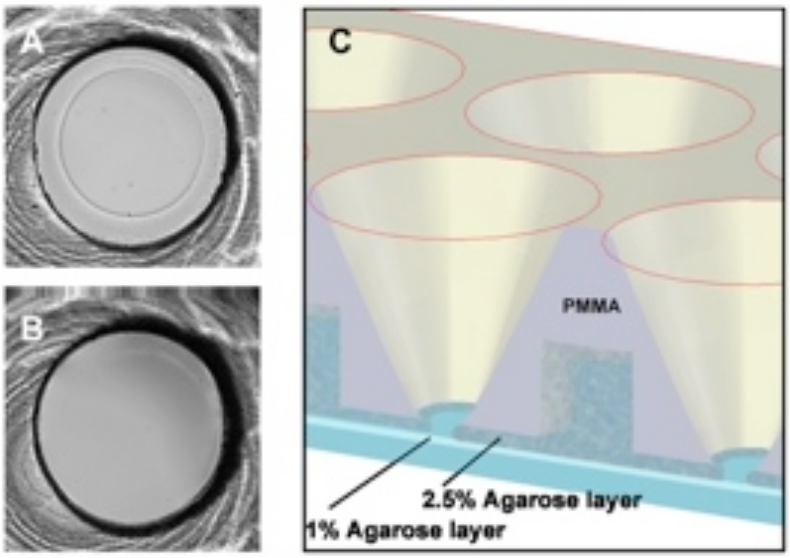

Figure 2.4: An assembled DIB device. **(A)** Base of a well (diameter: 500 μm) in a PMMA device resting on a coverslip. A thin substrate agarose layer coats the glass, surrounded by a thicker rehydrating layer that is held to the edges of the well by surface tension. **(B)** A well flooded by the thick agarose layer. **(C)** Assembled device cross section.

2.3.3.2 Devices for Electrical Recording Only

For experiments not requiring TIRF microscopy, an alternative device design can be used that ensures optimal electrical contact with the underside of the bilayer through a 1 mm thick supporting hydrogel. The supporting gel is cast from molten 2.5 % (w/v) agarose in buffer between two microscope slides spaced 1 mm apart. The gel is then cut to the size of a 1 mm deep recess on the underside of the PMMA device and placed on a plasma-cleaned coverslip. The device rests on the coverslip and the bottom edges of the well walls contact the gel. It is important that the gel be cast to the correct thickness as any pressure from the PMMA results in bulging of the gel into the wells. Further assembly then proceeds essentially as described above. The addition of a small amount of oil around the edge of the device on the coverslip can prevent drying out of the agarose slab.

2.3.4 Device Fabrication

Devices were fabricated from either polyoxymethylene (Delrin) or polymethyl methacrylate (PMMA) using designs prepared in a 3D computer-aided design package

(Solidworks). Small modifications to original designs by Andrew Heron[†] included the enlarging of the wells from 500 μm to 1 mm diameter with concomitant modification of the spacing between the wells to improve flow of the filling agarose during assembly; and the addition of a recess on the underside of the device to house the coverslip. This recess ensures that the position of the device with respect to the supporting hydrogel remains fixed, as the placing of electrodes and positioning of the assembled device on the microscope can otherwise shift the device and damage the underlying hydrogel. Devices for optical tweezing experiments were designed with a single large well with a diameter of 5 mm. These devices were otherwise identical to those described in section 2.3.3.2 above. 'Incubation tanks' for the equilibration of droplets in lipid-oil solution were designed to minimise wastage of solution and to enable the separation of different droplets to prevent exchange of lipid or aqueous components. The tank consists of a 6 × 1.5 × 0.4 cm block of PMMA with a series of parallel 10 × 0.2 × 0.2 mm trenches.

2.3.5 Preparation of Droplets and Formation of DIBs

Small droplets (~40 nL) of the required aqueous sample were manually pipetted (2 μL pipette, Gilson, set to ~0.07 μL) into the lipid oil solution in the incubation tank and left to equilibrate for 5 – 15 minutes unless otherwise specified to allow a monolayer of lipid to form on the surface of the droplet, before transferring them to the well in the PMMA device where they settle into contact with the supporting hydrogel. The optimal equilibration time depends to some extent on the time over which the hydrogel in the wells has equilibrated. The optimal droplet equilibration time was determined for each experiment by observing whether droplets burst when first brought into contact with the hydrogel. If sufficiently equilibrated, the droplet spontaneously forms a bilayer within a few minutes of contacting the agarose substrate.

'Pentaning' of Wells. In an alternative method, a drop of lipid dissolved in pentane to a concentration of 0.5 mg/mL was added to the bottom of a well containing

[†] Present address: Oxford Nanopore Technologies, 4 Robinson Avenue, Oxford Science Park, Oxford OX4 4GA, UK

no lipid-oil solution. The pentane was allowed to evaporate, presumably leaving a layer of lipid on the surface of the hydrogel. Pure alkane (e.g. hexadecane) was then added to the well before adding the droplet in the normal way. This method was employed primarily for the formation of asymmetric bilayers. Care has to be taken to completely evaporate the pentane, which can be aided by briefly warming the device to ~50 ℃.

2.3.6 Preparation of Electrodes

Ag/AgCl electrodes were prepared by soldering silver wire to shielded copper wire (2.24 mm outer diameter, 7 tinned copper core strands of 0.2 mm diameter, PVC shielded, Electrocomponents) and treating with a weak sodium hypochlorite solution. The other end of the wire was soldered to connectors suitable to interface with the headstage of the patch clamp amplifier. The ground electrode was made from 1.5 mm diameter silver wire (> 99.99 % pure, Sigma-Aldrich) that was roughened with a wire brush and then treated overnight in 5 % (w/v) sodium hypochlorite (NaClO, Fisher Scientific) in water. The droplet electrode was made from 100 μm diameter silver wire (99.9 % pure, Sigma-Aldrich) and was treated in 2 % (w/v) sodium hypochlorite in water for 3 hours. Both electrodes were rinsed with water after treatment and stored in the dark to protect the AgCl coating from UV breakdown. When treated, the electrodes have a matte grey appearance, but after prolonged use, white patches can appear, and recordings tend to be characterised by more noise. Minor patches can be removed by connecting the electrode together with a sacrificial electrode to a 9V battery. Alternatively, the coating has to be removed by wire brush and hypochlorite treatment is repeated. For each experiment, the tip of the droplet electrode was coated with a small amount of fresh agarose (an agarose 'anchor') by touching it to a molten drop of 3 % w/v of agarose in MQ water. This coating encourages the wetting of the electrode by the droplet.

2.3.7 Imaging DIBs

DIBs were imaged from below with a 10 × objective (Nikon Plan Fluor 10 ×/0.30 DIC L/N1 WD 16.0) on an inverted microscope (Nikon Eclipse T*i*, Nikon Instruments

UK). Images were captured on a CCD camera (640 × 480 pixel Philips Vesta Pro or Trust Webcam) driven by Microsoft VidCap (version 5.1, Microsoft Corporation) or VidCap (version 1.0.0.1, independent) and analysed with ImageJ software (Rasband, 1997) or Igor Pro (Wavemetrics, Portland, OR). Pixel size was calibrated using a graticule with 50 μm divisions.

2.3.8 Electrical Recording and Application of a Potential

Electrical recording across the bilayer was achieved by piercing droplets with the 100 μm diameter Ag/AgCl electrode (Figure 2.2 A) using a 3-axis mechanical micromanipulator (NMN-21, Narashige, Japan) mounted inside the Faraday cage. The corresponding 1.5 mm diameter Ag/AgCl electrode was inserted into the device to contact the agarose substrate. Electrical currents were recorded with a patch clamp amplifier (Axopatch 200B; Molecular Devices, Sunnyvale, CA) in voltage-clamp mode and set to 'whole cell' ($\beta = 1$) recording mode. Traces were digitised at 1 kHz (USB MiniDigi-1A, Molecular Devices or NI-PCI-6281 M-series DAQ connected to the patch clamp amplifier via a BNC-2090 board, both National Instruments). The droplet electrode was connected to the active electrode of the patch clamp amplifier headstage, and the hydrogel substrate electrode was connected to the virtual ground. Electrical traces were filtered post-acquisition (100 Hz low-pass Gaussian filter) and analysed using pClamp 9.0 (Molecular Devices) and Igor Pro (Wavemetrics) software. The triangular input voltage for capacitance measurements was provided by a function generator (4040A 20 MHz Sweep, B&K Precision) connected to the patch clamp amplifier on the (rear switched) external input. DC offset potentials were applied to the bilayer either manually through the voltage clamp on the patch clamp amplifier, or by stimulus protocols set up in WinEDR software (version 3.0.6, Strathclyde University, Dempster, 1997 – 2011) and fed into the (front switched) external input on the patch clamp amplifier via the data acquisition hardware above.

2.3.9 Microscope Stage and Faraday Cage

The PMMA chip, main body of the micromanipulator and the patch-clamp headstage were enclosed in a Faraday cage made from a 10 × 40 × 40 cm steel box

with 2mm thick walls. The box is grounded by connecting it to the common ground in the patch clamp amplifier and rests on the stage of the inverted microscope. A circular hole machined into the floor of the box allows for both the integration of the microscope sample holder into the box and access to the objective. A hole in the lid covered with wire mesh provides an opening for the microscope illumination. Three further holes are designed to let the arms of the micromanipulator protrude and the headstage cable exits the box through a groove in the top of the box wall. The microscope is positioned on a self-levelling vibration insulation table (Thorlabs, Ely, UK). Additional vibrational noise can be damped with a small amount of foam or rubber underneath the Faraday cage.

2.3.10 Optical Tweezing Experiments

2.3.10.1 Experimental Setup

Optical tweezer experiments were carried out in the laboratory of Dr Grant Ritchie[†] in collaboration with Lee Moore[†]. The optical tweezer setup as illustrated in Figure 2.5 was built by Lee Moore. Briefly, trapping light is provided by a 532 nm laser (Laser Quantum Torus, maximum power 400 mW). The raw output was passed through a half-wave plate, a polarising beam splitter and a second half-wave plate to provide light of controlled polarisation, and expanded to fully illuminate a spatial light modulator (SLM, Holoeye LC-R 2500). A series of lenses and mirrors image the SLM onto the back aperture of a microscope objective (Nikon E Plan, 100 ×/1.25). A fine pencil lead placed at a focal point of the beam before it reaches the objective blocks out the zero order diffraction from the SLM. A 532 nm dichroic mirror placed in the path of the beam before the objective allows the imaging of samples above the objective with a firewire camera (PixelLINK PL-A774).

2.3.10.2 Sample Preparation

Droplets were prepared by adding a small amount (20 % v/v) of aqueous buffer (water or HEPES pH 7.5) to a solution of DPhPC in hexadecane (1 mg/mL, prepared as

[†] Physical and Theoretical Chemistry Laboratory, University of Oxford

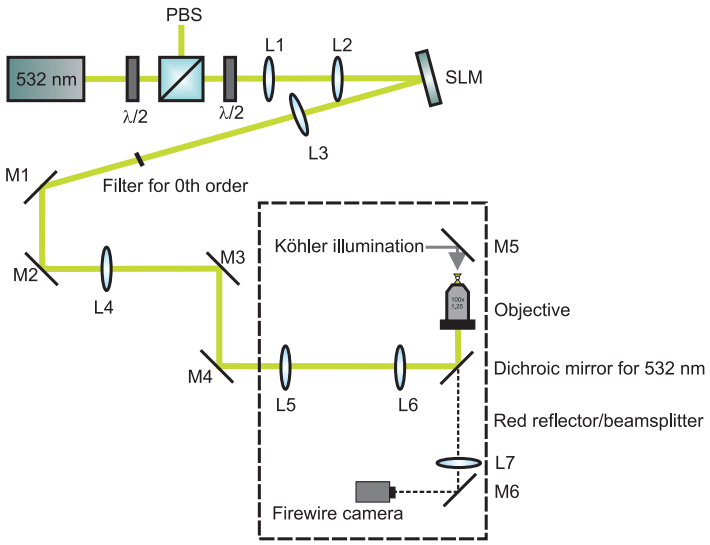

Figure 2.5: Experimental setup for SLM optical tweezers. *Figure courtesy of Lee Moore, Ritchie Group, Physical and Theoretical Chemistry Laboratory, University of Oxford*

described in section 2.3.2.2 above) and agitating vigorously. The resulting droplets with a diameter distribution of ~15 – 100 μm were placed in an incubation tank and examined under a low power microscope (Nikon Eclipse TS100). Droplets with a diameter of <~30 μm were selected and transferred with a pipette to the large well (3 mm diameter) of a device fabricated for these experiments as described in section 2.3.4 above. The droplets formed bilayers with the cast agarose gel at the bottom of the well. In preliminary experiments aiming to move droplets without bilayers, the droplets were instead transferred to a space between two coverslips separated by a thin rubber gasket and previously incubated with lipid-oil solution to prevent wetting of the coverslips by the droplets.

2.4 Results and Discussion: Bilayer Characterisation

2.4.1 Bilayer Formation

The time to formation of a bilayer when a droplet settles to the bottom of a well depends on a number of factors, including lipid concentration in the oil, lipid hydration, and how long droplet and device have equilibrated in the solution before contact is made. If bilayer formation is slow enough, a circular darker area can be observed through the inverted microscope prior to bilayer formation (Figure 2.6 A). A small increase in the baseline capacitance (about $1-2$ pF for a 50 nL droplet) is also detected. The contact region thins spontaneously to a bilayer, which is delineated by a high contrast ring. If the image is defocussed slightly, the bilayer edge appears white. Under ideal lipid conditions, as discussed in more detail below, the bilayer enlarges to form a perfect circle within a few seconds (Figure 2.6 A). The radius of the bilayer membrane (r_{m}) relative to the droplet radius (R_{d}) varies over a significant range ($\sim 0.2 < r_{\mathrm{m}}/R_{\mathrm{d}} < \sim 0.7$). As has also been observed in BLMs (Requena et al., 1975; White, 1986), large oil-lenses of typically >10 μm diameter can occasionally become trapped between the monolayers during bilayer formation. These lenses often spontaneously disappear by coalescing with the bulk oil phase. If the droplet is pierced with an electrode, the bilayer can be moved to bring the lens into proximity of the bilayer edge and encourage coalescence (Figure 2.6 B).

2.4.2 DIB Viscosity

The collective effect of factors such as lipid concentration, hydration, temperature, lipid hydration, and equilibration time not only determines the time to bilayer formation, as noted above, but also affects the way in which the droplet responds to force applied to it by the electrode, the degree of deformation that is achievable and the speed at which the shape reaches perfect circularity. Collectively, these properties will be hereafter referred to as DIB viscosity, a phenomenological, macroscopic definition not to be confused with the more rigorous concept of the viscosity of the bilayer liquid crystalline phase (ν_m).

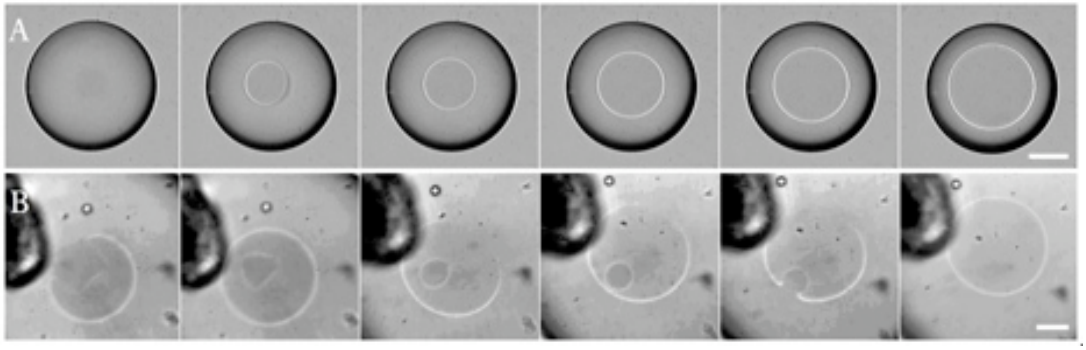

Figure 2.6: Bilayer formation. **(A)** Spontaneous bilayer formation. A region of contact can be observed as a slightly darker patch immediately before bilayer formation. Images were triggered manually at a rate of roughly 1.5 s^{-1}. Aqueous phase: TRIS-HCl pH 8.0, 0.5 M NaCl, symmetric. Lipid: 5 mg/mL DPhPC in hexadecane prepared from pentane stocks (→ 2.3.2.1). Scale bar: 100 μm. **(B)** An oil lens trapped during bilayer formation. Movement of the electrode encourages the lens to coalesce with the oil phase at the edge of the bilayer. Frame grabs from a video ~10 s apart on average. Aqueous phase: TRIS-HCl pH 8.0, 0.3 M KCl, symmetric. Lipid: 7.5 mg/mL DPhPC in hexadecane prepared from dry lipid stocks (→ 2.3.2.3). Scale bar: 50 μm.

DIB viscosity can vary substantially. Differences in DIB viscosity may not be immediately apparent from the morphology of a fully formed bilayer, and we do not at present have a method of quantifying this parameter. However, the time from contact of the aqueous phases to bilayer formation, the rate of bilayer formation, deviations from perfect circularity, and the rate of disappearance of lenses can give a good indication. Methods to improve on these metrics will be discussed in later sections. The degree of viscosity is very apparent when piercing the droplet with an electrode. A low viscosity bilayer can be moved with minimal contact, and the droplet behaves as if 'on ice'. Under these conditions, droplets can only be pierced by ensuring that the tip of the electrode is hydrophilic to encourage spontaneous wetting, as no mechanical pressure can be applied to the droplet. When pierced, there is no movement of the droplet relative to the electrode upon translating the electrode in the xy-plane with the micromanipulator. This condition is rare, and in most cases there is a lag between the movement of the electrode and that of the droplet, but the droplet holds its shape. In the case of a highly viscous bilayer, on the other hand, the droplet can be substantially deformed by the electrode, as illustrated in Figure 2.7 B. The top two images show a droplet formed in a solution of 10 mg/mL of DPhPC in hexadecane, pierced with an electrode. Since the bilayer only moves at

a very slow rate, deformation of the droplet results. The agarose coating, or 'anchor', on the tip of the electrode ensures that the droplet continues to wet the electrode. The lower two images show a droplet formed in a solution of 5 mg/mL of DPhPC in hexadecane. The lipid was prepared by direct dissolution in the alkane as described in section 2.3.2.3, and the droplet was incubated in the solution for 15 minutes before transferring it to the well in the device containing the same lipid-oil solution, where it formed a bilayer with the supporting hydrogel after 4 minutes. The droplet was then left for 30 hours. After this time, the oil-water interface appears mechanically resistant to pressure from the electrode, and deforms without wetting it. It is clear that the droplet in this case cannot be surrounded by a single monolayer of lipid, but that there are probably multilamellar lipid structures present at the interface. The bottom image in Figure 2.7 shows that the droplet can also be deformed by moving the electrode at a distance from the interface, which supports the above conjecture. Figure 2.7 A shows data from 160 droplets of aqueous buffer (TRIS-HCl pH 8.0, 0.5 M NaCl) formed in DPhPC in hexadecane prepared by direct dissolution of DPhPC in hexadecane and dilution with anhydrous hexadecane as described in section 2.3.2.3 above. Anecdotally, bilayers that take more than 10 minutes to form tend to be difficult to manipulate with an electrode. Taking the time to bilayer formation (top portion of graph) as a measure of DIB viscosity, this data therefore suggests that a lipid concentration of < 7.5 mg/mL should be used for experiments where bilayer manipulation with the electrode is required. In practice, the shape of the data shown varies with the method of preparation of the lipid solution. This variation can, to a limited extent, be compensated for by adjusting either the incubation time of the droplet and or that of the device. Furthermore, experiments by Sebastian Leptihn[†] have shown that the time to bilayer formation for droplets formed in high lipid concentrations can be reduced by working at a temperature of 37 °C.

[†] Experiments carried out in the Wallace Lab in 2010. Present address: University of Hohenheim, Institute of Microbiology, Garbenstr. 30, 70599 Stuttgart, Germany

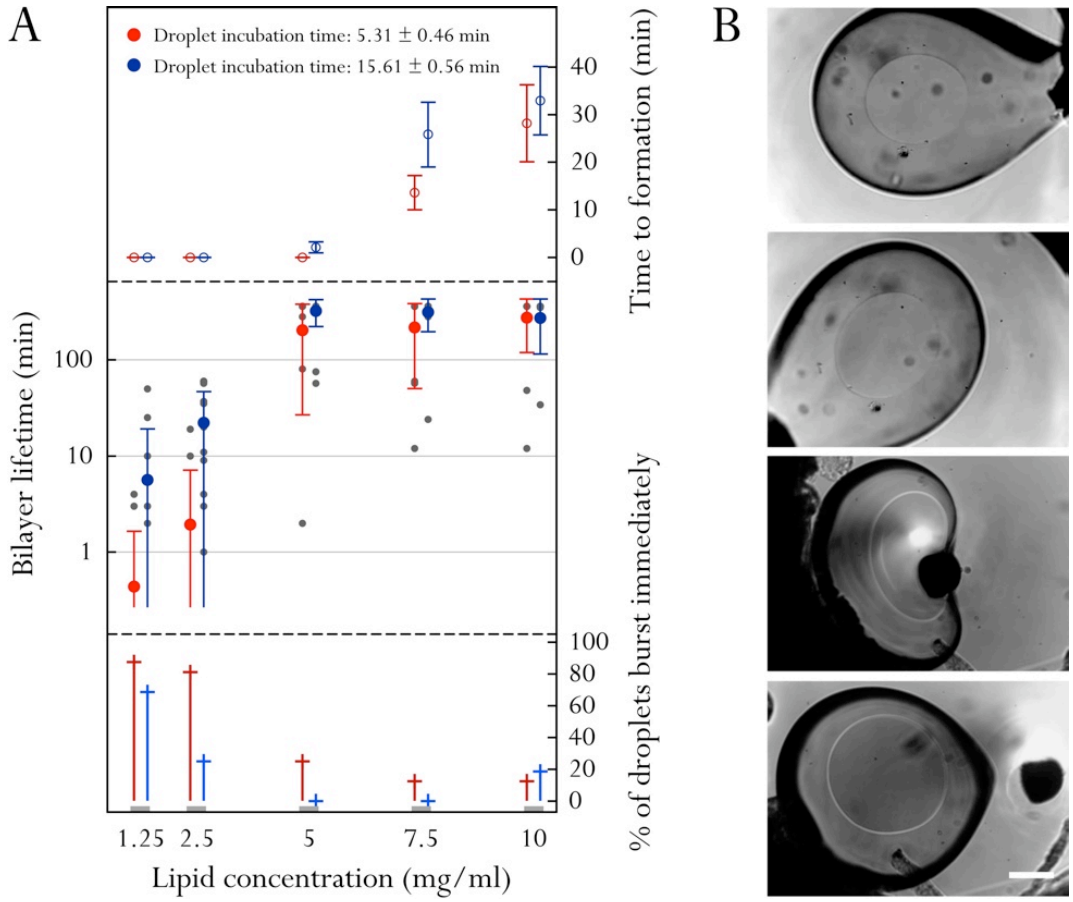

Figure 2.7: **(A)** Data from 160 droplets of aqueous buffer (TRIS-HCl pH 8.0, 0.5 M NaCl) formed in a range of concentrations of DPhPC. The lipid solutions were prepared from a single stock of directly dissolved of DPhPC in hexadecane and diluted with anhydrous hexadecane as described in section 2.3.2.3. The top portion of the graph shows that the time from droplet addition to a well to bilayer formation, which is inversely correlated with DIB viscosity, increases with lipid concentration and droplet incubation time. (In each data series, devices were equilibrated (incubated) for ~10 minutes longer than the droplet.) The middle section of the graph shows that bilayer lifetime is positively correlated with both lipid concentration and droplet incubation time. Devices were dismantled after 10 h. In the lower section the proportion of droplets that burst immediately is shown, which has an optimum at around 5–7.5 mg/mL. At 5 mg/mL with 15 minutes equilibration, 100% of droplets were stable for more than 1 hour. **(B)** Top two images: A droplet formed in 10 mg/mL DPhPC in hexadecane (TRIS-HCl pH 8.0, 0.5 M NaCl, 24 °C) Bottom two images: A droplet formed in 5 mg/mL DPhPC in hexadecane, 30 hours after bilayer formation. Scale bar: 100 μm.

2.4.3 Bilayer Lifetime

Like bilayer viscosity, bilayer lifetime depends on a variety of factors. Anectodal evidence collected in this laboratory suggests that lipid concentration, hydration, equilibration time, laboratory temperature and humidity all have an effect on bilayer stability. The experiments detailed here aim to summarise available data on these and other factors affecting bilayer lifetime, including the age of the lipid stock, the method of preparation of the stock and the salt concentration in the droplet.

Figure 2.7 A shows that bilayer lifetime is positively correlated with the time to bilayer formation, and thus inversely correlated with DIB viscosity. The data shown are derived from 16 droplets formed at each combination of lipid concentration and incubation time. Between one and three of such data sets were collected on a single day. The lipid solutions are dilutions from a single stock of 10 mg/mL of DPhPC directly dissolved in hexadecane, as described in section 2.3.2.3 above. At no point was the stock older than 7 days. For this particular lipid batch, the bilayer lifetime increases substantially above 5 mg/mL of lipid. As the lower section of Figure 2.7 shows, the majority of droplets formed in lipid solution of lower concentrations burst immediately upon contact with the supporting hydrogel. Longer equilibration times of droplets and device reduced this proportion, but only a small number lasted longer than 10 minutes, and none of the droplets lasted longer than 1.5 hours. Bursting happens faster than can be seen by eye, and no residue is left by the burst droplet. For this particular aqueous system (TRIS-HCl pH 8.0, 0.5 M NaCl) almost all droplets formed at lipid conentrations of 5 mg/mL or higher that did not burst upon contact lasted longer than 10 minutes, and most lasted for 10 hours, when the device was dismantled. Droplets formed at $>$ 5 mg/mL of lipid leave a visible residue on the surface of the hydrogel upon bursting, further evidence that the oil-water interface of such droplets probably does not consist of a simple lipid monolayer. It appears that there is an optimum in the proportion of bilayers that burst on contact, as this number increases unexpectedly at a lipid concentration of 10 mg/mL. Observation of the bilayer formation process shows that the bilayer often begins to form in irregular shapes, unlike the near perfect circle observed at lower lipid concentrations. This

may impose additional stress on some regions of the bilayer during formation that can lead to bursting.

2.4.3.1 Lipid Concentration and Droplet Equilibration

The data in Figure 2.7 A suggest that for experiments requiring the ability to manipulate the bilayer with an electrode, a lipid concentration of 5 mg/mL and a incubation time of 15 minutes, where the time to formation just begins to increase, is optimal in the trade-off of stability and viscosity of the bilayer. Based on observations in this laboratory however, this optimal point can shift substantially in practice, depending on the particular aqueous phase characteristics and the lipid stock. As pointed out in the case of the DIB viscosity above, this variation can be compensated for to some extent by empirically adjusting the equilibration time of droplet and device, but for some systems it is difficult to find a regime in which both stability and viscosity requirements can be satisfied.

Figure 2.8 shows data from 300 droplets collected over a period of four months during experiments using a fluorescent calcium indicator dye inside the droplet (TRIS-HCl pH 8.0, 0.6 – 1.7 M KCl, 44 – 59 μm Fluo-8, 1 – 3 mM EDTA) and calcium buffer (TRIS-HCl pH 8.0, 0.5 – 0.75 M $CaCl_2$) in the substrate. A small osmotic imbalance was incorporated to minimise calcium flux into the droplet in experiments with protein pores that will be described in Chapter 6. Work by other members of the laboratory has shown that DIBs can be stable in osmotically asymmetric conditions. Furthermore, it was determined that 10/12 droplets containing only EDTA and buffer (TRIS-HCl pH 8.0, 1 M KCl, 2 mM EDTA) and 8/9 droplets containing only the calcium sensitive dye Fluo-8 (TRIS-HCl pH 8.0, 1 M KCl, 50 μm Fluo-8) were stable for over 3 hours (see Table 2.2). Both controls were carried out on a hydrogel containing the same buffer (TRIS-HCl pH 8.0, 1 M KCl). Figure 2.8 shows that it is difficult to observe any clear correlation between a number of parameters and the bilayer lifetime. It is perhaps unsurprising that no correlation between droplet incubation time and bilayer lifetime can be observed in this data set (Figure 2.8 A), as this parameter was primarily adjusted to compensate for variations encountered in stability and viscosity. It is however interesting to note that although the lipid concentration was above

Table 2.1: Details of the preparation method of the lipid batches shown in Figure 2.8 C. New batches were prepared either when a stock was exhausted or when stability and viscosity characteristics were unsuitable for the experiments performed.

No.	Method of preparation	Dilution by	Method of mixing	Final conc.
1	via chloroform (→ 2.3.2.2)	-	vortex 2 min	5 mg/mL
2	via chloroform (→ 2.3.2.2)	-	vortex 2 min	5 mg/mL
3	via chloroform (→ 2.3.2.2)	-	vortex 2 hours	5 mg/mL
4	via chloroform (→ 2.3.2.2)	-	vortex 2 hours	5 mg/mL
5	dry DPhPC (→ 2.3.2.3)	-	vortex, leave overnight	15 mg/mL
6	dilution from 5	C16	50 °C for 5 mins	10 mg/mL
7	dilution from 5	anhydrous C16	50 °C for 5 mins	5 mg/mL
8	dilution from 5	anhydrous C16	50 °C for 5 mins	5 mg/mL
9	combination	6 and 8 (3:1)	pipette up and down	8.75 mg/mL
10	dry DPhPC (→ 2.3.2.3)	anhydrous C16	50 °C for 5 mins	6 mg/mL
11	dilution from 10	anhydrous C16	50 °C for 5 mins	5 mg/mL
12	combination	9 and 8 (2:1)	pipette up and down	7.5 mg/mL

5 mg/mL in all cases (see table 2.1), it was at times necessary to incubate droplets for over an hour before a stable bilayer could be observed.

2.4.3.2 Salt Concentration

As part of this series of experiments, the osmolyte concentration was adjusted frequently to optimise fluorescence, as will be described in more detail in Chapter 6. Experiments carried out in this laboratory by Sebastian Leptihn suggest that droplets are more stable at higher salt concentration (1 M NaCl vs. 0.1 M NaCl). It is difficult to observe this trend in Figure 2.8 B, but the proportion of droplets that burst on contact with the bilayer appears to be lower at higher salt concentration. It is possible however that the effect of salt concentration tails off above 0.5 M. To further investigate the effect of any osmotic imbalance present in the asymmetric conditions used in these experiments, the radius of the bilayer membrane (r_m) immediately after formation relative to the droplet radius (R_d) was measured in a subset of the data presented in Figure 2.8 (open circles, Figure 2.9 A), and compared to that of a set of droplets formed in symmetric conditions (TRIS-HCl pH 8.0, 0.75 M KCl in both the droplet and the substrate; closed circles, Figure 2.9 A). The result shows that any osmotic imbalance is not visible in the distribution of r_m/R_d, as both sets of data exhibit bilayer sizes characterised by an r_m/R_d of between 0.2 and 0.7. The only tentative conclusion that can be drawn from the data shown is that droplets with

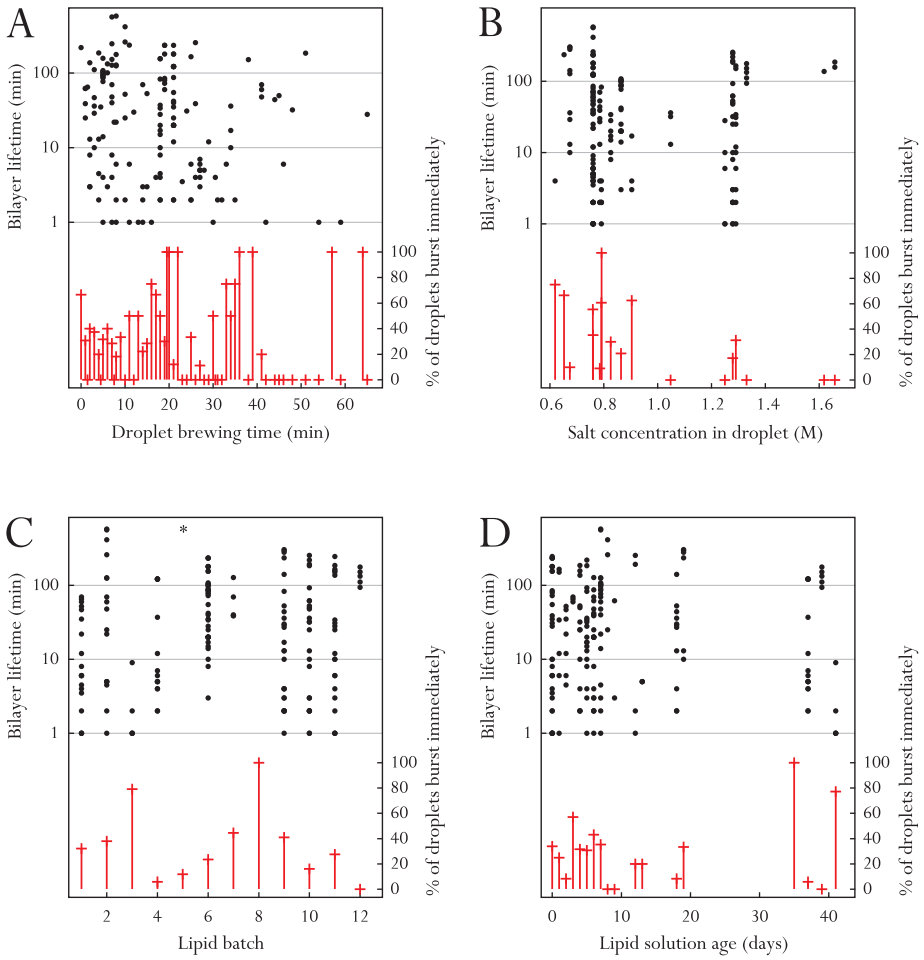

Figure 2.8: Droplet stability data from 300 droplets collected over a period of four months during experiments using a fluorescent calcium indicator dye inside the droplet (TRIS-HCl pH 8.0, 0.6 – 1.7 M KCl, 44 – 59 μm Fluo-8, 1 – 3 mM EDTA) and calcium buffer (TRIS-HCl pH 8.0, 0.5 – 0.75 M $CaCl_2$) in the substrate. **(A)** Droplet incubation time was adjusted to compensate for variations in droplet stability and viscosity on different days and for different lipid solutions. No correlation with bilayer lifetime such as that observed in Figure 2.7 A would therefore be expected. Despite a lipid concentration of >5 mg/mL in all cases, droplets at times had to be equilibrated for longer than 60 minutes before a stable bilayer could be observed. **(B)** Bilayer lifetime as a function of salt concentration. A lower proportion of droplets at higher salt concentration burst upon first contact with the substrate. **(C)** Bilayer lifetime as a function of lipid batch. For details of the method of preparation and concentration of the batches see Table 2.1. * denotes 15 bilayers that lasted longer than 10 hours. **(D)** Bilayer lifetime as a function of the age of the lipid solution.

Table 2.2: Controls for the dataset shown in Figure 2.8

			# of n droplets burst at			
Aqueous phase[a]	**Lipid method**	**Lipid conc.**	**0 min**	**<10 min**	**>180 min**	**n**
Buffer + 2 mM EDTA	dry DPhPC (→2.3.2.3)	5 mg/mL	0	1	10	12
Buffer + 50 μM Fluo-8	dry DPhPC (→2.3.2.3)	5 mg/mL	1	0	8	9
Buffer	via chloroform (→2.3.2.2) but dissolved in anhydrous hexadecane	5 mg/mL	11	1	0	12

[a] Aqueous phases were symmetric and the buffer was TRIS-HCl pH 8.0, 1 M KCl

the longest lifetime tend to have a large relative bilayer size upon formation. It is therefore not clear what parameter affects the surface tension of the droplet to result in the observed distribution of r_m/R_d.

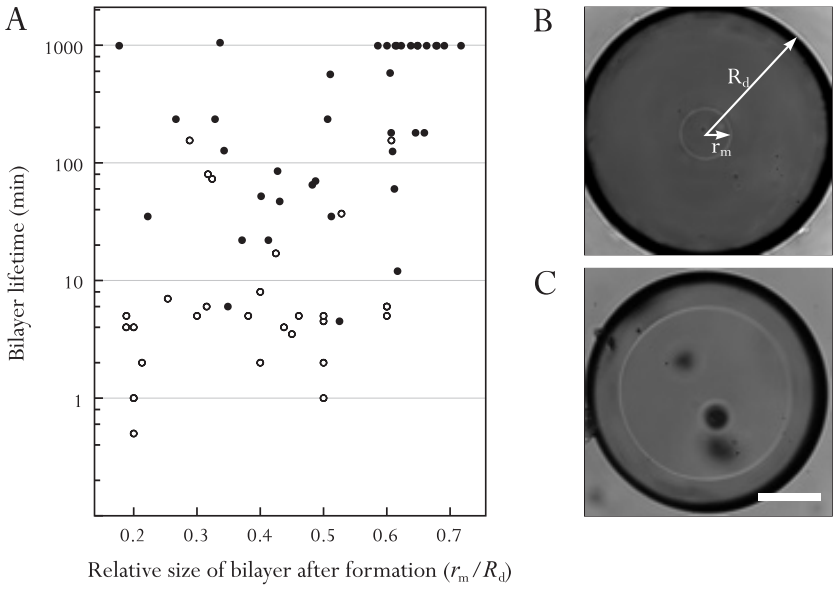

Figure 2.9: **(A)** Bilayer lifetime as a function of the relative size of the bilayer immediately after formation. Two data sets are shown: A subset of the droplets shown in Figure 2.8 (asymmetric aqueous buffer conditions; open circles) and a set of droplets formed in symmetric buffer conditions (TRIS-HCl pH 8.0, 0.75 M KCl; closed circles). Both data sets have similar random distributions of relative bilayer size. It appears as though the droplets with the longest lifetime tend to have a large r_m/R_d after bilayer formation. **(B)** A droplet with an r_m/R_d of 0.19. **(B)** A droplet with an r_m/R_d of 0.70. Scale bar: 100 μm.

2.4.3.3 Lipid Hydration

Large variations in the proportion of droplets that burst on contact with the substrate were observed between different batches of lipid-oil solution, with the implication that the relationship between lipid concentration and stability shown in Figure 2.7 A does not apply universally. Details of the preparation method and concentration of the lipid batches in Figure 2.8 C are listed in Table 2.1. For batches prepared by direct dissolution of DPhPC in hexadecane (methods section 2.3.2.3) it is likely that varying amounts of water in the 'dry' lipid stock lead to underestimation of the lipid concentration and therefore inconsistent results from batch to batch, or that water content in the lipid-oil solution impacts on the availability of dissolved lipid to assemble on the oil-water interface. This latter conjecture is supported by the fact that a lipid-solution of lower concentration but containing more anhydrous hexadecane than another originating from the same stock results in fewer droplets bursting on initial contact with the hydrogel (see batch numbers 9 and 12 in Table 2.1 and Figure 2.8). A control of dissolving lipid that had been dried under vacuum (see section 2.3.2.2) directly in anhydrous hexadecane yielded no stable droplets (Table 2.2), suggesting that some amount of water is needed to dissolve the dried lipid and that the lipid concentration in this control was most likely overestimated as a result. Anecdotally, lipid solutions in contact with an aqueous phase become more viscous over time (see also the bottom image in Figure 2.7 B). It is possible then to pull strings of lipid structures from the solution with a pipette. The mixing (by pipetting up and down) of such viscous lipid solutions with solutions of the same concentration that contain anhydrous hexadecane – thereby lowering the water content without changing the concentration – reduces the viscosity of the solution. Mixing alone does not have the same effect.

2.4.3.4 Age of the Lipid Solution

Finally, there does not appear to be a correlation between the age of the lipid solution and bilayer stability for ages < 50 days, which suggests that storage of the lipid solution at room temperature does not adversely affect bilayer stability (Figure 2.8 D).

2.5 Results and Discussion: Bilayer Manipulation

2.5.1 Changing Bilayer Area by Mechanical Manipulation

As Figure 2.10 illustrates, the size of the bilayer can be adjusted by moving the droplet relative to the hydrogel substrate with the inserted electrode (Heron et al., 2007). After each adjustment of the electrode, the bilayer area changes until a new equilibrium between the surface tension of the droplet and the force applied by the electrode is reached. The time lag between the adjustment and the new equilibrium depends on the viscosity of the bilayer. For low viscosity bilayers, no time lag is discernible whereas it can take up to five seconds for high viscosity bilayers to reach equilibrium.

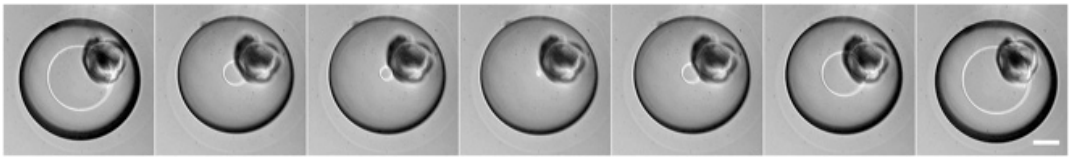

Figure 2.10: A series of images taken at intervals of 1 s illustrating the effect of changing the position of the electrode along the vertical axis. (Aqueous phase: TRIS-HCl pH 8.0, 0.5 M NaCl; lipid: 5 mg/mL DPhPC in hexadecane). Scale bar: 100 μm.

Bilayer viscosity is also the determinant of the range of bilayer areas that can be achieved with this method. At a critical bilayer size, the line tension term in equation 2.11 becomes dominant and increases rapidly, meaning that no new equilibrium can be reached. As a result of this instability, the bilayer size spontaneously begins to decrease in the absence of any change in the force applied by the electrode. The rate of this spontaneous decrease accelerates until the droplet disconnects from the supporting hydrogel. The critical bilayer size at which this occurs depends on the viscosity of the bilayer. Figure 2.11 A shows bilayer area data from a low viscosity droplet (aqueous phase: TRIS-HCl pH 8.0, 0.3 M KCl; lipid: 5 mg/mL DPhPC in hexadecane, droplet equilibrated for 5 minutes). By carefully adjusting the vertical position of the electrode upwards at a constant rate, it is possible to linearly decrease bilayer area in a controlled manner. For this bilayer, the critical point is characterised by an area of 880 μm^2, or a relative bilayer radius of $r_m/R_d = 0.096$, when the bilayer

area deviates from the straight line despite the absence of any change in the rate of movement of the electrode. By extrapolation, the area would have reached zero within less than ~500 ms. A brief downward adjustment of the electrode arrests this trend and the bilayer grows rapidly to reach equilibrium at the new position. By contrast, Figure 2.11 B shows the same experiment in a high viscosity droplet (aqueous phase in droplet: TRIS-HCl pH 8.0, 1.3 M KCl, 1.6 mM EDTA, 50 μm Fluo-8; aqueous phase in substrate: TRIS-HCl pH 8.0, 0.75 M $CaCl_2$; lipid: 6 mg/mL DPhPC in hexadecane). For this bilayer, the critical bilayer area is 30 μm^2, or a relative bilayer radius of $r_m/R_d = 0.015$.

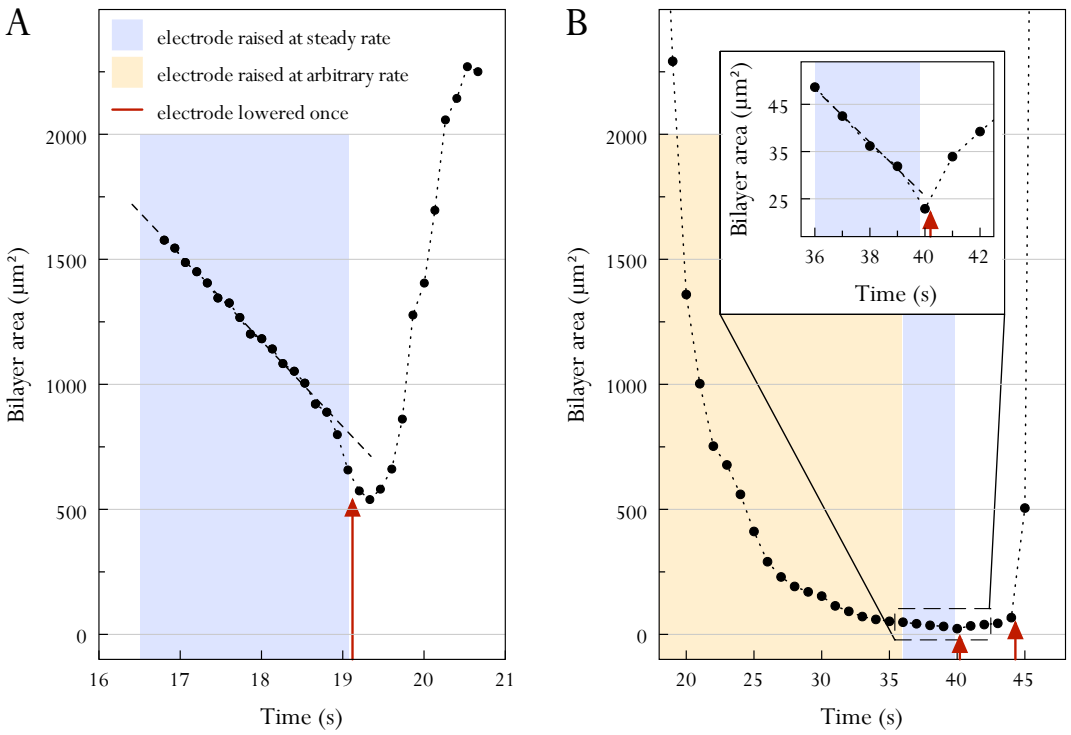

Figure 2.11: A DIB with a viscosity that is too low to maintain a small bilayer area. A a relative bilayer radius of $r_m/R_d = 0.096$ can be reached in a controlled manner by raising the electrode steadily. Upon raising the electrode further, the bilayer does not reach equilibrium but accelerates towards disconnecting from the supporting hydrogel as the line tension becomes dominant. **(B)** A bilayer of lower viscosity than that in A (see main text for details). Here, the bilayer can be maintained at a small size for a prolonged period, and instability only occurs at a relative bilayer radius of $r_m/R_d = 0.015$ (inset).

As discussed above, bilayer viscosity depends on the concentration and hydration of the lipid solution, and on the time the droplet is kept in the lipid solution before

allowing it to contact the supporting hydrogel. An applied potential shifts the point of instability to smaller bilayer sizes, and the incorporation of a transmembrane protein in the bilayer can provide additional stabilisation. As will be seen in Chapter 6, Bilayers more than 1500 × smaller than the resting bilayer size have been achieved with droplets containing 165 nM of the transmembrane protein pore α-Hemolysin (α-HL) held at an applied potential of -50 mV.

The data shown in Figure 2.11 should be understood in view of the fact that, at present, there is no way of quantifying the amount of force applied by the electrode and therefore no way of verifying whether it did in fact change at a steady rate where indicated. As a result, it is difficult to measure the critical bilayer area with confidence. If this limitation could be overcome, the experiment shown in Figure 2.11 could be a useful method of quantifying bilayer viscosity.

2.5.2 Manipulating the Size of the Bilayer with an Applied Potential

As noted in the previous section, the application of a potential shifts the point where a bilayer would spontaneously disconnect from the hydrogel towards a smaller area. As would be expected therefore, a potential applied when the bilayer is at its resting area, i.e. without any force applied by the electrode, results in a small spontaneous increase in bilayer area. Figure 2.12 B shows a cross-section through a stack of images of a bilayer taken every 10 seconds while an applied potential was cycled between -100 and $+100$ mV in a series of 10 mV steps at intervals of 10 seconds. The bilayer area peaks at $\pm$ 100 mV, i.e. once every 200 seconds. The changes in droplet contact angle associated with such spontaneous bilayer area changes can be described by the Young-Lippmann equation (equation 2.16), which considers the balance of forces arising from the applied potential across the bilayer and the interfacial surface tensions associated with the droplet.

Figure 2.13 shows a fit of equation 2.16 to the the average contact angle data from two droplets subjected to a series of voltage ramps as described above. At each point, the contact angle (θ_V) was calculated from the droplet diameter and the measured radius of the bilayer using equation 2.13. The contact angle began to deviate from

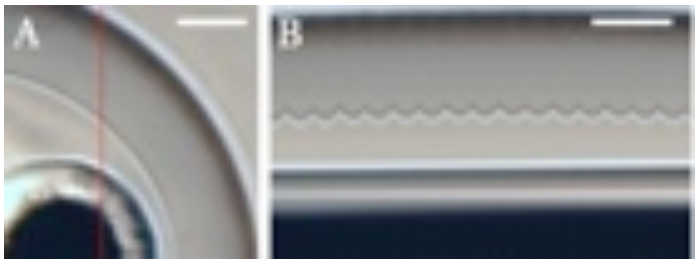

Figure 2.12: Change of bilayer area with an applied potential. **(A)** A partial view of a DIB (aqueous phase: TRIS-HCl pH 8.0, 0.3 M KCl; lipid: 5 mg/mL DPhPC in hexadecane). The dark spot in the bottom left is the electrode. Scale bar: 50 μm. **(B)** A cross section through a stack of images of the bilayer in A taken every 10 seconds. The applied voltage was cycled between −100 and +100 mV in a series of 10 mV steps at intervals of 10 seconds. The vertical dimension is the same as in A. The horizontal dimension shows the line marked in red in A over time. Scale bar (horizontal dimension): 10 minutes.

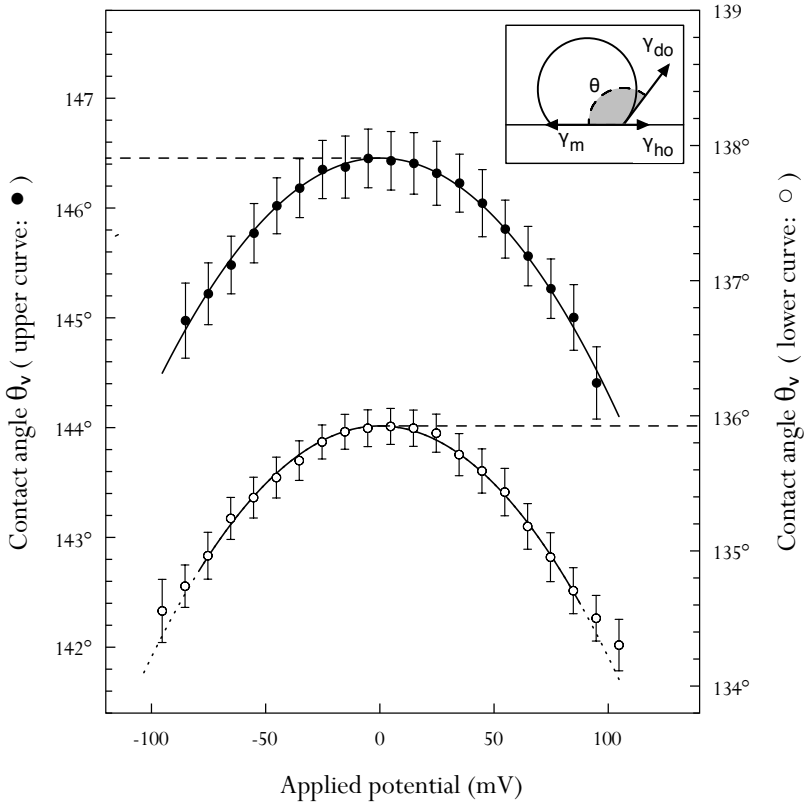

Figure 2.13: Examples of contact angle data from two separate droplets in voltage experiments (open circles: $\theta_0 = 135.9°$, closed circles: $\theta_0 = 146.5°$), fit with the Young-Lippmann Equation (equation 2.16, solid lines). With the assumption of a specific capacitance of $C_m = 0.65\ \mu F\,cm^{-2}$ the fit yields an average droplet surface tension (γ_{do}) of 1.61 mN m^{-1} ($n = 5$). The deviation of the measured contact angles from the ideal towards higher applied potentials shows the limit of applicability of the Young-Lippmann equation. This limit occurs at a lower applied voltage for droplets with a smaller θ_0 (lower curve).

the quadratic fit at potentials <100 mV for droplets with a smaller θ_0 (Figure 2.13, open circles). This would be expected from the considerations in section 2.2.6, but it is likely that in the DIB system the wetting of the electrode and resulting force normal to the surface is a simpler explanation for the observed deviation from the fit. Even when discounting these deviations and evaluating the area change from the quadratic fits, the magnitude of the bilayer area change varied considerably between droplets. For a sample of five DIBs, the bilayer area changed by 12.3 % ± 6.3 % over an applied potential of ± 100 mV. It is likely that here again, bilayer viscosity is the determining factor.

Assuming a value for the specific capacitance (C_m) of the bilayer of 0.65 μF cm^{-2}, the fit yields a surface tension of the droplet-oil interface of $\gamma_{do} = 1.61 \pm 0.33$ mN m^{-1} (n = 5 droplets). This value is rather lower than the surface tension commonly reported for an oil-water interface in the presence of a monolayer. The surface tension of a pure n-alkane-water interface (γ_i) is around 50 mN m^{-1} (Israelachvili, 2011), and the maximal surface pressure (Π) of lipid monolayers measured by traditional methods such as the film balance experiment (Marsh, 1996) is thought to be ~35 mN m^{-1} (Israelachvili, 2011; Marsh, 1996), which means that, as already indicated in section 2.2.2, the expected surface tension of the droplet oil interface in the presence of the monolayer would be $\gamma_{do} = \gamma_i - \Pi \approx 15$ mN m^{-1}. However, Guha et al. (2011), who have independently developed a system very similar to DIBs in the context of electrowetting studies, also use the Young-Lippmann equation and measure a surface tension of 3 mN m^{-1} for the oil-water interface in a solution of sorbitan trioleate in dodecane, and even smaller values for the same system with additional surfactants. The result is also in line with monolayer surface tensions determined by Requena and Haydon (1975), who employed the Young-Lippmann relation for the characterisation of bilayer area changes in the different geometry of conventional aperture-suspended BLMs for a number of lipid oil systems and found values between 1.68 and 4.38 mN m^{-1}.

While the Young-Lippmann equation is routinely used in pure EWOD sytems, the discrepancy in the surface tension associated with the monolayer could suggest that the model is too simplistic to describe the effects that arise in the presence of

surfactants. On the other hand, based on figures derived from hydrocarbon solubility data, it has been proposed that the figure for the alkane-water interface of $\gamma_i \approx 50\ \mathrm{mN\,m^{-1}}$ used in the consideration above, which describes the hydrophobic free energy density of the polar-apolar interface, is somewhat too large, and that a more relevant figure for the case of the bilayer would be $\gamma_i = 39\ \mathrm{mN\,m^{-1}}$ (Marsh, 1996). This would lead to an estimate of $\gamma_{do} \approx 4\ \mathrm{mN\,m^{-1}}$ which would be more in line with the experimentally determined value here, bearing in mind that there is some variation between different lipid-oil systems (Requena and Haydon, 1975). In addition to that, the traditional methods of determining lipid surface pressure are known to be unreliable due to difficulties in accurately determining monolayer area, which casts more doubt on the theoretical value. The method used here for the determination of the surface tension of the droplet-oil interface in the presence of a monolayer may therefore prove to be an interesting new approach to determining lipid monolayer surface pressure.

A final point to consider is that the Young-Lippmann equation assumes that voltage-dependent changes in the pre-quadratic term $C_m/2\gamma_{do}$, are negligible. Given the quality of the fits of equation 2.16 to the data, this assumption seems reasonable for applied potentials of $<\pm$ 100 mV, but will be discussed in more detail in Chapter 4 in the light of results obtained from the measurement of the response of bilayer specific capacitance to an applied potential.

2.5.3 Imposing Curvature on DIBs

Preliminary experiments have shown that the curvature of DIBs can be manipulated by translating the droplet across a patterned substrate. Patterning was attempted either by depositing 1 μm diameter silica beads onto the substrate before addition of lipid solution to the well (Figure 2.14 A), or by incorporating polydisperse Sephadex beads of 100 – 300 μm diameter into the substrate (Figure 2.14 C). In the latter case, the substrate was prepared in the usual way by the swiping method (see section 2.3.3.1), but a small amount of beads were suspended in the molten agarose shortly before pipetting onto the coverslip. Figure 2.14 B shows a bilayer formed on a substrate with 1 μm silica beads. Upon formation, the bilayer edge sweeps the majority

of the beads along the surface of the substrate. Only a small number of beads are visible within the bilayer (Figure 2.14 B, inset). As silica beads are hydrophilic, it is unlikely that they are between the monolayer leaflets. Electrical recording would have to be carried out to verify if the lipid bilayer has formed over the top of the beads, or if the beads puncture the bilayer.

Figure 2.14 D shows a bilayer that was pulled across a group of Sephadex beads incorporated into the substrate. Sephadex is a trademark name for crosslinked dextran, which, like agarose, is a polysaccharide hydrogel. The beads therefore form a reasonably similar substrate to the surrounding agarose. From the shape of the bilayer it can be inferred that the surface of the substrate next to the beads is at only a slightly lower position than the top of the beads, which means that the substrate is substantially thicker than when made without beads. This is to be expected, as the second coverslip used to swipe the agarose is spaced away from the first coverslip by the presence of the beads. To achieve a greater degree of change in the curvature of the substrate, alternative methods of depositing the beads such as spin coating of the bead-agarose suspension might be preferable.

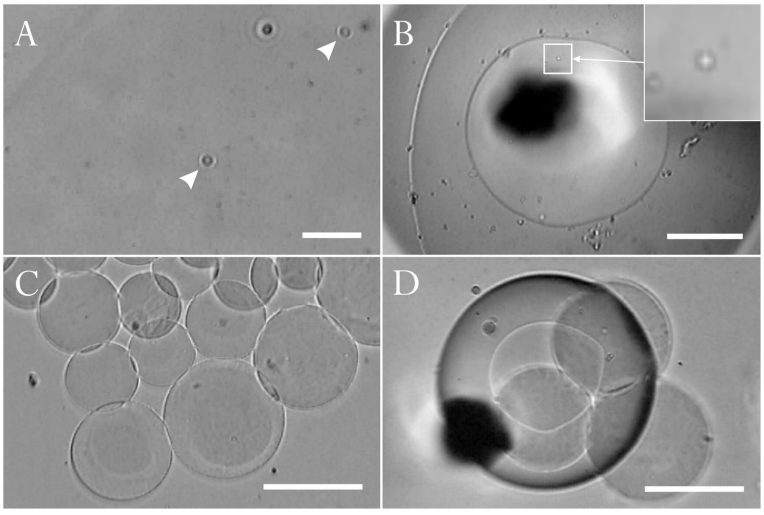

Figure 2.14: Preliminary experiments with bilayers on patterned substrates. **(A)** 1 μm silica beads deposited on the substrate. The arrows indicate beads that are in the focal plane of the substrate. Scale bar: 10 μm. **(B)** A bilayer on a substrate with 1 μm silica beads. Bilayer formation pushes the silica beads along the surface of the substrate. Only a small number of beads are visible within the bilayer. Scale bar: 100 μm. **(C)** Polydisperse Sephadex beads incorporated into the substrate. Scale bar: 100 μm. **(D)** A bilayer translated across undulations in the substrate formed by incorporated Sephadex beads. Scale bar: 100 μm.

2.5.4 Manipulation of DIBs with Optical Traps

Aqueous droplets in hexadecane have a lower refractive index than the surrounding medium and therefore cannot be trapped by conventional optical traps. The repulsive force at the interface means that droplets are pushed away from the focal point of the trapping beam. Two beam configurations that make use of this repulsion present themselves for the manipulation of droplets by optical traps and these were attempted in collaboration with Lee Moore. Firstly, a Laguerre-Gaussian beam (LG beam) was positioned such that it would fully encircle a droplet, effectively enabling 'low index trapping'. Secondly, an array of optical traps forming a 'cage' around the droplet were used to 'guide' the droplet to achieve lateral translation.

2.5.4.1 Low Index Trapping with a Laguerre-Gaussian Beam

Preliminary experiments with a Laguerre-Gaussian beam (LG beam) were carried out on droplets in a lipid-oil solution between two coverslips in the absence of a supporting hydrogel. The coverslips were spaced by a thin rubber gasket and pretreated with lipid-oil solution, which successfully prevented the droplets from wetting the surfaces. Figure 2.3 A shows a kinoform used to generate an LG beam ($\ell = 10$). To trap a droplet in an LG beam, the droplet has to be positioned precisely using the sample stage translation mechanism before the beam is switched on. It was possible to translate successfully trapped droplets and to bring one droplet in contact with another to form a bilayer between them. This is somewhat surprising, as the outer edge of the beam would be expected to repel other droplets. The most likely reason for the absence of this effect is that there were minor aberrations in the beam, resulting in regions of low trapping efficiency. In accordance with this, it was also observed that the droplet was more likely to escape the trap when moving in certain directions. In a series of experiments with droplets in devices with a supporting hydrogel that had formed bilayers, translation proved far more difficult as the additional friction of the bilayer resulted in frequent escape of the droplet from the trapping beam.

2.5.4.2 Translation of DIBs with an Optical Trap Array

Optical trap arrays were produced in the same way as the LG beam by kinoforms applied to the trapping beam by the SLM. Figure 2.3 B shows the required kinoform for 8 traps arranged in a square formation and the corresponding beam pattern. The spacing of the traps is 13.5 μm. Figure 2.15 shows a series of frames from a video of a droplet forming a DIB with a planar hydrogel substrate translated by an optical tweezer array. The white arrowheads in the image mark the position of 1.5 μm diameter silica beads that were incorporated into the substrate to act as distance markers. As the droplet was translated, other droplets on the right of the field of view were pushed away by the optical traps surrounding the translated droplet. DIB translation in this way could be another method of quantifying the viscosity of the bilayer. The droplets were, on average, characterised by low viscosity, but in some cases a slight time lag between the movement of the droplet and the movement of the bilayer was observed.

It is possible to apply a series of kinoforms dynamically to modify the arrangement of the traps, and successive tightening of the 'cage' around the droplet was attempted to see if it would be possible to deform the droplet. In the particular setup used here, the trapping efficiency falls off rapidly in the z-direction. Depending on the positioning of the traps on the z-axis therefore, different effects on bilayer area could be expected. Traps on a plane below the centre of the droplet would be expected to reduce bilayer size and possibly encourage escape of the droplet by disconnection from the substrate. The reduction of the spacing on a level above the centre of the droplet would be expected to result in flattening of the droplet. Unfortunately, preliminary results were inconclusive, as due to computational limitations the sizing of the cage had to be adjusted in a small number of large steps and droplets escaped from the cage in all cases before any deformation could be observed. One reason for this behaviour could be that the droplet continually drifts within the cage, and therefore it was difficult to begin the series of size changes with the droplet precisely at the centre of the cage. The sudden asymmetric forces produced by the large size changes then encouraged droplet escape. At present, the kinoforms to be applied

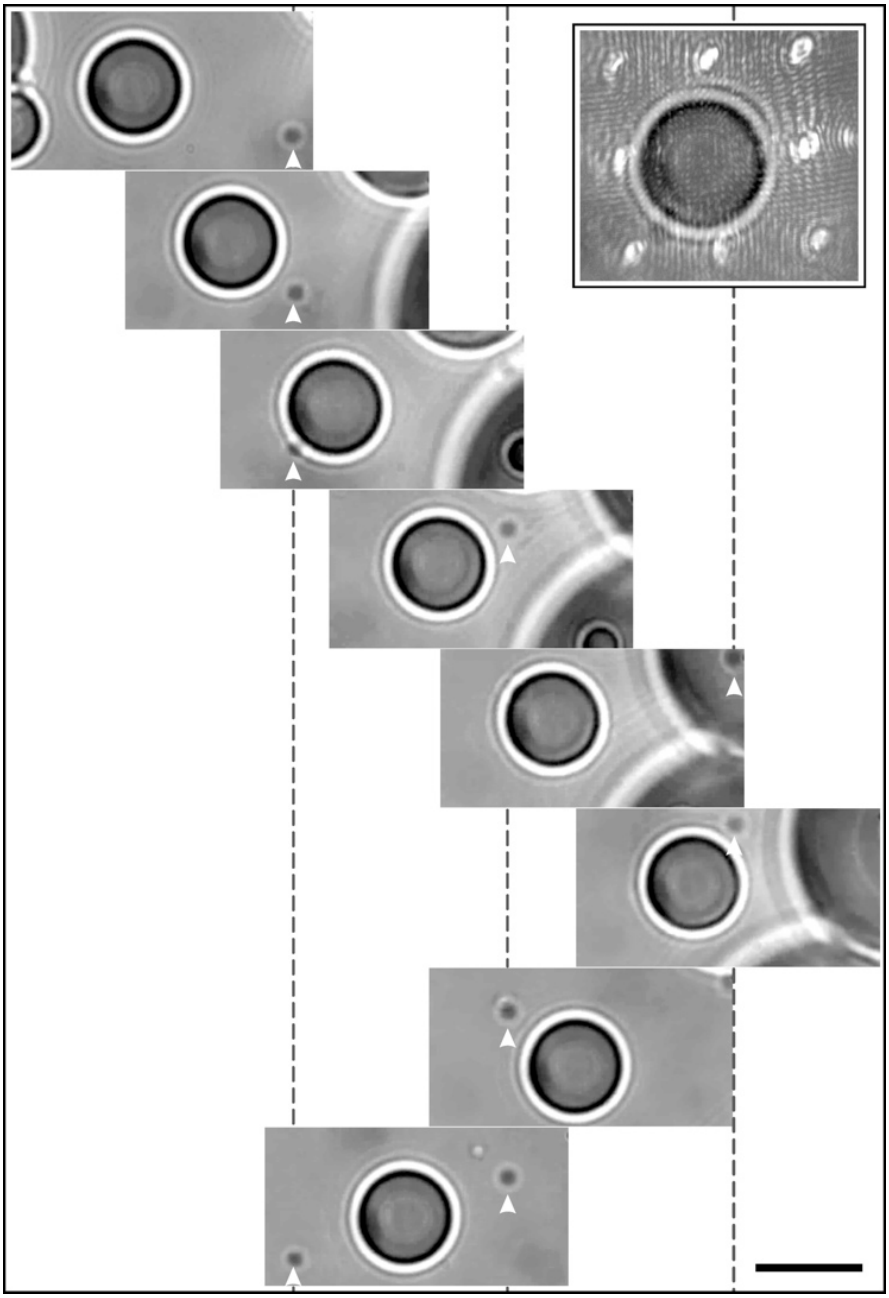

Figure 2.15: Frames from a video of a droplet forming a DIB with a planar hydrogel substrate translated by moving the sample stage relative to a fixed optical tweezer array (aqueous phase: HEPES pH 7.4, 1 M KCl; lipid: 1 mg/mL DPhPC in hexadecane). 1.5 μm diameter silica beads were incorporated into the substrate to act as distance markers (marked by white arrowheads in the image). Image interval: 8 s; scale bar: 20 μm. The inset shows the arrangement of the optical traps as determined by a computer-generated diffractive optical element (kinoform) applied to the trapping beam by a spatial light modulator (SLM)

dynamically have to be computed before the start of the experiment. Improvements in computational power that would allow kinoforms to be calculated in real time could enable the precise positioning of a droplet by adjusting the cage to the correct size. A slow size change may then give information as to whether droplet deformation is possible.

2.6 Summary

The experiments detailed in this chapter have shown that droplets are a complex system, and that careful control and fine-tuning of several parameters is needed to achieve optimal stability and viscosity. For DIBs formed in simple buffer systems, a clear dependence of stability on lipid concentration and droplet incubation time has been shown. In the case of more complex experimental conditions, it is clear that droplet stability remains a challenge. The best results were achieved by iterative tuning of the hydration of a lipid sample by means of the mixing of solutions that contained standard and anhydrous hexadecane, respectively.

This approach was also used here to maximise the range of bilayer area (relative to droplet size) that can be achieved by manipulating the droplet with an inserted electrode. The result is important for the experiments in the chapters that follow, which rely on the ability to modulate bilayer area mechanically. While this chapter focussed on optimising the lipid conditions that affect bilayer viscosity to maximise the area range, the 'pliability' of the droplet under some conditions (see, for example, Figure 2.7 B) suggests that it might be possible to achieve larger starting areas by devising ways of flattening the droplet. Indeed, a preliminary device design by Andrew Heron can be used to pull droplets by suction into a slot in a PMMA device, while retaining a bilayer with the underlying substrate. The work presented here could prove useful in improving the stability of such deformed droplet bilayers by optimising the lipid conditions. For a given volume, far greater area changes than those reported here might then be possible.

Preliminary results from experiments attempting to manipulate the bilayer by means other than direct mechanical manipulation have shown that both the induction of curvature in DIBs on patterned surfaces and the manipulation of DIBs by optical tweezers are possible. With the latter method, a droplet was moved over a distance of several 100 nm by means of an optical trap array, maintaining a DIB with an underlying substrate throughout. The system in this case was limited by the prototypcial nature of the tweezing setup, but a fully dynamic tweezing array with the ability to apply finely graded forces – either to compress the droplet laterally or to

translate it – would enable further characterisation of droplet viscosity. Future experiments could then aim to achieve the quantification of the effect of bilayer leaflet shear on membrane proteins present in the bilayer. For this purpose, an important next step is therefore the characterisation of the temperature in the centre of an LG beam or a trap array, and the development of a setup capable of fluorescence microscopy in the presence of the trapping laser (Candelli et al., 2011).

Bibliography

Ashkin, A., J. M. Dziedzic, J. E. Bjorkholm, and S. Chu (1986). Observation of a single-beam gradient force optical trap for dielectric particles. *Optics Letters 11*(5), 288–290.

Bayley, H., B. Cronin, A. Heron, M. A. Holden, W. L. Hwang, R. Syeda, J. Thompson, and M. Wallace (2008). Droplet Interface Bilayers. *Molecular BioSystems 4*(12), 1191.

Brandt, E. G., A. R. Braun, J. N. Sachs, J. F. Nagle, and O. Edholm (2011). Interpretation of fluctuation spectra in lipid bilayer simulations. *Biophysical Journal 100*(9), 2104–2111.

Candelli, A., G. J. L. Wuite, and E. J. G. Peterman (2011). Combining optical trapping, fluorescence microscopy and micro-fluidics for single molecule studies of DNA–protein interactions. *Physical Chemistry Chemical Physics 13*, 7263.

Chung, S. K., K. Rhee, and S. K. Cho (2010). Bubble actuation by electrowetting-on-dielectric (EWOD) and its applications: A review. *International Journal of Precision Engineering and Manufacturing 11*(6), 991–1006.

Curtis, J. E. and D. G. Grier (2003). Structure of optical vortices. *Physical Review Letters 90*(13), 133901.

Curtis, J. E., B. A. Koss, and D. G. Grier (2002). Dynamic holographic optical tweezers. *Optics Communications 207*(1-6), 169–175.

Dempster, J. (1997–2011). WinEDR: Strathclyde electrophysiology software. *Strathclyde University*. http://spider.science.strath.ac.uk/sipbs/software_ses.htm.

Drew, L. J. (2011). Sodium channel mechanosensitivity: Pay a-tension to voltage sensor movement. *The Journal of Physiology 589*(5), 1003–1004.

Fournier, J. B. and C. Barbetta (2008). Direct calculation from the stress tensor of the lateral surface tension of fluctuating fluid membranes. *Physical Review Letters 100*(7), 078103.

Funakoshi, K., H. Suzuki, and S. Takeuchi (2006). Lipid bilayer formation by contacting monolayers in a microfluidic device for membrane protein analysis. *Anal. Chem. 78*(24), 8169–8174.

Grahame, D. C. (1947). The electrical double layer and the theory of electrocapillarity. *Chemical Reviews 41*(3), 441–501.

Grahame, D. C. (1953). Diffuse double layer theory for electrolytes of unsymmetrical valence types. *The Journal of Chemical Physics 21*(6), 1054.

Gross, L. C. M., A. J. Heron, S. C. Baca, and M. I. Wallace (2011a). Determining membrane capacitance by dynamic control of Droplet Interface Bilayer area. *Langmuir 27*(23), 14335–14342.

Guha, I. F., J. Kedzierski, and B. Abedian (2011). Low-voltage electrowetting on a lipid bilayer formed on hafnium oxide. *Applied Physics Letters 99*(2), 024105.

Heron, A. J., J. R. Thompson, B. Cronin, H. Bayley, and M. I. Wallace (2009). Simultaneous measurement of ionic current and fluorescence from single protein pores. *Journal of the American Chemical Society 131*(5), 1652–1653.

Heron, A. J., J. R. Thompson, A. E. Mason, and M. I. Wallace (2007). Direct detection of membrane channels from gels using water-in-oil droplet bilayers. *Journal of the American Chemical Society 129*(51), 16042–16047.

Holden, M. A., D. Needham, and H. Bayley (2007). Functional bionetworks from nanoliter

water droplets. *Journal of the American Chemical Society 129*(27), 8650–8655.

Israelachvili, J. N. (2011). *Intermolecular And Surface Forces* (3rd ed.). Academic Press.

Jähnig, F. (1996). What is the surface tension of a lipid bilayer membrane? *Biophysical Journal 71*(3), 1348–1349.

Lewis, B. A. and D. M. Engelman (1983). Lipid bilayer thickness varies linearly with acyl chain length in fluid phosphatidylcholine vesicles. *Journal of Molecular Biology 166*(2), 211–217.

Loew, L. M. (1993). Electrical properties of biomembranes. *In:* M. Shinitzky (Ed.), *Biomembranes: Physical Aspects*, pp. 63–95. VCH: Weinheim.

Malmstadt, N., M. A. Nash, R. F. Purnell, and J. J. Schmidt (2006). Automated formation of lipid-bilayer membranes in a microfluidic device. *Nano Lett. 6*(9), 1961–1965.

Marsh, D. (1996). Lateral pressure in membranes. *Biochimica et Biophysica Acta (BBA) - Reviews on Biomembranes 1286*(3), 183–223.

Morris, C. E. and P. F. Juranka (2007). Nav channel mechanosensitivity: Activation and inactivation accelerate reversibly with stretch. *Biophysical Journal 93*(3), 822–833.

Mugele, F. and J. Baret (2005). Electrowetting: from basics to applications. *Journal of Physics: Condensed Matter 17*(28), R705–R774.

Padgett, M. J. and L. Allen (1995). The Poynting vector in Laguerre-Gaussian laser modes. *Optics Communications 121*(1-3), 36–40.

Paula, S., A. Volkov, A. Van Hoek, T. Haines, and D. Deamer (1996). Permeation of protons, potassium ions, and small polar molecules through phospholipid bilayers as a function of membrane thickness. *Biophysical Journal 70*(1), 339–348.

Rasband, W. S. (1997). ImageJ. http://rsb.info.nih.gov/ij/.

Rawicz, W., K. Olbrich, T. McIntosh, D. Needham, and E. Evans (2000). Effect of chain length and unsaturation on elasticity of lipid bilayers. *Biophysical Journal 79*(1), 328–339.

Requena, J. and D. A. Haydon (1975). The Lippmann equation and the characterization of black lipid films. *Journal of Colloid and Interface Science 51*(2), 315–327.

Requena, J., D. A. Haydon, and S. B. Hladky (1975). Letter: Lenses and the compression of black lipid membranes by an electric field. *Biophysical Journal 15*(1), 77–81.

Tanford, C. (1974). Thermodynamics of micelle formation: prediction of micelle size and size distribution. *Proceedings of the National Academy of Sciences of the United States of America 71*(5), 1811–1815.

Tanford, C. (1979). Hydrostatic pressure in small phospholipid vesicles. *Proceedings of the National Academy of Sciences of the United States of America 76*(7), 3318–3319.

Thompson, J. R., A. J. Heron, Y. Santoso, and M. I. Wallace (2007). Enhanced stability and fluidity in droplet on hydrogel bilayers for measuring membrane protein diffusion. *Nano Letters 7*(12), 3875–3878.

Tsofina, L. M., E. A. Liberman, and A. V. Babakov (1966). Production of bimolecular protein-lipid membranes in aqueous solution. *Nature 212*, 681–683.

Wallace, J. A. and S. Schürch (1990). Line tension of sessile drops placed on a phospholipid monolayer at the water–fluorocarbon interface. *Colloids and Surfaces 43*(2), 207–221.

White, S. H. (1980). Small phospholipid vesicles: Internal pressure, surface tension, and surface free energy. *Proceedings of the National Academy of Sciences of the United States of America 77*(7), 4048–4050.

White, S. H. (1986). The physical nature of planar bilayer membranes. *In:* C. Miller (Ed.), *Ion Channel Reconstitution*, pp. 3–35. Plenum Press, New York.

Widom, B. (1995). Line tension and the shape of a sessile drop. *The Journal of Physical Chemistry 99*(9), 2803–2806.

Chapter 3

Bilayer Specific Capacitance

This chapter describes experiments that use the ability to vary Droplet Interface Bilayer area over a range of several orders of magnitude to increase the precision of measurements of the area-independent 'specific' capacitance (C_m) made on a single bilayer. Specific capacitance is examined as a function of time, temperature, pH, protein binding and bilayer composition. The effect of an applied potential will be discussed in Chapter 4.

3.1 Introduction

A lipid bilayer membrane can be thought of as a biological parallel plate capacitor. This similarity has led to the extensive use of capacitance measurements to assess the area, thickness and surface potential of cell membranes (Cole, 1968; Kado, 1993). For example, under the assumption of constant membrane thickness (d) and dielectric permittivity (ε), the membrane capacitance (C_T) can be used to detect the minute stepwise changes (<1 fF) in membrane area (A_M) associated with single vesicle fusion events occurring during endo- or exocytosis (Lindau and Neher, 1988; Lollike et al., 1995; Schmitt and Koepsell, 2002; von Gersdorff and Matthews, 1999). However, C_T not only depends on area, but also on the area-independent 'specific' capacitance (C_m). Variations in membrane thickness due to lipid composition or phase, or modulation of dielectric properties upon protein binding affect C_m, and thus contribute to the difficulty of attributing any non-stepwise changes in *in vivo* membrane capacitance to a single phenomenon (Lollike et al., 1998).

Artificial black lipid membranes (BLMs) have been used extensively to characterise membrane specific capacitance changes in response to a wide range of factors, such as temperature, transmembrane potential, membrane composition, and pH (Alvarez and Latorre, 1978; Andrews et al., 1970; Babakov et al., 1966; Hanai et al., 1964, 1965b; Miller, 1986; Naumowicz, 2005; Ohki, 1969; Petelska and Figaszewski, 2000; Requena et al., 1975; Sakmann and Neher, 1995; White, 1970a, 1973, 1986). Conventional BLMs, which are typically formed across a small aperture in a PTFE film between two aqueous chambers (Montal and Mueller, 1972; Mueller et al., 1962; White et al., 1976), are difficult to image, and as a result the determination of bilayer area is challenging. In early experiments, the bilayer area was assumed to be constant, and derived from the size of the aperture (Alvarez and Latorre, 1978; Benz et al., 1975). Where BLMs can be imaged whilst carrying out simultaneous capacitance measurements, a sequence of independent experiments with bilayers of different sizes is necessary to precisely determine specific capacitance (Fujiwara et al., 2003; Hanai et al., 1965b; Naumowicz, 2005; Ohki, 1969; Picard et al., 1991; White, 1970a).

3.2 Background and Theory

3.2.1 The Ideal Parallel Plate Capacitor

A lipid bilayer is most simply described as consisting of two parallel conductive sheets, consisting of the polar head groups of the lipid, separated by an insulating layer formed by the aligned hydrocarbon lipid tails. This structure is analogous to that of a parallel plate capacitor, a simple model of a circuit device used to store electric charge. In a parallel plate capacitor, the two conductive plates, with a charge density of $+\sigma$ and $-\sigma$ respectively, are separated by a distance d and extend uniformly over an area A. When a voltage is applied, positive charges collect on one side of the capacitor, balanced by negative charges on the other. As a result, a static field forms across the capacitor. Since the area is large compared to d, the electric field E between the charges on the plates can be considered to be uniform:

$$E = \frac{\sigma}{\varepsilon} \tag{3.1}$$

where ε is the dielectric permittivity of the insulating material. The voltage is the integral of the electric field along the plate normal:

$$V = \int_0^d \frac{\sigma}{\varepsilon}\,\mathrm{d}z = \frac{\sigma d}{\varepsilon}. \tag{3.2}$$

The total amount of charge, $Q = \sigma A$, held on an ideal capacitor depends on the voltage V (externally applied or in the form of an intrinsic potential) and is determined by a constant capacitance (C):

$$Q = CV. \tag{3.3}$$

From equation 3.2 and equation 3.3 it can be seen that the total charge that can be accommodated is determined by the area of the capacitor (A), its dielectric properties and the thickness of the insulating material (d):

$$C = \frac{\varepsilon A}{d}. \tag{3.4}$$

A change in the voltage across the capacitor induces a charging current, the capacitve current (I_{C}) given by

$$I_{\mathrm{C}} = \frac{\mathrm{d}Q}{\mathrm{d}t} = C\,\frac{\mathrm{d}V}{\mathrm{d}t} + V\,\frac{\mathrm{d}C}{\mathrm{d}t}. \tag{3.5}$$

In lipid bilayers, the latter term describes reorientations, induced dipole deformations and geometric changes such as the voltage dependence of bilayer area and thickness, which will be discussed in detail in Chapter 4. For small applied voltages however, $\mathrm{d}C/\,\mathrm{d}t = 0$ is a reasonable assumption, and hence

$$I_{\mathrm{C}} = C\,\frac{\mathrm{d}V}{\mathrm{d}t}. \tag{3.6}$$

An applied voltage with a constant gradient will therefore result in a constant capacitive charging current I_{C}, from which the capacitance can be determined. By extension, an applied triangular potential induces a square wave capacitive current (Figure 3.1, dotted line in the middle panel).

3.2.2 The Non-Ideal Capacitor

In a non-ideal capacitor, i.e. one that is not perfectly insulating, an applied voltage will also induce a resistive, or Ohmic, current (I_{R}), described by

$$I_{\mathrm{R}} = \frac{V}{R}, \tag{3.7}$$

where R is resistance. In this case, the measured current (I_{M}) is the sum of the capacitive and resistive currents:

$$I_{\mathrm{M}} = I_{\mathrm{C}} + I_{\mathrm{R}}. \tag{3.8}$$

An applied voltage with a constant gradient will therefore result in a current with a gradient of $1/R$ and an offset of I_{C}. The resulting deviation from the ideal square wave is shown in Figure 3.1 (black line in the middle panel). The advantage of the triangular voltage method for the measurement of the capacitive current is that, by taking the average of the absolute values of I_{M} at an equal distance before and after

I_C changes sign, the ohmic current is cancelled, and thus I_C can directly be used to determine C. This method is illustrated in Figure 3.1, middle panel.

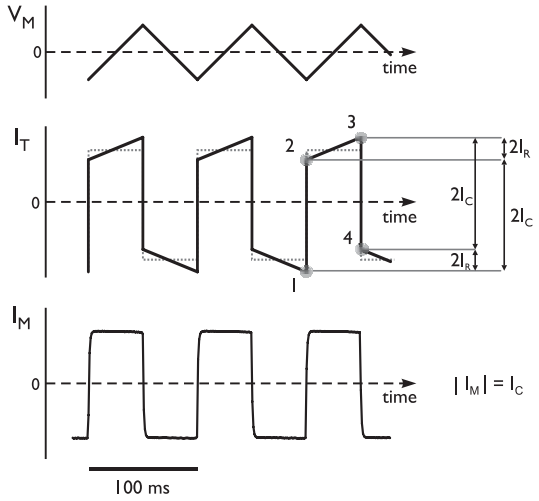

Figure 3.1: Determining bilayer capacitance with the application of a triangular potential. In an ideal bilayer, the application of a triangular potential (top) results in a square wave current (middle, dotted line, theoretical), the capacitive current ($I_C = C_T \times dV/dt$). In bilayers with a current leakage, the square wave is modified by an Ohmic component, I_R (middle, black line, theoretical). Both kinds of traces can be analysed for I_C by determining I at points 1 and 2 or 3 and 4, since $I_2 - I_1 = I_3 - I_4 = 2\,I_C$. In practice, DIBs formed from DPhPC in hexadecane have a tight (>100 GΩ) seal (Heron et al., 2007; Holden et al., 2007) and generally $I_R \simeq 0$ (bottom trace, data).

3.2.3 Specific Capacitance of Lipid Bilayers

Of particular interest as a means of characterising lipid bilayers is the capacitance normalised by area, known as the specific capacitance (C_m):

$$C_m = \frac{C}{A_M} \tag{3.9}$$

where A_M is the bilayer area. In lipid bilayers, the so-called geometric capacitance (C_g) is the specific capacitance of the hydrocarbon core:

$$C_g = \frac{\varepsilon_0\,\varepsilon_m}{d_m} \tag{3.10}$$

where ε_0 is the permittivity of free space, and ε_m is the dielectric coefficient of the hydrophobic core. d_m is defined as the thickness of the hydrophobic core of the

membrane.

Although it has been shown that the contribution of the polar head groups to bilayer specific capacitance is negligible (Hanai et al., 1965a), the measured bilayer specific capacitance (C_m) is not equal to the geometric capacitance (C_g). The reason for this is the capacitance of the electric double layer (C_{dl}), as already noted in 2.2.1. The measured bilayer specific capacitance thus consists of the double layer capacitance of each leaflet in series with the geometric capacitance:

$$\frac{1}{C_m} = \frac{1}{C_g} + \frac{2}{C_{dl}}. \tag{3.11}$$

At zero membrane surface charge and at potentials of less than about 25 mV, as apparent from equation 2.1, C_{dl} can be approximated to (Everitt and Haydon, 1968; Läuger et al., 1967; White, 1973)

$$C_{dl} = \frac{\varepsilon_w \, \varepsilon_0}{(1/\kappa)} \tag{3.12}$$

where ε_w is the dielectric coefficient of water and $1/\kappa$ is the Debye-Hückel length as given in equation 2.1. Under these assumptions, equation 3.11 rearranges to (Läuger et al., 1967)

$$C_m = \frac{C_g}{1 + \frac{2}{\kappa d_m} \frac{\varepsilon_m}{\varepsilon_w}}. \tag{3.13}$$

If the electrolyte concentration is high, and therefore $1/\kappa$ is small, double layer capacitance (C_{dl}) in equation 3.11 becomes large enough for the difference between C_m and C_g to be negligible (Fettiplace et al., 1971; White, 1970b, 1973) and therefore

$$C_m \approx C_g = \frac{\varepsilon_0 \, \varepsilon_m}{d_m}. \tag{3.14}$$

In an example of a bilayer of thickness $d_m = 60$ Å in a 0.1 M electrolyte, where $1/\kappa$ is about 10 Å, $C_m = 0.998 \; C_g$ (Läuger et al., 1967).

When the above conditions of a low potential and zero fixed surface charges cannot be satisfied, it is considerably more difficult to estimate the contribution of C_{dl} to C_m (Everitt and Haydon, 1968) and this case will be discussed in detail in Chapter 4.

3.2.4 Historical Background to Measurements of Specific Capacitance

A key element in the measurement of specific capacitance is the precise determination of bilayer area. As early as 1964, Hanai et al. assumed that optically black hydrocarbon films behaved as parallel plate capacitors and calculated their thickness from measurements of capacitance and bilayer area determined by looking at reflected light from the bilayer through a low power microscope with a graticule in the eyepiece. A constant film thickness for a range of films of different areas suggested that the parallel plate capacitor assumption was correct, but it was clear that it was desirable to have the ability to vary bilayer area to increase the precision of the thickness measurement. In a follow-up paper (Hanai et al., 1965b), hydrostatic pressure was used to bulge the bilayer to increase area by a factor of 10. The bilayer was formed across a 1 mm punched hole in a PTFE film, observable through a glass outer vessel. Assuming hemispherical bulging, a linear fit yielded a value for the specific capacitance of egg-lecithin membranes of 0.46 μF cm^{-2}. The authors concluded that capacitance indeed varies linearly with bilayer area, that the constant gradient, i.e. the specific capacitance, was characteristic of a given film composition, and that the total capacitance of a membrane may thus be used as an indication of its area. As will be described in more detail below, this is still the basis of many instances in experiments today where total capacitance is used as a measure of bilayer area.

However, in a dynamic system such as the lipid bilayer, it is clear that this relationship can only hold in otherwise unchanging conditions. As is apparent from equation 3.4, any changes in bilayer thickness or dielectric properties affect the specific capacitance. Such changes can arise from lipid reorientation or phase changes as a result of variations in pH, electrolyte concentration, lipid composition, temperature, protein binding or potential. A large number of studies have been undertaken in BLMs to determine specific capacitance in a range of systems and conditions. Collectively, these studies suffer from the difficulty of determining bilayer area in traditional bilayer systems in two respects: The accuracy of the absolute specific measurement depends on an accurate measurement of bilayer area, and any measured relative ef-

fect of a given parameter on specific capacitance depends on the assumption that the parameter does not also affect bilayer area.

A number of methods have attempted to address this problem by using frequency-based methods that measure capacitance on timescales too short to allow any area changes to take place (Hianik and Passechnik, 1995).

3.2.5 Bilayer Capacitance as a Tool for *in vivo* Characterisation of Membranes and Processes

In *in vivo* experiments, whole membrane capacitance is routinely used as a measure of membrane area. On the basis of estimates of cell surface area and capacitance measured in whole cell patch clamping experiments (Cole, 1968), a common literature value for the specific capacitance of bilayers *in vivo* is $\sim 1\ \mu\mathrm{F\,cm^{-2}}$ (Neher and Marty, 1982), which is significantly higher than that of artificial systems. The reason for this discrepancy is not understood, but has been attributed to a variety of possible phenomena, such as the stretching, and thus thinning, of the bilayer by proteins that bind to the leaflets, or the existence of microvilli and other protrusions that could result in underestimates of cell membrane area (Fettiplace et al., 1971). More recent measurements do indeed place the specific capacitance of certain cells closer to the values seen in artificial systems, with $0.8\ \mu\mathrm{F\,cm^{-2}}$ measured in nerve endings (Rosenboom and Lindau, 1994) and $0.5\ \mu\mathrm{F\,cm^{-2}}$ in chromaffin cells(Solsona et al., 1998). Despite these uncertainties, new methods of continuously monitoring capacitance *in vivo* (Schmitt and Koepsell (2002) and refs therein) mean that the specific capacitance has become a widely used tool to investigate processes involving step changes in bilayer area (Lollike and Lindau, 1999) and to uncover the real-time kinetics of processes such as signalling and synaptic transmission in living cells (Lindau and Neher, 1988; Lollike et al., 1995; Schmitt and Koepsell, 2002; von Gersdorff and Matthews, 1999). The cell-attached patch capacitance technique allows investigation of single exocytotic events for vesicles as small as 60 nm (Lollike et al., 1995). It is clear however, that any non-stepwise changes in capacitance are extremely difficult to interpret without a comprehensive understanding of all parameters that affect specific capacitance (Lollike et al., 1998). Such understanding could validate preliminary studies

such as that by Zimmermann et al., who observed a specific capacitance change of up to 30 % upon protein overexpression, since it is necessary to shed light on the question of whether such effects are due to a dielectric change or to bilayer compression, or whether in fact they exist at all and are not purely an area effect (Gentet et al., 2000).

3.2.6 The Effect of the Solvent Used in Artificial Bilayers

BLMs are often substantially thicker than their biological counterparts due to the chemical equilibrium between oil present within the bilayer and that in the bulk annulus (Andrews et al., 1970; Benz et al., 1975; White, 1975, 1986; White et al., 1976). The amount of oil that remains in the bilayer depends on the structure of the oil; smaller oils such as decane have a reduced entropic penalty within the bilayer as compared to larger molecules, where oil chain length approaches that of the lipid alkyl chain (White, 1977, 1978). Figure 3.2 shows a series of measurements of the specific capacitance of DIBs made with solvents of varying chain lengths. The data were acquired by Sylvan Baca[†] and Andrew Heron[‡] (Baca, 2006).

As would be expected from the entropy considerations (White, 1986) mentioned earlier, the data, converted to bilayer thickness using $\varepsilon_m = 2.2$ for DPhPC as determined by Valincius et al. (2008), confirms findings from BLM experiments that bilayer thickness decreases with increasing length of the alkane chain (Figure 3.2). Bilayers approach optimum oil-free conditions with longer-chain alkanes (Figure 3.2). The thickness of the hydrophobic core of the bilayer for DPhPC in heptadecane, which should be approaching the solvent-free limit (Fettiplace et al., 1971; White, 1986), is calculated to be 28.4 ± 0.7 Å in DIBs. While some caution should be exercised when quantitatively comparing results from different techniques, this value is in good agreement with that reported by Valincius et al. (2008) of 28.6 ± 1.4 Å, which was determined using neutron diffraction of solvent-free tethered bilayers on a solid support. Heptadecane is the longest saturated alkane that is liquid at room temperature. Alternative oils that are further disfavoured from remaining in the bilayer, but remain liquid at room temperature (White, 1978, 1986), were also tested

[†] Present address: Harvard Medical School, 25 Shattuck Street Boston, MA 02115, USA

[‡] Present address: Oxford Nanopore Technologies, 4 Robinson Avenue, Oxford Science Park, Oxford OX4 4GA, UK

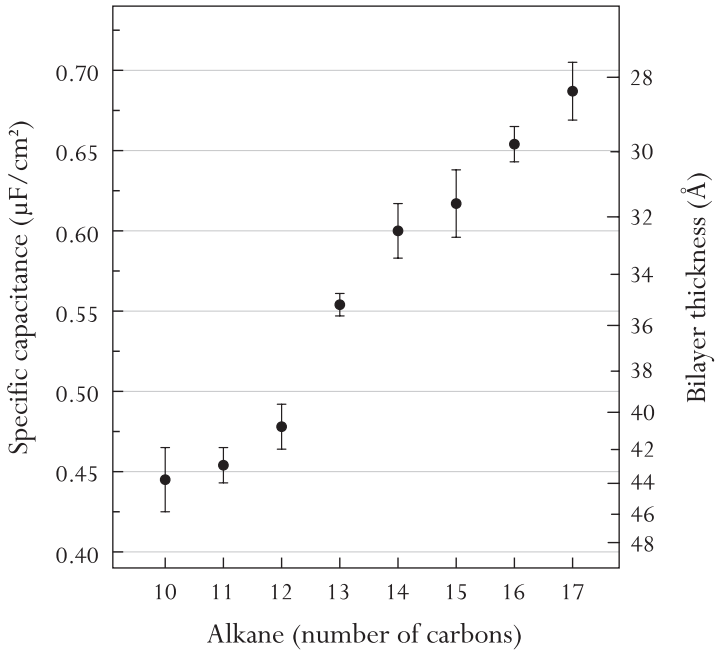

Figure 3.2: DIB capacitance as a function of oil composition. Measured specific capacitance (left axis) and calculated bilayer thickness (right axis) of DPhPC bilayers (10 mM Na_iPO_4 pH 7.0, 1 M KCl) in a series of C_n-alkane oils, from decane (C_{10}) to heptadecane (C_{17}). Bilayers formed in the shorter-chain alkanes are thicker (lower specific capacitance) as a result of the greater ability of the smaller oil molecules to interdigitate into the bilayer. The bilayer approaches an ideal oil-free state with longer chain length alkanes.
Adapted with permission from Gross et al. (2011a). Copyright (2011) American Chemical Society. This data was acquired by Andrew Heron (present address: Oxford Nanopore Technologies, UK) and Sylvan Baca (present address: Harvard Medical School, USA).

(Andrew Heron, personal communication): White (1978) reported near oil-free bilayers of GMO in squalene ($C_{30}H_50$), and it was found that DIBs do not form well in squalene, but are leaky and unstable (see also Figure 3.3 D below). However, DIBs formed favourably from DPhPC in cis-9-tricosene, a 23 carbon chain alkane with a single cis-unsaturation site that is disfavoured from entering bilayers (Vacklin et al., 2000). DPhPC DIBs in tricosene yielded a C_m of 0.721 ± 0.021 μF cm^{-2} and a d_m of 27.0 ± 0.8 Å. Under the assumption that bilayers formed in tricosene are solvent-free, or close to solvent-free, bilayers formed in hexadecane – the oil used in most instances described in this thesis and also more generally in DIB experiments (Heron et al., 2009, 2007; Holden et al., 2007; Sarles and Leo, 2009, 2010; Thompson et al., 2007) – which are 10.2 % (~2.5 Å) thicker, contain 9.2 % oil by volume. This represents a reasonably low oil content system when compared to bilayers formed in decane, which are 62 % (~17 Å) thicker and contain 38 % oil by volume.

3.3 Materials and Methods

3.3.1 Materials

Materials were as in Chapter 2. Additionally, 1,2-dioleoyl-*sn*-glycero-3-phosphocholine (DOPC), 1,2-dipalmitoyl-*sn*-glycero-3-phosphocholine (DPPC), 1-palmitoyl-2-oleoyl-*sn*-glycero-3-phospho-ethanolamine (POPE), 1,2-dioleoyl-*sn*-glycero-3-phospho-(1'-rac-glycerol) (sodium salt) (DOPG), 1-palmitoyl-2-oleoyl-*sn*-glycero-3-phos-pho-(1'-rac-glycerol) (sodium salt) (POPG), cholesterol and 1,2-dipalmitoyl-*sn*-glycero-3-phospho-ethanolamine-N-(biotinyl) (DPPE-Biotin, sodium salt) (all Avanti Polar Lipids, Alabaster, AL) were stored at −20 ℃ and were used without further purification. Alkane oils (pentane, decane, tetradecane, hexadecane were from Sigma-Aldrich (St Louis, MO) and were stored at room temperature. Squalene (also Sigma-Aldrich) was stored at 4 ℃. Annexin V from human placenta (A9460, Sigma-Aldrich) and Streptavidin (S4762, Sigma-Aldrich) were stored at −80 ℃ and also used without further purification.

3.3.2 Current Trace Analysis and Capacitance Measurement

Electrical recording of DIBs was achieved as described in Chapter 2. Total capacitance (C_{T}) was measured by the application of a triangular voltage on the basis of the equations in section 3.2.1. A 10 Hz triangular wave input signal (Figure 3.1, top trace, V_{a}) was applied in all experiments reported here to obtain a square wave capacitive current output. The square wave current traces (Figure 3.1, bottom, I_{M}), acquired from the application of a triangular potential, were analysed post-acquisition, either manually by viewing traces in pClamp software (Molecular Devices) or by algorithm using Igor Pro software (Wavemetrics), as described in more detail below. To determine whole membrane capacitance manually, the capacitive current I_{C} (Figure 3.1, bottom) was measured by determining the length of the capacitive spike ($2\,I_{\mathrm{C}}$, points 1 and 2 in Figure 3.1, middle). A model cell with a known capacitance of 100 pF (MCB-1U, Molecular Devices) was used to determine $\mathrm{d}V/\,\mathrm{d}t$ in each experiment. Capacitance was then calculated from the average of 10 spikes using $I_{\mathrm{C}} = C_{\mathrm{T}} \times \mathrm{d}V/\,\mathrm{d}t$.

3.3.3 Automation of Capacitance Measurement

In the algorithmic implementation of the capacitance measurement at a point (t_i), a 1 s section of trace of trace from ($t_i - 1$ s) to t_i was extracted. For measurements of specific capacitance, points t_i were chosen to coincide with images taken of the bilayer, either triggered manually or automatically at fixed intervals. The capacitive current was obtained by differentiating the square wave trace to locate each positive capacitive spike in that section, and averaging four data points either side of it to determine the length of the spike. The obtained $2\,I_C$ at all positive spikes in the 1 s section was averaged, and used to calculate capacitance as described above. (see Figure 3.22 for a comparison of manual vs. automatically acquired data). This approach results in inaccuracy when bilayer area is changing rapidly over time, such as immediately after bilayer formation (see Figure 3.8 for example) or after manipulation of the electrode. An alternative implementation of the algorithm would be to centre the 1 s section contributing to the analysis on t_i ($t_i \pm 0.5$ s). In practice, however, this is not worthwhile at present since the current experimental setup does not allow for the determination of the image time points with sufficient accuracy. All measurements were therefore taken when bilayer area had stabilised. The exception are the measurements at the start of the experiments described in section 3.4.1, and the results have to be considered with this in mind.

If both bilayer area measurements for the points t_i and pixel size calibration data are available, then the algorithm subsequently calculates specific capacitance and linearly fits the resulting C_m vs. A_M data. Additional functions specific to the voltage experiments described in Chapter 4 are also provided, which group the results according to the applied voltage and calculate the standard error of the C_m vs. V_a data. A detailed description of the Igor Pro algorithm is provided in Appendix B along with a reproduced procedure file.

3.3.4 Bilayer Area Measurement

In the simplest implementation, bilayer area was measured manually by overlaying images of the droplet (640 × 480 px, Phillips Vesta Pro or Trust webcam) with

perfectly elliptical selections in ImageJ (Rasband, 1997) and recording the area of the selection in pixels. Under slight defocus, the edge of bilayers of DPhPC formed in hexadecane is highlighted by a bright ring (see for example Figure 3.3 A, top). The centre of the ring was chosen as the bilayer edge. In the majority of cases, DPhPC in hexadecane bilayers are perfectly circular, but for other lipid-oil systems, several difficulties can arise. Firstly, the edge of the bilayer can be difficult to distinguish, (see for example bilayers of DPhPC in decane or tetradecane in Figure 3.3 A, middle) or the ring might have a clear outside edge, but the intensity falls off more gently inside the bilayer (see, for example, Figure 3.3 C, top). In these cases, a line within one pixel of the outer edge was chosen. In general, bilayers that were not perfectly circular were excluded from analysis. Even bilayers with slightly different orthogonal radii are difficult to fit, as the built-in ImageJ elliptical selection only enables the selection of radii in the x and y directions. Ellipses of other orientations therefore have to be fitted by subsequently rotating the selection. In some limited instances, the bilayer area was selected manually with a free-form selection. The latter two approaches are extremely time consuming when applied to stacks of images and are subject to significant human error due to the tendency to impose the expectation of the location of the bilayer edge on the image. This tendency was also found in sequences of bilayer images where the bilayer is circular, but reduces or enlarges consistently. Carrying out the area measurement on a randomised set of these images removed this bias. A further source of error can be the discretisation of available selection sizes at small bilayer sizes, due to the fact that the elliptical selection in ImageJ is bound to actual pixels. In these cases, the image was enlarged to two or three times the original size by interpolation before making the measurement. This approach gave satisfactory results, but can also be a source of systematic error as the placement of the selection boundary on the bilayer ring is judged under different conditions (see also Figure 3.5 below), and the criterion above of 'one pixel from the edge', for example, can no longer apply.

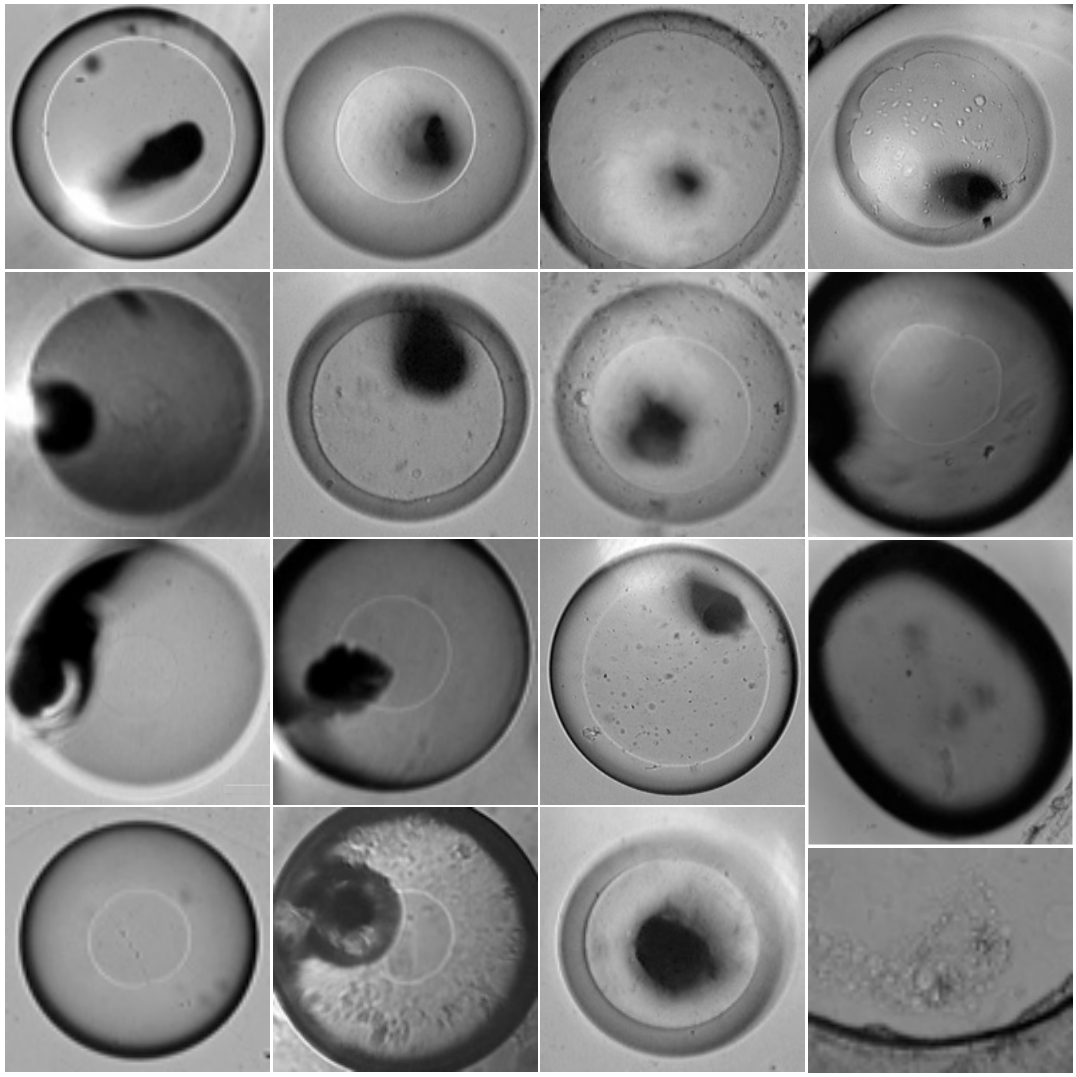

A	B	C	D
Hexadecane	DPhPC:Chol 6:4	DPhPC:DPPC:Chol 1:1:1	DOPC in hexadecane
Tetradecane	DOPC:Chol 8:2	DPhPC / DPhPC:DPPC:Chol 1:1:1	DPhPC in squalene
Decane	DPhPC:DOPG 9:1	DOPC:DPPC:Chol 6:2:2 / DOPC	DPhPC in squalene (3 hrs old)
Hexadecane with oil lens	DOPE:POPG 4:1	DOPC:DPPC:Chol 2:1:1 / DPhPC	DOPC:POPE 4:1

Figure 3.3: Morphology of droplet systems

3.3.5 Progress Towards the Automation of Bilayer Area Measurement

As is clear from the previous section, there are several points where bias can be introduced into a manual area measurement. Algorithmic analysis should be able to remove bias and not be subject to pixel size limitations. A number of methods of determining bilayer area were evaluated. The obvious candidates, edge detection algorithms such as 'Snake', available as plugins in ImageJ (Rasband, 1997), tend to have difficulties with the fact that parts of the bilayer edge are often obscured by the electrode or have different contrast profiles from one edge to another (see, for example, Figure 3.3 C, bottom). Even if the parameters of the algorithm can be set to achieve more or less correct fitting in one image, the fit rarely succeeds in a stack of images where the position of the electrode and the intensity profile of the edge tend to change. As a result, it seems prudent to make use of the expected perfect ellipticity of the bilayer. An earlier implementation in ImageJ by Andrew Heron iteratively improved an initial guess of circle centre and a possible range of values for the radius by least-squares minimisation of the distance of four points from the guessed centre. The four points were initialised by finding the maximal intensity gradient on a cross of lines through the guessed centre along the x and y directions. Again, the obscuring of portions of the bilayer by the electrode or even dust in the image path can hamper the success of this approach. In addition, the maximal gradient approach can create inconsistencies because it does not always select the same edge of the bright ring demarcating the bilayer.

The most promising approach attempted here relies on fitting circles to a sparse set of points using analytic geometry. The points are obtained by pre-processing the image sufficiently to primarily retain points on the bilayer edge.

Image Pre-processing. Image pre-processing was carried out by a macro in ImageJ. Images were bandpass filtered to retain structures of dimensions between one and three pixels, and auto scaled, resulting in images such as that shown in Figure 3.4 B. The macro then outputs a summed image of all images in the stack to be processed to enable the visualisation of the full range of bilayer areas in the stack.

Three clicks are requested from the user: one in the approximate centre of the bilayer, and two further ones at the inner and outer limits to all bilayer data (Figure 3.4 C). Information outside the resulting ring is discarded, and the data inside the ring is thresholded. Thresholding can be carried out manually by removing around 98 % of the grey values to retain only the brightest points. Alternatively, two automatic thresholding modes in ImageJ, 'minimum' (Figure 3.4 D, upper half) and 'intermodes' (Figure 3.4 D, lower half), were found to give good results throughout stacks containing images with variations typical of the data collected in this thesis. The macro is reproduced in full in Appendix B.

Circle Fitting to Sparse Points. An algorithm was created in Igor Pro to fit circles to the sparse data imported from the output of the ImageJ pre-processing macro. Circle fitting to sparse points is a surprisingly complicated problem (Chernov and Lesort, 2005), and there are a number of algebraic and geometric approaches in the literature (Al-sharadqah, 2009). However, many of these require rather complicated numerical analysis, and since the localisation of the circle for these purposes is unimportant and only the area needs to be found, a simple statistical approach was opted for here.

Any three points (x_1, y_1; x_2, y_2; x_3,y_3) that are not co-linear determine a unique circle. The algorithm implemented here iteratively selects a random set of three points from a set of sparse points such as that shown in Figure 3.4 D, determines the unique circle described by these three points, and records its radius and the coordinates of its centroid. Contrary to the manual ellipse fit in ImageJ, the recorded values in this implementation are not limited to integer values. The user determines the number of iterations to collect a set of radii and centroid coordinates. As long as the image pre-processing described above ensures that the majority of points remaining in the sparse data set originate from the bilayer edge, the statistical distribution of radii in the set determined in this way will have a maximum at the radius that fits the most number of points in the sparse image. The centroid distribution is more prone to error: a bright patch in the image can result in many small concentric circles. Since the radii of these circles will differ, this kind of noise does not significantly impact

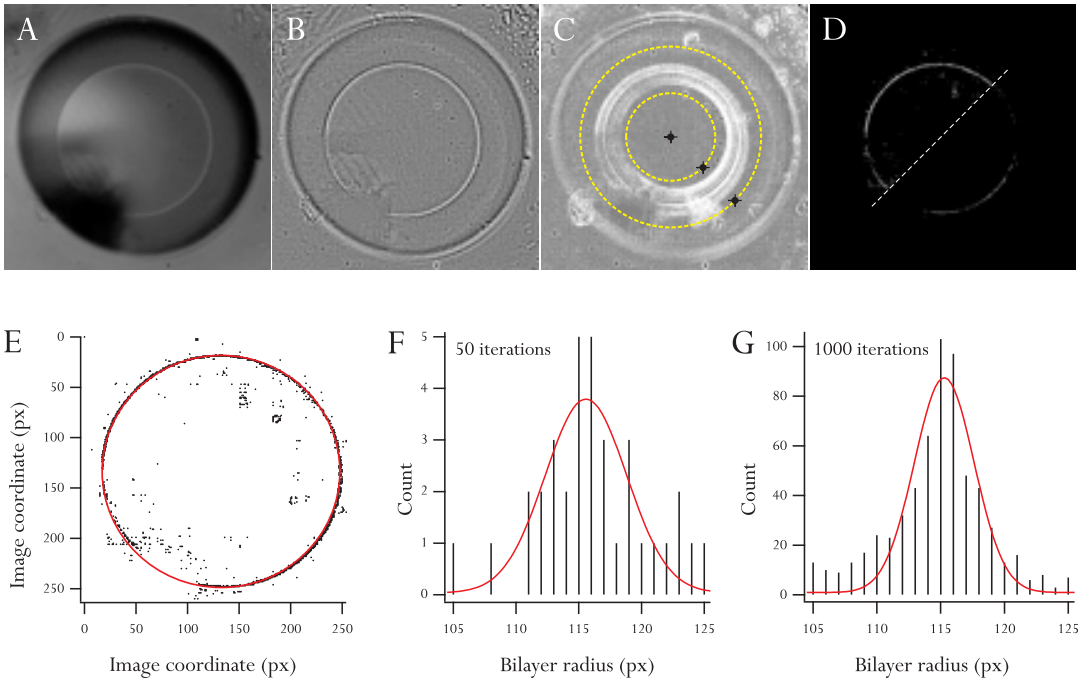

Figure 3.4: Automatic area fitting routine. **(A-D)** Image pre-processing implemented in an ImageJ macro. **(E-F)** Fitting a circle to a sparse set of points obtained from the above, implemented in Igor Pro. **(A)** First frame of a stack of images of a POPE:POPG 3:1 droplet in hexadecane. **(B)** Band-pass filtered image to retain structures of the order of 1 – 3 pixels. **(C)** Summed images of B through entire stack. Three clicks (black marks) are required to select the area containing all bilayer size data. This area is retained throughout the stack, the remaining areas are set to 0 intensity. **(D)** The frame shown in A and B thresholded to retain the ∼2 % brightest points. Two automatic thresholding modes built into ImageJ are shown: 'intermodes' (upper half) and 'minimum' (lower half). **(E)** The best fit circle determined by the fitting procedure implemented in Igor Pro (for details see text) run on the sparse data from D, upper half, 1000 iterations. **(F)** The radius is determined by finding the circles described by a user-set number of sets of three points randomly selected from the sparse data. A Gaussian fit to the distribution of radii in these sets yields the radius of the circle that fits the most number of points. For 50 sets of three points (iterations), r_m= 115.57 ± 0.127 px **(G)** For 1000 iterations, r_m= 115.279 ± 0.052 px

on the radius determined by the algorithm, but can lead to erroneous centroids. As already pointed out however, this is of little consequence for the purpose of specific capacitance measurements. Figure 3.4 F and G show distributions of the radii of 50 and 1000 random sets of three points respectively, collected from the 'intermodes'-thresholded data shown in the upper half of Figure 3.4 D. Figure 3.4 E shows the circle with a radius resulting from the maximum of the Gaussian fit to the distribution in Figure 3.4 G, centred at the maxima of Gaussian fits to the distribution of the coordinates of the circle centroids (not shown) and superimposed on the thresholded data derived from the image in Figure 3.4 A. A detailed description of the algorithm can be found in Appendix B alongside the reproduced Igor Pro procedure file.

A stack of 300 images, which would take one hour to measure by hand at the very least, takes just under a minute to process with a 1000 iterations. No representation of the computational efficiency of this algorithm is made here, but the processing time was more than adequate for the requirements of the experiments described in this and in the next chapter.

Evaluation of Area Determination Figure 3.5 A shows a series of area measurements of 10 sequential bilayer images from a stack that recorded a bilayer steadily reducing in size. The automatically determined area is largely within the error of the manual area measurement method, as evidenced by the errors (S.D.) of 5 repeated manual area measurements on the data. Since the manual measurements contain both systematic and random errors, there is no way of determining the real bilayer area. The automatic area measurement was therefore compared to both the average of the manual measurements and to a straight line fit to this data. The latter was intended to evaluate the performance of the algorithm under the assumption that the bilayer area may in fact be changing linearly in this particular data set.

Figure 3.5 B compares the standard deviation of the difference between each of 5 differently determined area data sets from the data in Figure 3.5 A and (1) the average of 5 manual measurements (light blue) or (2) the straight line fit to the average of 5 manual measurements (dark blue). The standard deviation of the difference was chosen as a parameter to measure the volatility in the data, and to exclude any systematic

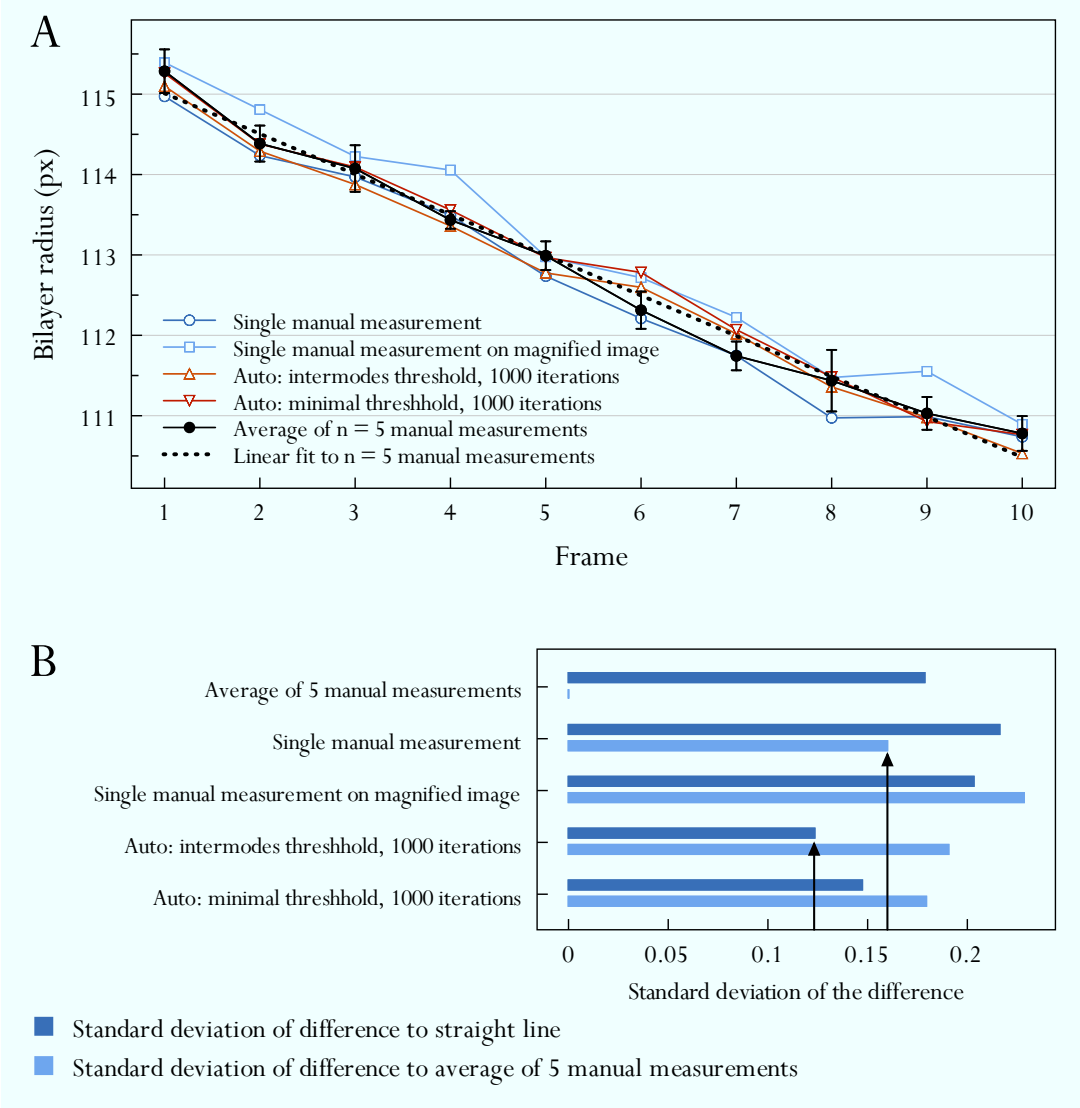

Figure 3.5: Comparison of methods for bilayer area determination. **(A)** Five differently acquired sets of bilayer radius measurements are shown. The raw data is a series of images of a POPE:POPG 3:1 droplet that is steadily reducing in size, taken at intervals of 5 seconds. Frame 1 is identical to Figure 3.4 A. The black line is an average of five manually acquired radius measurement sets (not shown individually) with errors (S.D.). A linear fit to this average is also shown (dotted line). **(B)** The five data sets from A are compared against (1) the straight line fit in A (dark blue) and (2) against the average of five manual measurements shown in A. The parameter of comparison is the standard deviation of the difference at each data point. This parameter excludes any systematic error that could be corrected for in a future implementation. The arrows highlight the best-performing method if the true bilayer size changes as described by case (1) or case (2) respectively.

error that could be compensated for in a future implementation. As expected, a single manual measurement performs best in case (1), but the automatic measurement still performs better than a dataset collected on a magnified image, a procedure that appears to introduce other errors. In case (2), i.e. under the assumption that the true bilayer area change follows a straight line, the automatic measurements outperform all other methods (left arrow in Figure 3.5).

The results presented here indicate that the algorithm is capable of measuring bilayer area with a precision at least equal to that of the manual approach. However, due to the fact that a thorough analysis of systematic errors resulting from the preprocessing step performed on different bilayer systems has not yet been carried out, the majority of the data presented in this thesis were also measured by hand to ensure that values presented are comparable.

3.3.6 Construction of a Temperature Control Stage

To enable temperature control of the DIB environment, methods such as water circulation, commercial objective heaters and Peltier-based methods were evaluated. Water circulation was not suitable as it proved impossible to eliminate electrical and

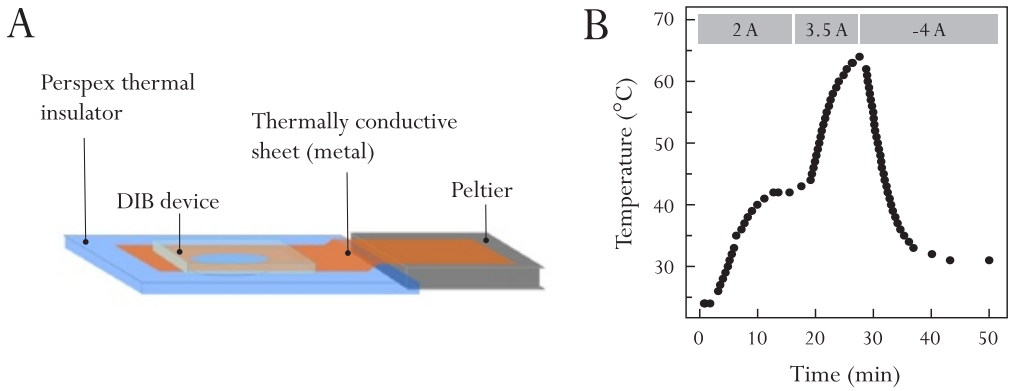

Figure 3.6: Construction of a preliminary temperature control stage. **(A)** Schematic illustration of the Peltier setup. A thermally conductive metal sheet transfers heat from the hot side (top) of the Peltier. The DIB device rests on the sheet, which in turn is thermally insulated from the bottom of the Faraday cage that supports it above the microscope objective. The temperature at the droplet is recorded during all experiments by a thermocouple placed into one of the oil wells of the device (not shown). **(B)** Example time course of temperature at the device upon the application of current to the Peltier by DC power supply. The positive change in temperature at a negative applied current arises from inefficiency of heat dissipation from the Peltier into the supporting Faraday cage when hot and cold sides are reversed.

vibrational noise introduced into the Faraday cage by the water circulation pump. The objective heater available had a limited range (<43 ℃), and the limitation to oil immersion objectives meant that it was not suitable for the experiments pursued here. As a result, the experimental setup described in section 2.3.9 was modified to include a Peltier regulated temperature stage. A 4 cm × 4 cm Peltier was placed on the floor of the Faraday cage next to the hole machined into the cage for objective access and connected to a DC power supply (1746, B&K Precision) by leading the wires through the holes in the Faraday cage designed for the arms of the micromanipulator. The Faraday cage thus acts as a sink for the cold side of the Peltier (the underside). Thermal conductivity was ensured by adding thermally conductive paste to the underside of the Peltier before positioning it. A 1.8 cm diameter hole was machined into a thermally conductive 5 cm × 10 cm × 2 mm sheet of metal (aluminium, Figure 3.6 A, orange sheet). Two-thirds of the sheet was placed on a 2 mm thick thermal insulator (perspex) sheet with a hole of the same dimensions and fixed to the existing microscope stage next to the Peltier, aligning the holes with the objective axis. The other third was shaped to fit to the hot side (top) of the Peltier and connected with thermally conductive paste. The DIB PMMA device was placed on the thermally conductive sheet.

In this setup, the temperature difference between the hot side of the operating Peltier and the DIB device was ~20 ℃ as measured by a K-couple thermometer (TC920, Electrocomponents plc, UK) inserted into the oil of a well on the device. Temperature was regulated by varying the current supplied to the Peltier under a constant voltage. Figure 3.6 B shows an example of the device temperatures recorded with different current settings, showing an equilibration time of ~10 minutes.

3.3.7 Droplet Coalescence

To change the composition of the aqueous phase of a droplet or the hydrogel after bilayer formation, an unincubated droplet can be added to the well and allowed to coalesce with the existing droplet, or it can be allowed to burst into the supporting hydrogel. Since the fresh droplet has not had sufficient time to assemble a stable

monolayer at the oil-water interface, coalescence or bursting usually occurs spontaneously, or can easily be achieved by applying pressure with the electrode. The electrode can also be used to ensure that the fresh droplet does not contact the aqueous phase that is to remain unchanged. If intending to coalesce two droplets, this can be achieved by 'catching' the fresh droplet with the electrode, which it will easily wet, and lowering it onto the existing droplet in a controlled manner. Alternatively, a fresh droplet can be confined close to the wall of the well with the electrode which is already wet by the existing droplet, and allowed to sink onto the existing droplet. Figure 3.7 A shows an existing droplet in the well that has not yet formed a bilayer, and a fresh droplet attached to the electrode. Upon applying a small pressure with the electrode, bilayers form both between the hydrogel and the existing droplet, and between the two droplets (Figure 3.7 B,C). Figure 3.7 D shows the coalesced droplet which is ready for electrical recording. The droplet coalescence was used for experiments investigating the effect on specific capacitance of the phospholipid binding protein Annexin V associating to the membrane.

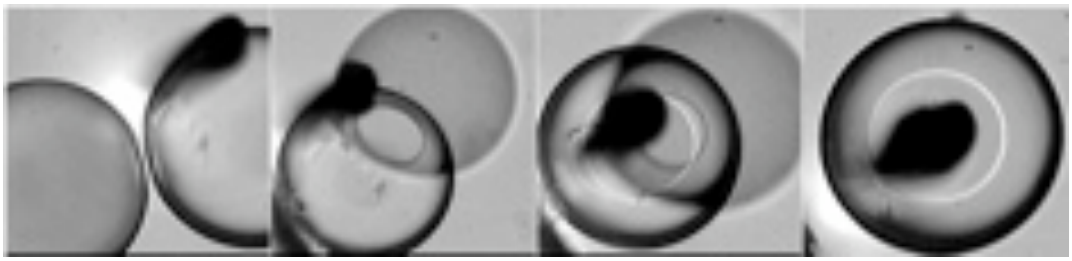

Figure 3.7: Droplet coalescence. An unincubated droplet added to a well already containing a droplet can be used to deliver a sample or change the buffer conditions of the existing droplet or of the substrate. In the images shown, the existing droplet is on the right in the first image, and on the left in the following two images. It forms a bilayer with the substrate in the second frame. By moving the existing droplet into the path of the sinking fresh droplet, the coalescence of the two droplets is ensured, as shown here. Alternatively, the existing droplet can be moved aside to allow fusion of the fresh droplet with the substrate.

3.3.8 Experimental Conditions

Unless otherwise specified, all experiments were performed at room temperature in a device optimised for electrical recording (see section 2.3.3.2) using droplets formed in 5 mg/mL DPhPC in hexadecane and a buffer consisting of 20 mM TRIS-HCl and

0.5 M NaCl adjusted to pH 8.0 both in the droplet and in the supporting hydrogel.

Annexin V Experiments. Experiments with Annexin V were carried out in droplets consisting of 10 % w/w DOPG in DPhPC at a total concentration of 5 mg/mL, dissolved in hexadecane via pentane as described in section 2.3.2.1. To ensure complete dissolution and mixing of both lipids, the required amount of stock solution in pentane was added to a vial and both lipids were dried down together before redissolving in hexadecane. Droplet and substrate buffers consisted of 20 mM TRIS-HCl, 20 mM $CaCl_2$ and 150 mM NaCl at pH 8.0. For experiments in the concentration series, droplets were left to rest for 10 minutes after bilayer formation and electrode piercing before making capacitance measurements. For time series experiments, a droplet containing only buffer was added to the well to form a bilayer, and recording of capacitance was initiated with images at 5 second intervals after delivering the required amount of Annexin V to the droplet using the coalescence method described in section 3.3.7.

Biotin-Streptavidin Experiments. Experments with biotin-labelled lipids and Streptavidin were performed in droplets consisting of 10 % w/w DPPE-Biotin in DPhPC and hexadecane, prepared as above. Buffers in both droplet and substrate consisted of 10 mM HEPES, 150 mM NaCl, adjusted to 7.4 with NaOH. Streptavidin was dissolved in buffer to a stock concentration of 100 μM and used at final concentrations in the droplet of 0.2 nM, 2 nM and 20 nM.

pH Experiments. All buffers in pH experiments contained 150 mM KCl and were adjusted to final pH value with HCl or KOH. Low pH experiments were carried out in buffer containing 10 mM succinic acid adjusted to pH 4. Mid-range buffers were 10 mM HEPES, adjusted to pH 6.75 and 10 mM HEPES, adjusted to pH 7.5. High pH buffer consisted of 10 mM TRIS-HCl adjusted to pH 8.0 and 8.5.

Cholesterol Experiments. Cholesterol experiments were prepared by mixing the requisite amount of lipid and cholesterol stocks in chloroform and drying and redis-

solving in hexadecane as described in section 2.3.2.2. For asymmetric experiments, the well was prepared by the 'pentaning' method (section 2.3.5).

Temperature Experiments. Simple, binary and ternary lipid-oil systems for temperature experiments were prepared as for the cholesterol experiments above. Asymmetric bilayers were either achieved by 'pentaning' (section 2.3.5), or in some cases where bilayer formation was difficult to achieve, by bursting droplets containing vesicles of the desired lipid concentration into the supporting hydrogel to form the first monolayer. Vesicles were prepared by sonication of 0.2 mg/mL total lipid concentration in buffer for two minutes.

3.4 Results

DIBs formed from DPhPC in hexadecane are characterised by a high resistance of several gigaohms and do not leak current at applied potentials $< |100|$ mV. Consequently, the Ohmic deviation (I_R) from the ideal square-wave output is minimal. Figure 3.8 shows the capacitance current trace in response to an applied triangular potential recorded during the formation of a DIB by a droplet of DPhPC in hexadecane. The characteristics of the simple, binary and ternary systems shown in Figure 3.3 A-C that contain DPhPC are similar, as are bilayers made from droplets containing POPE and POPG, such as those shown in Figure 3.10 B. Lipid systems containing DOPC (for examples see Figure 3.3 B,C) tend to have a lower resistance, but I_R remains small compared to I_C and thus capacitance measurement by the method shown in Figure 3.1 was easily achievable. In contrast, bilayers in pure DOPC systems and DPhPC in squalene (Figure 3.3 D) had Ohmic currents $I_R \gg I_C$, and therefore determination of capacitance in these systems was not feasible.

3.4.1 Time-Invariance of Specific Capacitance

Figure 3.9 shows a number of sequential single point measurements of specific capacitance for DIBs from DPhPC in hexadecane, tetradecane and decane as well as an

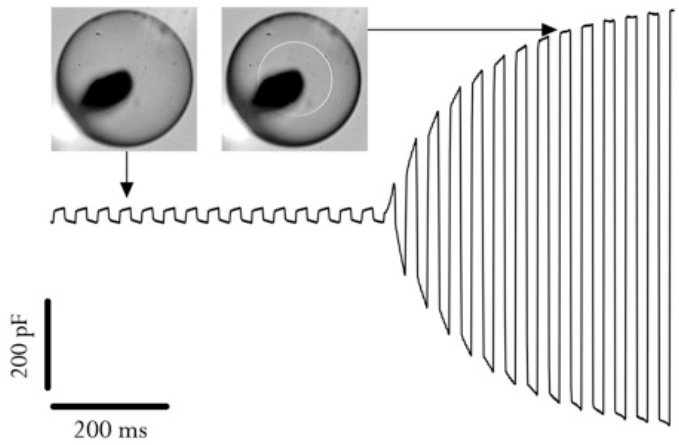

Figure 3.8: Total capacitance, C_T, measured during bilayer formation by the application of a triangular potential. Prior to bilayer formation, the background capacitance, C_0, is in the range of 8-12 pF, as can be seen in the left half of the trace shown.

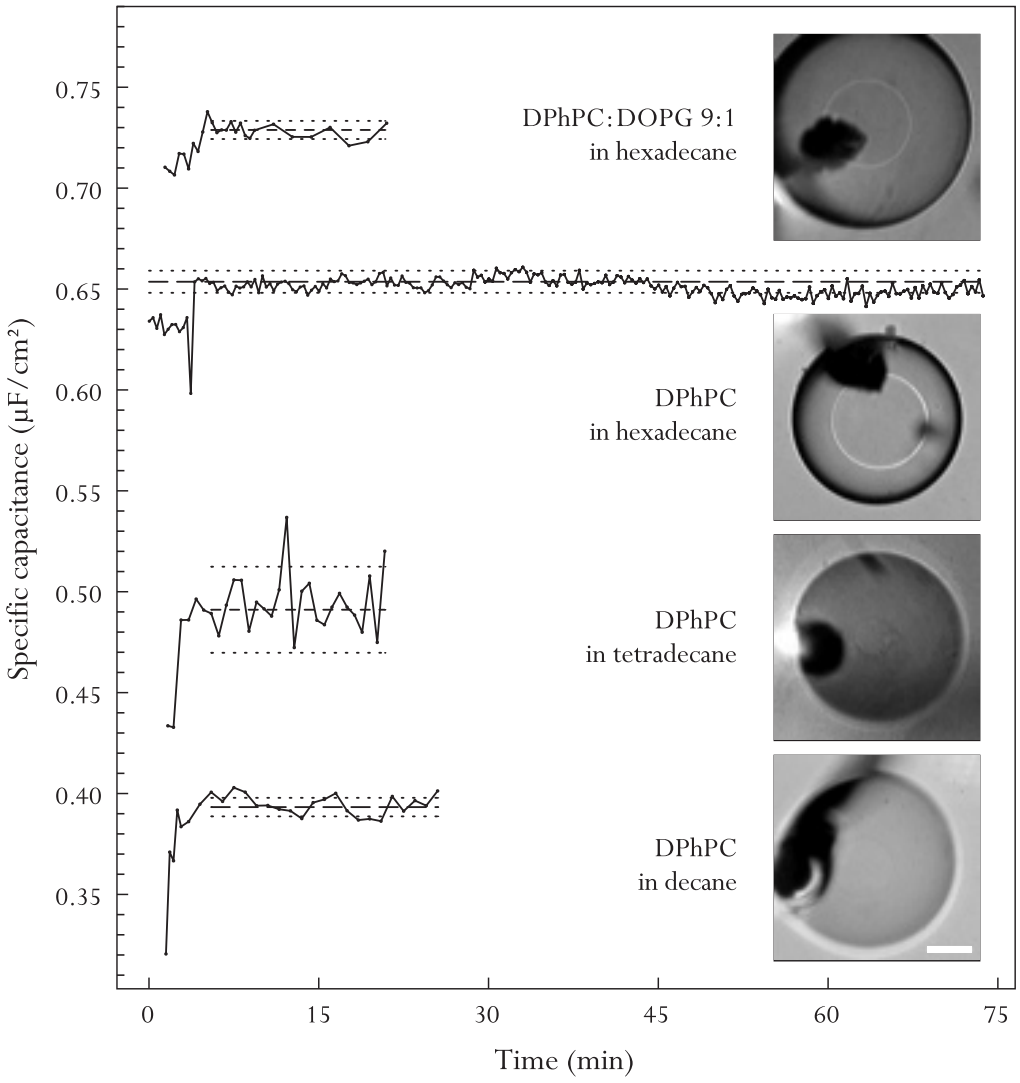

Figure 3.9: Stability of specific capacitance over time. We find that specific capacitance remains constant (0.653 ± 0.005 μF cm^{-2} for the dataset shown). Measurement commences after bilayer formation and subsequent insertion of the electrode into the droplet (within $<$ 1 minute). Both decane (C_m = 0.393 ± 0.005 μF cm^{-2}) and tetradecane (C_m = 0.491 ± 0.021 μF cm^{-2}) bilayers are difficult to distinguish under conventional white light illumination. The larger error in the tetradecane data is a result of bilayers that were not perfectly elliptical. The behaviour of binary lipid systems is similar, as shown for the case of DPhPC:DOPG 9:1 (C_m = 0.729 ± 0.004 μF cm^{-2}) Scale bar: 100 μm.

example of a binary system in the form of DPhPC:DOPG 9:1 in hexadecane. In all cases, bilayer capacitance remains stable after an initial period of about five minutes from bilayer formation. This equilibration period can be shortened by briefly applying a potential, as shown in the case of DPhPC in hexadecane, where a transient +50 mV bias was applied four minutes after bilayer formation, resulting in a step change to the final stable specific capacitance.

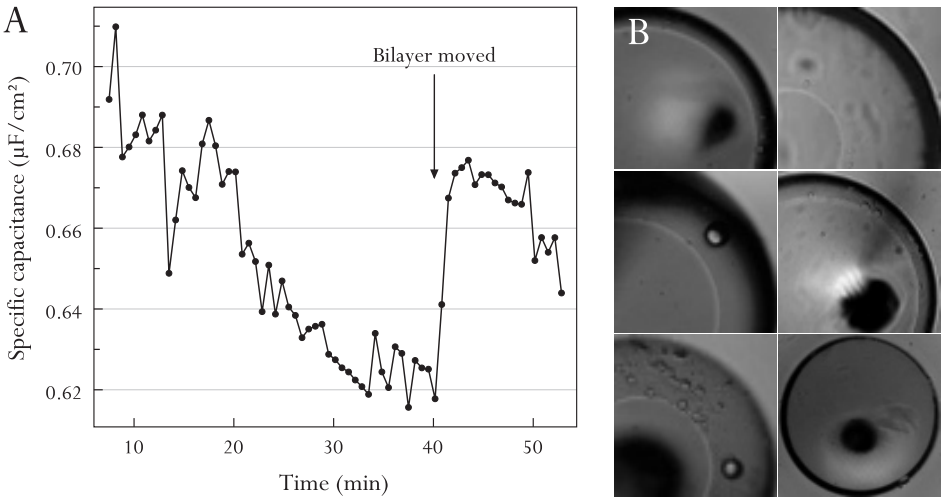

Figure 3.10: Variability of POPE:POPG bilayers **(A)** Specific capacitance of a POPE:POPG 3:1 droplet in hexadecane over time. **(B)** A range of morphologies observed in droplets of POPE:POPG 3:1 in hexadecane.

A notable exception to the constant specific capacitance observed in the systems above are DIBs formed in a mixture of POPE and POPG. Figure 3.10 A shows specific capacitance over time for a droplet of POPE and POPG at a ratio of 3:1 (w:w), a lipid system commonly used to emulate the properties of the inner membrane of gram-negative bacteria. Specific capacitance decreases steadily until the bilayer is disturbed, which partially resets the specific capacitance before it decreases again. The reason for this decrease is not clear. Since both POPE and POPG contain unsaturated lipid chains, it is possible that saturation over time results in the straightening and thus thickening of the bilayer. However, the fact that the effect is partially reset by moving the bilayer with the inserted electrode speaks against this conjecture. It is possible that increased order between the charged POPG and uncharged POPE over time results in bilayers that are less fluid and thus have lower capacitance. Contrary

to other lipid-oil systems investigated here that result in relatively reproducible bilayer morphologies (Figure 3.3), the morphology of bilayers made from POPE and POPG varies considerably from droplet to droplet (Figure 3.10 B), and also, to a more limited extent, over time. These results are consistent with those reported by Sylvan Baca in a short project report, where he found that he was unable to discern a trend in the specific capacitance of POPE:POPG DIBs with increasing POPG content. Values ranged from 0.65 μF cm^{-2} for pure POPE to 0.60 μF cm^{-2} for POPE:POPG 3:1 and 0.66 μF cm^{-2} for POPE:POPG 3:2 (Baca, 2006).

3.4.2 Bilayer Specific Capacitance Measured by Dynamically Varying Area

Figure 3.11 shows a representative capacitance measurement sequence acquired from a single DIB of DPhPC in hexadecane at a range of bilayer areas. The size of the bilayer was altered by varying the vertical height of the droplet relative to the hydrogel surface using the inserted electrode. The contact angle of the bilayer responds to the additional force applied by the electrode, until a new equilibrium is achieved. The bilayer area was adjusted in discrete steps (Figure 3.11 A): changes in area are achieved in a matter of a few seconds, and after each adjustment the bilayer is left to settle for 60 seconds before making A_M and C_T measurements. A plot of C_T as a function of A_M for all the points in both sections of the sequence shows a linear relationship (Figure 3.11 B), which can be fit with

$$C_T = C_m A_M + C_0 \tag{3.15}$$

where C_0 is the background capacitance arising from residual capacitance in the acquisition electronics and device components. C_0 is small (~10 pF) compared to C_T and varies by less than ± 5 pF between experiments.

The linear relationship of equation 3.15 is representative of all the C_T vs. A_M measurements acquired in this work, regardless of type of lipid or oil. The linear fits to C_T vs. A_M data have R^2 values of > 0.999 in all systems where a low viscosity – and therefore perfectly circular – bilayer minimises the error in the area

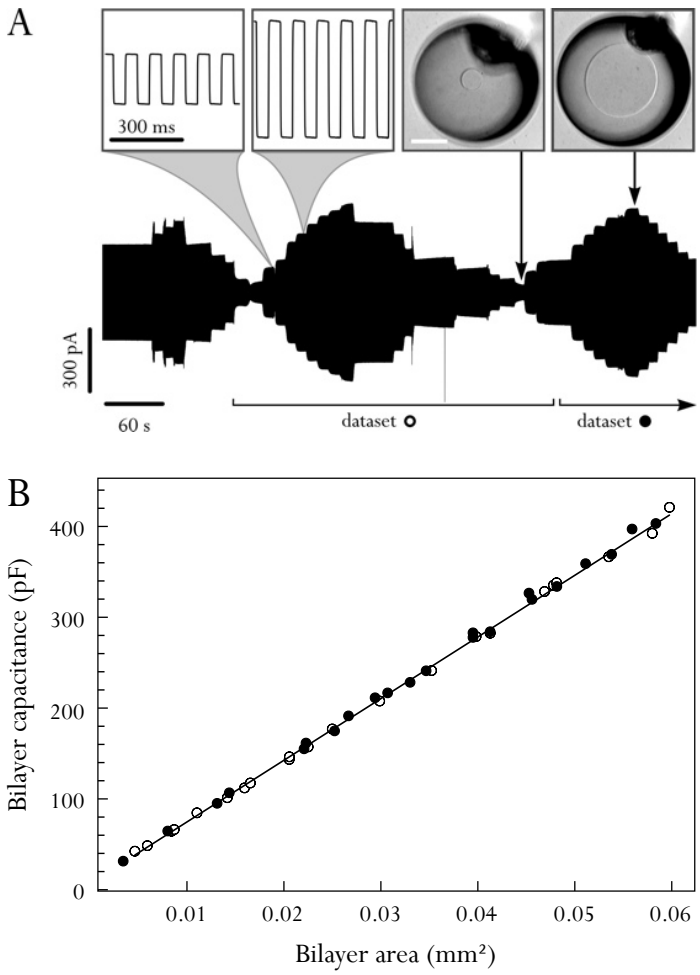

Figure 3.11: Measurements of specific bilayer capacitance with a single DIB. **(A)** A plot of two sets of individual point measurements of bilayer area as a single DIB (DPhPC/ hexadecane, 10 mM TRIS-HCl pH 8.0, 0.3 M KCl) is varied in successive steps using the inserted electrode, while simultaneously measuring bilayer capacitance. The sequence shows the bilayer being progressively enlarged and reduced. Scale bar: 200 μm. **(B)** Capacitance as a function of bilayer area for the step sequence shown in A. The combined C_{m} gradient is $0.662 \pm 0.004\ \mu\mathrm{F\,cm^{-2}}$ ($R^2 = 0.9998$). The plot shows that both datasets can be fit to a straight line, indicating that there is no hysteresis between successive increases and decreases in bilayer size.

measurement (c.f. Figure 3.3). Upon raising the droplet electrode far enough to disconnect the droplet from the supporting hydrogel, and then allowing the bilayer to reform, specific capacitance remains unchanged. The single DPhPC/hexadecane experiment shown in Figure 3.11 has a relative standard error of 0.5 % in the C_m which is determined to be 0.662 ± 0.004 μF cm^{-2} from the gradient obtained by fitting to the point measurements. This value agrees with that reported for DIBs elsewhere (0.65 μF cm^{-2} (Holden et al., 2007)), but it is difficult to find values for this particular system in the BLM literature. Benz et al. (1975) have measured a specific capacitance of 0.66 μF cm^{-2} for a 16-carbon monounsaturated monoglyceride in hexadecane, which would be expected to have higher capacitance than DPhPC due to the greater flexibility of the alkyl chains. Jeon et al. (2008) report a specific capacitance of 0.62 μF cm^{-2} for DPhPC in 80:20 hexadecane:decane, a system that would be expected to have lower capacitance due to the preferential partitioning of the shorter-chain hydrocarbon decane into the bilayer. Examples of data from bilayers formed in a number of different lipid-oil systems are shown in Figure 3.12.

3.4.3 The Effect of Protein Binding to the Bilayer

3.4.3.1 Streptavidin

In the first instance, the effect of protein in proximity to the bilayer on specific capacitance was investigated in a system of droplets containing Streptavidin. The DIBs were formed from biotinylated lipid (10 % DPPE-biotin) doped into DPhPC in hexadecane. As already noted in section 3.2.3, the polar layer of the head groups and the electric double-layer are thought to contribute minimally to the specific capacitance of lipid bilayers, and therefore the binding of Streptavidin to a flexible biotin linker on a lipid head group, where the surface of the bilayer remains accessible to water, would not be expected to have a measureable effect on specific capacitance. Streptavidin was added to droplets at a series of final concentrations ranging from 0.2 nM – 20 nM. The latter represents enough protein to allow complete coverage of the internal surface of the droplet. Figure 3.13 shows bilayer capacitance vs. area fits for a droplet in the presence and absence of 20 nM Streptavidin, and a further control of Strepta-

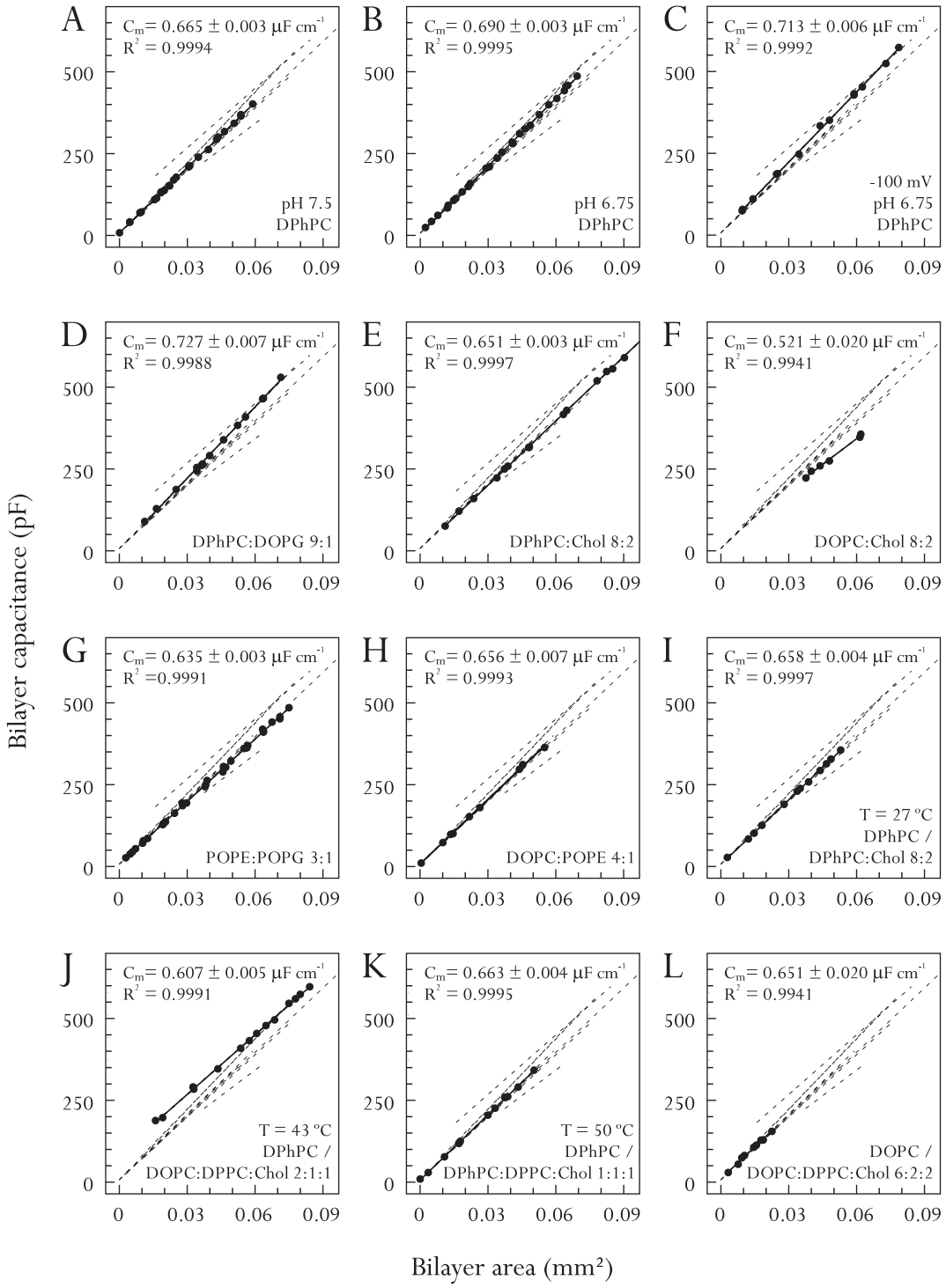

Figure 3.12: Examples of bilayer capacitance vs. bilayer area measurements and quality of linear fits in a number of different systems and conditions. Unless otherwise indicated, measurements were made in hexadecane at pH 8.0, 24 °C. The dotted lines represent the data from all panels. Stated errors are the standard error of the linear fit. **(A-C)** Pure DPhPC bilayers. **(D-H)** Various lipid compositions in symmetric bilayers. **(I-L)** Various asymmetric bilayers. The lipid composition in the bottom line in each panel refers to the composition in the droplet leaflet, the second line from the bottom to the lipid in the leaflet in contact with the supported hydrogel. **(F,J)** A positive offset in the linear fit indicates the presence of a region of constant size in the bilayer with a higher specific capacitance and is therefore a sign of phase separation in the bilayer.

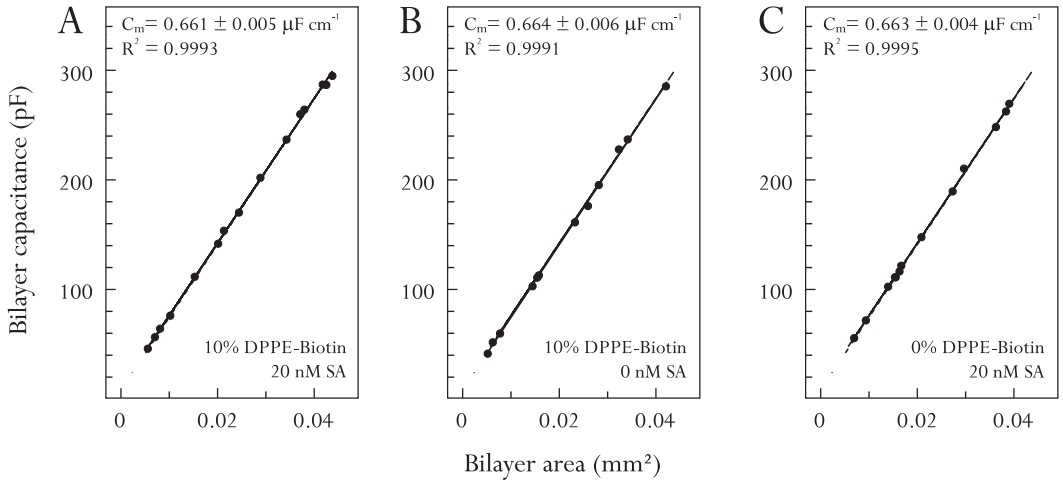

Figure 3.13: Specific capacitance is not affected by Streptavidin binding to DPPE-biotin. **(A)** The largest concentration of Streptavidin used (20 nM) is shown. The specific capacitance in the presence of 0.2, 2 and 20 nM was unchanged from that of pure DPhPC in hexadecane (c.f Figure 3.12 A). **(B)** Control of a droplet containing 10 % DPPE-biotin but no Streptavidin. **(C)** Control of 20 nM Streptavidin in a droplet of pure DPhPC in hexadecane.

vidin added to a droplet that did not contain any DPPE-biotin. As expected, and as was also the case at lower Streptavidin concentration, no significant change in specific capacitance is observed (c.f. also the data in pure DPhPC/hexadecane systems shown in Figures 3.11 and 3.12 A). The possibility that DPPE-biotin partitions out of the droplet monolayer and into the oil phase before bilayer formation, and that therefore there are no attachment sites for Streptavidin at the bilayer, has to be considered, but it is unlikely that this is the case. With its larger hydrophilic head group, DPPE-biotin is likely to encounter a barrier to leaving the oil-water interface that is at least equal to that of DPhPC and it could therefore be naively expected to be encountered in the bilayer at a fraction similar to that present in the bulk solution. Further experiments with fluorescently labelled Streptavidin could confirm this.

3.4.3.2 Annexin V

Annexin V is a member of a eukaryotic membrane-associating protein family (Gerke and Moss, 2002) that interacts with charged phospholipid head groups in the presence of calcium ions (Figure 3.15 B, Swairjo et al. (1995)). The structure of Annexin V has been extensively studied and crystal structures of both its monomeric and trimeric form, as illustrated in Figure 3.15, are available (Burger et al., 1994; Oling et al., 2000;

Sopkova et al., 1993). Although well described *in vitro*, the physiological importance of the calcium-dependent binding is not well understood. A role in cartilage and bone calcification and cell proliferation has been proposed for Annexin V, on the basis of observations that the protein interacts with collagen and can show voltage-dependent calcium channel activity that also depends on the interaction with collagen (Gerke and Moss, 2002).

Annexin V forms two-dimensional crystals on planar lipid bilayers containing acidic phospholipids, as shown in Figure 3.15 C-E (Gerke et al., 2005; Gerke and Moss, 2002; Oling et al., 2001; Reviakine and Brisson, 2000). Supported by indications from electron paramagnetic resonance (EPR) studies (Megli et al., 1998), this crystalline arrangement has long been thought to affect membrane properties such as rigidity and fluidity, and therefore to be capable of stabilising and regulating membrane domains.

Figure 3.14 shows a sequence of images of a DIB formed by a droplet containing 10 % (w/w) of the negatively charged lipid DOPG, 20 mM $CaCl_2$ and 6 μM Annexin V. As is evident from the deformation of the droplet when moving the electrode, the

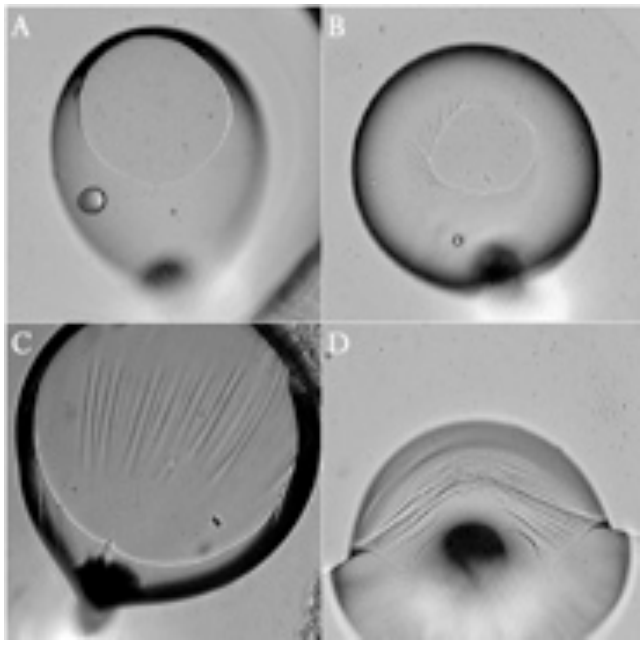

Figure 3.14: Bilayer rigidity in the presence of the phospholipid binding protein Annexin V. The droplets consist of DPhPC:DOPG 9:1 in hexadecane and contain 20 mM $CaCl_2$ and 6 μM Annexin V. **(A-C)** Bilayers 'frozen' by Annexin V. **(D)** A droplet that was disconnected from the bilayer and suspended in the oil phase. The image shows the moment of the tearing of the rigid protein-lipid film encasing the droplet. The aqueous content of the droplet subsequently fused with the supporting hydrogel. For details see main text.

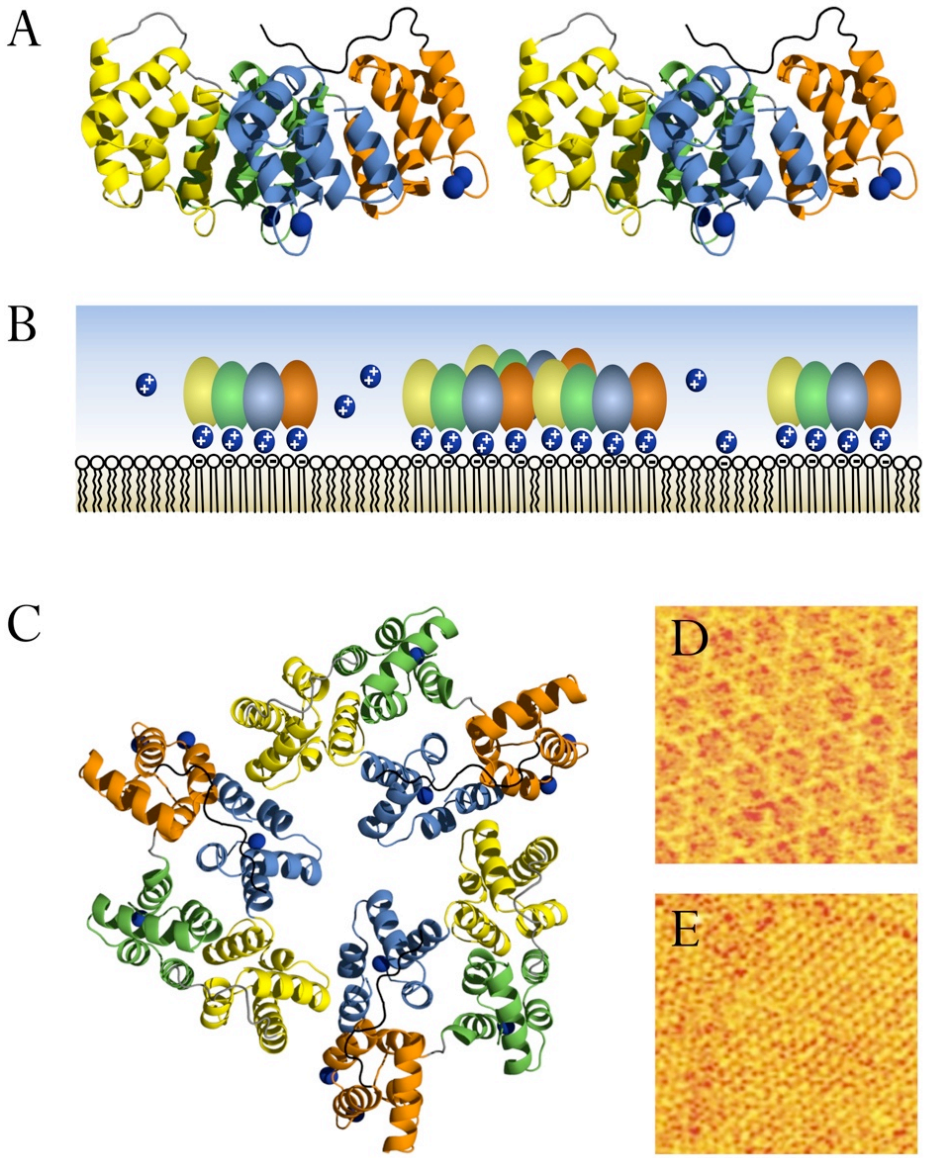

Figure 3.15: Annexin V forms 2D crystals on phospholipid membranes. **(A)** Stereo of the Annexin V monomer (PDB:1HVD). There are four homologous domains that bind to negatively charged phoshoplipid head groups via Ca^{2+} ions (blue spheres). **(B)** Schematic illustration of Annexin V monomers binding to a phospholipid bilayer and assembling into extended 2D structures. **(C)** Trimeric structure of crystalline Annexin. (see also PDB:1ANX) **(D,E)** On artificial supported lipid bilayers, Annexin V trimers as shown in C have been shown to assemble into contiguous 2D crystals of p6 (D) or p3 (E) morphology. *AFM images in* D *and* E *courtesy of Dr Ilya Reviakine.*[†]

[†]Present address: CIC biomaGUNE, University of the Basque Country, Paseo Miramón 182, 20009 San Sebastián, Gipuzkoa, Spain.

protein effectively 'freezes' the bilayer, preventing both the dissociation of the bilayer leaflets at the bilayer edge and the sliding of the bilayer leaflets relative to each other. The folds that are visible outside the edge of the bilayer in Figure 3.14 indicate that Annexin not only rigidifies the bilayer, but also the adjacent monolayer, which in the absence of Annexin would be sufficiently fluid to eliminate any strain caused by the twist imparted on the droplet by the electrode. This is also indicated by the image in Figure 3.14 D: in this instance, it was possible to disconnect the droplet from the substrate despite the rigidity of the bilayer by carefully raising the electrode to pull the droplet upwards. Under standard conditions, a droplet suspended in the oil phase never 'bursts', as the monolayer adjusts to the shape of the droplet that is dictated by the surface tension of the interface. In this instance, however, the tearing of the film at the interface was observed a few seconds after complete disconnection of the droplet from the substrate. Due to the apparent lack of elasticity of the protein-lipid film encasing the droplet, it appears that the force of gravity alone was sufficient to allow the aqueous phase 'pour' out from the droplet. No new monolayer can form on the exposed pure oil-water interface in time before the droplet contents fuse with the underlying substrate.

Figure 3.16 A shows the effect of Annexin V on the specific capacitance of a DPhPC:DOPG 9:1 bilayer in hexadecane. Annexin was added to the droplet buffer, and the droplet was left for 10 minutes to equilibrate before measuring capacitance by fitting a straight line to several measurements at different areas for each concentration. The specific capacitance is inversely proportional to Annexin V concentration. This effect indicates that the increased bilayer stiffness imparted by Annexin V, shown in Figure 3.14, goes hand in hand with an increase in bilayer thickness. While the exact mechanism of Annexin binding is not understood, it is reasonable to expect the rigidity to be an effect of increased order in the lipid acyl chains that is favoured by the limitation of the movement of the head groups by the binding of the protein. As in the lipid phase transitions described in Chapter 1, such increased order is generally accompanied by a change in thickness that could account for the differences in specific capacitance observed here. As a further control, fresh droplets containing Annexin V were added to a device that had been incubated with 6 μM Annexin V overnight. The

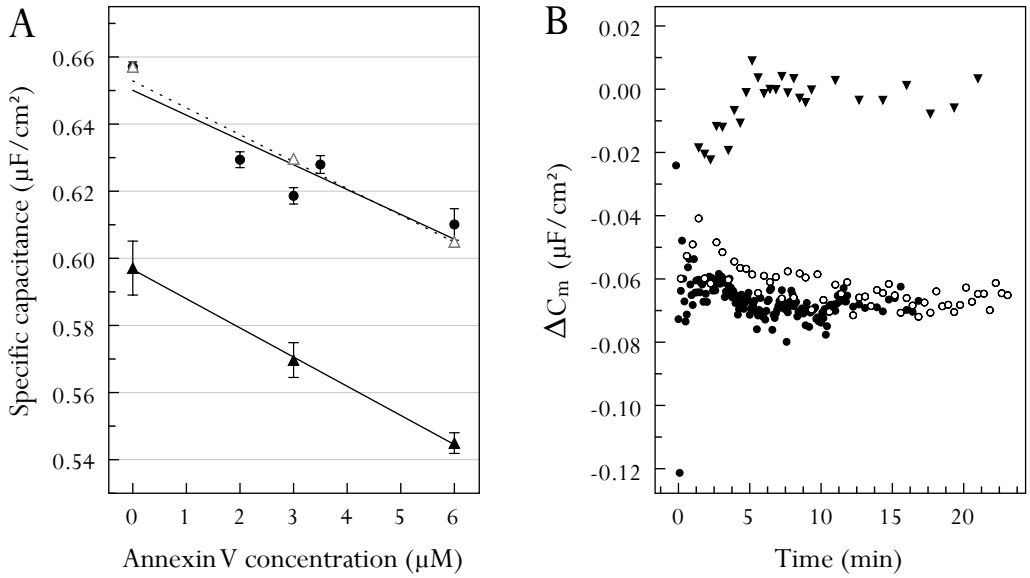

Figure 3.16: The effect of Annexin V on specific capacitance **(A)** Data from droplets made from DPhPC:DOPG 9:1 in the presence of 20 mM $CaCl_2$ in the buffer. Error bars show standard error of the straight line fit to capacitance vs. area data. Concentration of Annexin was varied in the droplet. Concentration in the supporting hydrogel was either 0 μM (closed circles) or the devices were incubated with 6 μM Annexin V overnight (closed triangles). The open triangles represent the latter normalised by the value at 0 μM Annexin. **(B)** The binding of Annexin V to the membrane shown by single point measurements of specific capacitance over time. In the absence of Annexin V (black triangles), specific capacitance equilibrates to a steady value after bilayer formation at t = 0. In a second data series, Annexin V was delivered to the droplet by coalescence at t = 0 (black circles). The third series shows the effect of moving the bilayer at $t = 0$ (open circles).

additive effect on specific capacitance of Annexin V binding to both leaflets can be seen in Figure 3.16 A. Figure 3.16 B shows that the majority of the change in specific capacitance upon delivery of Annexin V to the droplet happens within the first thirty seconds. It therefore occurs on a timescale that is too fast to be measured when using the method of bursting droplets together, since the rate of change of the bilayer area at this stage introduces errors arising from the currently implemented manual method of aligning the time points of images taken of the bilayer with capacitance measurements. The data series shown as open circles in Figure 3.16 B shows that the effect of Annexin V is partially reversed when the bilayer is disturbed by moving the electrode inserted into the droplet, before settling back to a steady value.

3.4.4 The Effect of Cholesterol on C_m

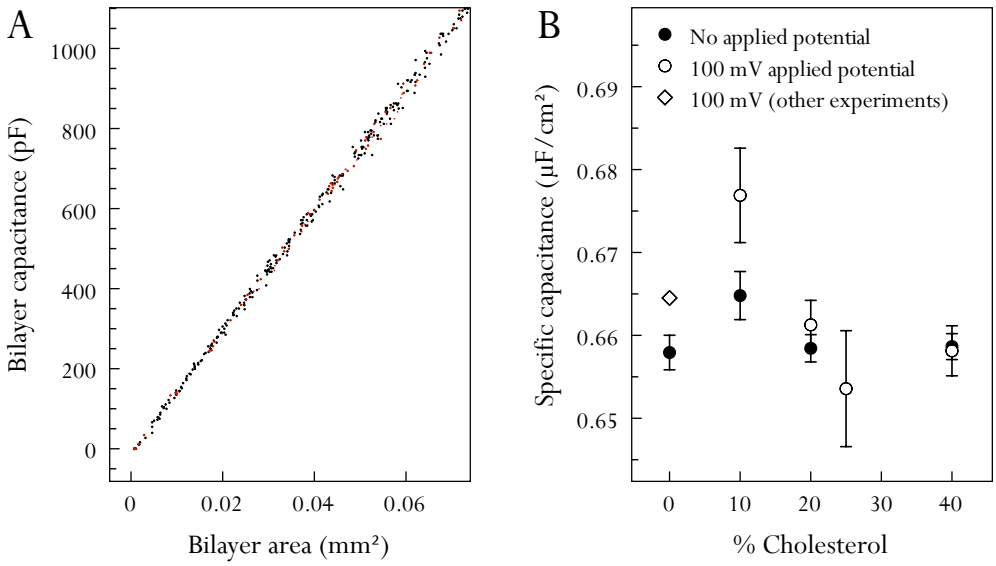

Figure 3.17: The specific capacitance of DPhPC:cholesterol bilayers. **(A)** Combined data from 13 droplets of DPhPC in hexadecane, containing between 0 and 40 % (w/w) of cholesterol. Red points were measured under the application of a 100 mV potential. The spread in the data shows that cholesterol affects the specific capacitance of the bilayer. **(B)** It is difficult to see a clear trend in the dependence. It appears that the effect of cholesterol is greatest at a low proportion (10 %, black circles) which would indicate that the bilayer is most fluid at this level. This is supported by the fact that the pattern is amplified by the application of a potential, which would be expected to have a greater compressive effect on a more fluid bilayer (for details see main text).

Motivated by the known effect of membrane cholesterol on membrane fluidity noted in Chapter 1, the specific capacitance of DIBs doped with 0 – 40 % (w/w) choles-

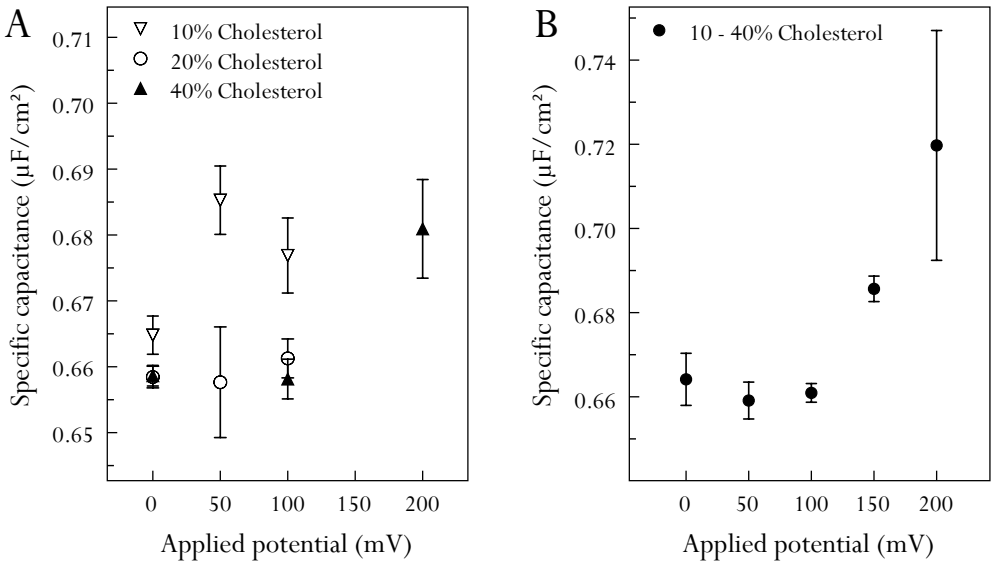

Figure 3.18: The effect of applied potential on the specific capacitance of DPhPC/cholesterol bilayers. **(A)** Data from linear fits to measurements of bilayer capacitance and area in individual droplets. Error bars represent the standard error of the fit. All linear fits had an R^2 value of >0.999. The C_m of DPhPC bilayers with a low proportion of cholesterol responds more strongly to an applied potential. **(B)** Data points represent linear fits to all capacitance and area measurements made in bilayers containing between 10% and 40% cholesterol, showing that there is a significant effect of an applied potential on specific capacitance in cholesterol containing bilayers.

terol was investigated. Figure 3.17 A contains data from all droplets, and shows that there is a spread in the specific capacitance data, indicating that cholesterol does indeed have an effect on C_m. However, upon examination of individual droplet specific capacitance – as obtained from linear fits – there is no discernible trend in bilayers in the absence of an applied potential, aside from a small increase in C_m for DIBs with low cholesterol content (DPhPC:cholesterol 9:1 w/w, Figure 3.17 B, closed circles). It is difficult to explain this pattern, which may be considered to be insignificant. However, it is possible that a small proportion of cholesterol increases bilayer fluidity, while a larger amount rigidifies the membrane, where again, a more rigid membrane would be expected to display a lower capacitance. Interestingly, the trend is amplified when a potential is applied. In Chapter 4, it will be shown that an applied potential increases specific capacitance, presumably by thinning the bilayer as a result of compressive forces arising from the electric field. Such compression would be expected to have a greater effect on a bilayer that is more fluid, as fluid bilayers are characterised by acyl chains that possess a degree of freedom to fold and kink. The amplification of

the trend observed here would therefore support the above conjecture of a maximal effect of cholesterol at a low proportional content. Figure 3.18 A shows further evidence that the C_m of DPhPC bilayers with a low cholesterol content (DPhPC:cholesterol 9:1) is most affected by the application of a potential, again suggesting that the acyl chains in this mixture have the greatest degree of freedom to bend and kink in response to compressive forces on the bilayer, corresponding to the greatest fluidity. In general, it can be shown that the specific capacitance of DIBs consisting of DPhPC and containing cholesterol increases significantly upon the application of a potential Figure 3.18 B.

3.4.5 The Effect of Temperature on C_m

In an effort to measure the specific capacitance of a lipid bilayer undergoing a phase transition, an attempt was made to form DIBs from from ternary systems containing DPPC, which undergoes a transition at at 41 ℃. The aim was to heat the system past a possible miscibility transition temperature (T_{misc}). Following ternary phase diagrams shown by Veatch and Keller (2003), where a miscibility transition from one continuous phase to two coexisting phases occurs in DOPC:DPPC:Cholesterol systems between 29 ℃ and 34 ℃, the formation of DIBs containing ratios of 1:1:1, 2:1:1 and 2:2:1 of these lipids was attempted. In the majority of cases, it was difficult to form droplets that were stable for sufficient time to perform specific capacitance measurements. In addition to that, bilayers possessed very low resistance, which impeded specific capacitance measurements. However, it was possible to obtain some limited data from asymmetric systems, where ternary droplets were added to wells containing pure DOPC or DPhPC. By using the pentaning method (section 2.3.5) to deposit the substrate leaflet lipid, the lipid contained in the oil phase of the well can be minimised, and therefore the ternary system in the droplet would not be expected to be perturbed significantly. Figure 3.19 shows bilayer capacitance vs. area data from an asymmetric droplet with DOPC:DPPC:Chol 2:1:1 in the droplet bilayer leaflet and pure DPhPC in the substrate bilayer leaflet. At 41 ℃ it was possible to obtain capacitance measurements at a series of areas, yielding a specific capacitance of 0.54 ± 0.02 $\mu F\,cm^{-2}$. The large offset of this line (129 pF) is a feature that would

be expected if the bilayer contained a region of higher specific capacitance that did not change in size as the bilayer area was increased (see also Figure 3.12 J for another instance of this observation). This observed feature could therefore be indicative of a miscibility transition at a temperature lower than 41 °C. According to Veatch and Keller (2003), the T_{misc} of DOPC:DPPC:Chol 2:1:1 lies at 30 °C. It is tempting to linearly fit the points taken at lower temperature, but this fit results in a value of ~ 2.77 μF cm^{-2} with a negative offset. This extremely high value, viewed in combination with the fact that the bilayer area appeard to be characterised by regions of differing viscosity during the manipulation, would lead to the conclusion that perhaps distinct areas of different specific capacitance were also present at temperatures below 30 °C, whose relative size changed during the manipulation. It is also possible that the asymmetry of the system here could be the reason for this observation. However, a separate droplet consisting of the same system had a specific capacitance of 0.64 ± 0.01 μF cm^{-2} at 24 °C, which is probably more representative of the C_{m} of this system at room temperature. The capacitance measurements at low temperature in Figure 3.19 are likely to contain a significant error, as the bilayer at this temperature showed extremely low resistance, with $I_{\mathrm{R}} \gg I_{\mathrm{C}}$, as shown by the triangular current response to the triangular applied potential illustrated in Figure 3.19 C.

In systems where no transition would be expected, an increase in temperature leads to a slow decrease of specific capacitance. The data shown in Figure 3.20, measured in a droplet of DPhPC:Cholesterol 8:2 in hexadecane, are a representative example of this decrease. The variation of temperature is also generally accompanied by spontaneous changes in bilayer area. Figure 3.20 A shows this area change during a sequence in which the droplet was heated from 27 °C to 53 °C. The bilayer area in this instance reduced rapidly at first, becoming small enough for line tension to dominate and therefore the droplet disconnected from the substrate. When the bilayer had been reformed by lowering the electrode and care was taken to ensure a large bilayer area, no further bilayer area change took place. Before cooling the droplet, the bilayer was adjusted a second time to ensure that enlargement upon cooling was possible, which did indeed take place (blue points in Figure 3.20 A). In Figure 3.20 B, the specific capacitance appears to reduce steadily by ~3.5 % over the entire tem-

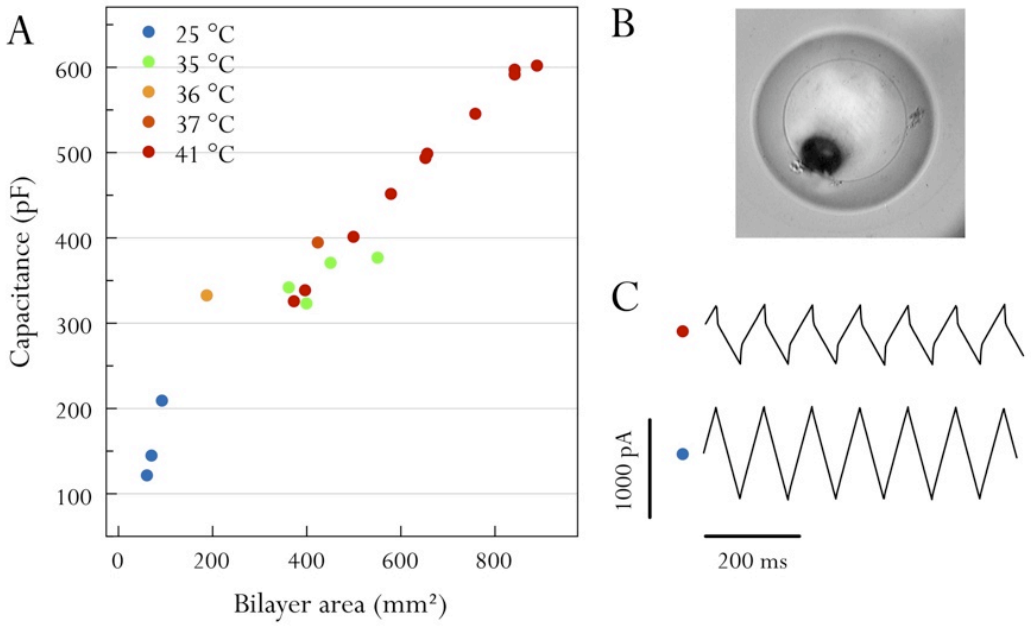

Figure 3.19: Effect of temperature on a ternary lipid system of DOPC:DPPC:cholesterol 2:1:1. The data shown are from an asymmetric bilayer containing pure DPhPC in the lower leaflet, as it did not prove feasible to form stable bilayers in symmetric ternary systems. **(A)** Bilayer capacitance vs. bilayer area data obtained while the droplet was heated from 25 °C to 41 °C. The gradient of a linear fit to points at 41 °C is 0.54 ± 0.02 μF cm^{-2}. The intercept of this fit at 129 pF indicates that there may be a region with a constant area of higher specific capacitance present in the bilayer, suggesting that a miscibility transition has taken place at this temperature. **(B)** An asymmetric DIB of DOPC:DPPC:cholesterol 2:1:1, lower leaflet: DPhPC. **(C)** At low temperature, the bilayer had very low resistance, and $I_R \gg I_C$. Measurements of specific capacitance at low temperature (blue dots) are therefore likely to contain significant errors.

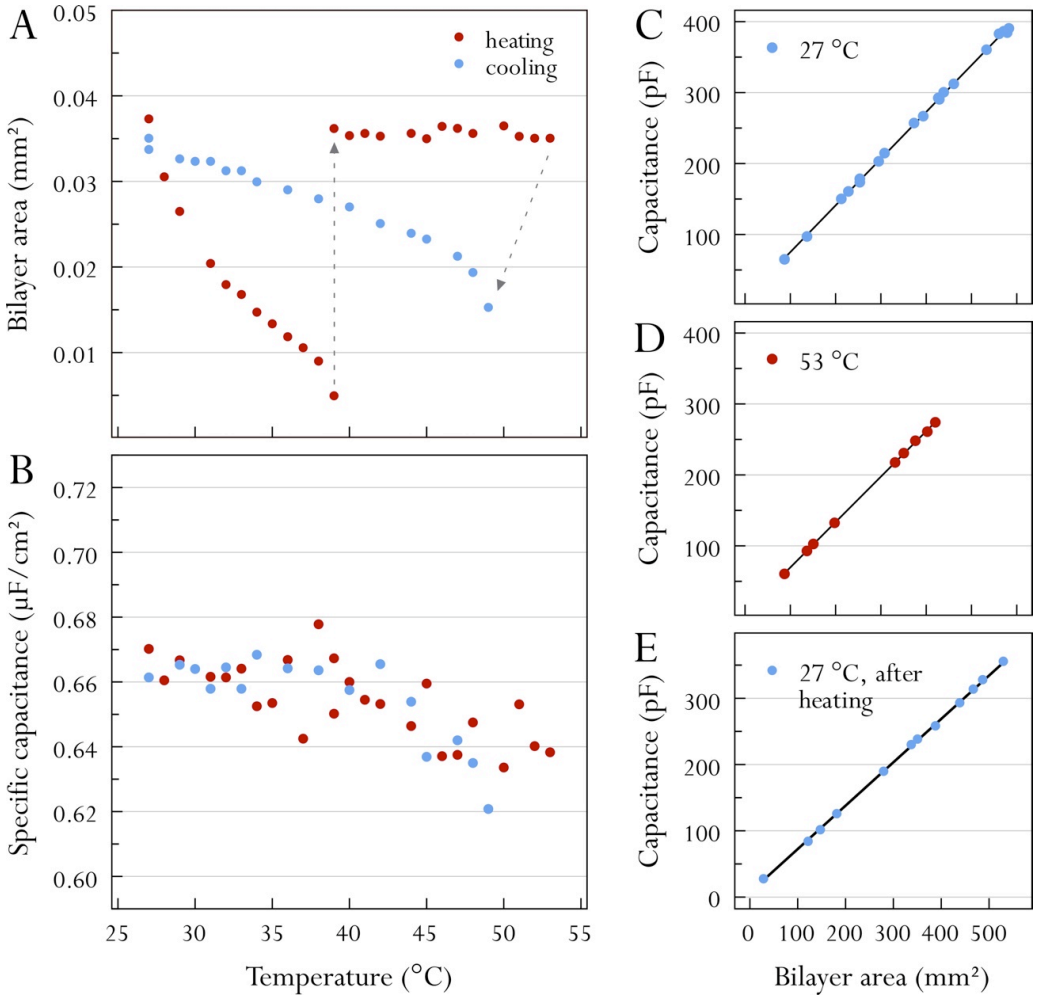

Figure 3.20: The effect of temperature on a DIB consisting of DPhPC:cholesterol 8:2 **(A)** The bilayer area reduces spontaneously upon heating, resulting in disconnection of the droplet from the substrate at 39 °C. The bilayer was reformed by lowering the electrode (first grey arrow). After carrying out the size change series in D, the bilayer area was set to a medium size before cooling (second grey arrow) **(B)** Single point measurements of $C_m = (C_T - C_0)/A_M$, calculated using the average intercept of the fits in C-E, $C_0 = 7.04 \pm 1.97$ pF. **(C)** Size change series at 27 °C, before heating. $C_m = 0.659 \pm 0.004\ \mu F\,cm^{-2}$. **(D)** Size change series at 53 °C, after heating. $C_m = 0.640 \pm 0.003\ \mu F\,cm^{-2}$. **(E)** Size change series at 27 °C, after heating and cooling. $C_m = 0.658 \pm 0.004\ \mu F\,cm^{-2}$.

perature range measured, and return to its original value somewhat quicker upon cooling, by around 38 °C. However, single point measurements of specific capacitance should be interpreted with caution, as the value shown depends on the background capacitance assumed. In this instance, area size change series carried out before and after heating and after cooling to determine the background capacitance from the average of the intercepts of the straight line fits to these series (7.04 ± 1.97 pF). In fact, bilayer specific capacitance reduces by 2.67 % over the entire temperature difference of 26 °C, as determined by the linear fits shown in Figure 3.20 C-E. In pure DOPC bilayers, a linear decrease of specific capacitance from ~0.48 μF cm^{-2} to ~ 0.42 μF cm^{-2} (12.5 %) was observed over the same temperature range by single specific capacitance measurement. However, due to the limited lifetime of the droplets and the irregular appearance of their bilayers (see also Figure 3.3 D), this could not be verified by determining the specific capacitance at the extremes of the temperature range examined by the more accurate method of linear fits to data from size change series.

3.4.6 The Effect of pH on C_m

The effect of pH on a simple system of DPhPC in hexadecane was investigated by forming droplets in a range of buffer systems. The zwitterionic phosphatidylcholines are fully ionised over almost the full range of pH. The pKa of the phosphate group lies at around pH = 1, at which point the molecule carries a net positive charge (Marsh, 1990).

As a result, no sharp transitions in specific capacitance arising from molecular rearrangements that would affect the geometric bilayer capacitance would be expected in the range of pH examined here. However, the data in Figure 3.21 show that there is a greater spread in specific capacitance measurements taken at the edge of the ideal buffering range of the particular buffer used. This is apparent, for example, in the case of the points taken at pH 6.75 in HEPES buffer, which has an ideal buffering range of pH 6.8 – 8.25. This alone demonstrates that the pH of the aqueous phase has an effect on specific capacitance. It appears that there is a maximum of specific capacitance at a pH of around 6. This is unexpected, as it is the exact opposite

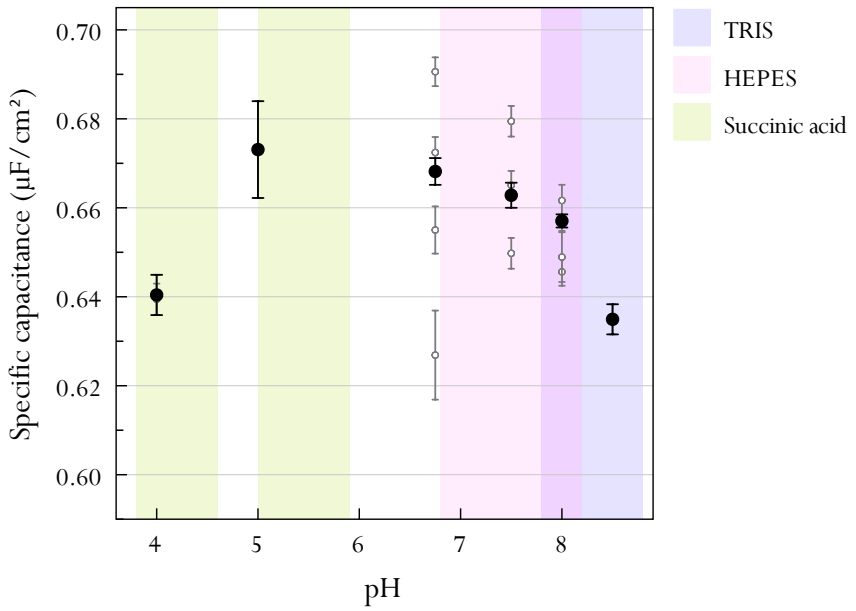

Figure 3.21: The effect of pH on specific capacitance. Measurements at pH 4-5 were made in succinic acid buffer, those at pH 6.75 – 7.5 and two droplets at pH 8.0 in HEPES buffer, and those at 8.0 and 8.5 in TRIS-HCl buffer. The grey points denote regression fits to data obtained from separate droplets, black points show data from a single regression fit to all points at that pH. Error bars represent the standard error of the fit. The exception is the data at pH 8.0, where the grey points denote points acquired on separate days from several droplets.

profile of that reported by Ohki (1969), who measured the specific capacitance of eggPC bilayers in n-decane and found a curve with a minimum at ~pH 5. It is unclear what might be the reason for this discrepancy, since the DPhPC and eggPC differ only in the form of their acyl chains. Interestingly, and more in line with the data presented here, Sylvan Baca also reported a lower specific capacitance at pH 4 than at pH 7 in DIBs formed from POPE in work carried out in this laboratory (Baca, 2006). Phosphatidylethanolamine groups have a similar ionisation profile to that of PC described above, with the exception that the amine groups become deprotonated at high pH (pKa = 11.25), leaving the molecule with a net negative charge.

Even considering the fact that the surface pH can differ substantially from that of the bulk solution (Tsui et al., 1986), it is unlikely that the changes in specific capacitance observed here arise from the deionisation of the zwitterionic lipid and concommitant molecular rearrangements that would affect the geometric capacitance. Furthermore, as detailed in section 3.2.3, the contribution of the double layer capac-

itance, C_{dl}, should be too small to account for the changes observed here. A third possibility is that changes in surface potential, occurring as a result of changes in pH, significantly affect the net potential difference experienced by the bilayer (see section 2.2.1). As already suggested by the results obtained in connection with the cholesterol experiments described above, the potential across the membrane does appear to affect specific capacitance, presumably by means of electrostrictive forces that impact on the thickness and thus the geometric capacitance (Blatt, 1982). However, the fractional change of capacitance of biological membranes with applied potential is not well established (see also Chapter 4), and so at this point it is not clear whether they are of a magnitude that could account for the changes observed here.

Despite the uncertainties surrounding the origin of the observed changes, these experiments highlight the importance of working in a well-buffered system when using artificial bilayers to study membrane proteins. If the effect on bilayer thickness in the conjecture above is correct, they suggest that pH-dependent changes in membrane protein activity could also have a root in geometric changes in the bilayer.

3.5 Discussion

3.5.1 Precision of Dynamic Area Measurements

Provided that the background capacitance is known, the precision of a single measurement of specific capacitance made within an individual droplet, and hence any C_m measurement made using just a single point, can be assessed by examining the residuals from the linear fit to capacitance vs. area plots. The residuals from the linear fits are normally distributed and show no correlation with bilayer size. For the example shown in Figure 3.12 A, the standard deviation of the residuals from the fit is ± 2.65 pF or ± 398 μm^2. Taking the mean bilayer capacitance of ~194 pF or mean bilayer area of ~27895 μm^2 in this experiment, these standard deviations represent measurement errors of ± 1.4 % for any single A_M vs. C_T point. Separately, from repeated measurements on a single stable DIB, the measurement precision was determined to be <0.5 % for both A_M and C_T. The slightly larger single point error of ~1.4 % observed in the A_M vs. C_T fits can be attributed primarily to deviations from the assumed perfect ellipticity, and secondly to stochastic noise in the current recording that can introduce a small number of erroneous points in the algorithmic determination of total capacitance (3.3.3). These sources of error could be addressed by improved area fitting methods and data filtering respectively.

The precision of each single point measurement compares favourably with the best previously reported errors of ± 0.5 − 3 % which were obtained by careful imaging of single BLMs (White, 1970a; White and Thompson, 1973). Using a straight line fit to several such single point measurements taken at different areas of a single DIB (Figure 3.11 B, 0.4 % relative standard error) enables the determination of specific capacitance with greater precision than was previously possible.

3.5.2 Equilibration of Droplet Interface Bilayers

The single point measurements for area vs. capacitance fits such as those shown in Figure 3.12 were taken both during reduction and enlargement of bilayer area (see also Figure 3.11 A), indicating that there is no significant hysteresis. This is the case

regardless of which oil or lipid used and suggests that there is no difference between newly formed bilayer regions (arising from monolayers at the water-lipid-oil interface that zip together and exclude oil) and existing regions. Removing and reforming a new bilayer also appears to have no effect on C_{m}, suggesting that the bilayers are essentially identical each time they form.

Contrary to previous observations in BLMs, where specific capacitance tends to increase slowly over time (White, 1970a; White and Thompson, 1973), no substantial changes in C_{m} are observed in DIBs over time in the majority of lipid systems (Figure 3.9). These results are somewhat unexpected as it is known that BLMs contain excess oil in the bilayer after initial formation, and it can take time for the amount of oil within the bilayer to reach equilibrium with the oil in the bulk phase. For example, for short chain oils such as decane, which are energetically more favoured in the bilayer, equilibration can take a few hours in a BLM, over which time C_{m} increases by >10 % (White, 1970a). A possible explanation for this discrepancy is that in DIBs the system reaches equilibrium quickly due to the mechanical force applied on the droplet when inserting the electrode.

3.5.3 Variablity Observed Between Droplets

Contrary to the reproducibility observed in a single droplet, where disconnection and reconnection to the substrate does not affect the specific capacitance, far more significant variation is observed between different droplets, especially when examined on different days and in different devices. A good example is the data taken from three droplets at pH 7.5 in Figure 3.21. These were carried out on different days under identical conditions of 5 mg/mL DPhPC in hexadecane, 150 mM KCl in 10 mM HEPES buffer. The standard error of individual linear fits to data from each of the three droplets is 0.0034 ± 0.0001 μF cm^{-2} (S.D.). However, the standard deviation of the specific capacitance determined from the gradient of these three separate fits is 0.015 μF cm^{-2}, around an average value of 0.6648 μF cm^{-2}. By comparison, a linear regression fit to all single point measurements from the three droplets yields a value of 0.6628 ± 0.0028 μF cm^{-2}, which is that plotted in black in Figure 3.21. The reasons for this inter-droplet variability are unclear, but there are several possible causes. As

already discussed in Chapter 2, the hydration of the lipid batch used appears to have significant effects on droplet characteristics. While the lipid batch was not changed in the example above, it is possible that laboratory humidity and temperature over a period of a few days are able to modify lipid hydration, which may result in different bilayer characteristics. It is, however, not clear how lipid hydration might impact on specific capacitance. Another possible cause of variability is the substrate agarose, which is unlikely to have identical properties between devices. Small variations in initial agarose concentration or age of the device that allow the agarose to dehydrate may have an effect on the properties of the bilayer resting on it. Finally, it is likely that the pH of the system contributes to the variability observed. Even where buffer pH is carefully controlled, it is possible that pH changes can occur upon addition of agarose to form the substrate and of other reagents to the final droplet volume if the correct buffering range is not observed.

3.5.4 Background Capacitance

The comments on the precision of single point specific capacitance measurements made above assume that the intercept of the fit, C_0, is known. If assumed to be constant, the background capacitance can be used to determine specific capacitance from single point measurements over a range of conditions, as was described in the capacitance time-course and temperature experiments (see sections 3.4.1 and 3.4.5). However, in practice, the intercept of linear fits to capacitance vs. area data varies. Even for fits to data taken in very similar conditions, such as, for example, the three panels in Figure 3.12 A-C, the intercept of the fit ranges from 4.7 pF to 9.3 pF. Furthermore, this variation is not only observed between different droplets, but also over time in a single experiment, as was already pointed out in section 3.4.5 (see also Figure 3.20). The contributors to the intercept are not known definitively. It is clear that the capacitive current measured before bilayer formation, shown in Figure 3.8, must be a result of residual background capacitance in the device components. However, as the linear fit in, for example, Figure 3.12 J clearly shows, a large offset can also arise from non-uniformity within the bilayer during area changes, as also discussed in the context of Figure 3.19.

The sensitivity of single point specific capacitance measurements to the error in the assumed capacitance offset (C_0) depends on bilayer size, and therefore varies from point to point. The effect of this differing sensitivity can clearly be seen in Figure 3.22, which shows data from the temperature experiment from Figure 3.20, where the bilayer area spontaneously reduced over time. In this instance, the interpretation of the effect of temperature would change depending on the assumed value of the background capacitance. It is therefore important that single point measurements of

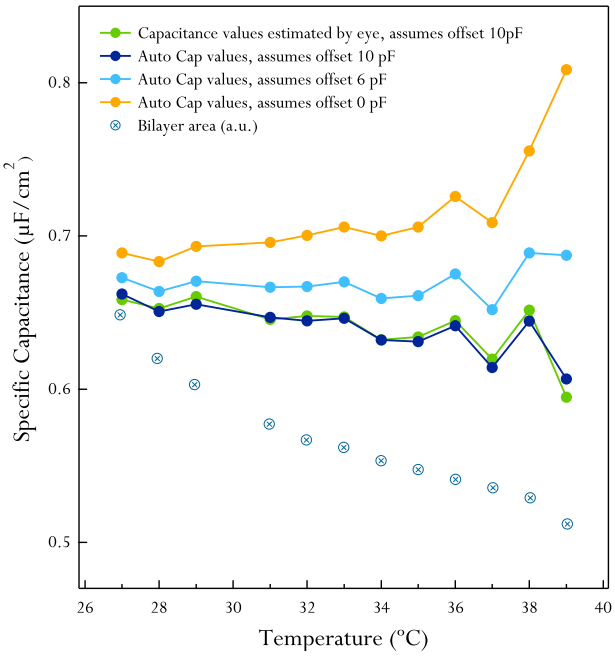

Figure 3.22: Data from the temperature experiment shown in Figure 3.20, which assumes a background capacitance, C_0, of 7 pF in the calculation of specific capacitance. The sensitivity of the data to the C_0 used in the calculation of specific capacitance ($C_m = (C_T - C_0)/A_M$) depends on bilayer area. In this example, the choice of C_0 significantly affects the interpretation of the effect of temperature on specific capacitance. This shows that single point capacitance measurements should only be used where linear fits to capacitance vs. area data – made at regular intervals – can verify C_0. Alternatively, changes in bilayer size have to be minimised.

specific capacitance only be used where this offset can be determined accurately by linear fits of capacitance vs. area plots, and where can be shown not to vary over the course of the experiment. Alternatively, the bilayer area has to be either very large or be maintained at a constant size.

3.6 Summary

Droplet Interface Bilayers in the on-hydrogel configuration are better suited to optical bilayer area measurements than conventional, aperture-suspended BLMs. This, in combination with the ability to control bilayer area, results in a system uniquely suited to the precise measurement of bilayer capacitance. This system is able to eliminate the error arising from uncertainty in the background capacitance, which is a problem in the those systems of fixed bilayer area which are limited to single point measurements of specific capacitance.

Significant steps towards the automation of capacitance measurement have been taken here, but the ultimate aim must be to enable the real time and continuous measurement of specific capacitance. This would require an algorithm that can determine bilayer area directly from the raw image input of the bilayer, in the absence of any user input, as well as the automatic synchronisation of current and image information. The latter would be easily achievable with an implementation in an integrated data acquisition software such as Labview for example. The former is a greater challenge, and may require a better imaging system, illumination from below to eliminate the shadow of the electrode, or the investigation of methods to increase the contrast of the bilayer, such as phase contrast or difference interference contrast microscopy.

A clear limitation of the DIB system is apparent in the investigation of mixed lipid systems. At present, it is not possible to control the relative proportion of each lipid component that partitions into either the bilayer, the curved monolayer surrounding the droplet, the planar monolayer on the substrate, or into the bulk oil phase. The stated lipid compositions thus remain unverified. Before meaningful capacitance data of these systems can be obtained in DIBs, further work, using perhaps fluorescently labelled lipids or lipid-phase sensitive dyes, is necessary to understand how the bulk lipid composition relates to that in the bilayer.

Given the findings of droplet to droplet variability discussed above, it would be desirable to construct a system whereby conditions could be changed within a single droplet, for example by perfusion of the droplet to enable the exchange of the buffer. At present, it is possible to inject a sample into a droplet with a nano-injector, or to

use the coalescence technique described above, but these methods result in significant perturbation of the bilayer and the introduction of electrical noise. The resulting errors in specific capacitance measurements mean that the system is not yet optimised for the investigation of kinetic processes, as is clear from the data presented in relation to the binding of Annexin to the bilayer.

The final point to consider, both in DIBs and in other artificial systems, is that it is important to understand the solvent content bilayers formed with the aid of alkane oils. This feature distinguishes many artificial bilayers from their biological counterparts, and caution is required in considering any findings of the effect of diverse parameters on specific capacitance to be of relevance for biological membranes.

In view of the limitations detailed here, the next chapter focusses on the investigation of the effect of an applied potential on the specific capacitance of DIBs. In this case, a simple lipid system can be used, and the parameter under observation can be changed within a single droplet without the need to perturb the bilayer, thereby eliminating inter-droplet variation as well as the errors referred to above. The effect of an applied potential is of great interest in many respects, as compressive forces applied by the electric field can give information on the compressibility of the lipid bilayer, which in turn must be a function of solvent content and composition, as already indicated by the results from the experiments on cholesterol-containing bilayers.

Bibliography

Al-sharadqah, A. (2009). Error analysis for circle fitting algorithms. *Electronic Journal of Statistics 3*, 886–911.

Alvarez, O. and R. Latorre (1978). Voltage-dependent capacitance in lipid bilayers made from monolayers. *Biophys. J. 21*(1), 117.

Andrews, D. M., E. D. Manev, and D. A. Haydon (1970). Composition and energy relationships for some thin lipid films, and the chain conformation in monolayers at liquid-liquid interfaces. *Special Discussions of the Faraday Society 1*, 46–56.

Babakov, A. V., L. N. Ermishkin, and E. A. Liberman (1966). Influence of electric field on the capacity of phospholipid membranes. *Nature 210*(5039), 953–955.

Baca, S. (2006). *Capacitance Measurements of Artificial Planar Bilayers Formed on a Hydrated Semi-solid Support*. Short project report, University of Oxford.

Benz, R., O. Fröhlich, P. Läuger, and M. Montal (1975). Electrical capacity of black lipid films and of lipid bilayers made from monolayers. *Biochimica et Biophysica Acta (BBA) - Biomembranes 394*(3), 323–334.

Blatt, F. J. (1982). Elastic energy stored in a membrane due to electrostriction. *Journal of Biological Physics 10*(4), 219–222.

Burger, A., D. Voges, P. Demange, C. R. Perez, R. Huber, and R. Berendes (1994). Structural and electrophysiological analysis of Annexin V mutants: Mutagenesis of human Annexin V, an *in vitro* voltage-gated calcium channel, provides information about the structural features of the ion pathway, the voltage sensor and the ion selectivity filter. *Journal of Molecular Biology 237*(4), 479–499.

Chernov, N. and C. Lesort (2005). Least squares fitting of circles. *Journal of Mathematical Imaging and Vision 23*(3), 239–252.

Cole, K. S. (1968). *Membranes, ions and impulses: a chapter of classical biophysics*. University of California Press.

Everitt, C. T. and D. A. Haydon (1968). Electrical capacitance of a lipid membrane separating two aqueous phases. *Journal of Theoretical Biology 18*(3), 371–379.

Fettiplace, R., D. M. Andrews, and D. A. Haydon (1971). The thickness, composition and structure of some lipid bilayers and natural membranes. *Journal of Membrane Biology 5*(3), 277–296.

Fujiwara, H., M. Fujihara, and T. Ishiwata (2003). Dynamics of the spontaneous formation of a planar phospholipid bilayer: A new approach by simultaneous electrical and optical measurements. *The Journal of Chemical Physics 119*(13), 6768–6775.

Gentet, L. J., G. J. Stuart, and J. D. Clements (2000). Direct measurement of specific membrane capacitance in neurons. *Biophysical Journal 79*(1), 314–320.

Gerke, V., C. E. Creutz, and S. E. Moss (2005). Annexins: Linking Ca^{2+} signalling to membrane dynamics. *Nature Reviews Molecular Cell Biology 6*(6), 449–461.

Gerke, V. and S. E. Moss (2002). Annexins: From structure to function. *Physiological Reviews 82*(2), 331–371.

Gross, L. C. M., A. J. Heron, S. C. Baca, and M. I. Wallace (2011a). Determining membrane capacitance by dynamic control of Droplet Interface Bilayer area. *Langmuir 27*(23), 14335–

14342.

Hanai, T., D. A. Haydon, and J. Taylor (1964). An investigation by electrical methods of Lecithin-in-Hydrocarbon films in aqueous solutions. *Proceedings of the Royal Society of London. Series A. Mathematical and Physical Sciences 281*(1386), 377–391.

Hanai, T., D. A. Haydon, and J. Taylor (1965a). Polar group orientation and the electrical properties of lecithin bimolecular leaflets. *Journal of Theoretical Biology 9*(2), 278–296.

Hanai, T., D. A. Haydon, and J. Taylor (1965b). The variation of capacitance and conductance of bimolecular lipid membranes with area. *Journal of Theoretical Biology 9*(3), 433–443.

Heron, A. J., J. R. Thompson, B. Cronin, H. Bayley, and M. I. Wallace (2009). Simultaneous measurement of ionic current and fluorescence from single protein pores. *Journal of the American Chemical Society 131*(5), 1652–1653.

Heron, A. J., J. R. Thompson, A. E. Mason, and M. I. Wallace (2007). Direct detection of membrane channels from gels using water-in-oil droplet bilayers. *Journal of the American Chemical Society 129*(51), 16042–16047.

Hianik, T. and V. I. Passechnik (1995). *Bilayer lipid membranes*. Springer.

Holden, M. A., D. Needham, and H. Bayley (2007). Functional bionetworks from nanoliter water droplets. *Journal of the American Chemical Society 129*(27), 8650–8655.

Jeon, T., J. L. Poulos, and J. J. Schmidt (2008). Long-term storable and shippable lipid bilayer membrane platform. *Lab on a Chip 8*(10), 1742–1744.

Kado, R. T. (1993). Membrane area and electrical capacitance. *Methods in Enzymology 221*, 273–299.

Läuger, P., W. Lesslauer, E. Marti, and J. Richter (1967). Electrical properties of bimolecular phospholipid membranes. *Biochimica et Biophysica Acta (BBA) - Biomembranes 135*(1), 20–32.

Lindau, M. and E. Neher (1988). Patch-clamp techniques for time-resolved capacitance measurements in single cells. *Pflügers Archiv European Journal of Physiology 411*(2), 137–146.

Lollike, K., N. Borregaard, and M. Lindau (1995). The exocytotic fusion pore of small granules has a conductance similar to an ion channel. *J. Cell Biol. 129*(1), 99–104.

Lollike, K., N. Borregaard, and M. Lindau (1998). Capacitance flickers and pseudoflickers of small granules, measured in the Cell-Attached configuration. *Biophysical Journal 75*(1), 53–59.

Lollike, K. and M. Lindau (1999). Membrane capacitance techniques to monitor granule exocytosis in neutrophils. *Journal of Immunological Methods 232*(1-2), 111–120.

Marsh, D. (1990). *CRC handbook of lipid bilayers*. CRC Press.

Megli, F. M., M. Selvaggi, S. Liemann, E. Quagliariello, and R. Huber (1998). The calcium-dependent binding of Annexin V to phospholipid vesicles influences the bilayer inner fluidity gradient. *Biochemistry 37*(29), 10540–10546.

Miller, C. (1986). *Ion Channel Reconstitution*. Plenum Press: New York.

Montal, M. and P. Mueller (1972). Formation of bimolecular membranes from lipid monolayers and a study of their electrical properties. *Proceedings of the National Academy of Sciences of the United States of America 69*(12), 3561–3566.

Mueller, P., D. O. Rudin, H. Ti Tien, and W. C. Wescott (1962). Reconstitution of cell mem-

brane structure *in vitro* and its transformation into an excitable system. *Nature 194*(4832), 979–980.

Naumowicz, M. (2005). Impedance analysis of lipid domains in phosphatidylcholine bilayer membranes containing ergosterol. *Biophysical Journal 89*(5), 3174–3182.

Neher, E. and A. Marty (1982). Discrete changes of cell membrane capacitance observed under conditions of enhanced secretion in bovine adrenal chromaffin cells. *Proceedings of the National Academy of Sciences of the United States of America 79*(21), 6712–6716.

Ohki, S. (1969). The electrical capacitance of phospholipid membranes. *Biophysical Journal 9*(10), 1195–1205.

Oling, F., W. Bergsma-Schutter, and A. Brisson (2001). Trimers, dimers of trimers, and trimers of trimers are common building blocks of Annexin A5 two-dimensional crystals. *Journal of Structural Biology 133*(1), 55–63.

Oling, F., J. S.-d. O. Santos, N. Govorukhina, C. Mazères-Dubut, W. Bergsma-Schutter, G. Oostergetel, W. Keegstra, O. Lambert, A. Lewit-Bentley, and A. Brisson (2000). Structure of membrane-bound Annexin A5 trimers: A hybrid cryo-EM - X-ray crystallography study. *Journal of Molecular Biology 304*(4), 561–573.

Petelska, A. D. and Z. A. Figaszewski (2000). Effect of pH on the interfacial tension of lipid bilayer membrane. *Biophysical Journal 78*(2), 812–817.

Picard, G., N. Denicourt, and J. H. Fendler (1991). Simultaneous electrical and optical interferometric measurements of pressure- and applied-potential-induced bilayer lipid membrane deformation. *The Journal of Physical Chemistry 95*(9), 3705–3715.

Rasband, W. S. (1997). ImageJ. http://rsb.info.nih.gov/ij/.

Requena, J., D. A. Haydon, and S. B. Hladky (1975). Letter: Lenses and the compression of black lipid membranes by an electric field. *Biophysical Journal 15*(1), 77–81.

Reviakine, I. and A. Brisson (2000). Formation of supported phospholipid bilayers from unilamellar vesicles investigated by atomic force microscopy. *Langmuir 16*(4), 1806–1815.

Rosenboom, H. and M. Lindau (1994). Exo-endocytosis and closing of the fission pore during endocytosis in single pituitary nerve terminals internally perfused with high calcium concentrations. *Proceedings of the National Academy of Sciences of the United States of America 91*(12), 5267–5271.

Sakmann, B. and E. Neher (1995). *Single-Channel Recording*. Plenum Press, New York.

Sarles, S. A. and D. J. Leo (2009). Tailored Current—Voltage relationships of Droplet-Interface bilayers using biomolecules and external feedback control. *Journal of Intelligent Material Systems and Structures 20*(10), 1233 –1247.

Sarles, S. A. and D. J. Leo (2010). Regulated attachment method for reconstituting lipid bilayers of prescribed size within flexible substrates. *Analytical Chemistry 82*(3), 959–966.

Schmitt, B. M. and H. Koepsell (2002). An improved method for Real-Time monitoring of membrane capacitance in xenopus laevis oocytes. *Biophysical Journal 82*(3), 1345–1357.

Solsona, C., B. Innocenti, and J. M. Fernández (1998). Regulation of exocytotic fusion by cell inflation. *Biophysical Journal 74*(2), 1061–1073.

Sopkova, J., M. Renouard, and A. Lewit-Bentley (1993). The crystal structure of a new high-calcium form of Annexin V. *Journal of Molecular Biology 234*(3), 816–825.

Swairjo, M. A., N. O. Concha, M. A. Kaetzel, J. R. Dedman, and B. A. Seaton (1995). Ca^{2+}-bridging mechanism and phospholipid head group recognition in the membrane-binding protein Annexin V. *Nature Structural Biology 2*(11), 968–974.

Thompson, J. R., A. J. Heron, Y. Santoso, and M. I. Wallace (2007). Enhanced stability and fluidity in droplet on hydrogel bilayers for measuring membrane protein diffusion. *Nano Letters 7*(12), 3875–3878.

Tsui, F. C., D. M. Ojcius, and W. L. Hubbell (1986). The intrinsic pKa values for phosphatidylserine and phosphatidylethanolamine in phosphatidylcholine host bilayers. *Biophysical Journal 49*(2), 459–468.

Vacklin, H., B. J. Khoo, K. H. Madan, J. M. Seddon, and R. H. Templer (2000). The bending elasticity of 1-Monoolein upon relief of packing stress. *Langmuir 16*(10), 4741–4748.

Valincius, G., F. Heinrich, R. Budvytyte, D. J. Vanderah, D. J. McGillivray, Y. Sokolov, J. E. Hall, and M. Lösche (2008). Soluble amyloid [beta]-Oligomers affect dielectric membrane properties by bilayer insertion and domain formation: Implications for cell toxicity. *Biophysical Journal 95*(10), 4845–4861.

Veatch, S. L. and S. L. Keller (2003). Separation of liquid phases in giant vesicles of ternary mixtures of phospholipids and cholesterol. *Biophysical Journal 85*(5), 3074–3083.

von Gersdorff, H. and G. Matthews (1999). Electrophysiology of synaptic vesicle cycling. *Annual Review of Physiology 61*(1), 725–752.

White, S. H. (1970a). A study of lipid bilayer membrane stability using precise measurements of specific capacitance. *Biophys. J. 10*(12), 1127–1148.

White, S. H. (1970b). Thickness changes in lipid bilayer membranes. *Biochimica et Biophysica Acta (BBA) - Biomembranes 196*(2), 354–357.

White, S. H. (1973). The surface charge and double layers of thin lipid films formed from neutral lipids. *Biochimica et Biophysica Acta (BBA) - Biomembranes 323*(3), 343–350.

White, S. H. (1975). Phase transitions in planar bilayer membranes. *Biophys. J. 15*(2_Pt_1), 95117.

White, S. H. (1977). Studies of the physical chemistry of planar bilayer membranes using high-precision measurements of specific capacitance. *Annals of the New York Academy of Sciences 303*, 243–265.

White, S. H. (1978). Formation of "solvent-free" black lipid bilayer membranes from glyceryl monooleate dispersed in squalene. *Biophysical Journal 23*(3), 337–347.

White, S. H. (1986). The physical nature of planar bilayer membranes. *In:* C. Miller (Ed.), *Ion Channel Reconstitution*, pp. 3–35. Plenum Press, New York.

White, S. H., D. C. Petersen, S. Simon, and M. Yafuso (1976). Formation of planar bilayer membranes from lipid monolayers. a critique. *Biophys. J. 16*(5), 481489.

White, S. H. and T. E. Thompson (1973). Capacitance, area, and thickness variations in thin lipid films. *Biochimica et Biophysica Acta (BBA) - Biomembranes 323*(1), 7–22.

Zimmermann, D., A. Zhou, M. Kiesel, K. Feldbauer, U. Terpitz, W. Haase, T. Schneider-Hohendorf, E. Bamberg, and V. Sukhorukov (2008). Effects on capacitance by overexpression of membrane proteins. *Biochemical and Biophysical Research Communications 369*(4), 1022–1026.

Chapter 4

Dynamic Response of Bilayer Specific Capacitance to an Applied Potential

The purpose of the experiments described in this chapter is to determine the effect of an applied potential on bilayer thickness. To achieve this, the experiments take advantage of the geometry of DIBs, which are unrestricted by an aperture, to measure spontaneous voltage-dependent bilayer area changes. These data are used to deconvolute the two contributors to total membrane capacitance (C'_{T}): bilayer area (A_M) and specific capacitance (C_m).

4.1 Introduction

The total membrane capacitance ($C'_{\mathrm{T}} = C_{\mathrm{T}} - C_0$) measured from BLMs is well known to respond to an applied potential (V_{a}) (Picard et al., 1991; Requena and Haydon, 1975; Requena et al., 1975; White, 1970a, 1972, 1986; White and Chang, 1981; White and Thompson, 1973; Wobschall, 1972). Since C'_{T} is a measure of both bilayer area and thickness, two questions have arisen in the study of this phenomenon in artificial bilayers. Firstly, can the increase in C'_{T} be accounted for by voltage-dependent bilayer area changes, or is there also a change in bilayer thickness upon the application of a

potential? Secondly, what is the mechanism of any bilayer thinning, and is it relevant for physiological bilayers that do not contain any solvent?

4.1.1 Bilayer Thinning or Area Increase?

Observed increases in C'_{T} have been partially attributed to changes in C_{m}, as a result of bilayer thinning under a compressive force generated by the applied potential (Picard et al., 1991; White, 1970a; White and Chang, 1981; Wobschall, 1972), an effect known as electrostriction. However, even for BLMs in a constricting aperture, spontaneous changes in A_{M} in response to an applied potential similar to those described for DIBs in Chapter 2 have been observed (Picard et al., 1991; Punnamaraju and Steckl, 2011; Requena and Haydon, 1975; Requena et al., 1975; White, 1970a; White and Chang, 1981; White and Thompson, 1973; Wobschall, 1972). Since it is difficult to define the boundary of the film using reflected light, precise determination of A_{M} in BLMs is challenging (White and Thompson, 1973; Wobschall, 1972), and since

$$C'_{\mathrm{T}} = C_{\mathrm{m}}\, A_{\mathrm{M}}, \tag{4.1}$$

the relative contribution of bilayer area increase and bilayer thinning to overall changes in C'_{T} is contentious, and the degree of bilayer thinning has often been overestimated (White and Chang, 1981; Wobschall, 1972).

4.1.2 Mechanisms of Bilayer Thinning

In artificial bilayers, changes in specific capacitance are understood to arise from two mechanisms of bilayer thinning. The primary mechanism, observed in bilayers formed with short-chain alkanes such as decane (Requena et al., 1975) is the exclusion of solvent from the bilayer to the surrounding annulus. This exclusion is thought to occur as a result of a change in the relative chemical potential of the alkane in the bilayer and the annulus in the presence of electrostrictive forces generated by an applied electric field (White and Chang, 1981). The second mechanism consists of the thinning of both monolayers, accompanied by a small increase in area per surfactant molecule, i.e. a constant-volume compression of the lipid (Alvarez and Latorre, 1978;

White and Chang, 1981). This mechanism could be relevant in bilayers considered to be relatively solvent-free, such as those formed in longer-chain alkanes such as hexadecane (Andrews et al., 1970) or squalene (White, 1978). An understanding of the first mechanism is relevant to the study of membrane proteins in artificial bilayers, since a method to quantify solvent content could be used to help develop increasingly suitable model membrane systems. If the second mechanism exists at physiologically relevant potentials, it has implications for studies carried out *in vivo* that equate total capacitance to membrane area and therefore assume a constant specific capacitance. Furthermore, with our increasing understanding of the role of lipid-protein interactions in membrane protein function (Phillips et al., 2009), it is conceivable that such potential-induced thickness changes could play a role in processes such as synaptic transmission and signal transduction. To date, however, electrostrictive bilayer thinning has only been reliably measured in bilayers formed with short-chain alkanes such as n-decane (Andrews et al., 1970; White, 1978). The experiments described in this chapter re-examine the effect of an applied potential on bilayers formed in the 16-carbon alkane hexadecane.

4.2 Background and Theory

In early studies, black films were formed across a roughly 1 mm diameter aperture that was punched into the side of a PTFE pot, which formed the aqueous chamber on one side of the film. The pot was inserted into a glass vessel, which formed the other aqueous chamber. The hole was then observed through the glass wall with a low power microscope in reflected light, and the area of the film was assessed by means of a graticule in the microscope eyepiece (Babakov et al., 1966; Hanai et al., 1964; Läuger et al., 1967; Ohki, 1969; Rosen and Sutton, 1968). Often, the film area was only measured at the start of an experiment, and assumed to remain constant Rosen and Sutton (1968), and some researchers measured the area of the PTFE hole before the assembly of the apparatus and deduced the film area with the assumption of an annulus of 5 % (Benz et al., 1975; Carius, 1976). As a result, observed dependence of whole-film capacitance on the square of the potential was either directly attributed to total capacitance changes in response to a potential to bilayer thickness changes (Läuger et al., 1967), or to interactions of the electrolyte with the phospholipid head groups (Ohki, 1969; Rosen and Sutton, 1968).

As early as 1966, the influence of electric fields on the capacitance of phospholipid membranes was called into question. Babakov et al. (1966) observed capacitance changes, and postulated that potential differences of the order of 100 mV would produce substantial mechanical forces which could compress the membrane (Babakov et al., 1966). However, because they observed no changes in bilayer thickness using an optical method, they assumed a non-compressible membrane in a bid to quantify the work of the electrical field against membrane surface tension. They ascribed the observed changes to a reversible transformation of the edge of the membrane ring into a bimolecular layer.

White (1970a) followed this by stressing the importance of continuously measuring the bilayer area to accurately measure specific capacitance. Film diameter measurements in early studies show errors of 2 – 20 %, corresponding to errors in area ranging from 2.8 – 28 % and cannot account for irregular bilayer shapes (White and Thompson, 1973). White (1970a) reports an error in specific capacitance measure-

ments of 1 %, achieved by photographing the septum, cutting out the area that is visually black, and weighing the paper. Even when accounting for area changes in this way, however, he observed the dependence of specific capacitance on the square of the applied voltage, and formalised the observation with the empirical relation:

$$C_m(V) = C_{m,0} + \beta\, V^2 \tag{4.2}$$

where $C_{\mathrm{m,0}}$ is the specific capacitance at $V = 0$ mV and β is a constant. White (1970b) found that for membranes made from oxidised cholesterol in decane, $\beta = 0.0123 \pm 0.0036$ $\mu\mathrm{F\,cm^{-2}/mV^2}$ (Table 4.1). While there is general agreement that the dependence of capacitance on an applied potential follows the form of equation 4.2, the value of β and the interpretation of changes in capacitance differ widely. Some of these interpretations will be further discussed below and are summarised in Table 4.1. For ease of comparison with literature data and following more recent convention, we define

$$\beta' \equiv \beta / C_{\mathrm{m,0}}. \tag{4.3}$$

This means we can rewrite equation 4.2:

$$C_{\mathrm{m}}(V) = C_{\mathrm{m,0}}\,(1 + \beta'\, V^2) \tag{4.4}$$

where β' is numerically equal to the percentage change in C_{m} over 100 mV.

At this point it is worth re-examining the contribution of the double layer capacitance, C_{dl}, to the measured capacitance, which is presumed to be a possible reason for the observed changes in some instances (Rosen and Sutton, 1968). While deemed experimentally unobservable in other literature (Läuger et al., 1967; White, 1970a), we do know the effect should depend on the thickness on the bilayer, as can be seen by referring back to equation 3.13. For thinner bilayers than the example given on page 91, such as those of interest in the typical system used in DIBs ($d_{\mathrm{m}} \approx 30$ Å, see Figure 3.2), we obtain $C_{\mathrm{m}} = 0.982\ C_{\mathrm{g}}$ in a 0.1 M electrolyte. In other words, ~2 % of the measured specific capacitance can be ascribed to the double layer.

Table 4.1: Voltage dependence of capacitance in the literature

System[a]	$C_{\mathrm{m},0}$ $\frac{\mu F}{cm^2}$	β' [b] $\frac{1}{V^2}$	**Interpretation**	**Comment**	**Ref.**
egg-PC or DOPC / C10	0.33	10	Thickness change.	Assumes constant area.	Läuger et al. (1967)
phospholipid solution	0.37	0.8	Area change.	Measures no change in bilayer thickness with optical method (74 ± 15Å).	Babakov et al. (1966)
egg-PC / C10	0.38	1-3	Interaction of electrolyte with polar head groups, insignificant.	Measures area using microscope eye-piece for each measurement.	Ohki (1969)
oxidised cholesterol / C10	0.56	2.2	Thickness change, dielectric effects cannot be excluded.	Introduces area measurement method based on photographing septum, cutting out black film and weighing paper.	White (1970b)
GMO / C10 GMO / C16	0.38 0.65	6–8 −2	Thickness change.	Re-equilibration after change of potential takes minutes to hours. Observes appearance of lenses upon application of potential. Area measurement not detailed.	Andrews et al. (1970)
Cholesterol / detergent [c] / C12	_ [d]	0.02	Thickness change.	Measures only fast capacitance response, slow component is thought to arise from area changes.	Wobschall (1972)
BDSPC [e] / C10	0.38–0.50	>12	Primarily average thickness change. Microlenses are not a dominant effect.	C_{T}, A_{M} and C_{m} varied with time, non-reproducible from film to film: $C_{\mathrm{m},0}$ varied by 20 %.	White and Thompson (1973)
Oxidised cholesterol / C10	_ [d]	4.3–5.9	Electrostrictive phenomena: 4 different mechanisms of dipole or molecule reorientation with different time constants.	Multi-exponential analysis of capacitance relaxation after step-change in potential. Does not comment on area.	Sargent (1975)

[a] formed by Müller-Rudin unless otherwise specified.
[b] $\beta' = \beta / C_{\mathrm{m},0}$, which, given in units of V^{-2}, is numerically equal to $\Delta C_{\mathrm{m}} / C_{\mathrm{m},0}$ over 100 mV in percent.
[c] hexadecyltrimethylammonium (HDTAC).
[d] only relative capacitance changes reported.
[e] 1,2-bisdihydrosterculoyl-3-sn-glycerophosphorylcholine.

Table 4.2: Voltage dependence of capacitance in the literature - continued

System[a]	$C_{m,0}$ $\frac{\mu F}{cm^2}$	β' [b] $\frac{1}{V^2}$	Interpretation	Comment	Ref.
GMO / C10	0.39	6.7	Thickness change by solvent exclusion.	Observes increase in visible microlenses upon applying voltage. Criticises constant-volume compression theory.	Requena et al. (1975)
GMO / C10	0.39	5.4	Thickness change by solvent exclusion.	Assumes constant area. β' is time dependent, reported value is for voltage pulse of 500 ms duration. Measures no change in films made by the Montal-Müller method→ "solvent-free".	Benz et al. (1975)
DPhPC / C10 DOPC / C10 DOPC / C16	0.37 0.37 0.62	7.6 12 1.8	Thickness change by solvent exclusion.	Finds that films with larger torus/film areas give different response, but assumes constant area in films with torus <5% total membrane area. β' (= α on p. 732 of Benz and Janko (1976)) is time-dependent, and is quoted here for voltage pulses applied for 10 s.	Benz and Janko (1976)
Oxidised cholesterol / C10	_ [d]	0.26–0.52	Thickness changes. Only components faster than solvent exclusion are measured.	Uses 2nd and 3rd harmonic response in AC-based capacitance measurement to access fast component of capacitance increase. States that β' can be as high as 10 for slow components due to solvent exclusion and area changes.	Carius (1976)
GMO / C6 [f]	0.75	0.036	Membrane thinning with proportional increase in area (constant volume).	Changes stated for <10μs pulses. Area estimated from hole area. Films referred to as solvent-free, but white petrolatum in pentane was applied to the septum.	Alvarez and Latorre (1978)
GMO / C10	0.49–0.55	2.6–4.3	Thickness change, 'squeezing out' of solvent from the bilayer.	Found variation between bilayers → shows data from three representative BLMs. Area determined from frame-grabbed video images.	Picard et al. (1991)

[a] formed by Müller-Rudin method unless otherwise specified.
[b] $\beta' = \beta / C_{m,0}$, which, given in units of V^{-2}, is numerically equal to $\Delta C_m / C_{m,0}$ over 100 mV in percent.
[d] only relative capacitance changes reported.
[f] formed by the Montal-Müller method.

This is a significant percentage relative to the magnitude of the changes observed in C_{m} in response to an applied voltage, and therefore the effect of the voltage on C_{dl} has to be considered before drawing any conclusions on its effect on C_{g}. Equation 3.13 is an approximation based on a potential of $V_{\mathrm{a}} \ll RT/F \simeq 25$ mV. The full equation for the case of no fixed surface charges, determined by Läuger et al. (1967), is:

$$C_{\mathrm{m}} = \frac{\sinh \alpha}{\sinh \alpha + \frac{2\alpha}{\kappa d_{\mathrm{m}}} \frac{\varepsilon_{\mathrm{m}}}{\varepsilon_{\mathrm{w}}}} \tag{4.5}$$

where κ is the inverse of the Debye-Hückel length (equation 2.1), ε_{m} and ε_{w} are the dielectric constants of the hydrocarbon core and water respectively, and α is a parameter that can be determined from a graphical solution to the transcendental equation

$$\kappa d_{\mathrm{m}} \frac{\varepsilon_{\mathrm{m}}}{\varepsilon_{\mathrm{w}}} \sinh \alpha + 2\alpha = \frac{V_{\mathrm{a}} F}{2RT}. \tag{4.6}$$

This shows that the applied voltage has an effect on the magnitude of C_{dl}, and could therefore be responsible for a measured specific capacitance response. However, when solving the equations above, it becomes apparent that a potential of >10 V would be needed to change the contribution of C_{dl} by more than 0.5 %, making a geometric capacitance change the likely candidate for explaining the observed capacitance response.

Haydon and Overbeek (1966) point out that a potential of 100 mV across a membrane of 50 Å corresponds to a field strength of 200,000 V/cm, which implies a great pressure on the film that could compress the bilayer. This effect is termed 'electrostriction' (Wobschall, 1972) and describes the uniform normal stress (force per unit area) (σ_{t}) on the bilayer as a result of a potential. This electrostrictive stress is given by (Picard et al., 1991; White, 1970b):

$$\sigma_{\mathrm{t}} = \frac{\varepsilon_{\mathrm{m}} \varepsilon_0}{2 {d_{\mathrm{m}}}^2} V^2. \tag{4.7}$$

The thinning of the bilayer – mediated by this pressure – is opposed by steric interactions of the hydrocarbon tails of the lipid and any solvent present in the bilayer. If changes in carefully measured specific capacitance can be interpreted as changes

in bilayer thickness, the obvious question is whether electrostriction effects a change in the conformation of the lipids, or whether the thinning is purely the result of the removal of solvent from within the bilayer to the annulus (Requena et al., 1975). The former mechanism can be considered as an elastic compression, the latter as an inelastic compression.

4.2.1 Elastic Compression of Bilayers

The elastic compression model of a bilayer, often referred to as constant-volume compression, is characterised by a conformational change of the lipid chain in response to a pressure normal to the bilayer that leads to a larger surface area per lipid molecule. A decrease in monolayer thickness, and consequently bilayer thickness, therefore results in a proportional increase in bilayer area. Essentially, the bilayer is modelled as a uniform compressible material. If the changes in bilayer capacitance are interpreted as thickness changes from an initial thickness d_0 to a voltage-dependent thickness d_m, the isothermal thickness compressibility modulus (K_t) of the bilayer in response to electrostriction (σ_t, from equation 4.7) can be calculated (Marsh, 1993):

$$\sigma_\mathrm{t} = K_\mathrm{t}\frac{\Delta d_\mathrm{m}}{d_0}. \tag{4.8}$$

Combining equations 4.7 and 4.8, we obtain

$$\frac{\Delta d_\mathrm{m}}{d_0} = \frac{1}{K_\mathrm{t}}\frac{\varepsilon_\mathrm{m}\varepsilon_0}{2\,{d_\mathrm{m}}^2}V^2. \tag{4.9}$$

As d_m decreases from d_0 by Δd_m, C_m can be written as:

$$C_\mathrm{m} = \frac{\varepsilon_\mathrm{m}\varepsilon_0}{d_\mathrm{m}} = \frac{\varepsilon_\mathrm{m}\varepsilon_0}{d_0 - \Delta d_\mathrm{m}} = \frac{\varepsilon_\mathrm{m}\varepsilon_0}{d_0} \times \frac{1}{1 - \dfrac{\Delta d_\mathrm{m}}{d_0}}. \tag{4.10}$$

If $\Delta d_\mathrm{m} \ll d_0$ then this can be approximated to:

$$C_\mathrm{m} = \frac{\varepsilon_\mathrm{m}\varepsilon_0}{d_0} \times (1 + \frac{\Delta d_\mathrm{m}}{d_0}). \tag{4.11}$$

Substituting equation 4.9 into equation 4.11 gives:

$$C_{\mathrm{m}} = \frac{\varepsilon_{\mathrm{m}}\varepsilon_0}{d_0}\left(1 + \frac{1}{K_{\mathrm{t}}}\frac{\varepsilon_{\mathrm{m}}\varepsilon_0}{2\,{d_{\mathrm{m}}}^2}V^2\right). \tag{4.12}$$

By comparison of equation 4.12 with the empirical fit to the voltage response of C_{m} (equation 4.4):

$$C_{m,0} = \frac{\varepsilon_{\mathrm{m}}\varepsilon_0}{d_0} \text{ and } \beta' = \frac{1}{K_{\mathrm{t}}}\frac{\varepsilon_{\mathrm{m}}\varepsilon_0}{2\,{d_{\mathrm{m}}}^2}. \tag{4.13}$$

Hence, K_{t} can be expressed in terms of the parameters obtained from fits of equation 4.4 to measured capacitance data (Picard et al., 1991):

$$K_{\mathrm{t}} = \frac{1}{\beta'}\frac{\varepsilon_{\mathrm{m}}\varepsilon_0}{2{d_{\mathrm{m}}}^2}. \tag{4.14}$$

If K_{t} is a constant, equation 4.13 implies that β' is not constant, as it depends on d_{m}. This means that the form of the dependence of specific capacitance on applied potential is not an exact parabola, but that β' increases at higher applied voltage. This seems counter-intuitive, as one would expect bilayer compression to saturate. White (1973) points out that K_{t} is a partial measure of the repulsive potential energy of the bilayer that depends on thickness, which would imply β' could be constant. At low applied voltage, where $d_{\mathrm{m}} \approx d_0$, equation 4.13 indicates that β' should be a strong function of $C_{\mathrm{m},0}$, an observation that could not be verified in experiments carried out by White and Thompson (1973). These considerations will be discussed further in the light of the results from experiments detailed below.

4.2.2 Inelastic Compression of Bilayers

As already discussed in Chapter 3, artificial bilayers can contain substantial amounts of solvent. If aliphatic hydrocarbon solvent molecules are not fully interdigitated with the lipid hydrocarbon tails, but mediate a distance between the lipid monolayers, then one would expect the thinning by means of removal of solvent to the annulus to be energetically more favourable than the elastic compression of lipid hydrocarbon tails. The resulting change in the distance between the lipid monolayers defines the inelastic compression model of a bilayer. Contrary to the constant-volume compression

described in section 4.2.1, the total volume of the bilayer here changes under inelastic compression.

White (1970a) found that newly formed membranes were much more sensitive to applied voltage than membranes that had been left for 10–20 minutes under an applied potential of 100 mV. Andrews et al. (1970) and Requena et al. (1975) report that bilayers of GMO in decane depend strongly on voltage, while those in hexadecane do not. Benz et al. (1975) found that bilayers made by the Montal-Müller method (Montal and Mueller, 1972) that were thought to be "solvent-free", did not respond to an applied voltage at timescales of less than 1 s. These results suggest that removal of solvent is a likely mechanism of bilayer thinning in artificial membranes.

The term 'inelastic' may be somewhat misleading as it refers to the monolayer, but not the bilayer. If the equilibrium solvent content of the bilayer has been attained before the application of the potential, then the voltage merely shifts this equilibrium, resulting in a reversible change in thickness.

4.2.3 Microlenses and the Torus

The proposed existence of submicroscopic areas containing pockets of solvent complicates the interpretation of changes in specific capacitance (Sargent, 1975; White and Thompson, 1973). Benz and Janko (1976) observed a large change in capacitance (Table 4.1), concluding that this cannot be accounted for by whole bilayer area changes alone. They postulated that since the "pressure" exerted by the electric field (equation 4.7) is larger at the thin bilayer parts of the membrane, the resulting imbalance pushes any solvent into thicker areas. However, it is difficult to see how this would result in a higher capacitance overall. Another possible conjecture is that, analogously to the voltage-dependent bilayer area changes discussed in Chapter 2, the application of a potential causes the relative surface free energy of the bilayer to decrease, which would result in changes in the contact angle of microlenses. Even if bilayer diameter can be accurately measured, bilayer area and thus capacitance could effectively be increased by changes in the contact angle of such microlenses (White and Thompson, 1973). While it is not clear to what degree slightly thicker regions in

the bilayer contribute to capacitance, they are likely to be equivalent to the immediate region of the torus surrounding the bilayer. White (1972) has found that if the bilayer film area is large compared to the torus, then the torus contributes on the order of 0.01% to total measured capacitance (C_{T}). A large number of microlenses would mean that the ratio of film area to the total length of film edge would be smaller, which could make the contribution of the edge more significant. The increased accessibility of supported lipid bilayers to surface characterisation techniques is likely to yield more data on the precise structure of the bilayer in these systems, but it has not been resolved how the presence of these submicroscopic lenses in could be assessed in BLMs (Ries et al., 2004; White and Thompson, 1973).

4.3 Materials and Methods

Experiments investigating the effect of an applied potential were performed in DIBs formed in 5 mg/mL lipid in hexadecane at 22 ± 1 °C, in a buffer of 10 mM TRIS and 0.3 M KCl at pH 8.0 both in the supporting agarose and in the droplet. Materials were as described in Chapter 3.

4.3.1 Electrical Recording and Measurement of Specific Capacitance

Electrical recording and the application of a potential across the bilayer were essentially achieved as described in Chapter 2. Electrical currents were recorded with a patch clamp amplifier (Axopatch 200B; Axon Instruments), and digitized at 1 kHz (NI-PCI-6281 M-series DAQ, National Instruments). Capacitance measurement was performed by an automatic routine, as described in section 3.3.3, and bilayer area determination was carried out by randomised manual measurement on original size images as described in section 3.3.4. The background capacitance was determined before the start of the experiment by a linear fit to data from several measurements of capacitance at different areas, and used for all subsequent calculations of specific capacitance in that droplet. Errors arising from fixing the background capacitance (see section 3.5.4) are expected to be insignificant, as the bilayer area change in these experiments is minimal compared to the bilayer size.

4.3.2 Voltage Ramps

The initial size of the bilayer was controlled using the inserted electrode. The DIBs were left for half an hour with the electrode inserted before collecting data to ensure that the system was at mechanical equilibrium, and thus the free energy changes produced by the applied field were independent of any mechanical force from the electrode. A DC voltage offset was applied on top of the 10 Hz triangular (sawtooth) wave. The offset was stepped between +100 mV and −100 mV in 10 mV increments for several cycles, as illustrated in Figure 4.1. In separate experiments, the step time was varied between 10, 40 or 120 seconds to test equilibration differences. Images to measure bilayer area were acquired automatically at the end of each ramp step.

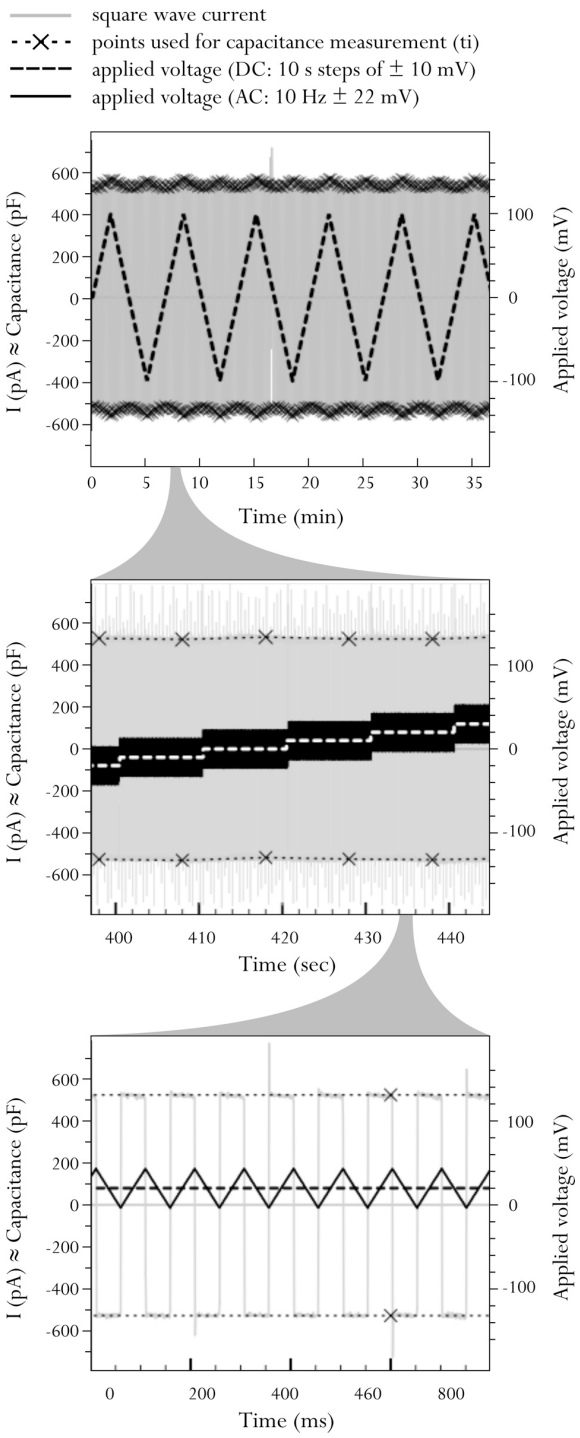

Figure 4.1: Voltage experiment protocol. A typical voltage ramp experiment is shown (**Top**). An additional DC offset (**- - -**) was applied on top of the triangular wave. The DC offset was incremented in ± 10 mV steps between −100 and +100 mV. Images were acquired at the end of each step (· · · × · · ·), ensuring sufficient time for the bilayer to settle after a step increment. The step sequence from ± 100 mV was repeated for a number of loops until droplet breakdown occurred (at 40 minutes in the dataset shown here and in Figure 4.2) to improve precision. An AC triangular wave (10 Hz, ± 22 mV) was applied to generate the square wave current response (∼± 500 pA).(**Bottom**). C_T (—, grey) was determined from the average of the capacitive current determined in the manner described in Figure 3.1 at 10 consecutive current peaks in a 1 s section of measured current (I_M) trace before each point of imaging. (· · · × · · ·)

4.4 Results and Discussion

4.4.1 The Effect of an Applied Potential on Total Membrane Capacitance

DIBs made from DPhPC in hexadecane respond significantly and reversibly to applied DC voltages (V_a) across the bilayer, with no obvious hysteresis between positive and negative V_a changes or across successive ramps (see Figure 4.3 for the a typical full data set). In the example shown in Figure 4.2, the total capacitance (C'_T) increases by approximately 6.3% for V_a of ± 100 mV (Figure 4.2a), following an approximately quadratic relationship that is in keeping with previous BLM studies. In accordance with equation 4.4, the C'_T changes can be fitted with a simple empirical equation of the form

$$C_{T'} = C_{T,0'} \, (1 + a \, V_a^2) \tag{4.15}$$

where $C_{T,0'}$ is the total membrane capacitance at $V_a = 0$ mV.

4.4.2 Changes in Bilayer Area Explain the Majority of the Capacitance Response

As already discussed in Chapter 2, imaging of the DIB during the application of a potential shows that the C'_T increase is accompanied by a similar quadratic increase in bilayer area (A_M) (Figure 4.2b). As in the case of the total capactance above, the A_M changes of the data shown in Figure 4.2b can also be fitted with an empirical quadratic (White, 1970a; White and Chang, 1981):

$$A_M = A_{M,0} \, (1 + B \, V_a^2) \tag{4.16}$$

where $A_{M,0}$ is the bilayer area at $V_a = 0$ mV. The magnitude of the pre-quadratic parameter B reflects a significant area change (Table 4.3). The bilayer area increases on average by 5.6 % over ± 100 mV in the dataset shown in Figure 4.2 B. Contrary to results shown by Punnamaraju and Steckl (2011), we observe no hysteresis in the area changes. Substituting equation 4.15 and equation 4.16 into equation 3.15, we

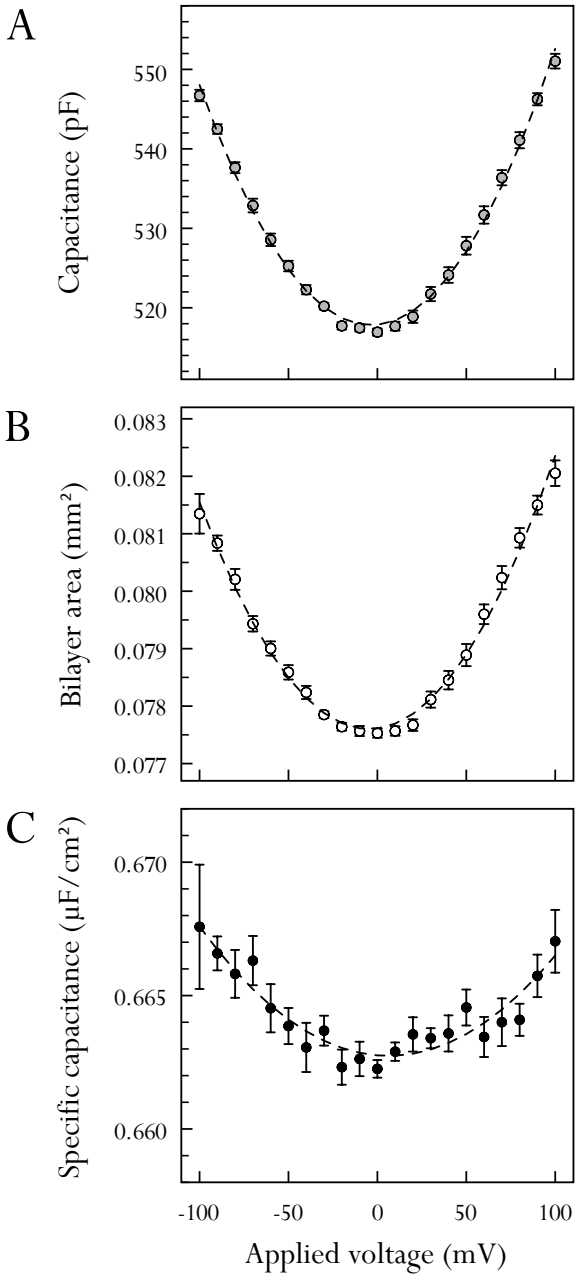

Figure 4.2: Variation of DIB capacitance with applied potential. DPhPC in hexadecane DIBs (10 mM TRIS-HCl pH 8.0, 0.3 M KCl) were subjected to an externally applied DC potential. The potential was incremented in 10 mV steps every 10 s between ± 100 mV. Bilayer capacitance, C'_{T}, was measured continuously and images for area measurement were taken shortly before each potential step change. The data are an average from 10 voltage sweeps over a run lasting 35 min. (Error bars: standard error) **(A, B, C)** Quadratic fits to whole membrane capacitance (C'_{T}), bilayer area (A_{M}) and bilayer specific capacitance (C_{m}) plotted versus the applied DC voltage (V_{a}). *Adapted with permission from Gross et al. (2011a). Copyright (2011) American Chemical Society.*

find that in the case of the dataset in Figure 4.2, the area change accounts for 89 % of the parameter a in equation 4.15, and thus for the majority of the overall C'_T increase. A series of experiments with different droplets showed that the magnitude of the area changes described by the parameter B is dependent on the initial contact angle (θ_0) of the droplet (Figure 4.4 B) and ranges from 5 – 23 % (Table 4.3). The fitted B values are in the range of those predicted theoretically for BLMs small enough to experience little confinement by the aperture (White and Chang, 1981).

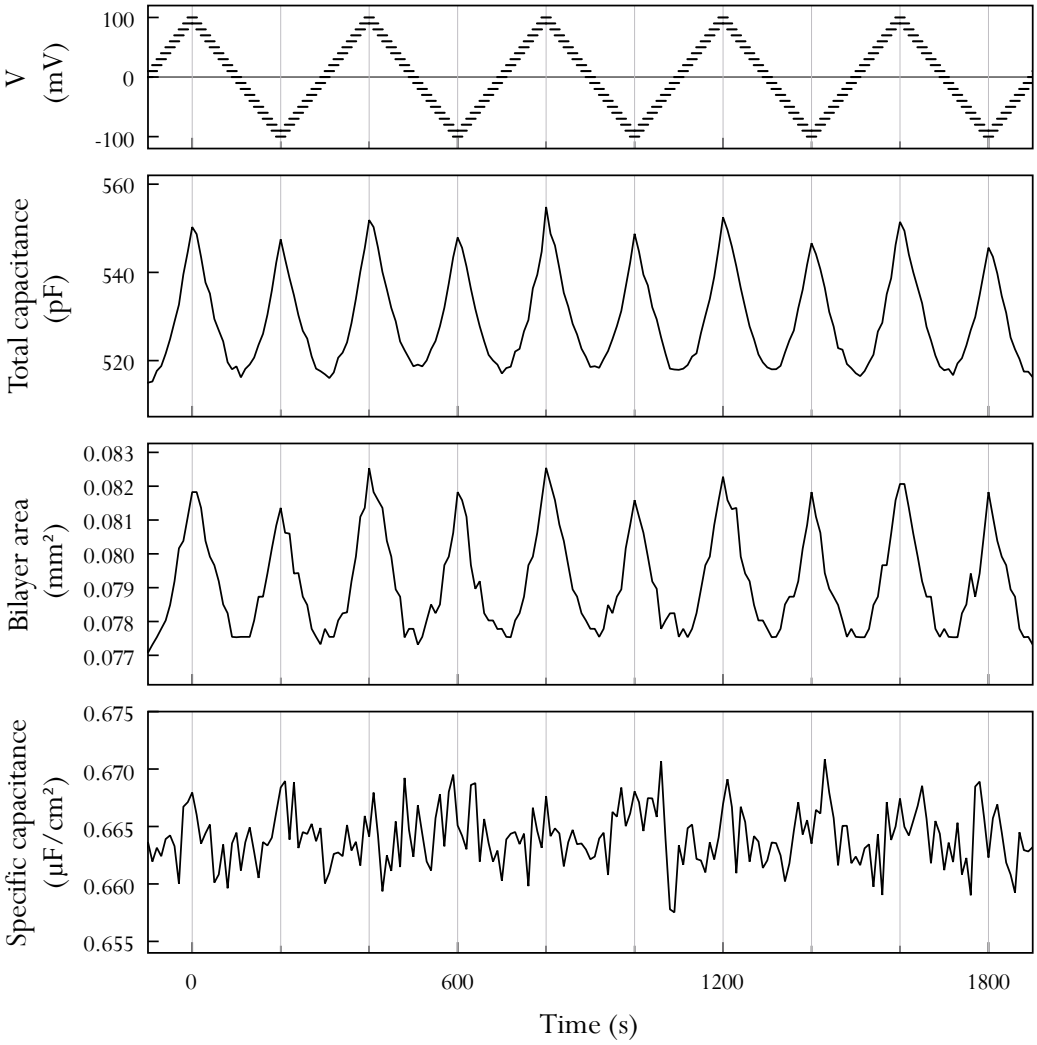

Figure 4.3: Full data obtained from a voltage experiment in a droplet formed in 5 mg/mL DPhPC in hexadecane. Buffer conditions were 10 mM TRIS-HCl, 0.3 M KCl, pH 8.0. The applied voltage was incremented by 10 mV at 10 s intervals and the step sequence was cycled between ± 100 mV (top). The droplet remained intact for just over 35 minutes, enabling the completion of 5 complete cycles, or ~20 data points at each applied voltage. It is apparent that the majority of the change in total capacitance arises from a change in bilayer area.

4.4.3 The Effect of Applied Potential on Specific Capacitance

The simultaneous monitoring of total capacitance and bilayer area changes enables the measurement of voltage-dependent changes in the specific capacitance of the bilayer. Specific capacitance is determined for each simultaneous measurement in the voltage ramps using $C_m = C'_T/A_M$. A quadratic increase in C_m is observed, which, in a bilayer system with a long-chain alkane such as hexadecane, has previously either not been measured (Andrews et al., 1970), or was within the stated error of the area measurement method (Benz and Janko, 1976; Punnamaraju and Steckl, 2011). Equation 4.4, which was derived for experiments with BLMs containing decane, provides a good fit to the data (Figure 4.2c). C_m increases by 0.64 % at ± 100 mV ($\beta' = 0.64$) in the example in Figure 4.2c, and therefore accounts for ~10 % of the overall C'_T increase. The quadratic voltage-dependent C_m increase is smaller in magnitude than that observed in BLMs formed in decane (see Table 4.1/4.2).

In multiple experiments, a small range of ΔC_m from 0.6 – 1.5 % is observed (Table 4.3). Considering equations 3.15, 4.4, 4.15 and 4.16, which give $a = \beta' + B$, it is apparent that the specific capacitance changes described by β' account for ~5 – 13 % of the overall C'_T increase. This is contrary to some assumptions made in the consideration of area changes in aperture-confined BLMs, where both $\Delta C'_T$ and ΔA_M were thought to arise from constant lipid volume compression ($\beta' = B$) (Alvarez and Latorre, 1978) and confirms that area changes are a distinct phenomenon driven by changes in surface tension (equation 2.16).

From equation 3.14, the maximum ΔC_m increase of ~0.01 $\mu F\,cm^{-2}$ in DPhPC/hexadecane DIBs ($V_a = \pm$ 100 mV) can be interpreted as a decrease in the bilayer thickness of ~0.44 Å, or an increase in the bilayer dielectric permittivity ε_m of ~ 0.033 $F\,cm^{-1}$, or a combination of the two. However, it is generally accepted that the membrane dielectric permittivity does not change under electric fields of this magnitude as the lipids undergo no significant change in state or composition (Picard et al., 1991; White, 1970a, 1986). If interpreted as a change in bilayer thickness, the observed decrease could arise from either a decrease in lipid monolayer thickness (constant lipid volume compression), a change in the distance between the bilayer

leaflets by a reduction in the amount of oil within the bilayer, or a combination of the two. Our results cannot easily deconvolute these two components.

To assess if constant-volume compression is taking place, the bilayer elastic thickness compressibility, as calculated from the data obtained here, can be compared to known values for lateral lipid compressibility. Under the assumption of lipid incompressibility – a necessary condition for constant-volume compression – the force required to compress the bilayer is directly proportional to the force required to stretch the bilayer in the plane (Cevc, 1993). The thickness compressibility, K_t, is related to the elastic area compressibility, K_A, by:

$$K_t = K_A / d_m. \tag{4.17}$$

As detailed in section 4.2.1, the elastic thickness compressibility modulus (K_t) associated with compressing the bilayer can be calculated from the specific capacitance data presented, under the assumption that the changes in specific capacitance can be ascribed to changes in bilayer thickness. Using equation 4.14, K_t for the DPhPC/hexadecane DIBs examined here is $7-17 \times 10^5$ N m^{-2} (Table 4.3).

For bilayers of ~3.0 nm thickness, this results in a K_A of ~$2.2-5.1$ mN m^{-1}, which is two orders of magnitude lower than values obtained by stretching oil-free bilayers such as vesicles (~$50-200$ mN m^{-1}) (Cevc, 1993; Israelachvili, 2011). This clearly shows that the K_t from these data underestimates the force required for constant-volume compression (Evans and Simon, 1975). It is therefore likely that the observed changes in C_m are a measure of the elasticity of removing oil from the bilayer. This interpretation would also be consistent with the fact that values for K_t obtained from electro-compression studies of BLMs formed in decane, which contain more solvent at equilibrium (see section 3.2.6), are smaller. For example, 0.35×10^5 N m^{-2} for phosphatidyl-choline/decane BLMs (White and Thompson, 1973), and 0.42×10^5 N m^{-2} for GMO in decane (Andrews et al., 1970). For further comparative results from different lipid/solvent systems, the reader is referred to the table on p.45 of Hianik and Passechnik (1995).

The magnitude of the ΔC_m changes is directly dependent on $C_{m,0}$ (Figure 4.4 C).

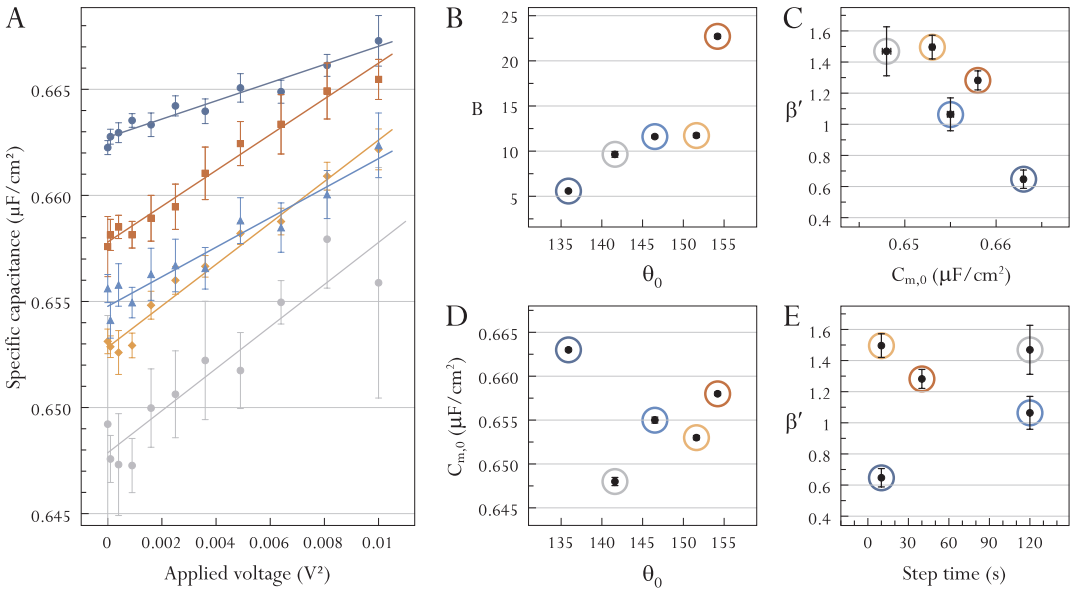

Figure 4.4: Electric field experiment results from multiple droplets. **(A)** The change in specific capacitance in five separate droplets plotted vs. the square of the applied voltage. The data includes that shown in Figure 4.2 (dark blue). **(B)** Change in bilayer area: the magnitude of the area change over ± 100 mV described by the parameter B in equation 4.16 depends on the initial contact angle θ_0. **(C)** Change in specific capacitance: the magnitude of the specific capacitance change over ± 100 mV described by the parameter β' in equation 4.4 shows dependence on the initial bilayer capacitance at $V_a = 0$ mV ($C_{m,0}$). **(B,C)** The circles mark data from the same experiment, highlighting that area changes and specific capacitance changes are independent. **(D)** There is no correlation between $C_{m,0}$ and the initial contact angle, θ_0 **(E)** The magnitude of the response of specific capacitance to voltage (β') does not depend on the step time used in the experiment. Buffer: 10 mM TRIS-HCl and 0.3 M KCl at pH 8.0 both in the supporting agarose and in the droplets.

Table 4.3: The Effect of an Applied Voltage on DPhPC Bilayers: Summary of Fit Results

#	**Step time** (s)	θ_0 (°)	b	$C_{m,0}$ (μFcm^{-2})	β	K_t (Nm^{-1})
1	10	135.9	5.59	0.663	0.65	1.74×10^{6}
2	10	151.6	11.74	0.653	1.50	7.31×10^{5}
3	40	154.2	22.71	0.658	1.28	8.66×10^{5}
4	120	141.6	9.64	0.648	1.47	7.33×10^{5}
5	120	146.5	11.61	0.655	1.06	1.03×10^{5}

This is contrary to results shown by White and Thompson (1973), but confirms the expectation detailed in section 4.2.1 on the basis of equation 4.13. However, this expectation is based on a model of the bilayer as a uniform compressible material. A far more likely explanation for the observed dependence is that bilayers of lower $C_{m,0}$, which presumably contain more oil and are slightly thicker, respond more to the compressive force of the applied field with inelastic compression, as described in section 4.2.2. However, it is difficult to fully explore this dependence as $C_{m,0}$ cannot be easily altered. The equilibrium chemical potential of the alkane would not be expected to vary significantly between droplets. The data show no dependence of $C_{m,0}$ on the initial bilayer contact angle, θ_0 (Figure 4.4 D), which is dependent on the force on the droplet applied by the electrode, indicating that any mechanical force has a negligible effect on C_m or $C_{m,0}$. Figure 4.4 E also shows that there is no correlation between the magnitude of ΔC_m changes and the equilibration time period between voltage ramp steps (10 s – 120 s, Table 4.3), indicating that the system has equilibrated to the applied field within the shortest period. Further kinetic experiments would be required to confirm this.

4.4.4 The Effect of Applied Potential on the C_m of Other Lipid Systems

The effect of an applied voltage on specific capacitance was investigated in two further lipid systems: DOPC:POPE 4:1 and POPE:POPG 3:1. These have acyl chains that are more commonly found in biology than the methylated chains on the archaeal analogue DPhPC. DOPC:POPE 4:1 bilayers have recently been used to investigate pore forming activity of viral proteins (Chew et al., 2009; Mehnert et al., 2008) and POPE:POPG 3:1 is a common system used to mimic the bacterial inner membrane.

4.4.4.1 DOPC:POPE 4:1

This lipid system contains neutral lipids of different chain length with two 18-carbon unsaturated acyl chains in DOPC and a 16-carbon saturated and 18-carbon unsaturated chain in POPE, and would therefore be expected to possess a very different

compressibility to DPhPC. Bilayers from DOPC:POPE 4:1 in hexadecane proved to be less stable than those formed from DPhPC. Figure 4.5 shows a limited set of data, with only four data points where $n > 11$ (black points). Other points have $n < 2$ (grey points). A quadratic fit to all points yields $\beta' = 6.47\ V^{-2}$. Using only the four points with adequate data, $\beta' = 4.31\ V^{-2}$. While these data clearly are non-ideal, it is apparent that β' is at least an order of magnitude greater than in DPhPC bilayers.

The maximal specific capacitance reached at ± 100 mV implies a bilayer thickness of 28 Å, which is thinner than DPhPC bilayers. Given that three out of four acyl chains in DOPC:POPE are one carbon longer than in DPhPC, this would indicate that this system contains less oil by volume at this point than DPhPC in hexadecane. This, taken together with the larger value for β', suggests that a greater degree of elastic compression may take place in this system.

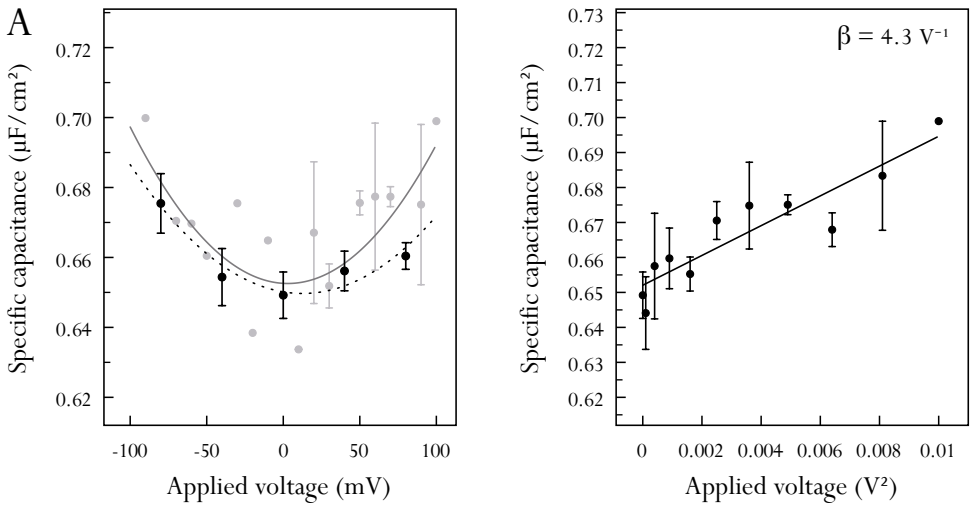

Figure 4.5: Response of a DOPC:POPE 4:1 bilayer to an applied voltage. **(A)** Only four data points with $n > 11$ (black points). Other points $n < 2$. Fit from all points: $\beta' = 6.47\ V^{-2}$, fit from only four points: $\beta' = 4.31\ V^{-2}$. **(B)** Linear fit of the data in A plotted against the square of the applied voltage. The buffer was 10 mM TRIS-HCl and 0.3 M KCl at pH 8.0 both in the supporting agarose and in the droplet.

4.4.4.2 POPE:POPG 3:1

This lipid system is similar to DOPC:POPE 4:1 in that both POPE and POPG have one unsaturated C–C bond and the chain lengths are unequal (16:18). The unsaturated bond imparts a kink onto one of the chains, which is thought to impart

fluidity to the membrane. A key difference to DOPC:POPE is that POPG carries a negative charge. Figure 4.6 B shows that, in analogy to DPhPC DIBs, the total membrane capacitance (C'_{T}) of POPE:POPG DIBs depends on the square of the applied voltage, which, as in both the previous cases, is largely due to a quadratic increase of bilayer area with applied potential. Specific capacitance also follows a quadratic relationship. For the dataset shown in Figure 4.6, $\beta' = 2.5\ \mathrm{V}^{-2}$, which is larger than the value determined for DPhPC DIBs, but significantly smaller than that found in DOPC:POPE. Another marked difference between the two systems is the fact that, in the case of POPE:POPG DIBs, an offset of the voltage dependence is observed. Such an offset would be expected if an intrinsic membrane potential existed. A difference in the surface potential across the dielectric ($\Delta\Psi_m$) could give rise to such an additional potential drop across the membrane (see also section 2.2.1). To fit the data, equations 4.15, 4.16 and 4.4 therefore have to be restated as follows (Alvarez and Latorre, 1978):

$$C'_{\mathrm{T}} = C_{\mathrm{T},0'}\,(1 + a\,(V_{\mathrm{a}} + \Delta\Psi_m)^2), \tag{4.18}$$

$$A_{\mathrm{M}} = A_{\mathrm{M},0}\,(1 + B\,(V_{\mathrm{a}} + \Delta\Psi_m)^2), \tag{4.19}$$

$$C_{\mathrm{m}} = C_{\mathrm{m},0}\,(1 + \beta'\,(V_{\mathrm{a}} + \Delta\Psi_m)^2). \tag{4.20}$$

In the dataset shown, the offset as measured from the fit to capacitance data is -44 mV. There are a number of possible reasons for the observation of an offset. Since the patch clamp electrode is balanced before each experiment, an electrode imbalance is unlikely to account for it. Solutions of different ionic strength could be one reason, and this is the most likely explanation in the case of small offsets occasionally observed in the simple DPhPC lipid system described in the previous section. However, the reproducible and large offset observed in DIBs made from a 3:1 POPE:POPG mixture in particular suggests that the offset might arise from a surface potential difference: such a potential difference would be observed if these bilayers are not symmetric, for example if the negatively charged POPG preferentially partitioned into one of the monolayers. Since the monolayers in DIBs form independently and in different

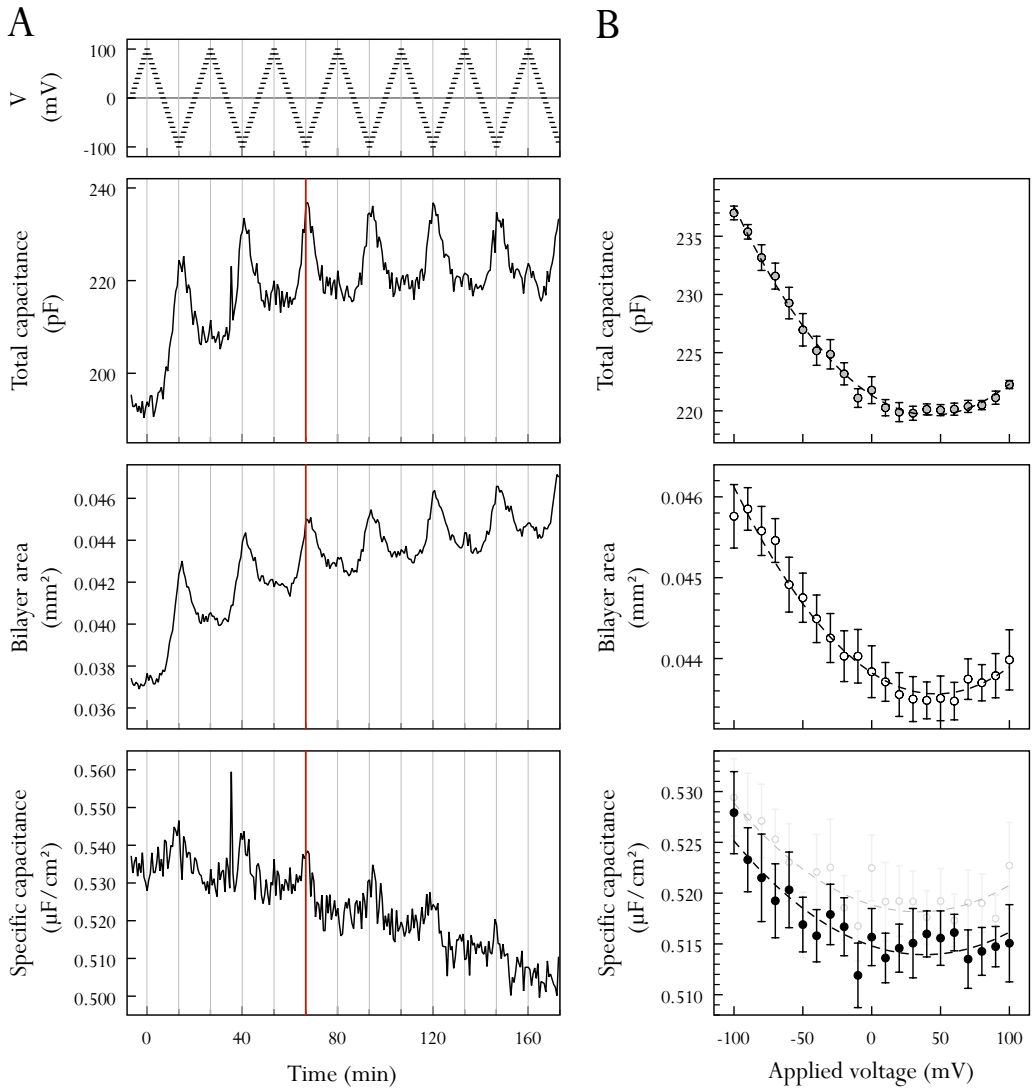

Figure 4.6: Response of a POPE:POPG 3:1 bilayer to an applied voltage. **(A)** Full data from the experiment. Voltage was incremented in 10 mV steps at intervals of 40 s. There is substantial drift in the bilayer area during the first hour of the experiment. As in the case of DPhPC, the majority of the capacitance change arises from changes in bilayer area. In a pattern only observed in POPE:POPG bilayers, specific capacitance decreases steadily over time. **(B)** Data from A plotted against the applied voltage. Only the data to the right of the red line are included. In the case of the specific capacitance (B, bottom), the grey points indicate the full data. The voltage offset is 44 mV, and $\beta' = 2.5\ \mathrm{V}^{-2}$.The buffer was 10 mM TRIS-HCl and 0.3 M KCl at pH 8.0 both in the supporting agarose and in the droplet.

environments, it is easy to envisage that this might occur. A substrate with fixed or associated negative charges, for example, could mean that charged lipids in the lipid-oil solution are less likely to partition into the lower leaflet. Alternatively, charged lipids could be removed from the lipid-oil solution that is used for the incubation of the droplet by electrostatic interactions with the surfaces of the incubation tank, leaving the droplet with a higher proportion of neutral lipids.

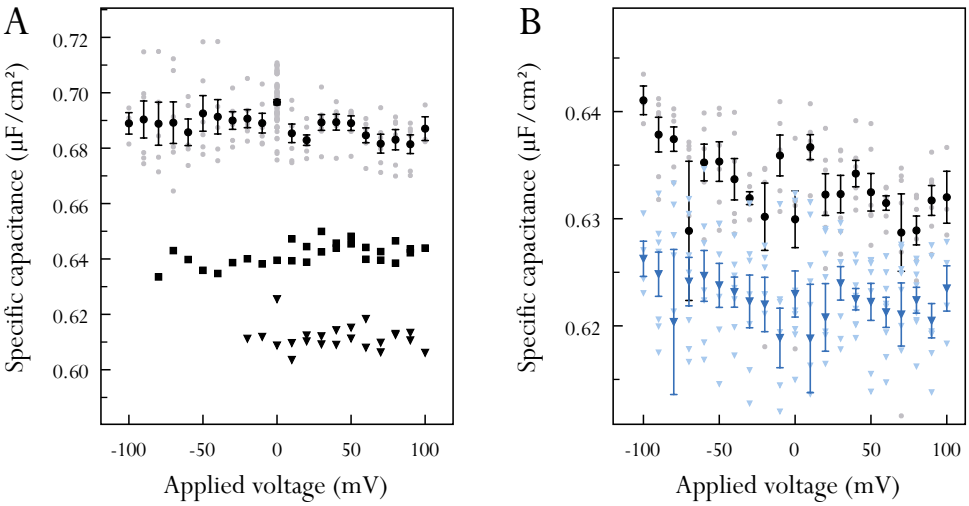

Figure 4.7: Further datasets showing the response of POPE:POPG 3:1 bilayer to voltage. **(A,B)** Five experiments carried out on different days. The buffer was 10 mM TRIS-HCl and 0.3 M KCl at pH 8.0 (22 °C) both in the supporting agarose and in the droplet. Error bars represent the standard error of the full data shown in grey.

The area of DIBs formed from POPE/POPG frequently drifts substantially over a period of approximately an hour after the start of the experiment, but the direction of the drift is not reproducible. In some instances the contact angle can approach 90° (see Figure 3.10). Figure 4.6 A shows the full dataset recorded. To ensure that the droplet had fully equilibrated, only the data to the right of the red line were used in Figure 4.6 B. However, while the total capacitance is clearly driven by the area changes, specific capacitance is not affected by the drift in area at the start of the experiment. In fact, contrary to observations on other systems in Chapter 3 and in the literature (where capacitance has often been seen to increase over time as solvent drains from the bilayer), specific capacitance decreases steadily for the full duration of the experiment (~3 hrs, Figure 4.6 A, bottom). A linear fit shows that

specific capacitance decreases at a rate of 0.01 μF cm^{-2} h^{-1} or ~2 % per hour. There are a number of possible interpretations of this effect. Oxidisation of the lipids (Zhu et al., 2006) is unlikely to be the reason, as a perturbation of the bilayer can partially reset the drift (see Figure 3.10). It is possible that unequal partitioning of the lipid components into the bulk oil phase could occur, although POPE and POPG have identical acyl chains and so it is difficult to see how this could result in the observed effect. Experiments monitoring the specific capacitance in alternative artificial bilayer systems without a large oil reservoir could shed more light on whether this effect is particular to DIBs.

Figure 4.6 appears to show unequivocally that specific capacitance in POPE:POPG 3:1 bilayers follows that same quadratic voltage dependence described by equation 4.20. However, as already pointed out, POPE:POPG bilayers appear to be highly variable, both in terms of their morphology and their specific capacitance at 0 mV applied voltage ($C_{\mathrm{m},0}$). Figure 4.7 shows data from five further droplets. It appears that there are two populations, with the three droplets in Figure 4.7 A showing no dependence on the applied voltage, while the two in B appear similar to the data shown in Figure 4.6. The five droplets were recorded on different days, but in identical conditions. Further experiments with large datasets from several droplets on the same device, as well as a search for the parameters affecting $C_{\mathrm{m},0}$, which varies widely, will be necessary to gain a better understanding of this lipid system.

4.5 Summary

This chapter has presented experiments that take advantage of the benefits of the DIB system to measure bilayer specific capacitance as a function of applied potential. DIBs are able to eliminate at least one ambiguity among the many factors that influence the bilayer response to an applied potential; namely they unequivocally separate area effects from specific capacitance effects. These two phenomena appear to be largely independent. Previously, researchers had attempted to circumvent the ambiguity of area changes by using frequency-based methods that measured only those changes in capacitance that occur on very short timescales, attributing these to an elastic compression of the lipids in the bilayer. The disadvantage of this approach is that the exclusion of solvent from artificial bilayers is likely to occur across all timescales, complicating the picture. However, for most artificial systems, the movement of solvent is of great interest, as it allows the determination of solvent content, which should be known when comparing results from experiments in artificial bilayers to physiological data. If the bilayer compression observed here can be exclusively attributed to solvent content, and thus to inelastic compression, this method could be used to find lipid-oil systems where the solvent content is minimal.

Unfortunately, it is not yet possible to attribute the observed compression to either elastic or inelastic compression. The difference in the results observed with bilayers consisting of lipids with saturated chains suggests that the elasticity of the lipid does play a role. However, it cannot be ruled out that these bilayers are simply able to accommodate more solvent.

Of great relevance to many experiments in artificial bilayers are the findings of the variability of POPE:POPG bilayers. POPE:POPG 3:1 is very commonly used in artificial bilayer systems to mimic the bacterial inner membrane, but the results presented here indicate that it is difficult to obtain reproducible bilayer characteristics with this system, which should be taken into account when attempting to interpret membrane protein function from results obtained in these bilayers.

For experiments *in vivo*, any elastic compression of the bilayer would have important implications on studies that equate capacitance with area to detect events such

as vesicle fusion, synaptic signalling or exocytosis. The assumption of constant specific capacitance to measure such events should only be made with extreme caution as it could easily lead to an overestimation of area changes.

Further work on the voltage response of specific capacitance could explore the ability to form asymmetric DIBs (Hwang et al., 2008), which would be of greater relevance to many biological systems and could also yield information pertaining to the question of the mechanism of compression posed above. A systematic study of the effect of an applied potential on symmetric and asymmetric DIBs – consisting of lipids of varying hydrocarbon tail flexibility and formed in an alkane that minimises solvent intercalation – could shed more light on the question of whether lipids change conformation under an applied potential and thus whether constant volume lipid compression takes place.

The rationale behind the desire to understand the structure and behaviour of artificial bilayers is, of course, connected with one of their primary purposes: the study of membrane proteins in a minimal environment. BLMs have been instrumental in elucidating the electrical characteristics of membrane proteins such as ion channels and protein pores. With respect to understanding the effect of membrane thickness on protein function, DIBs have the same limitation as BLMs: capacitance can only be measured when single-channel electrical characterisation of a membrane protein is not taking place. However, a major advantage of DIBs over conventional BLMs is that the bilayer can be simultaneously imaged by total internal reflection fluorescence (TIRF) microscopy (Heron et al., 2009, 2007; Thompson et al., 2007). The combination of single molecule fluorescent methods to study membrane proteins, which will be discussed in the following chapters, with the ability to continuously monitor bilayer specific capacitance, will no doubt find numerous applications in the study of the role of membrane lipids in lateral protein interactions, their membrane insertion and their function (Marsh, 2008; Phillips et al., 2009).

Bibliography

Alvarez, O. and R. Latorre (1978). Voltage-dependent capacitance in lipid bilayers made from monolayers. *Biophys. J. 21*(1), 117.

Andrews, D. M., E. D. Manev, and D. A. Haydon (1970). Composition and energy relationships for some thin lipid films, and the chain conformation in monolayers at liquid-liquid interfaces. *Special Discussions of the Faraday Society 1*, 46–56.

Babakov, A. V., L. N. Ermishkin, and E. A. Liberman (1966). Influence of electric field on the capacity of phospholipid membranes. *Nature 210*(5039), 953–955.

Benz, R., O. Fröhlich, P. Läuger, and M. Montal (1975). Electrical capacity of black lipid films and of lipid bilayers made from monolayers. *Biochimica et Biophysica Acta (BBA) - Biomembranes 394*(3), 323–334.

Benz, R. and K. Janko (1976). Voltage-induced capacitance relaxation of lipid bilayer membranes effects of membrane composition. *Biochimica et Biophysica Acta (BBA) - Biomembranes 455*(3), 721–738.

Carius, W. (1976). Voltage dependence of bilayer membrane capacitance : Harmonic response to ac excitation with dc bias. *Journal of Colloid and Interface Science 57*(2), 301–307.

Cevc, G. (1993). *Phospholipid Handbook*. Marcel Dekker: New York.

Chew, C., R. Vijayan, J. Chang, N. Zitzmann, and P. Biggin (2009). Determination of Pore-Lining residues in the hepatitis c virus p7 protein. *Biophysical Journal 96*(2), L10–L12.

Evans, E. and S. Simon (1975). Mechanics of bilayer membranes. *Journal of Colloid and Interface Science 51*(2), 266–271.

Gross, L. C. M., A. J. Heron, S. C. Baca, and M. I. Wallace (2011a). Determining membrane capacitance by dynamic control of Droplet Interface Bilayer area. *Langmuir 27*(23), 14335–14342.

Hanai, T., D. A. Haydon, and J. Taylor (1964). An investigation by electrical methods of Lecithin-in-Hydrocarbon films in aqueous solutions. *Proceedings of the Royal Society of London. Series A. Mathematical and Physical Sciences 281*(1386), 377–391.

Haydon, D. A. and J. T. G. Overbeek (1966). General discussion. *Discussions of the Faraday Society 42*, 66.

Heron, A. J., J. R. Thompson, B. Cronin, H. Bayley, and M. I. Wallace (2009). Simultaneous measurement of ionic current and fluorescence from single protein pores. *Journal of the American Chemical Society 131*(5), 1652–1653.

Heron, A. J., J. R. Thompson, A. E. Mason, and M. I. Wallace (2007). Direct detection of membrane channels from gels using water-in-oil droplet bilayers. *Journal of the American Chemical Society 129*(51), 16042–16047.

Hianik, T. and V. I. Passechnik (1995). *Bilayer lipid membranes*. Springer.

Hwang, W. L., M. Chen, B. Cronin, M. A. Holden, and H. Bayley (2008). Asymmetric droplet interface bilayers. *Journal of the American Chemical Society 130*(18), 5878–5879.

Israelachvili, J. N. (2011). *Intermolecular And Surface Forces* (3rd ed.). Academic Press.

Läuger, P., W. Lesslauer, E. Marti, and J. Richter (1967). Electrical properties of bimolecular phospholipid membranes. *Biochimica et Biophysica Acta (BBA) - Biomembranes 135*(1), 20–32.

Marsh, D. (1993). Bilayers, monolayers, multilayers and Non-Lamellar lipid phases. In *Biomembranes: Physical Aspects*, pp. 1—28. Weinheim: VCH.

Marsh, D. (2008). Protein modulation of lipids, and vice-versa, in membranes. *Biochimica et Biophysica Acta (BBA) - Biomembranes 1778*(7-8), 1545–1575.

Mehnert, T., A. Routh, P. J. Judge, Y. H. Lam, D. Fischer, A. Watts, and W. B. Fischer (2008). Biophysical characterization of Vpu from HIV-1 suggests a channel-pore dualism. *Proteins: Structure, Function, and Bioinformatics 70*(4), 1488–1497.

Montal, M. and P. Mueller (1972). Formation of bimolecular membranes from lipid monolayers and a study of their electrical properties. *Proceedings of the National Academy of Sciences of the United States of America 69*(12), 3561–3566.

Ohki, S. (1969). The electrical capacitance of phospholipid membranes. *Biophysical Journal 9*(10), 1195–1205.

Phillips, R., T. Ursell, P. Wiggins, and P. Sens (2009). Emerging roles for lipids in shaping membrane-protein function. *Nature 459*(7245), 379–385.

Picard, G., N. Denicourt, and J. H. Fendler (1991). Simultaneous electrical and optical interferometric measurements of pressure- and applied-potential-induced bilayer lipid membrane deformation. *The Journal of Physical Chemistry 95*(9), 3705–3715.

Punnamaraju, S. and A. J. Steckl (2011). Voltage control of droplet interface bilayer lipid membrane dimensions. *Langmuir 27*(2), 618–626.

Requena, J. and D. A. Haydon (1975). The Lippmann equation and the characterization of black lipid films. *Journal of Colloid and Interface Science 51*(2), 315–327.

Requena, J., D. A. Haydon, and S. B. Hladky (1975). Letter: Lenses and the compression of black lipid membranes by an electric field. *Biophysical Journal 15*(1), 77–81.

Ries, R. S., H. Choi, R. Blunck, F. Bezanilla, and J. R. Heath (2004). Black lipid membranes: Visualizing the structure, dynamics, and substrate dependence of membranes. *The Journal of Physical Chemistry B 108*(41), 16040–16049.

Rosen, D. and A. Sutton (1968). The effects of a direct current potential bias on the electrical properties of bimolecular lipid membranes. *Biochimica et Biophysica Acta (BBA) - Biomembranes 163*(2), 226–233.

Sargent, D. F. (1975). Voltage jump/capacitance relaxation studies of bilayer structure and dynamics. *Journal of Membrane Biology 23*(1), 227–247.

Thompson, J. R., A. J. Heron, Y. Santoso, and M. I. Wallace (2007). Enhanced stability and fluidity in droplet on hydrogel bilayers for measuring membrane protein diffusion. *Nano Letters 7*(12), 3875–3878.

White, S. H. (1970a). A study of lipid bilayer membrane stability using precise measurements of specific capacitance. *Biophys. J. 10*(12), 1127–1148.

White, S. H. (1970b). Thickness changes in lipid bilayer membranes. *Biochimica et Biophysica Acta (BBA) - Biomembranes 196*(2), 354–357.

White, S. H. (1972). Analysis of the torus surrounding planar lipid bilayer membranes. *Biophysical Journal 12*(4), 432–445.

White, S. H. (1973). The surface charge and double layers of thin lipid films formed from neutral lipids. *Biochimica et Biophysica Acta (BBA) - Biomembranes 323*(3), 343–350.

White, S. H. (1978). Formation of "solvent-free" black lipid bilayer membranes from glyceryl monooleate dispersed in squalene. *Biophysical Journal 23*(3), 337–347.

White, S. H. (1986). The physical nature of planar bilayer membranes. *In:* C. Miller (Ed.), *Ion Channel Reconstitution*, pp. 3–35. Plenum Press, New York.

White, S. H. and W. Chang (1981). Voltage dependence of the capacitance and area of black lipid membranes. *Biophysical Journal 36*(2), 449–453.

White, S. H. and T. E. Thompson (1973). Capacitance, area, and thickness variations in thin lipid films. *Biochimica et Biophysica Acta (BBA) - Biomembranes 323*(1), 7–22.

Wobschall, D. (1972). Voltage dependence of bilayer membrane capacitance. *Journal of Colloid and Interface Science 40*(3), 417–423.

Zhu, M., Z. Qin, D. Hu, L. A. Munishkina, and A. L. Fink (2006). Alpha-synuclein can function as an antioxidant preventing oxidation of unsaturated lipid in vesicles. *Biochemistry 45*(26), 8135–8142.

Chapter 5

Total Internal Fluorescence Imaging of DIBs

This chapter describes the experimental setup and methods for the imaging of DIBs by total internal reflection fluorescence (TIRF) microscopy. The bacterial β-barrel protein α-Hemolysin (α-HL) from Staphylococcus aureus is introduced, and an account of its expression and purification is given. Optical patch clamping, a method of localising unlabelled membrane channels by fluorescence, is described, followed by results from the single-particle tracking (SPT) of α-HL in a DIB.

5.1 Introduction

Since DIBs in the 'on-hydrogel' configuration are planar and are formed on transparent substrates, they are suited to optical microscopy. The development of a very thin supporting hydrogel in particular has enabled the use of TIRF for high resolution single molecule fluorescence detection and particle tracking, while retaining bilayer fluidity and the capability of electrical recording of the bilayer (Thompson et al., 2007). Simultaneous recording of fluorescence intensity and single-channel conductivity from individual pores diffusing in a DIB was recently reported by Heron et al. (2009).

5.2 Background and Theory

5.2.1 Principles of TIRF Microscopy

TIRF is particularly suited to the study of interfaces as it exploits an optical effect to illuminate exclusively the region in close proximity to the interface, thus minimising background fluorescence.

A light beam encountering an interface from a medium of higher refractive index to one of lower refractive index will be totally internally reflected if the angle of incidence is greater than a critical angle of incidence for total internal reflection (ϕ_c):

$$\phi_c = \sin^{-1}(n_2/n_1) \tag{5.1}$$

where n_1 and n_2 are the refractive indices of the high-index medium and the low-index medium respectively. In objective-based TIRF microscopy, the beam is focused on the back aperture of a high numerical aperture (NA) objective in such a way that it leaves the objective at an angle to the objective axis (the sample normal) equal to or greater than the critical angle. The high-index medium in this case consists of an index-matching immersion oil and the glass sample slide. The lower index medium is the aqueous sample. This arrangement is illustrated in Figure 5.1. As a result of total internal reflection, the beam returns back through the objective.

At the region of reflection, an electromagnetic field that penetrates a small distance into the low refractive index medium is created, which propagates parallel to the surface in the plane of incidence (Axelrod et al., 1984). The intensity of this field, known as the 'evanescent wave', decays exponentially into the low-index medium along the normal to the surface (z-axis):

$$I(z) = I_0 e^{-z/d} \tag{5.2}$$

where

$$d = \frac{\lambda_0}{4\pi}(n_1^2 \sin^2\phi - n_2^2)^{-1/2} \tag{5.3}$$

for angles of incidence $\phi > \phi_c$. λ_0 is the wavelength of the light in vacuum. The

penetration depth, d, decreases with increasing angle of incidence, ϕ, but is of the order of λ_0 (Axelrod et al., 1984). I_0, the intensity at the interface, depends on both the angle of incidence and the polarisation of the incident beam, but can be several times stronger than the incident intensity for angles close to ϕ_c(Axelrod et al., 1984).

5.2.2 α-Hemolysin as a Model Membrane Protein

In the experiments described here, the bacterial pore-forming toxin α-HL is used as a model membrane protein. α-Hemolysin monomer is secreted as a water-soluble monomer of 33.2 kDa by *Staphylococcus aureus* (*S. aureus*) and inserts into host cell membranes by means of a conformational change upon oligomerisation, resulting in osmotic imbalance, cell lysis, necrosis or apoptosis. The oligomeric protein is a heptameric structure which is thermodynamically highly stable, only dissociating into monomers in solutions of sodium dodecyl sulfate (SDS) above 60 °C (Gouaux, 1998). It has therefore been extensively studied, and has become the archetypal member of the family of β-pore forming toxins (β-PFTs) that form β-barrel transmembrane pores with defined but non-specific conductance (Gouaux, 1998; Menestrina, 1986). The protein measures approximately 100 Å in height, and the ectopic domain is approximately 100 Å wide. Spanning the height of the protein is a central aqueous channel with a diameter ranging from ~16 to ~46 Å. Each monomer contributes

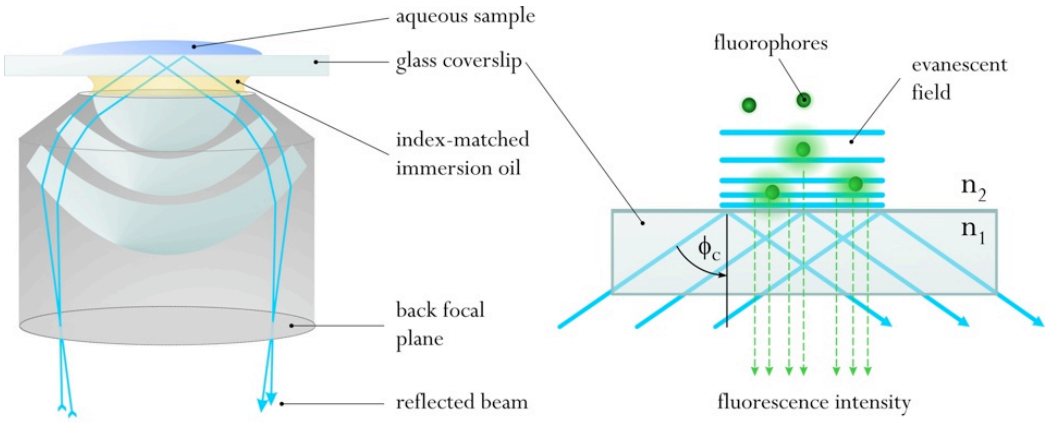

Figure 5.1: Principles of objective-based total internal reflection fluorescence microscopy. n_1 is the refractive index of the glass slide, n_2 is the refractive index of an aqueous sample, $n_1 > n_2$. ϕ_c is the critical angle of incidence for total internal reflection.

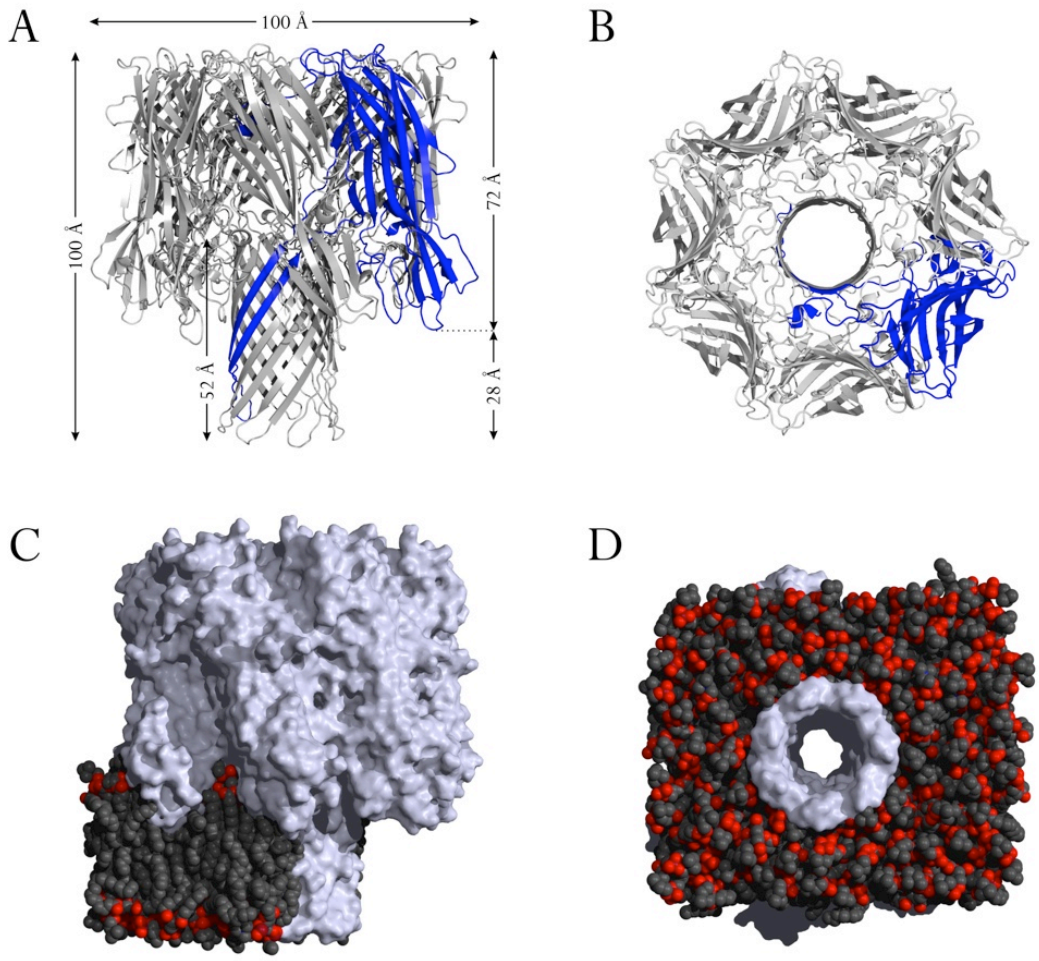

Figure 5.2: **(A)** Image of α-HL structure (PDB:7AHL), with one of the monomers highlighted in blue. **(B)** Top view **(C)** Surface view, schematically embedded in a membrane to show relative location of bilayer leaflets. **(D)** The end of the β-barrel, showing the water-filled pore that penetrates the membrane.
Figures were created with MacPyMol (Delano Scientific LLC, http://www.pymol.org) and rendered using PovRay (Persistence of Vision Pty. Ltd., http://www.povray.org). Lipid coordinates are from MD simulations of POPC in the fluid phase by Helmut Heller (Heller, 1993; Heller et al., 1993). The lipid PDB structure files are available at http://www.lrz.de/~heller/membrane/membrane.html.

one β-hairpin to the β-barrel of the heptamer, resulting in an overall mushroom-like shape where the β-barrel defines the transmembrane domain, as illustrated in Figure 5.2 (Song et al., 1996). Of great advantage for *in vitro* experiments such as those described in this chapter is the fact that α-Hemolysin, purified in heptameric form and stabilised by minimal amounts of detergent, spontaneously inserts into artificial bilayers and has a well defined conductance (Braha et al., 1997; Heron et al., 2007; Holden et al., 2007).

5.2.3 Optical Patch Clamping

Functional unlabelled protein pores in a bilayer can be visualised by a method called optical patch clamping, a term coined by Demuro and Parker (2005), who first combined it with TIRF microscopy. In optical patch clamping, the use of a dye sensitive to an analyte such as Ca^{2+} on one side of the bilayer means that the flux of that analyte through pores in the bilayer from the opposite side results in a fluorescent spot. Localised Ca^{2+}-dependent fluorescence has been observed in cells from the transient opening of ryanodine receptors, IP_3 receptors or other ion channels (Zou et al., 1999). Such events are short-lived, and have been described as 'puffs', 'blips' or, in a term coined by Zou et al. (1999), single-channel calcium fluorescence transients (SCCaFTs). As the flux of Ca^{2+} ions depends on the membrane potential, the fluorescence intensity observed mirrors the current measured by conventional patch clamping (Zou et al., 1999, 2002). The simultaneous recording of fluorescence and current from single protein pores in an artificial bilayer was first achieved in DIBs using α-Hemolysin and the calcium-sensitive dye Fluo-8 in the droplet (Heron et al., 2009). Since the rigid β-barrel of α-HL forms a permanently open pore, the fluorescent spots arising from Ca^{2+} flux through α-Hemolysin will hereafter be referred to as single-channel calcium fluorescence *in*transients (SCCaFITs). Figure 5.3 illustrates the principle of optical patch clamping.

5.3 Materials and Methods

5.3.1 Materials

Buffer reagents, salts, agarose, DPhPC, hexadecane and Milli-Q water were as described in Chapter 2. Additionally, the calcium-sensitive fluorophore Quest™ Fluo-8 (pentapotassium salt, Invitrogen, UK) was dissolved in Milli-Q water at a concentration of 1 mg/mL and stored in 50 μL aliquots at -20 °C until required. EDTA (Sigma-Aldrich) was used without further purification. Chelex resin (Chelex 100 Resin, 100 – 200 mesh, biotechnology grade), Triton X-100, and nucleic acid gel loading buffer were from Bio-Rad (Bio-RadLaboratories Ltd, Hemel-Hempstead, UK). *E. coli* bacteria stocks were from Promega (Promega, Madison, WI) and dioxane-free isopropyl-β -D-1-thiogalactopyranoside (IPTG) was from Calbiochem (Merck KGaA, Darmstadt, Germany).

5.3.2 Protein Expression and Purification

Recombinant overexpression of His-tagged α-Hemolysin in *E. coli*. Wild-type α-HL with a 6-histidine tag attached to the C-terminus via a 9 amino acid linker (WT-$(GS)_2\,S\,G_2\,S_2\,H_6$; hereafter referred to as WT-H_6 α-HL, see Appendix C

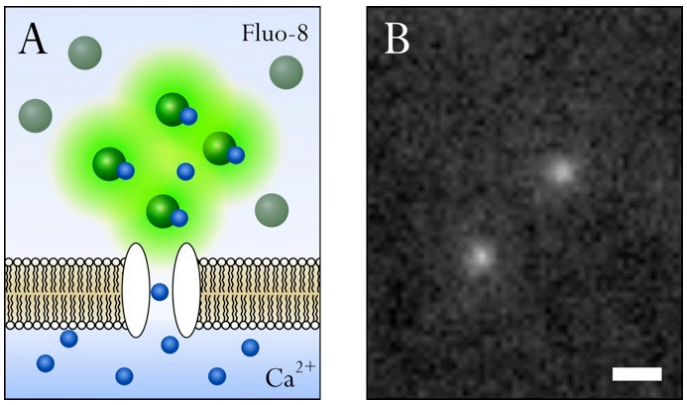

Figure 5.3: Optical patch clamping of α-Hemolysin in DIBs. **(A)** The droplet contains a calcium-sensitive dye such as Fluo-8. Upon the application of a negative potential, increased Ca^{2+} ion flux into the droplet from the substrate allows the dye to chelate calcium, resulting in a bright fluorescent spot. **(B)** Two single-channel calcium fluorescence *in*transients (SCCaFITs) arising from Ca^{2+} ions that enter the droplet through α-Hemolysin pores diffusing in the bilayer. Scale bar: 2 μm.

for sequence) was made by recombinant expression following the standard laboratory protocol (Thompson, 2009). Briefly, competent *E. coli* BL21(DE3)pLysS cells (Appendix C) were transformed by heatshock with a pT7SC1-plasmid (Cheley et al., 1997) encoding WT-H_6 α-HL (prepared in a Qiagen Maxi-prep by James Thompson). Single-colony transformants were picked and incubated overnight in 10 mL Luria-Bertani (LB) medium containing 50 μg/mL carbenecillin at 37 °C and then transferred to incubate in 0.5 L of the same medium for a further 4 hours at 37 °C until an optical density of ~0.6 at 600 nm was reached. At this point, expression was induced by 1 mM IPTG and left to continue for three hours. The cells were then centrifuged at 8000 rpm for 15 minutes, resuspended and centrifuged for a further 20 minutes at 3000 rpm, before freezing at −80 °C until needed for purification by immobilised metal-affinity chromatography (IMAC), which was carried out either by Ni-NTA FPLC or on a disposable TALON cobalt gravity column.

α-HL monomer (WT_1-H_6) purification by immobilised metal-affinity chromatography on a TALON gravity column. Cell pellets were resuspended in a washing buffer of 1 % Triton X-100, 20 mM TRIS-HCl, 0.5 M NaCl, 50 mM imidazole, 1 unit Protease Inhibitor Cocktail I (Novagen, Merck KGaA, Darmstadt, Germany) and 25 μg/mL DNAase 1 at pH 8.0 and pipetted up and down vigorously. The resulting cell debris was centrifuged at 20000 rpm at 4 °C for 1 hour. The supernatant was filtered through 0.22 μm polyethersulfone filters (Steriflip, Millipore Corporation, Billerica, MA) and kept for no longer than 1 hour at 4 °C before purification. IMAC was carried out by adding the recovered supernatant to cobalt TALON resin (Clontech, Mountain View, CA), previously washed in washing buffer and leaving the resulting bead slurry at 4 °C for 15 minutes under gentle agitation to prevent bead sedimentation. The slurry was then loaded into a TALON column (Clontech) and washed with 70 mL of washing buffer. The elution buffer, consisting of 20 mM TRIS-HCl, 0.5 M NaCl, 0.5 M imidazole at pH 8 was added while stopping the flow for 15 minutes by sealing the column, before collecting elution fractions. Fractions were stored at 4 °C in the cation exchange elution buffer for characterisation by gel electrophoresis. Before use, the elution buffer was exchanged to the experimental buffer by washing

and spinning 4 times in 4 ml concentrating centrifuge tubes (Amicon Ultra, Millipore Corporation).

α-HL heptamer (WT_7-H_6) purification by FPLC immobilised metal-affinity chromatography. Cell pellets were resuspended as above with minor modifications. The resuspension buffer consisted of 1 % Triton X-100, 1 % SDS, 50 mM TRIS-HCl, 150 mM NaCl and 1 unit Protease Inhibitor Cocktail I (Novagen) at pH 8.0. The SDS was added to the resuspension buffer to provide additional stabilisation for the heptameric protein. The remainder of the procedure was therefore carried out at room temperature to avoid precipitation of SDS. The cell debris was centrifuged at 20,000 rpm at 22 ℃ for 30 minutes before adding 25 μg/ml DNAase 1 and repeating centrifugation at 20,000 rpm for a further 30 minutes. The supernatant was filtered as above and kept for no longer than 1 hour at 22 ℃. IMAC was carried out on a Ni^{2+}-NTA column (HiTrap Chelating HP, GE-Biosciences, Fairfield, CT) with an Äkta Purifier FPLC system (GE). The binding and washing buffer contained 50 mM TRIS-HCl, 0.5 M NaCl and 0.1 % SDS at pH 8.0, the elution buffer was the same with an additional 0.5 M imidazole. After loading the sample onto the column via a Superloop, the elution buffer was mixed with the binding buffer at a ratio changing at a constant gradient from 0 – 100 %. The elute was monitored by UV absorbance at 280 and 260 nm to identify monomer and heptamer peaks. The relative size of the monomer peak can be increased by carrying out the purification in the same way but without SDS. Fractions were stored at 4 ℃ in the cation exchange elution buffer for characterisation by gel electrophoresis.

5.3.3 TIRF Microscope Setup for Optical Patch Clamping

The bilayer manipulation device and amplifying headstage were enclosed in a Faraday cage as described in Chapter 2 and attached to an inverted microscope (Eclipse T*i*, Nikon Instruments, UK) equipped with a webcam (640 × 480 px, Trust) for taking white light images and a cooled 128 × 128 pixel frame transfer electron-multiplying charge-coupled device camera (emCCD, iXon+ DU-860, Andor Technology, UK) for fluorescence imaging. The excitation source was a 473 nm diode-pumped solid-state

laser (Shanghai Dream Lasers Technology Co, China). The beam was expanded and collimated, and focused on the back aperture of a TIRF-optimised high numerical aperture oil immersion objective (Plan Apo TIRF, 60 ×, NA 1.49 , WD 0.12, Nikon) via a dichroic mirror (500DLRP, XF2037, Omega Optical Inc, Brattleboro, VT). It was then aligned with the aid of optics encased in a 'TIRF attachment' to the microscope (Nikon) to achieve total internal reflection at the glass-agarose interface. Figure 5.4 shows a simplified illustration of the main components in the setup (mirrors present purely for the optimisation of space on the laser table have been omitted). Fluorescence emission was passed through a bandpass filter (510AF23, XF3080, Omega Optical), and captured by the emCCD in images acquired at 33 Hz (30 ms exposure). The data were converted to 16-bit TIFF image stacks using Andor Solis software (v. 4.3, Andor Technology).

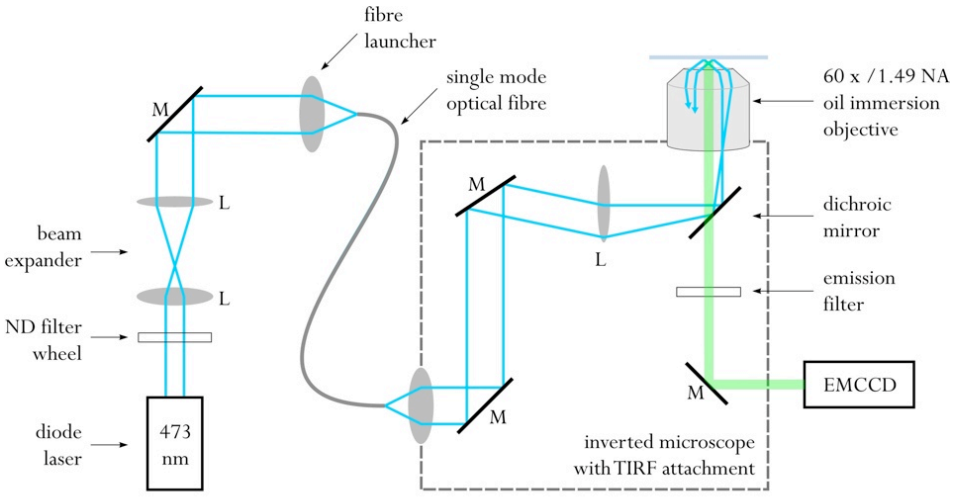

Figure 5.4: Simplified illustration of the total internal reflection fluorescence microscopy setup for optical patch clamping experiments. Mirrors present only for the optimisation of space on the laser table are omitted. M = mirror, L = lens.

5.3.4 Optical Patch Clamping Conditions

Optical patch clamping was carried out in the following solutions (see also section 5.4.2). The substrate hydrogel was hydrated with a buffer consisting of 10 mM TRIS-HCl and 750 mM $CaCl_2$ at pH 8.0. The aqueous droplet contained 10 mM TRIS-HCl,

1.3 M KCl, 1.35 mM EDTA, 50 μm Quest™ Fluo-8 and 100 nM of α-HL heptamer. The potassium chloride droplet buffer was treated with Chelex resin for at least 1 hour at 37 °C, prior to filtering as described previously (section 2.3.1), to minimise the concentration of divalent cations in solution and thus reduce background fluorescence.

5.3.5 Image Analysis

TIFF image stacks were analysed with both ImageJ software (Rasband, 1997), using the particle tracker plugin developed by the Computational Biophysics Lab at the ETH Zurich (Sbalzarini and Koumoutsakos, 2005), and with Igor Pro (v5.05, Wavemetrics).

5.3.5.1 Single-Particle Tracking

Single-particle tracking (SPT) of SCCaFITs was carried out by means of the 2D Particle Detector and Tracker plugin[†] for ImageJ written by Guy Levy (CBL, ETH Zurich), based on algorithms described by Sbalzarini and Koumoutsakos (2005). In the following, the key elements of the algorithm are summarised.

Background Removal. Prior to particle detection, the background of an image frame at time t, represented as a matrix $A^t(x, y)$ of floating point intensity between 0 and 1, was removed by a box-car average over a square region with a side length of $2w + 1$ pixels, resulting in $A^t_w(x, y)$:

$$A^t_w(x, y) = \frac{1}{(2w + 1)^2} \sum_{i=-w}^{w} \sum_{j=-w}^{w} A^t(x + i, y + j) \tag{5.4}$$

where w is a user-defined parameter an integer larger than the particle's apparent radius but smaller than the smallest inter-particle separation. This process, essentially a convolution of the image with a kernel of support $2w + 1$, was carried out by the Background_Subtractor plugin (source as above) which is included in recent

[†] Downloaded from www.cbl.ethz.ch/Downloads/ in June 2008. An updated version (Particle-Tracker_3D), maintained by Janick Cardinale (janick@vision.ee.ethz.ch), is available currently as part of the mosaic_plugins.jar package at www.mosaic.ethz.ch/Downloads/ParticleTracker/. See also https://weeman.inf.ethz.ch/ParticleTracker/.

versions of the particle detector plugin[†]. ImageJ (v. 1.45, Rasband (1997)) contains a background subtraction menu option based on the same principle, which uses a rolling-ball window instead of a box-car but gives very similar results and can be used interchangeably. The convolution effectively eliminates problems caused by uneven TIRF illumination.

Particle Detection. Particle detection as developed by Sbalzarini and Koumoutsakos (2005) is implemented in the plugin by finding local intensity maxima in the image A_w^t. A pixel is set as the approximate location if no other pixel within a distance of w is brighter. A further user parameter, η, sets a percentile cut-off such that the local maximum is discarded if it is not within the upper ηth percentile of the current image frame. The position of the particle is then refined to reduce noise-induced positioning errors by minimising the distance of centre of the found particle p $(\hat{x}_p, \hat{y}_p)$ to the brightness-weighted centroid of the particle. Finally, spurious detections of non-specific signals, dust and particle aggregates are rejected by a classification algorithm based on calculating the $0th$ and $2nd$ order intensity moments of particle p, m_0 and m_2, where

$$m_0(p) = \sum_{i^2+j^2 \leq w^2} A_w^t(\hat{x}_p + i, \hat{y}_p + j), \tag{5.5}$$

$$m_2(p) = \frac{1}{m_0(p)} \sum_{i^2+j^2 \leq w^2} (i^2 + j^2)\, A_w^t(\hat{x}_p + i, \hat{y}_p + j). \tag{5.6}$$

Particle rejection operates under the assumption that correct particles form a dense cluster in the (m_0, m_2) plane. A user determined cut-off particle discrimination parameter (χ) defines the size of the cluster (0 for no exclusion), resulting in the exclusion of particles of different size or brightness than that typical of the population.

Particle Trajectory Linking. The linking algorithm implemented in the ETH plugin identifies points corresponding to the same particle in subsequent frames and links the positions into trajectories. The implementation is based on a particle matching algorithm which uses a graph theory technique to determine optimal associations between two sets (Sbalzarini and Koumoutsakos (2005) and refs therein), and is ex-

tended in the plugin to allow for intermittent particle disappearance for a duration of a user-set number of frames (trajectory linking parameter ξ).

Particle Tracking Parameters. In the experiments described in this chapter, particle tracking was carried out with an expected particle diameter of $w = 3$. The expected particle percentile (η) depended on the density of SCCaFITs and was determined by evaluating the result by eye to ensure that the majority of particles were correctly detected but avoiding false positives. η ranged from 0.2 % for images with fewer than 5 SCCaFITs to ~6 % for images with >100 SCCaFIT. For the data that will be shown in Figure 5.10, η was 0.5 %. χ was set to 0, as images of SCCaFITs in DIBs rarely contain any significant fluorescence not arising from calcium flux through pores. Finally, the linking parameter was set to $\xi = 2$. Of the obtained output of particle trajectories, those longer than 1000 frames were retained and analysed for their lateral diffusion coefficient as described below.

5.3.5.2 Determination of the Lateral Diffusion Coefficient

The lateral diffusion coefficient (D_{lat}) of α-HL diffusing in the bilayer was calculated from the mean-squared displacement (MSD) determined for each of the trajectories using an algorithm in Igor Pro (Wavemetrics), which was as described by Thompson (2009) with the exception of minor corrections. Briefly, the characteristic MSDs for each track are determined by the running window method (Qian et al., 1991; Saxton, 1997). For a given time window (more commonly referred to as a time lag), Δt_n, the average square 2D displacement of a particle within all possible overlapping windows of Δt_n over the duration of a trajectory is calculated. The gradient of a linear fit (weighted by the standard deviation) to the MSD vs. Δt_n data of a single particle is equal to $4D_{\text{lat}}\Delta t_n$ and thus yields the lateral diffusion coefficient for that particular trajectory. A histogram of the D_{lat} values for all tracks is then fitted with the probability density function of a gamma distribution to obtain the lateral diffusion coefficient of the population.

5.4 Results and Discussion

5.4.1 Characterisation of α-Hemolysin Expression and Purification

5.4.1.1 Purification of WT-H_6 α-HL by TALON IMAC

Figure 5.5 A shows a gel documenting the TALON purification of WT-H_6. The intention was to make monomeric α-Hemolysin (WT_1-H_6), and hence, no SDS was used in the purification, as small amounts of SDS are generally used to stabilise the heptameric form (Thompson, 2009). Unexpectedly, very pure samples of WT_7-H_6 were obtained instead, as shown in lanes 4-6 of the gel in Figure 5.5 A. A spontaneously assembling very pure heptamer such as this is unusual (Steve Cheley, personal communication) and could be extremely useful. However, electrical recordings of the sample from lane 6 do not show clean step insertions of α-HL, but a noisy trace characterised by irregular step sizes (Figure 5.5 B). The reason for these observations is unclear. It is possible that the heptamer is stabilised by residual Triton X-100 from the cell shearing step, although this has not previously been observed in this laboratory to result in a pure heptamer sample (James Thompson, personal communication). Alternatively,

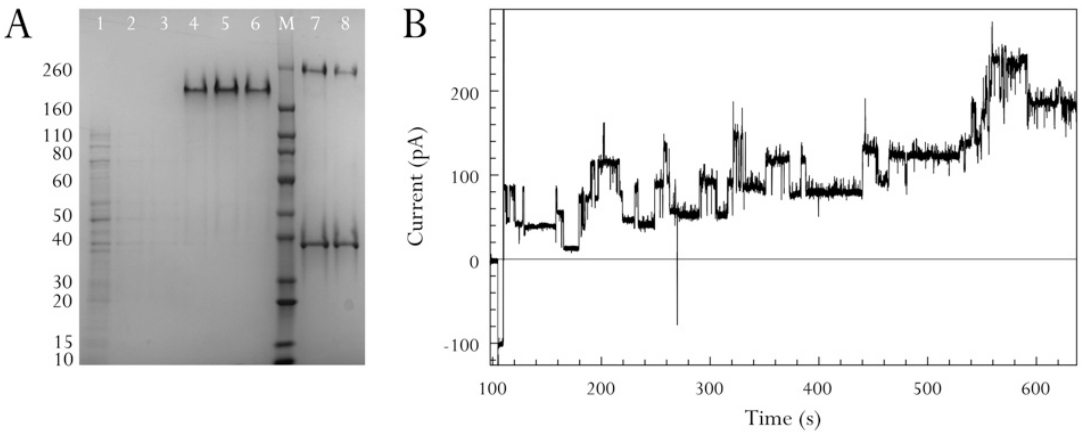

Figure 5.5: Purification of WT-H_6 by TALON IMAC. **(A)** 10% SDS-PAGE gel. Loaded volume in lane 1 is 0.1 × and lane 6 is 0.5 × that of the other lanes. Unexpectedly, the purification yielded no α-HL monomer as intended, but exclusively heptameric α-HL. *Lanes 1-3:* Flowthrough (50 mM imidazole). *Lanes 4-5:* Elute (0.5 M imidazole). *Lane 6:* Lane 5 after buffer exchange to 10 mM TRIS-HCl, 0.5 M NaCl, pH 8.0. *Lanes 8-9:* Lanes 5 and 6 heated to 98 °C for 10 minutes. The upward shift of the heptameric band upon heating is commonly observed for α-HL and is thought to arise from different mobility in the gel due to partial denaturation. **(B)** Electrical recording of the sample in lane 6 of the gel in A. The noise in the trace and irregular pore conductance suggest that the heptamer unexpectedly obtained by the purification is not in its native state.

chelation of the histidine tags by cobalt ions from the TALON resin is possible. This possibility could also explain the low-quality electrical trace, as the heptamer in this case might not be correctly assembled. However, the pure heptameric stoichiometry cannot be explained in this scenario. The noisy electrical trace could also be a result of the buffer exchange by spin concentration, which can be too harsh for proteins to remain intact. In a repetition of this purification in future work it would be advisable to carry out buffer exchange by an alternative method, such as gel filtration.

5.4.1.2 Purification of WT-H_6 α-HL by FPLC IMAC

Figure 5.6 A shows the absorbance profile of the elute of a Ni-NTA FPLC purifcation with a constant imidazole gradient (dashed line). The first peak represents the elution of weakly bound contaminating proteins, followed by the elution of the monomer in the second peak (lane 2 in Figure 5.6 B). The heptamer, with seven 6-histidine tags bound to the column, elutes only at a higher molarity of imidazole (third peak, lane 3 in Figure 5.6 B). This fraction appears to contain a small proportion of heptamer that is not correctly folded, indicated by the faint band at the top of the lane. The stability of the heptamer obtained from the purification after buffer exchange and various forms of storage was evaluated by a diagnostic gel two weeks after the purification (Figure 5.6 C), showing that the heptamer remains intact both when stored at 4 ℃ and when flash frozen and kept at −80 ℃. The faint band above that of intact heptamer disappears after storage of the protein for 14 days, presumably because any partially denatured protein precipitates out of the solution over time.

Figure 5.7 shows characteristic traces of the α-HL samples obtained from the Ni-NTA FPLC purification. Both the monomeric and the heptameric fraction readily and spontaneously insert into the bilayer. Figure 5.7 C is an example of noise that was frequently observed at a positive applied potential in the case of experiments carried out in buffer conditions required for optical patch clamping experiments (see section 5.4.2). However, at a negative applied potential in otherwise identical conditions, this noise was absent (Figure 5.7 B).

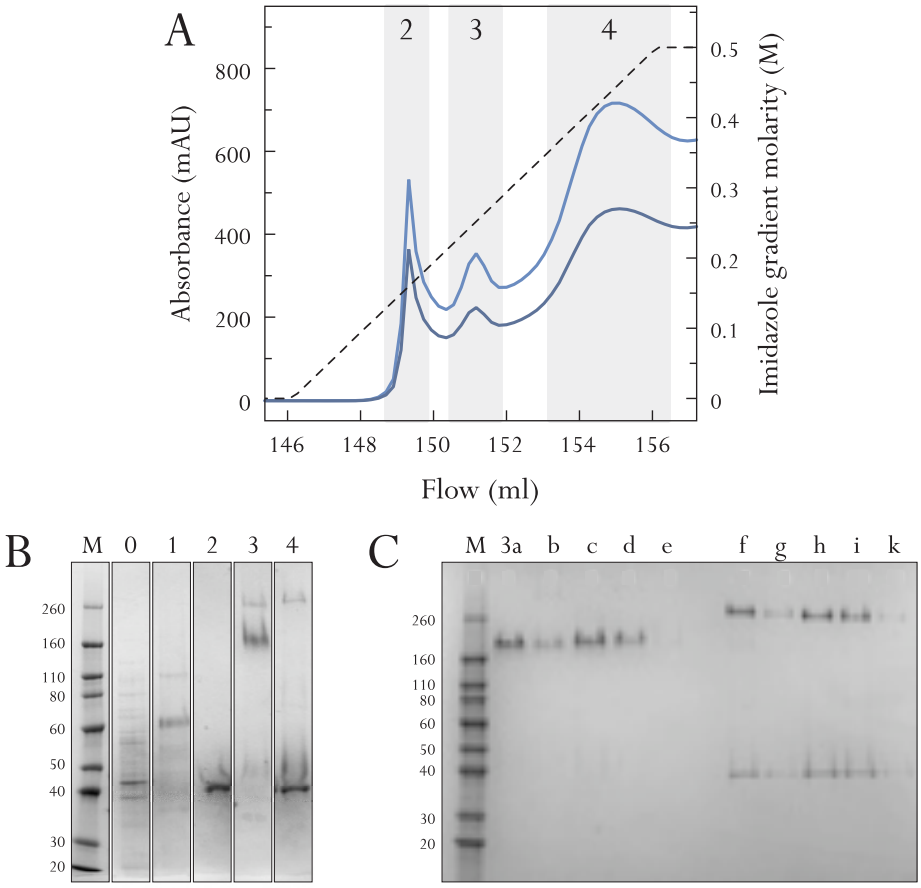

Figure 5.6: **(A)** IMAC purification of WT-H_6 α-HL by Ni-NTA FPLC using a constant imidazole gradient (dashed line). Absorbance of the elute at 260 nm (dark blue line) and 280 nm (light blue line) is shown. **(B)** Composite image of gel showing selected purification fractions. *Lane 0:* Flowthrough. *Lane 1:* First peak after commencement of imidazole gradient. *Lane 2:* Second peak: α-HL monomer (WT_1-H_6). *Lane 3:* Third peak: α-HL heptamer (WT_7-H_6). *Lane 4:* Sample from lane *3* heated to 98 °C for 10 minutes. **(C)** Diagnostic gel of the heptameric fraction (lane *3* of B) after 14 days of storage. *Lane a:* Stored in elution buffer at 4 °C. *Lane b:* Exchanged to 10 mM TRIS-HCl, 0.5 M NaCl, pH 8.0 and stored at 4 °C. (Buffer exchange by spin concentration) *Lanes c-d:* As lane *a* but flash frozen and stored at −80 °C. *Lane e:* Buffer exchange by dialysis, stored 4 °C. *Lanes f-k:* Lanes *a-e* heated to 98 °C for 10 minutes.

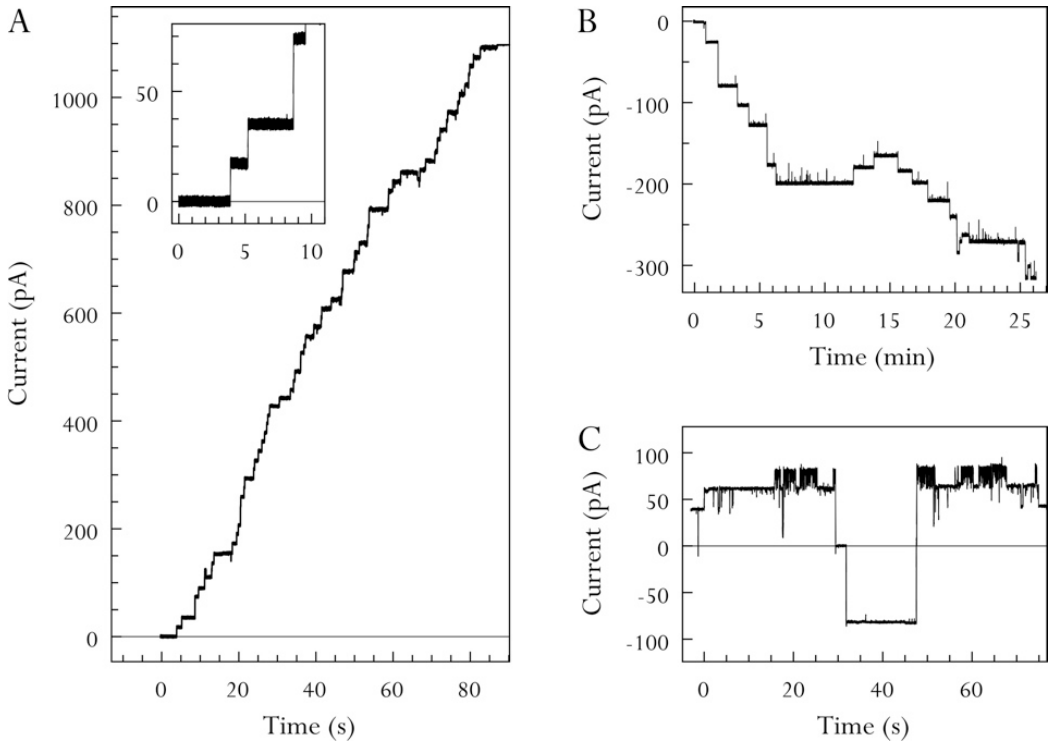

Figure 5.7: Electrical recordings of α-HL insertion. **(A)** A sample of the monomer purified by FPLC (WT_1-H_6, see lane *2* in Figure 5.6 A). Buffer: 10 mM TRIS-HCl, 0.5 M NaCl, pH 8.0. Applied potential: +100 mV. **(B)** Heptamer purified by FPLC (WT_7-H_6, see lane *b* in Figure 5.6 B) in optical patch clamping conditions. Droplet: 10 mM TRIS-HCl, 1 M KCl, 25 μM Fluo-8 and 0.5 mM EDTA. Substrate: 10 mM TRIS-HCl, 0.5 M $CaCl_2$. Applied potential: +50 mV. **(C)** Conditions as in B. Applied potential: +40 mV.

5.4.2 Optimisation of Optical Patch Clamping Conditions

The key parameter for optimal imaging of DIBs by TIRF is the thickness of the underlying agarose, which determines whether the bilayer remains within the reach of the evanescent field. The spin-coating method of depositing the agarose developed by Oliver Castell (section 2.3.3.1) has improved the reproducibility and uniformity of an appropriate bilayer thickness. A further factor is the flatness of the bilayer: in order to ensure that the entire bilayer remain within the evanescent field, it is important to maintain iso-osmotic conditions between the droplet and the supporting hydrogel. An imbalance can result in bulging of the bilayer. Depending on the direction of the imbalance, either the central area of the bilayer or a broad ring near the edge can be lifted above the penetration depth of the evanescent field, and is therefore not visible in the fluorescent image.

Osmolarity The osmolarity (Υ) of a solution is a measure of the osmotic pressure exerted by the solution across a perfect semi-permeable membrane. It is dependent on the number of particles in solution, but independent of their nature. Υ has units of osmoles per litre (osm/L) and is given by:

$$\Upsilon = \sum_i \varphi_i n_i C_i, \tag{5.7}$$

where φ is the osmotic coefficient, n is the number of particles into which a molecule dissociates and C is the molar concentration of the solute. The osmotic coefficient of each species depends on its molarity. For $CaCl_2$ ($n = 3$) at 750 mM, $\varphi \approx 0.97$ (Rard and Clegg, 1997), and thus $\Upsilon(CaCl_2) = 2.1825$ osm/L. For KCl ($n = 2$) at around 1.2 M, $\varphi \approx 0.9$ (Thiessen and Wilson, 1987), and therefore the iso-osmotic concentration of KCl is ~1.21 M. The effect of the agarose in the substrate is negligible, as the average molecular weight of agarose polymers lies between 100 – 200 kDa (Normand et al., 2000), meaning that the concentration of 1 % (w/v) agarose is less than 1 μM. Working at relatively high ionic strength also means that any salt impurities in, for example, the agarose can be disregarded.

To ensure that there is a net outward flux through pores in the bilayer at zero

applied potential, a slight osmotic imbalance was chosen. This reduces fluorescence from Ca^{2+} diffusion into the droplet in the absence of an applied potential. In general, no fluorescence can be observed in the image in this case until a negative potential is applied (see also Figure 6.7 C in Chapter 6).

Background Fluorescence and Magnitude of Calcium Response. Figure 5.8 shows that the addition of 0.23 mM EDTA, which chelates divalent ions and thus competes for the binding of Ca^{2+}, is sufficient to reduce the background fluorescence of 50 μm Fluo-8 in buffer pre-treated with Chelex resin (grey line) to less than 2 % of the maximal fluorescence intensity response observed in the presence of excess calcium. The inset in the figure highlights that, within the range of concentrations examined (0.2 – 3 mM of EDTA), the fluorescence response is dependent only on the ratio of EDTA to Ca^{2+} ions in solution, and is independent of the absolute concentrations. The inflection point of the response lies at a ratio of [EDTA]/[Ca^{2+}]=1.5, meaning that the region of highest contrast in an image surrounds areas where [Ca^{2+}] $\geq$ 2/3 [EDTA].

5.4.3 Beam Incidence

When the angle of the incident beam is adjusted for optimal contrast between the background and the SCCaFITs in the bilayer, it appears to undergo total internal reflection. However, when the droplet is moved laterally in a direction away from the incident beam, such that the region of beam incidence is exposed to the oil phase surrounding the droplet, a large amount of scattering of excitation light is observed on one side of the droplet (Figure 5.9 E). If the droplet is moved in the opposite direction, towards the incident beam, contrast in the image remains optimal (Figure 5.9 D). There are several factors that could account for this observation. Firstly, the critical angle of incidence for total internal reflection (ϕ_c) at a glass/oil interface is ~10° larger than that at a glass/water interface. Since the aqueous substrate deposited on the coverslip is of the order of 100 nm thick (Thompson, 2009; Thompson et al., 2007), the interface outside of the droplet is essentially a glass/oil interface. A beam that would totally internally reflect at the glass/water interface would be refracted into the

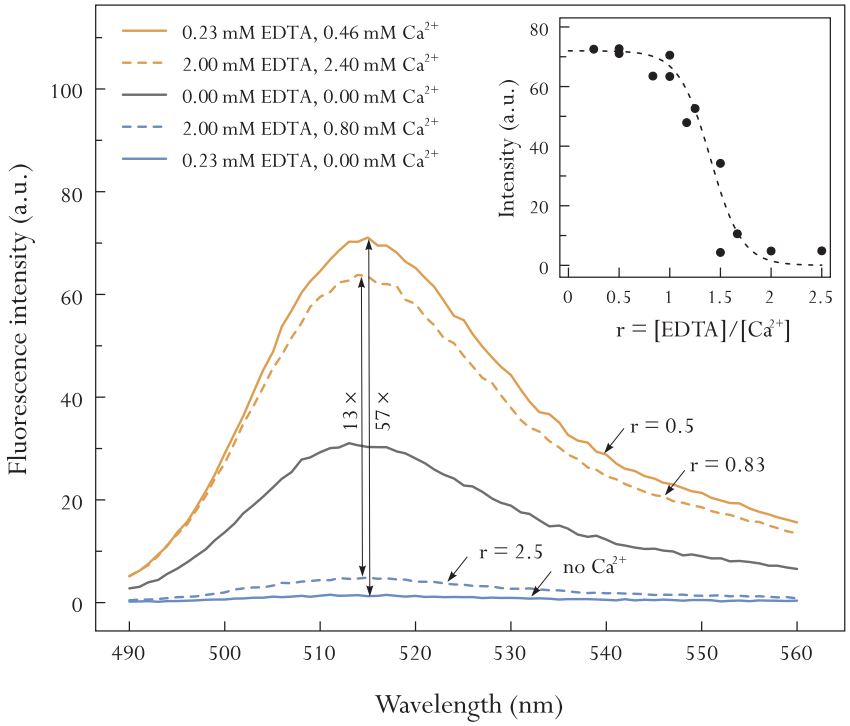

Figure 5.8: Fluorescence response of Quest™ Fluo-8 to calcium. The Excitation wavelength was 473 nm and all samples contained 50 μM Quest™ Fluo-8. A concentration of 0.23 mM EDTA is sufficient to reduce the background fluorescence of 50 μM Fluo-8 (grey line) to less than 2 % of the maximal response in the presence of Ca^{2+} (blue solid line). The inset contains points with absolute EDTA concentrations ranging from 0.2 – 3 mM, showing that the magnitude of the response only depends on the *relative* concentration of EDTA and Ca^{2+}. The inflection point is at a ratio of [EDTA]/[Ca^{2+}] = 1.5, meaning that the highest region of contrast in an image surrounds areas where [Ca^{2+}] $\geq$ 2/3 [EDTA]. All samples contained 1 M KCl and 10 mM TRIS-HCl at pH 8.0.

oil at a shallow angle in this region, and refract a second time when encountering the droplet surface, scattering light into the droplet (Figure 5.9 C). A second factor could be that the beam may not be perfectly collimated, and therefore a proportion of the incident light does not totally internally reflect, but refracts at a shallow angle to the surface as above, as illustrated in Figure 5.9 B. When the angle is sufficiently shallow, background fluorescence within the bilayer would not be significantly impacted until the droplet is moved away from the incident beam, such that refraction occurs outside of the bilayer region. As above, the refracted light would then encounter the oil/water interface at the side of the droplet, refracting a second time to be directed into the droplet at a steeper angle (Figure 5.9 C). Since a limited amount of scattered laser light can be observed above the sample plane, it is clear that perfect collimation is not achieved and that this effect must play a role. Finally, it is conceivable that the optimal contrast between SCCaFIT and the background is in fact achieved when the angle of incidence is smaller than ϕ_c, and the entire beam refracts into the droplet at a shallow angle. Since the field of view is small, the illumination in the region indicated by the dashed black line in Figure 5.9 B would appear similar to that expected from a totally internally reflecting beam. In fact, this type of illumination has previously been shown to be highly versatile for the study of cells, in a technique referred to as highly inclined laminated optical sheet (HILO) microscopy (Tokunaga et al., 2008).

5.4.4 Lateral Diffusion of α-Hemolysin in DIBs

The lateral mobility of α-Hemolysin pores in DIBs was characterised by single-particle tracking, as described in section 5.3.5. Figure 5.10 A shows an example of a background subtracted image frame in which the particle detection algorithm detected seven SCCaFITs. The detection plugin was run on a background subtracted image with the following parameters: particle radius, $w = 3$, particle discrimination parameter, $\chi = 0$, and expected particle percentile, $\eta = 0.5\,\%$. The inverted image on the right shows the tracks longer than 30 frames (trajectory linking parameter, $\xi = 2$). Figure 5.10 B shows the mean square displacements (MSDs) of SCCaFITs over time windows (time lags, Δt_n) of up to ~3.5 seconds for a population of $n = 104$ tracks (grey points). The gradient of a linear fit (red line, weighted by the standard

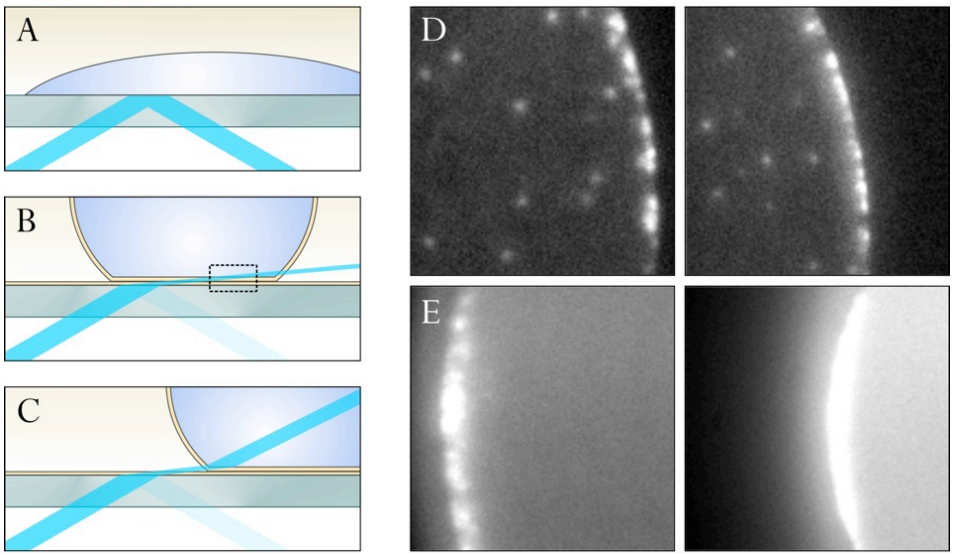

Figure 5.9: Image contrast depends on the position of the droplet relative to the incident beam. **(A)** Total internal reflection at a glass/water interface. **(B)** A beam refracting into the droplet at a shallow angle. The dashed black frame indicates a region where contrast would be expected to be similar to that achieved by an evanescent wave resulting from a totally internally reflecting beam. **(C)** The droplet moved laterally relative to the region of incidence of the beam. The refracted light encounters the oil/water interface at the side of the droplet and refracts a second time, entering the droplet at a steeper angle to the surface. **(D)** The angle of incidence of the beam optimised for maximal contrast of SCCaFITs over the background in a DIB. **(E)** The effect of moving the droplet relative to the region of incidence of the beam without adjusting the angle of incidence.

deviation) to the average MSDs over all tracks (blue line) yields a lateral diffusion coefficient of $D_{\text{lat}} = 1.62\ \mu\text{m}^2\,\text{s}^{-1}$. A more appropriate method of determining the diffusion coefficient representative of the population is to fit the probability density function of the gamma distribution that would be expected for 2D Brownian diffusion to a histogram of the lateral diffusion coefficients calculated for all individual tracks, as shown in Figure 5.10 C (Qian et al., 1991; Saxton, 1997). This gives a value of $D_{\text{lat}} = 1.61\ \mu\text{m}^2\,\text{s}^{-1}$, which corresponds very well with that measured in giant unilamellar vesicles (GUVs) for proteins of a similar intra-membrane diameter (Gambin et al., 2006).

The lateral diffusion of integral membrane proteins depends in part on the reciprocal of the radius of the intra-membrane portion of the protein (Gambin et al., 2006), and has been found to follow a Stokes-Einstein-like expression:

$$D_{lat} = \frac{k_B T \lambda}{4\pi \nu_m d_{\text{m}} R_{\text{tm}}} \tag{5.8}$$

where k_B is the Boltzmann constant, T is the absolute temperature, ν_m is the lipid bilayer viscosity in the liquid crystalline phase, d_{m} is the thickness of the lipid bilayer, R_{tm} is the radius of the embedded protein, and λ is a characteristic length that is introduced for dimensional reasons and relates to the extent of membrane perturbation induced by the diffusing object (Gambin et al., 2006). The diffusional properties of a protein can therefore give information about its aggregation state, and the agreement of the value determined here with literature values suggests that the diffusing SCCaFITs do indeed arise from single pores of α-Hemolysin. Equation 5.8 is based on experimental observations in GUVs and should thus be used with caution in the context of a supported bilayer. Diffusion in supported bilayers can be significantly attenuated by interactions of the diffusing species with the substrate (Sonnleitner et al., 1999). However, previous experiments carried out in this laboratory have shown that the attenuation due to the supporting agarose matrix is minimal (Thompson, 2009).

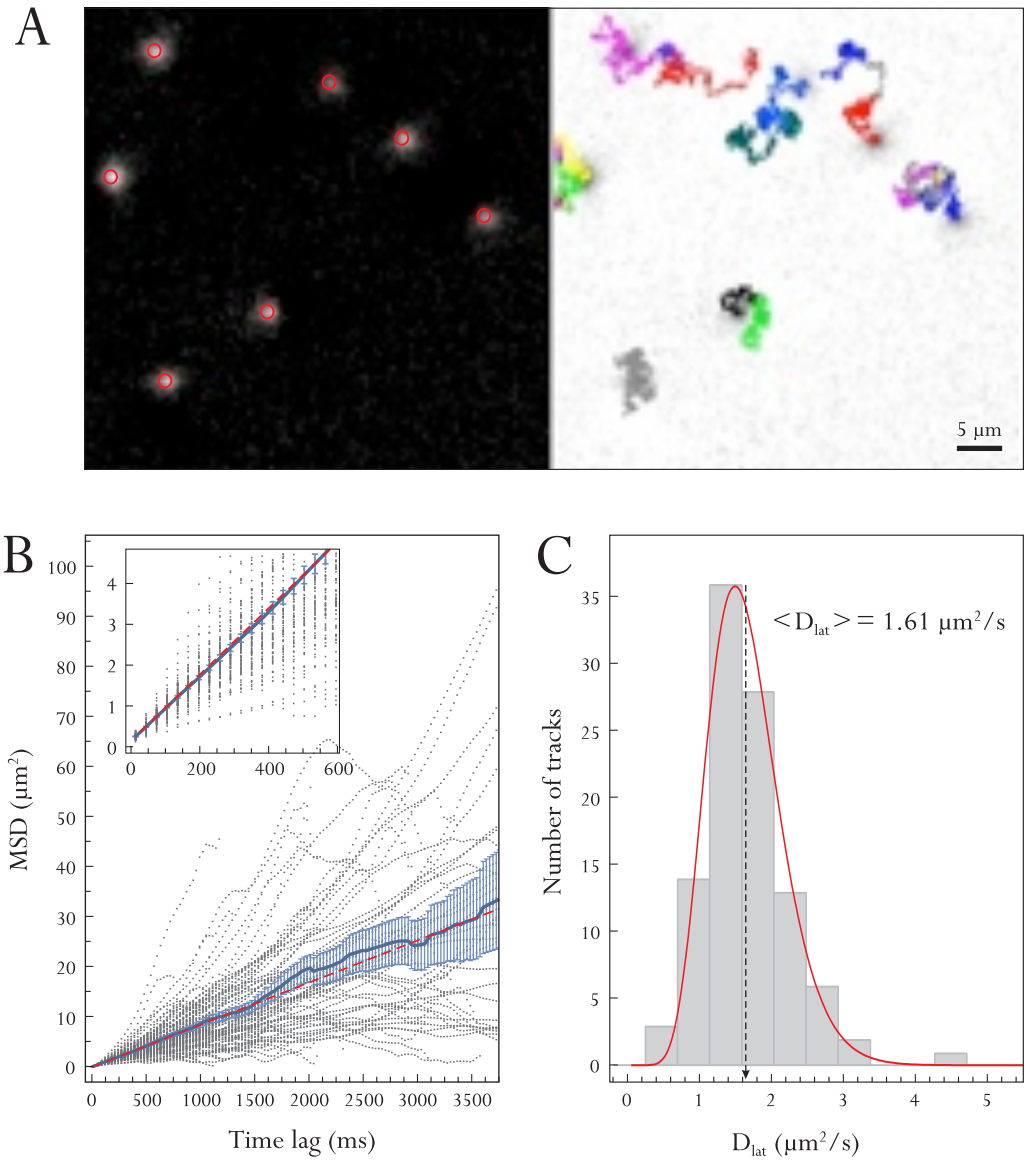

Figure 5.10: Single-particle tracking of α-Hemolysin in DIBs **(A)** SCCaFITs detected by the ETH Particle Detector and Tracker plugin in a background subtracted image (left). Particle trajectories longer than 30 frames are shown (right, image inverted) **(B)** Mean square displacements of tracked particles plotted against a series of time lags, Δt_n. Data from $n = 104$ individual tracks is shown (grey points). A linear fit to the average of the data (blue line), weighted by the standard deviation yields a lateral diffusion coefficient for the population of $D_{\text{lat}} = 1.62\ \mu\text{m}^2\,\text{s}^{-1}$. **(C)** Fitting a histogram of all individual trajectory lateral diffusion coefficients with the probability density function of a gamma distribution yields $D_{\text{lat}} = 1.61\ \mu\text{m}^2\,\text{s}^{-1}$.

5.5 Summary

The experiments described here primarily reproduce work carried out previously in this laboratory (Heron et al., 2009; Thompson, 2009; Thompson et al., 2007), and show that DIBs are suitable for fluorescence studies by TIRF microscopy. The work shown here introduces the caveat that care has to be taken that the bilayer is large enough to prevent any refraction of the excitation illumination into the droplet as a result of the differing refractive index of the interface outside of the region of the bilayer.

While agarose has proved to be a very useful substrate for maintaining bilayer fluidity, other methods of depositing a substrate of a defined thickness could be investigated. This could improve the reproducibility of the TIRF field and minimise the necessity of adjusting the angle of incidence in each experiment. Another possible way of addressing the problem of beam refraction outside the area of the bilayer could be the investigation of oils with a lower refractive index, or with different absorbance properties.

Optical patch clamping is a very useful method to localise unlabelled protein pores in the bilayer, at the same time providing evidence of a functional reconstitution of the pore into the membrane. It was shown that the fluorescence intensity of the calcium-sensitive dye Fluo-8 in the presence of the divalent cation-chelating agent EDTA and calcium only depends on the ratio of the concentrations of these two species, with maximal fluorescence below below a ratio of 1 and minimal fluorescence above a ratio of 2. By varying the concentration of EDTA in the droplet, the size of the SCCaFITs can thus be tuned. Optimal contrast is obtained when the inflection point in the intensity ($[EDTA]/[Ca^{2+}] = 1.5$) coincides with the maximal absolute concentration gradient of calcium around a membrane pore.

Bibliography

Axelrod, D., T. P. Burghardt, and N. L. Thompson (1984). Total internal reflection fluorescence. *Annu Rev Biophys Bioeng 13*, 247268.

Braha, O., B. Walker, S. Cheley, J. J. Kasianowicz, L. Song, J. E. Gouaux, and H. Bayley (1997). Designed protein pores as components for biosensors. *Chemical Biology 4*(7), 497–505.

Cheley, S., M. S. Malghani, L. Song, M. Hobaugh, J. E. Gouaux, J. Yang, and H. Bayley (1997). Spontaneous oligomerization of a staphylococcal α-hemolysin conformationally constrained by removal of residues that form the transmembrane β-barrel. *Protein Engineering 10*(12), 1433–1443.

Delano Scientific LLC (2008). *The PyMOL Molecular Graphics System (MacPyMOL)*. (now Schrödinger LLC).

Demuro, A. and I. Parker (2005). "Optical patch-clamping": single-channel recording by imaging Ca^{2+} flux through individual muscle acetylcholine receptor channels. *Journal of General Physiology 126*(3), 179–192.

Gambin, Y., R. Lopez-Esparza, M. Reffay, E. Sierecki, N. S. Gov, M. Genest, R. S. Hodges, and W. Urbach (2006). Lateral mobility of proteins in liquid membranes revisited. *Proceedings of the National Academy of Sciences of the United States of America 103*(7), 2098–2102.

Gouaux, E. (1998). alpha-Hemolysin from staphylococcus aureus: an archetype of beta-barrel, channel-forming toxins. *Journal of Structural Biology 121*(2), 110–122.

Heller, H. (1993). *Simulation einer Lipidmembran auf einem Parallelrechner*. Doctoral dissertation, Technical University of Munich, Germany.

Heller, H., M. Schaefer, and K. Schulten (1993). Molecular dynamics simulation of a bilayer of 200 lipids in the gel and in the liquid crystal phases. *Journal of Physical Chemistry 97*, 8343–8360.

Heron, A. J., J. R. Thompson, B. Cronin, H. Bayley, and M. I. Wallace (2009). Simultaneous measurement of ionic current and fluorescence from single protein pores. *Journal of the American Chemical Society 131*(5), 1652–1653.

Heron, A. J., J. R. Thompson, A. E. Mason, and M. I. Wallace (2007). Direct detection of membrane channels from gels using water-in-oil droplet bilayers. *Journal of the American Chemical Society 129*(51), 16042–16047.

Holden, M. A., D. Needham, and H. Bayley (2007). Functional bionetworks from nanoliter water droplets. *Journal of the American Chemical Society 129*(27), 8650–8655.

Menestrina, G. (1986). Ionic channels formed by Staphylococcus aureus alpha-toxin: Voltage-dependent inhibition by divalent and trivalent cations. *The Journal of Membrane Biology 90*(2), 177–190.

Normand, V., D. L. Lootens, E. Amici, K. P. Plucknett, and P. Aymard (2000). New insight into agarose gel mechanical properties. *Biomacromolecules 1*(4), 730–738.

Persistence of Vision Pty. Ltd. (2004). *Persistence of Vision™ Raytracer*. Persistence of Vision Pty. Ltd: Williamstown, Victoria, Australia.

Qian, H., M. P. Sheetz, and E. L. Elson (1991). Single particle tracking. analysis of diffusion and flow in two-dimensional systems. *Biophysical Journal 60*(4), 910–921.

Rard, J. A. and S. L. Clegg (1997). Critical evaluation of the thermodynamic properties of aqueous calcium chloride. 1. Osmotic and activity coefficients of 0-10.77 mol kg^{-1} aqueous calcium chloride solutions at 298.15 K and correlation with extended pitzer ion-interaction models. *Journal of Chemical & Engineering Data 42*(5), 819–849.

Rasband, W. S. (1997). ImageJ. http://rsb.info.nih.gov/ij/.

Saxton, M. J. (1997). Single-particle tracking: the distribution of diffusion coefficients. *Biophysical Journal 72*(4), 1744–1753.

Sbalzarini, I. and P. Koumoutsakos (2005). Feature point tracking and trajectory analysis for video imaging in cell biology. *Journal of Structural Biology 151*(2), 182–195.

Song, L., M. R. Hobaugh, C. Shustak, S. Cheley, H. Bayley, and J. E. Gouaux (1996). Structure of staphylococcal α-Hemolysin, a heptameric transmembrane pore. *Science 274*(5294), 1859–1865.

Sonnleitner, A., G. Schütz, and T. Schmidt (1999). Free Brownian motion of individual lipid molecules in biomembranes. *Biophysical Journal 77*(5), 2638–2642.

Thiessen, D. B. and A. J. Wilson (1987). An isopiestic method for measurement of electrolyte activity coefficients. *AIChE Journal 33*(11), 1926–1929.

Thompson, J. R. (2009). *Imaging the Assembly of the Staphylococcal Pore-Forming Toxin α-Hemolysin*. Doctoral thesis, University of Oxford.

Thompson, J. R., A. J. Heron, Y. Santoso, and M. I. Wallace (2007). Enhanced stability and fluidity in droplet on hydrogel bilayers for measuring membrane protein diffusion. *Nano Letters 7*(12), 3875–3878.

Tokunaga, M., N. Imamoto, and K. Sakata-Sogawa (2008). Highly inclined thin illumination enables clear single-molecule imaging in cells. *Nature Methods 5*(2), 159–161.

Zou, H., L. M. Lifshitz, R. A. Tuft, K. E. Fogarty, and J. J. Singer (1999). Imaging Ca^{2+} entering the cytoplasm through a single opening of a plasma membrane cation channel. *The Journal of General Physiology 114*(4), 575–588.

Zou, H., L. M. Lifshitz, R. A. Tuft, K. E. Fogarty, and J. J. Singer (2002). Visualization of Ca^{2+} entry through single stretch-activated cation channels. *Proceedings of the National Academy of Sciences of the United States of America 99*(9), 6404–6409.

Chapter 6

Corralling and 2D-Concentration of Membrane Proteins

This chapter demonstrates the dynamic control of the 2D concentration of a membrane protein reconstituted in a Droplet Interface Bilayer. A brief background of existing methods to directly manipulate membrane proteins is given, followed by a description of experiments that use the mechanical manipulation of a droplet with respect to the supporting hydrogel to control the size of the bilayer formed at the interface, effectively creating an adjustable 'corral' around transmembrane proteins diffusing in the membrane. The surface density of the β-barrel pore-forming toxin α-Hemolysin (α-HL) was modulated over a range of over three orders of magnitude within a timeframe of a few seconds. The concentration changes are fully reversible. Membrane protein function and diffusion are unaltered, as measured by total internal reflection fluorescence microscopy and single-channel electrical recording.

6.1 Introduction

An important goal in the development of model bilayer systems for the study of membrane proteins has been the ability to isolate the species under study from the

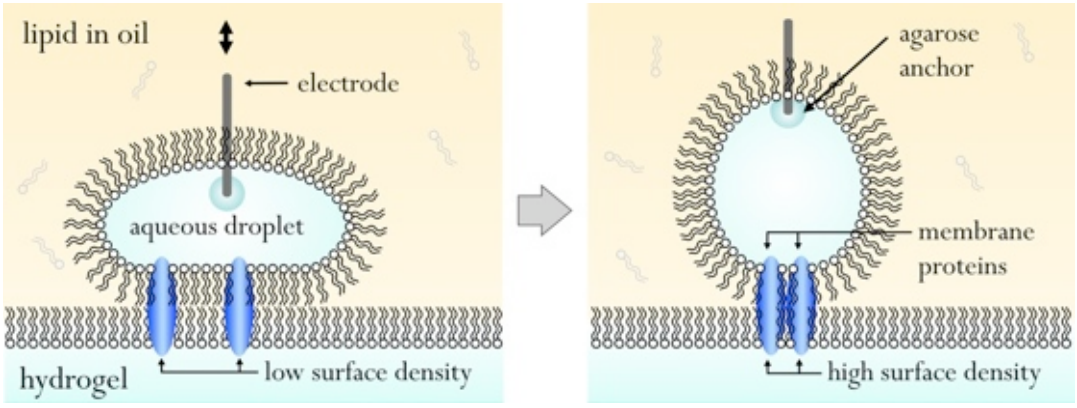

Figure 6.1: The principle of membrane protein corralling. An agarose 'anchor' on the electrode inserted into a droplet on a hydrogel surface ensures that the droplet does not easily release the electrode during manipulation. As a result, it is possible to deform the droplet by raising and lowering the electrode, resulting in changes in bilayer area. A contracting bilayer edge restricts the diffusion of transmembrane proteins present in the bilayer, resulting in their concentration. *Adapted with permission from Gross et al. (2011b). Copyright (2011) American Chemical Society.*

complex environment of the cell that can complicate the interpretation of experimental data, while at the same time providing a medium that mimics that of the biological membrane as accurately as possible. In cell membranes, proteins occupy ~ 35 % of the surface area, and recent theoretical considerations have suggested that this crowded environment experienced by membrane proteins has important implications for protein function (Zhou, 2009). These findings highlight that the very property of artificial systems that has enabled the gathering of unprecedented detail with techniques such as single molecule optical imaging and single-channel electrical recording - the ability to isolate proteins at low concentrations - detracts from the relevance of these model systems to the physiological environment experienced by a membrane protein. Methods to study the effect of membrane surface density on protein function are still few and far between, and often rely on macroscopic techniques such as co-sedimentation to quantify the membrane occupancy of protein in the systems studied. As already indicated in Chapter 2, DIBs are a promising model membrane system for the direct manipulation of integral membrane proteins. The experiments in this chapter show that DIBs can be used to control the surface density of functional integral membrane proteins, and demonstrate a 1500-fold increase in the surface density of the β-barrel pore forming toxin α-HL that is fully reversible. The control is provided

by the ability to modulate the DIB area. The bilayer edge thus acts as an adjustable 'corral' for diffusing transmembrane proteins. If the rate of bilayer area reduction is slower than the rate of protein diffusion, 2D protein concentration is controlled. If the rate of bilayer area reduction is greater than the rate of protein diffusion, proteins are concentrated in 1D at the bilayer edge. To assess the effect of corralling on the integrity of the membrane proteins, the lateral diffusion coefficients before and after corralling were measured by TIRF microscopy and SPT, showing that the mobility of the membrane proteins remains constant. The experiments also establish that the macroscopic current passing through a bilayer containing a number of protein pores remains constant throughout the mechanical manipulation, indicating that protein function is not perturbed.

6.2 Background

6.2.1 Macromolecular Crowding

The theoretical framework of the effects of a crowded medium on protein dynamics and function was originally developed in the context of the three-dimensional crowding of macromolecules present in the cytosol. Strictly, the term macromolecular crowding refers to the increase in the effective concentration of species in a given volume that is the result of a portion of that volume being taken up by other solutes and therefore being unavailable as diffusional volume. This is also referred to as the 'excluded volume effect' and requires the other solutes, generally referred to as 'crowders', to be inert with respect to the interactions under investigation. Methods of investigating the effects of membrane protein crowding have centred on theoretical analyses (Chatelier and Minton, 1996; Dell'Orco and Schmidt, 2008; Grasberger et al., 1986; Minton, 1999, 2000; Zuckermann and Heimburg, 2001) and the consequences of crowding remain a controversial topic (Dix and Verkman, 2008).

6.2.1.1 Membrane Crowding

As in the case of three-dimensional crowding, the mutual exclusion of the solid volume of membrane proteins as available diffusion space results in an increase in the chemical potential of each species in the membrane (Zhou, 2009). The term 'Membrane Crowding' thus refers to high densities of proteins present in biological membranes that alter kinetic and thermodynamic processes of individual species (Zhou, 2009). Such processes can include the partitioning of a single protein between the membrane and the solution, the relative concentrations of proteins existing in different membrane orientations or conformations with respect to the membrane plane, and the association of proteins into dimers and oligomers.

6.2.1.2 Traditional Experimental Approaches

To date, experimental approaches to elucidating the effects of the surface density of membrane-associated proteins on binding kinetics and function have consisted of

macroscopic titration of lipid vesicles into an aqueous peptide solution (Aisenbrey et al., 2008) or of co-sedimentation of proteins with lipid dispersions, liposomes or vesicles to quantify membrane occupancy (Aranovich et al., 2006; Heimburg and Marsh, 1995; Leventis and Silvius, 2010). Aisenbrey et al. have used titration of lipid vesicles into an aqueous peptide solution to consider the effects of 'self-crowding' (Zhou, 2009) on the model peptide LAH_4. Their experiments showed that membrane association characteristics, measured by circular dichroism and fluorescence, could not be described by a simple partitioning equilibrium. They concluded that high surface concentration of the peptide shifts the helical peptide from an in-planar into a transmembrane conformation. Aranovich et al. (2006) used a series of co-sedimentation experiments of the membrane-associated chromosomal replication initiation protein of *E. coli* (DnaA) with liposomes of varying compositions to quantify a range of protein-lipid ratios that they equated to membrane occupancies. They measured an inverse dependence of membrane-induced substrate dissociation kinetics on membrane occupancy in these samples and concluded that the protein surface density (crowding) acts as an inhibitor of DnaA activity. In a final example, Leventis and Silvius (2010) examined the binding of soluble *E. coli* dihydrofolate reductase to vesicles crowded with either grafted PEG chains or bilayer-anchored maltose binding protein (MBP) and found that affinity varies roughly exponentially with the surface density of anchored PEG or MBP. It is controversial whether a protein-lipid ratio determined by macroscopic titration or by co-sedimentation techniques can be equated to the membrane surface density of the protein under investigation. Moreover, as is exemplified by the examples detailed here, these studies have been limited to membrane-associated proteins, which is unsurprising given that the native functionality of integral transmembrane proteins in such dispersions is extremely difficult to verify.

6.2.1.3 Direct Manipulation of Membrane Components

Methods that enable the direct manipulation of membrane proteins in their native environment would eliminate many of these problems. Some progress has been made through the use of electric fields to control the positioning of charged membrane components (Ryan et al., 1988; Stelzle et al., 1992) or tethered charged vesicles (Yoshina-

Ishii and Boxer, 2003, 2006). Proteins tethered to membrane lipids have also been corralled into concentrated regions (Groves et al., 1996; Jönsson et al., 2010). Most recently, Cheetham et al. achieved a 30-fold increase in the local concentration of the tetraheme c-type cytochrome CymA using nested traps patterned into a supported lipid bilayer in an AC electric field (Cheetham et al., 2011). Other methods to enable sorting of membrane lipids and membrane-tethered or -associated proteins that add the capability to manipulate uncharged species include micropatterned substrates (Nabika et al., 2009) or the use of standing surface acoustic waves (Neumann et al., 2010). With the possible exception of the early experiments carried out by Ryan et al. (1988), who succeeded in demonstrating the asymmetric crowding of the immunoglobulin E receptor complex (IgER) on the cell surface by subjecting cells to an applied electric field, none of the techniques above have been yet been applied to integral transmembrane proteins.

6.3 Materials and Methods

6.3.1 Materials and Experimental Setup

All reagents were as described in Chapter 5. Unless otherwise indicated, the experimental setup and the buffer conditions for optical patch clamping were as described in section 5.3.3 and 5.3.4, respectively.

6.3.2 Protein Expression and Purification

α-HL heptamers were expressed as described in Chapter 5 and purified by FPLC (section 5.3.2), with the exception of the WT_7-H_6 α-HL heptamers that were used in the experiments shown in Figures 6.2, 6.5, 6.6 and 6.7, which were made by Oliver Castell, following the TALON purification protocol described in section 5.3.2.

6.4 Results and Discussion

6.4.1 The Conductance of α-HL During Bilayer Area Manipulation

A series of experiments was carried out to characterise the conductance of a population of pores in the bilayer while changing the bilayer area. The bilayer area was monitored using white light illumination as described in earlier chapters. Figure 6.2 A shows the bilayer edge, visible as a bright ring, during a manipulation of the electrode such that the diameter of the bilayer is controlled to between less than 1 % and 70 % of the droplet diameter. Under optimised lipid conditions (see Chapter 2), the bilayer area can be maintained at a particular size for an extended period (Figure 6.2 B).

The droplet shown in Figure 6.2, containing 165 nM of α-HL heptamer, was left to rest for 10 minutes before the start of the experiment to allow pore insertion to

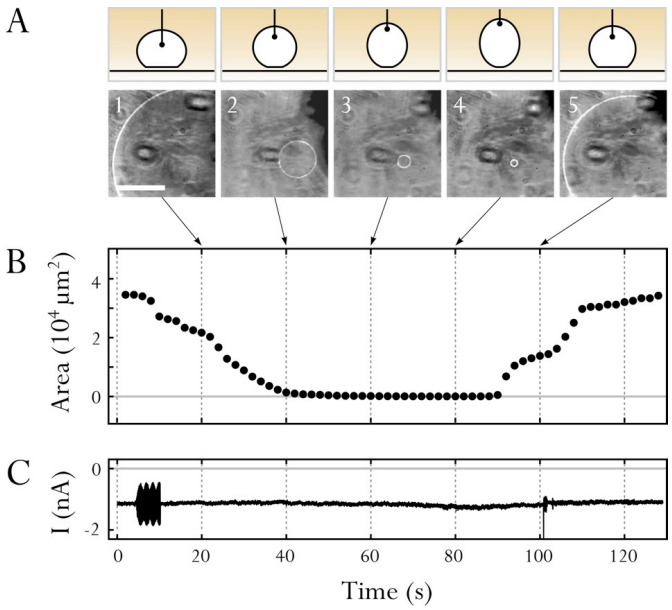

Figure 6.2: Direct control over bilayer area: (A) Top: Schematic illustration of droplet manipulation. Bottom: White light images of the bilayer during manipulation. The bilayer edge can be seen as a bright ring. Scale bar: 50 μm. **(B)** Variation in bilayer area. By careful manipulation of the electrode inserted into the droplet, a minimal bilayer area can be maintained for an extended period. The dotted lines correspond to the images in A. **(C)** The macroscopic electrical current across the bilayer of -1061 ± 80 pA at an applied voltage of -50 mV indicates that the number of functional pores in the bilayer remains constant during the manipulation, resulting in a 1500-fold increase in the surface density of functional α-HL. The large amplitude current oscillation at $t = 5$ s is electrical noise arising from a breach of the Faraday cage upon contact with the micromanipulator. It was removed by a small adjustment of the cage at $t = 10$ s. *Adapted with permission from Gross et al. (2011b). Copyright (2011) American Chemical Society.*

occur. Based on a pore conductance of 660 pS (Figure 6.7 A), the macroscopic current (Figure 6.2 C) is indicative of 32 ± 2 functional pores in the bilayer at the start of the experiment. The bilayer area at the start of the experiment was 34,500 μm^2. The series of images shows a controlled reduction of the area to 22.9 μm^2 at the smallest point, representing a size change factor of over 1500. The constant nature of the macroscopic current (Figure 6.2 C) shows that the number of pores inserted in the bilayer remains unchanged, and suggests that pore conductivity is not affected by the bilayer manipulation.

6.4.2 Fluorescence Imaging of Membrane Protein Corralling

To further investigate the effect of the manipulation of the bilayer size on protein pores diffusing in the membrane, functional α-Hemolysin pores were imaged by optical patch clamping, as described in Chapter 5. Figure 6.3 shows a series of images taken at intervals of ~5 s that illustrate the successive increase of the local surface density of α-HL SCCaFITs brought about by the contracting edge of the bilayer as the electrode is carefully raised. The first frame, showing a bilayer that was reduced in size to fit within the field of view of the emCCD camera (50 × 50 μm), was taken under the application of a positive potential of 50 mV and therefore there was minimal calcium flux into the droplet and no SCCaFITs can be discerned.

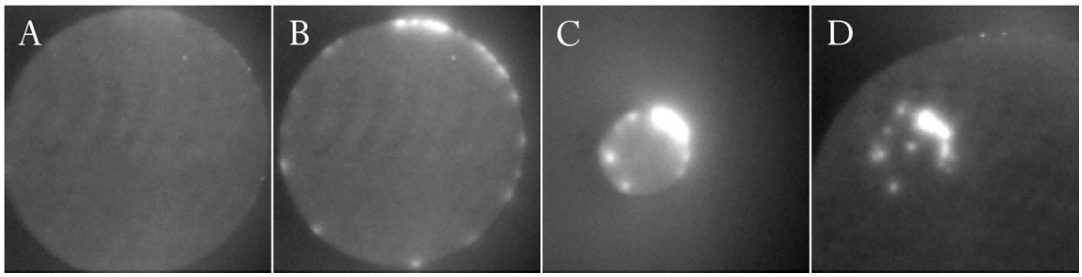

Figure 6.3: A series of images showing the successive increase in the local surface density of α-Hemolysin pores in a DIB upon the manipulation of bilayer area with an inserted electrode, as indicated by single-channel calcium fluorescence *in*transients (SCCaFITs). The droplet contained 40 nM WT_7-H_6 α-HL. **(A)** A large bilayer was first reduced to the size of the field of view of the emCCD under an applied potential of +50 mV to prevent influx of Ca^{2+}, thus maintaining a low background fluorescence. **(B)** Upon reversal of the potential, the location of α-HL pores, which have collected at the bilayer edge as a result of the size change, becomes apparent. **(C)** The diffusing pores are corralled by the edge of the bilayer to a central region of a diameter of 15 μm. **(D)** The subsequent enlargement of the bilayer allows the pores to diffuse apart. The field of view measures 50 × 50 μm.

Upon a reversal of the potential in the second frame, SCCaFITs that have collected at the bilayer edge during the size change appear. A further reduction in size demonstrates the corralling of the pores in a central region of the bilayer of ~15 μm diameter. Upon subsequent enlargement of the bilayer, the pores begin to diffuse apart. Figure 6.4 shows a composite image of a large bilayer with a greater starting density of pores. After reducing and enlarging the bilayer size, the majority of the SCCaFITs are concentrated in the centre of the bilayer. Pores in the outer region of the bilayer have either diffused away from the centre, are new spontaneous insertions from residual protein in solution, or have been pulled outwards by the receding edge of the bilayer upon bilayer enlargement.

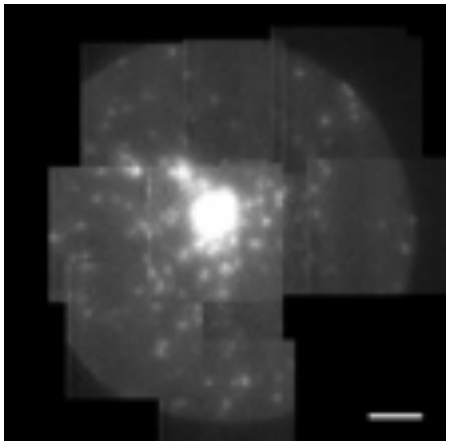

Figure 6.4: Composite bilayer image after corralling. The droplet contained standard optical patch clamping buffers and 250 nM of WT_7-H_6 α-HL. Applied potential: −50 mV. Scale bar: 20 μm.

Figure 6.5 highlights that although a large increase in fluorescence is observed, which is correlated with the change in bilayer area, the increase exceeds that expected from the combined calcium flux of the corralled pores. The actual fluorescence intensity for the area highlighted by the arrow in Figure 6.5 A, Image 1, is plotted in Figure 6.5. The dramatic increase in fluorescence observed when the bilayer is small is due to refraction of the excitation illumination into the droplet that can occur at the edge of the bilayer, as already noted in Chapter 5. The fluorescence intensity was therefore rejected as a reliable measure of α-HL concentration for small bilayers. However, the fluorescence intensity when the bilayer is returned to its original

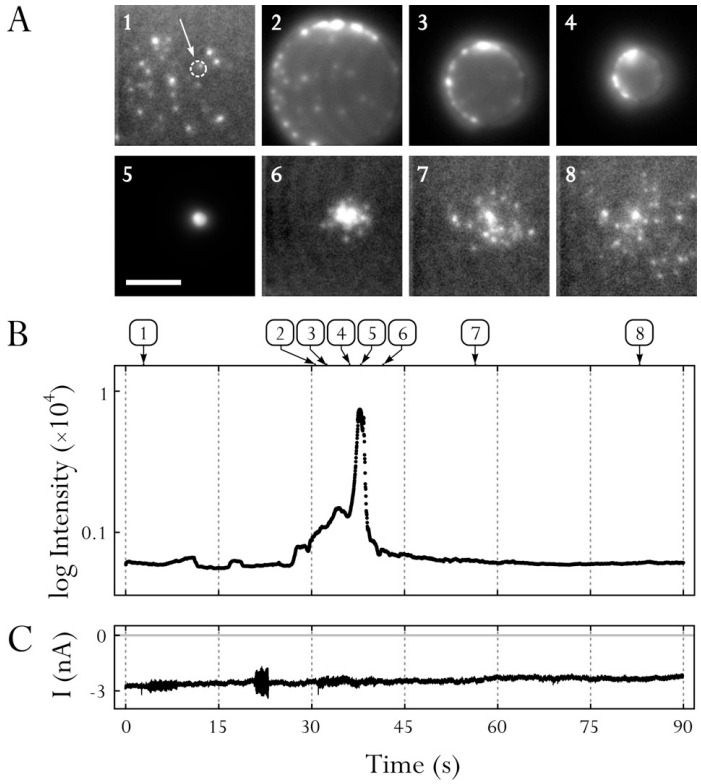

Figure 6.5: Imaging the manipulation of the surface density of α-HL pores. **(A)** Fluorescence intensity arising from Ca^{2+} flux through functional α-HL pores during droplet manipulation. Each image is normalised to facilitate viewing. Scale bar: 20 μm. **(B)** Plot of absolute fluorescence intensity within the circular area highlighted by the white arrow in image A1. The numeric labels correspond to the images in A. **(C)** The macroscopic current across the bilayer over the entire experiment is constant at -2443 ± 159 pA at an applied voltage of -100 mV, indicating that the pores remain functional throughout. *Adapted with permission from Gross et al. (2011b). Copyright (2011) American Chemical Society.*

size also returns to the level before the experiment, indicating that the surface density change is reversible. As in the white light experiment, the trace in Figure 6.5 C confirms that pores are not being disturbed significantly during the manipulation as the current remains roughly constant throughout. Based on a pore conductance of 660 pS (see Figure 6.7 A), the total current of -2443 ± 159 pA indicates the presence of 37 ± 2 functional pores. The smallest bilayer size was 11.8 μm^2, giving a maximal surface density of 3.13 ± 0.2 pores/μm^2. This translates to a protein-lipid ratio of 1 in 2.5×10^6 and represents an area fraction of proteins in the membrane of 0.025 %. Data from further experiments are shown in 6.1.

6.4.3 2D Concentration is Reversible

The reversibility of the 2D concentration was characterised by using single-particle tracking (SPT), as described in Chapter 5, to prove that the number of functional pores in the bilayer before and after the manipulation remains constant. Figure 6.6 A shows a series of frames from the same dataset as that in Figure 6.5, highlighting the pores detected by the algorithm. It should be noted that here again, the images are normalised to facilitate viewing, which means that as the central area becomes very bright, single pores in dark regions may not be discernible. The bilayer size as measured from the images is plotted in Figure 6.6 B. Due to the limits of detection of the algorithm, fewer pores are detected as the bilayer reduces in size and fluorescent spots begin to overlap. Figure 6.6 C shows that after the manipulation, the number of particles detected within the frame of the image returns to the level at the start of the experiment. This indicates that proteins do not associate permanently and are able to diffuse apart once the bilayer is enlarged. Upon the increase of the bilayer size, the number of spots detected recovers at a slower rate than the area increase, highlighting that the proteins are not pulled apart by the action of increasing the size of the bilayer, but rather diffuse apart slowly. In addition, the reappearance of diffusing spots shows that the pores remain intact during the bilayer manipulation. To characterise any effect on the inserted protein pores further, the lateral diffusion of manipulated α-HL was measured before and after corralling. Lateral diffusion coefficients were calculated from the averaged MSD of the proteins plotted against a given time interval, Δt_n. The average MSD vs. Δt_n for all tracks were fitted with a linear function weighted by the standard deviation calculated for each time-lag (Qian et al., 1991; Saxton, 1997). Data was fitted over all track-lengths (maximum: 120 s). Figure 6.7 B shows time lags up to 180 ms to highlight the constant nature of the diffusion coefficient. The D_{lat} value for α-Hemolysin before corralling ($D_{\text{lat}} = 1.47 \pm 0.09\ \mu\text{m}^2\ \text{s}^{-1}$) is comparable to that of the protein after corralling ($D_{\text{lat}} = 1.56 \pm 0.18\ \mu\text{m}^2\ \text{s}^{-1}$). The expected behaviour of the optical patch-clamp fluorescence signal upon a reversal of the applied voltage is reproducible after the manipulation has taken place, indicating that all fluorescence arises from Ca^{2+} flux through functional α-HL pores. 6.7 C

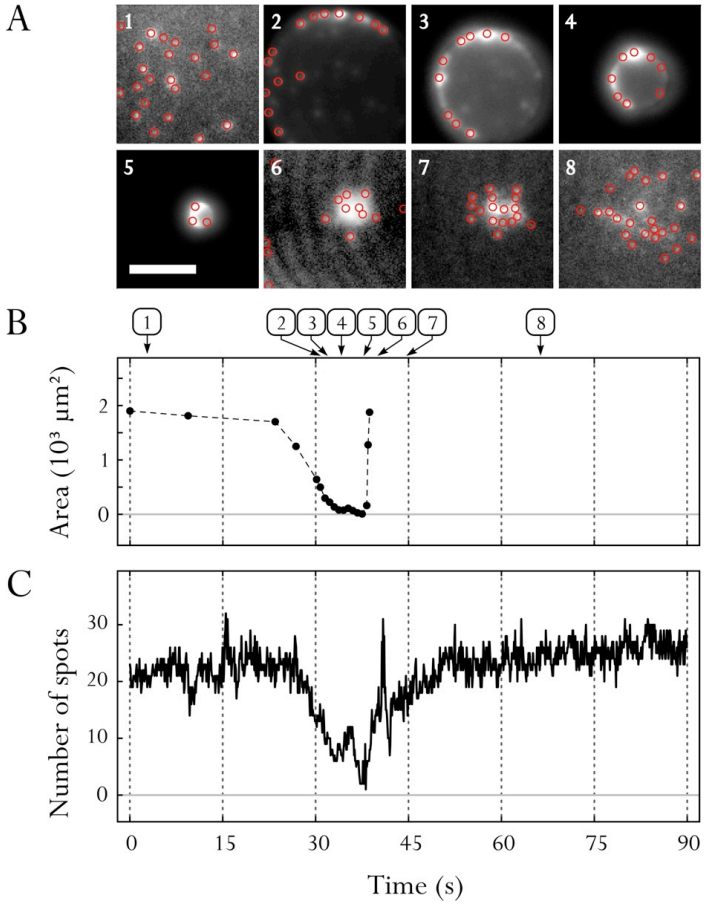

Figure 6.6: Reversible control over α-Hemolysin surface density. A Fluorescence intensity arising from Ca^{2+} flux through functional α-HL pores during the droplet manipulation. Images are normalised to facilitate viewing. Fluorescence spots identified by the single-particle tracking algorithm are highlighted with a bright circle. Scale bar: 20 μm. **(B)** Bilayer area vs. time. At $t > 40$ s, the bilayer edge is outside the field of view and hence can no longer be reported. The numeric labels correspond to the images in A. **(C)** Number of fluorescence peaks identified by the tracking algorithm. As the surface density increases, overlap of fluorescent spots results in a decrease in the number of spots detected. The spike at $t = 40$ s derives from false positives that arise as the edge of the bilayer temporarily causes fringes in the TIRF field during the manipulation (image A6). *Adapted with permission from Gross et al. (2011b). Copyright (2011) American Chemical Society.*

Table 6.1: Changes in Pore Surface Density

Number of pores[a] *(total)*	Largest bilayer [b] *(μm^2)*	Smallest bilayer [b] *(μm^2)*	maximal surface density *(pores/μm^2)*	surface density reduction factor *(multiple)*
37 ± 2	22168	11.8	3.1 ± 0.20	1878-fold
32 ± 2	34500	22.9	1.4 ± 0.11	1506-fold
143 ± 3	39804	32.5	4.4 ± 0.10	1224-fold
49 ± 6	22168	19.2	2.6 ± 0.31	1154-fold
36 ± 4	33505 [c]	116.7	2.2 ± 0.03	287-fold
297 ± 4	38329 [c]	196.2	1.5 ± 0.02	195-fold

[a] derived from macroscopic current across bilayer, assumes pore conductance of 660 pS
[b] mean of 10 replicate measurements of images of bilayer area, S.E. <0.5 %
[c] bilayer edge outside imaging frame, area derived from number of pores diffusing within image frame assuming uniform distribution before the start of manipulation.

illustrates the expected disappearance of any fluorescent signal above the background upon a reversal of the applied voltage (images 1, 2 and 3). The same behaviour is observed after the manipulation (images 4, 5 and 6), which shows that all measured fluorescence arises from calcium flux into the droplet.

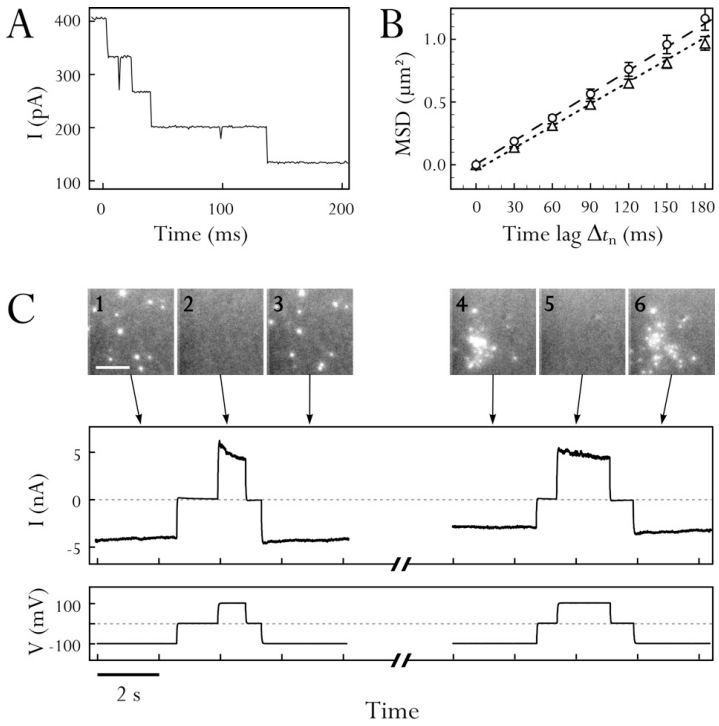

Figure 6.7: **(A)** α-HL, conductance. Single-channel electrical recording of α-HL, heptamers in a DIB at an applied voltage of 100 mV. **(B)** Mean MSD versus time-lag. α-HL before corralling (open triangles) with corresponding weighted linear fit (dotted line), show a coefficient of $D_{\text{lat}} = 1.47 \pm 0.09\ \mu\text{m}^2\ \text{s}^{-1}$. α-HL after corralling (open circles) with corresponding weighted linear fit (dashed line), diffuses with $D_{\text{lat}} = 1.56 \pm 0.18\ \mu\text{m}^2\ \text{s}^{-1}$. Error bars show the standard error of the mean for the averaged data. **(C)** Effect of reversal of the applied potential on fluorescence intensity. The expected disappearance of a fluorescence signal upon a reversal of the applied potential occurs both pre-manipulation (images 1-3) and post-manipulation (images 4-6), showing that all fluorescence arises from Ca^{2+} ion flux. Scale bar: 20 μm. *Adapted with permission from Gross et al. (2011b). Copyright (2011) American Chemical Society.*

6.5 Discussion

As noted above, the quantification of surface density on the basis of fluorescence intensity is complicated by the occurrence of refraction of the excitation light into the droplet when the bilayer area is small. As discussed in Chapter 5, this effect occurs due to imperfect total internal reflection and a secondary refraction of any direct illumination at the oil/water interface at the side of the droplet. As a result, the primary means of quantifying surface density in the experiments described is by bilayer conductance per area. However, fluorescence intensity could still be of interest as a means of quantifying pore concentration in two special cases where illumination remains relatively uniform. Firstly, in the case of a region of previously corralled pores diffusing apart within a large bilayer (see Figure 6.4), and secondly, when pores are concentrated by using the edge of a large bilayer distal to the incident beam to 'sweep' diffusing pores together. Figure 6.8 illustrates that the problem of refraction is absent in this configuration and that it may therefore be possible to quantify pore density during the manipulation using fluorescence intensity. The data shown in Figure 6.8 A is from the same dataset as that showing the concentration of 37 pores in a bilayer in Figure 6.5. The manipulation of those pores using the bilayer edge, shown in Figure 6.8 B, was carried out in the same droplet shortly afterwards. Under the assumption of 37 SCCaFITs present in this droplet (see Table 6.1, first line), a preliminary analysis of the total image intensities during these two manipulations (Figure 6.8 C and D respectively) gives an approximate intensity per SCCaFIT of 39485 ± 43791 a.u. during the first and 3756 ± 913 a.u. during the second of the respective manipulations. While the error in the first value proves that variations in the excitation illumination are too large to attempt any quantification of SCCaFIT by means of intensity, the second value compares well to that determined for individual SCCaFIT in the same stack of 2226 ± 484 a.u. ($n = 5$). However, even in a hypothetical situation of uniform and constant excitation illumination, it is important to be aware of the fact that a linear relationship between fluorescence intensity and the number of pores should not be expected to hold over a large range of protein surface density. There are a variety of factors that play a role in the observed intensity

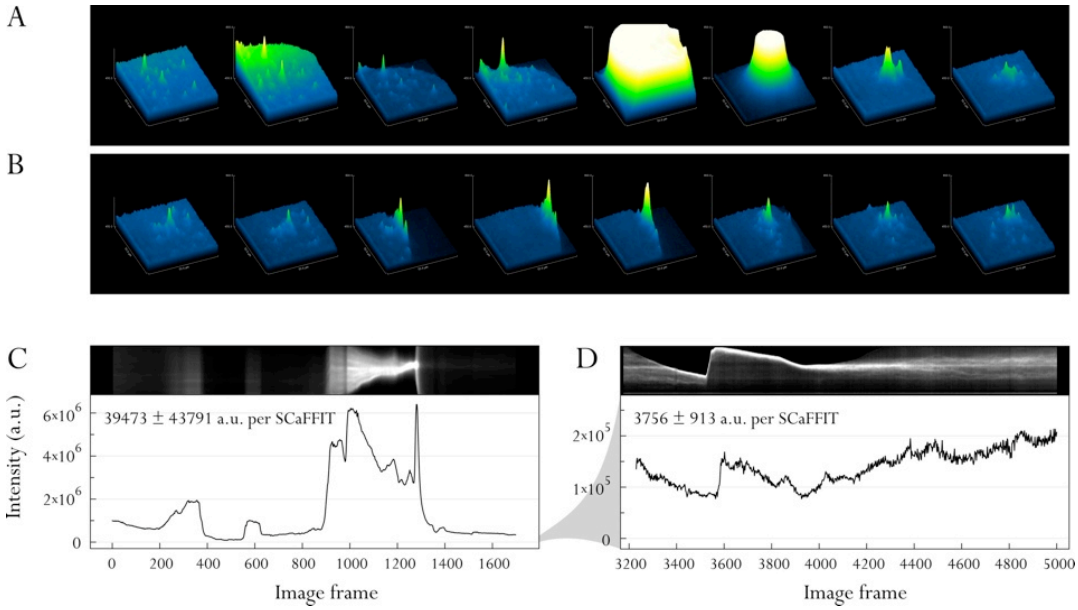

Figure 6.8: Differences in excitation light refraction into the droplet. **(A)** The modulation of pore surface density by reducing bilayer area results in increased refraction of incident illumination into the droplet. Fluorescence intensity is not directly proportional to the number of overlapping SCCaFITs. **(B)** It appears that the problem of refraction into the droplet can be sufficiently minimised by concentrating SCCaFITs with the edge of the bilayer that is distal to the incident light. Patch size shown measures 50 μm^2. **(C)** Background subtracted and summed image intensity during the manipulation shown in A. **(D)** Background subtracted and summed image intensity during the manipulation shown in A.

of a SCCaFIT, including the relative local concentrations of EDTA and calcium, which depend on the rate of flux of calcium through the protein pores; the absolute concentration of Fluo-8; and the relative rates of diffusion and photobleaching of Fluo-8, a ratio which affects both the size and the brightness of the SCCaFIT. In the conditions studied here, it appears that the intensity of a small number of overlapping SCCaFITs is indeed additive, as illustrated by the data in Figure 6.9 A. However, the maximal fluorescence in a given local volume in the droplet is limited by the availability of Fluo-8, and therefore the intensity would be expected to saturate at a high local density of pores. Indeed, in experiments where calcium flux through a large number of pores is permitted to occur for periods longer than around 5 minutes, the proportion of fluorescing Fluo-8 in the droplet is significant. Corralling of pores and subsequent enlargement of the bilayer under these conditions results in a plateau region of uniform fluorescence intensity that is significantly larger than the area of the minimal bilayer area, i.e. than the region where the pores would be expected to be localised immediately after minimising the size of the bilayer. Diffusion of pores within this region cannot be discerned until the pores have diffused apart by a substantial distance. An example of this effect is shown in Figure 6.9 C.

In the experiments detailed in this chapter, the surface density of pores is estimated on the basis of the bilayer conductance, under the assumption that pore

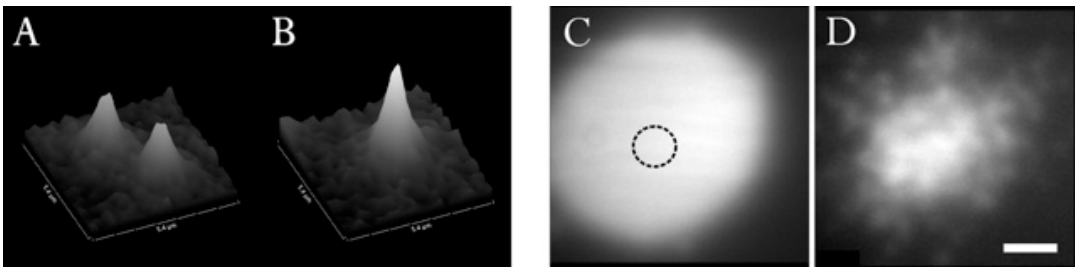

Figure 6.9: The effect of SCCaFIT overlap **(A-B)** Fluorescence intensity of two SCCaFITs diffusing in proximity to one another and overlapping. The patch size shown measures 5.4 μm^2. **(C)** Saturation of available Fluo-8 immediately after corralling of a large number of pores is characterised by a plateau region of fluorescence intensity. This occurs where large numbers of SCCaFIT have been concentrated into a small region and calcium flux into a droplet has persisted for longer than ~5 minutes. The black dashed line indicates the minimum size of the bilayer immediately (<1 s) before this image was taken. **(D)** Image taken 5 s after C. **(C,D)** Standard optical patch clamping conditions were used. The bilayer is larger than the field of view, ensuring that there is no refraction of the excitation light into the droplet. Concentration of α-HL heptamer in the droplet: 250 nM. Scale bar: 10 μm

conductance is independent of protein surface density. In the case of a rigid protein pore such as α-Hemolysin, it is possible that this assumption may be justified. However, a method of determining the surface density of membrane proteins by alternative means is desirable. When investigating the effect of membrane protein crowding on other membrane proteins, conductivity could be a prime readout parameter to detect changes in protein conformation or function. The advantage of optical patch clamping is that pore functionality is immediately established. However, due to the limitations discussed above, it is possible that single-molecule fluorescence of labelled proteins could prove to be a more useful method of surface density quantification, providing that the problem of eliminating any fluorescence not arising from a functional pore can be overcome.

6.6 Summary

From a detailed investigation of the literature, this appears to be the first time that the 2D concentration of a functional integral membrane protein has been controlled in an artificial bilayer system. However, the method is not without its limitations: firstly, the magnitude of the change in surface density is limited by the size of the bilayer at the start of the experiment. This parameter can be modified either by working with larger droplets, or by deforming the droplet at the start of the experiment. Here, droplets of approximately 50 nL volume were used, as small bilayers reduce noise in the electrical recording. The second limitation is the maximally achievable absolute surface density within the bilayer upon minimising the bilayer area. This is determined by the starting density of integral membrane pores. In these experiments the number of pores was limited by the desire to retain both the ability to image individual pores using optical patch clamping, and to work at macroscopic currents within the range of our patch clamp amplifier. With further refinement of the method for the quantification of surface density, much larger starting concentrations of protein could be used. As a rule, crowding effects are thought to come into play when the ratio of lipid to protein molecules is around 100 or less (Zhou, 2009). The maximal concentration described here is several orders of magnitude smaller. However, unlabelled membrane protein could be used as an inert 'crowder' for the membrane protein under investigation, increasing the attainable degree of crowding in this system. In the data presented, the surface density of membrane protein was estimated from the macroscopic current across the bilayer, and the bilayer area as measured by fluorescence or white light imaging. This approach is convenient in the case of a robust protein such as α-HL, where a modulation of pore conductance by the limited degree of crowding achieved here would not be expected, and where the aim of the experiment was the demonstration of the ability to control surface density. In future investigations, however, it is likely that the electrical conductance will be a key parameter for measuring the effects of crowding on membrane proteins. It is therefore desirable not only to refine the quantification of surface density, but also to enable the determination of surface density exclusively by fluorescence. While optical

patch clamping is a useful method to localise calcium-conducting pores and establish their functionality, direct single-molecule fluorescence imaging of a fluorescently tagged protein could be a more suitable method for the investigation of membrane proteins at high surface density.

It is important to bear in mind that the reported maximal surface density was calculated as an average across the bilayer area at its smallest. In these experiments, the concentration at the edge of the bilayer where the pores are collected as the bilayer reduces in size is likely to be much higher. The reported maximal value is representative of the actual 2D concentration of the protein only once proteins that collect at the edge of the bilayer during the manipulation have diffused away from the edge and redistributed across the now more limited bilayer area available. As shown in Figure 6.2, the bilayer can be maintained at a particular size for a sufficiently long time for this redistribution to occur. Alternatively, the manipulation can be carried out at a rate slow enough to allow for continuous redistribution, giving complete control over 2D concentration.

The results presented here show that the manipulation of DIB area enables the direct control over the surface density of protein pores diffusing in the lipid bilayer. Contrary to electrophoretic approaches to the manipulation of membrane components, which have so far achieved the two-dimensional concentration of lipids (Stelzle et al., 1992), membrane-associated proteins and tethered vesicles (Yoshina-Ishii and Boxer, 2003, 2006), surface density control using DIBs is capable of concentrating transmembrane components, and is effective in the case of both charged and uncharged species. The experiments described here were carried out in a simple model system consisting of α-HL in synthetic DPhPC bilayers. However, DIBs can be created with a variety of physiological lipids in both symmetric and asymmetric configurations (Hwang et al., 2008), and a wide variety of other membrane proteins such as ion channels and pore-forming peptides can be observed (Bayley et al., 2008; Heron et al., 2009). With further improvements to the achievable range of concentrations, DIBs could be used not only to study binding equilibria and kinetics of lateral interactions for a variety of integral membrane proteins, but perhaps also to achieve two-dimensional crystallisation of such proteins.

Bibliography

Aisenbrey, C., B. Bechinger, and G. Gröbner (2008). Macromolecular crowding at membrane interfaces: Adsorption and alignment of membrane peptides. *Journal of Molecular Biology 375*(2), 376–385.

Aranovich, A., G. Y. Gdalevsky, R. Cohen-Luria, I. Fishov, and A. H. Parola (2006). Membrane-catalyzed nucleotide exchange on DnaA. *Journal of Biological Chemistry 281*(18), 12526–12534.

Bayley, H., B. Cronin, A. Heron, M. A. Holden, W. L. Hwang, R. Syeda, J. Thompson, and M. Wallace (2008). Droplet Interface Bilayers. *Molecular BioSystems 4*(12), 1191.

Chatelier, R. and A. Minton (1996). Adsorption of globular proteins on locally planar surfaces: models for the effect of excluded surface area and aggregation of adsorbed protein on adsorption equilibria. *Biophysical Journal 71*(5), 2367–2374.

Cheetham, M. R., J. P. Bramble, D. G. G. McMillan, L. Krzeminski, X. Han, B. R. G. Johnson, R. J. Bushby, P. D. Olmsted, L. J. C. Jeuken, S. J. Marritt, J. N. Butt, and S. D. Evans (2011). Concentrating membrane proteins using asymmetric traps and AC electric fields. *Journal of the American Chemical Society 133*(17), 6521–6524.

Dell'Orco, D. and H. Schmidt (2008). Mesoscopic monte carlo simulations of stochastic encounters between photoactivated rhodopsin and transducin in disc membranes. *The Journal of Physical Chemistry B 112*(14), 4419–4426.

Dix, J. A. and A. Verkman (2008). Crowding effects on diffusion in solutions and cells. *Annual Review of Biophysics 37*(1), 247–263.

Grasberger, B., A. P. Minton, C. DeLisi, and H. Metzger (1986). Interaction between proteins localized in membranes. *Proceedings of the National Academy of Sciences of the United States of America 83*(17), 6258–6262.

Gross, L. C. M., O. K. Castell, and M. I. Wallace (2011b). Dynamic and reversible control of 2D membrane protein concentration in a droplet interface bilayer. *Nano Letters 11*, 3324–3328.

Groves, J., C. Wülfing, and S. Boxer (1996). Electrical manipulation of glycan-phosphatidyl inositol-tethered proteins in planar supported bilayers. *Biophysical Journal 71*(5), 2716–2723.

Heimburg, T. and D. Marsh (1995). Protein surface-distribution and protein-protein interactions in the binding of peripheral proteins to charged lipid membranes. *Biophysical Journal 68*(2), 536–546.

Heron, A. J., J. R. Thompson, B. Cronin, H. Bayley, and M. I. Wallace (2009). Simultaneous measurement of ionic current and fluorescence from single protein pores. *Journal of the American Chemical Society 131*(5), 1652–1653.

Hwang, W. L., M. Chen, B. Cronin, M. A. Holden, and H. Bayley (2008). Asymmetric droplet interface bilayers. *Journal of the American Chemical Society 130*(18), 5878–5879.

Jönsson, P., A. Gunnarsson, and F. Höök (2010). Accumulation and separation of membrane-bound proteins using hydrodynamic forces. *Analytical Chemistry 83*(2), 604–611.

Leventis, R. and J. R. Silvius (2010). Quantitative experimental assessment of macromolecular crowding effects at membrane surfaces. *Biophysical Journal 99*(7), 2125–2133.

Minton, A. P. (1999). Adsorption of globular proteins on locally planar surfaces. II. models

for the effect of multiple adsorbate conformations on adsorption equilibria and kinetics. *Biophysical Journal 76*(1), 176–187.

Minton, A. P. (2000). Effects of excluded surface area and adsorbate clustering on surface adsorption of proteins: I. equilibrium models. *Biophysical Chemistry 86*(2-3), 239–247.

Nabika, H., N. Iijima, B. Takimoto, K. Ueno, H. Misawa, and K. Murakoshi (2009). Segregation of molecules in lipid bilayer spreading through metal nanogates. *Analytical Chemistry 81*(2), 699–704.

Neumann, J., M. Hennig, A. Wixforth, S. Manus, J. O. Rädler, and M. F. Schneider (2010). Transport, separation, and accumulation of proteins on supported lipid bilayers. *Nano Letters 10*(8), 2903–2908.

Qian, H., M. P. Sheetz, and E. L. Elson (1991). Single particle tracking. analysis of diffusion and flow in two-dimensional systems. *Biophysical Journal 60*(4), 910–921.

Ryan, T. A., J. Myers, D. Holowka, B. Baird, and W. W. Webb (1988). Molecular crowding on the cell surface. *Science 239*(4835), 61–64.

Saxton, M. J. (1997). Single-particle tracking: the distribution of diffusion coefficients. *Biophysical Journal 72*(4), 1744–1753.

Stelzle, M., R. Miehlich, and E. Sackmann (1992). Two-dimensional microelectrophoresis in supported lipid bilayers. *Biophysical Journal 63*(5), 1346–1354.

Yoshina-Ishii, C. and S. G. Boxer (2003). Arrays of mobile tethered vesicles on supported lipid bilayers. *Journal of the American Chemical Society 125*(13), 3696–3697.

Yoshina-Ishii, C. and S. G. Boxer (2006). Controlling two-dimensional tethered vesicle motion using an electric field: Interplay of electrophoresis and electro-osmosis. *Langmuir 22*(5), 2384–2391.

Zhou, H. (2009). Crowding effects of membrane proteins. *The Journal of Physical Chemistry B 113*(23), 7995–8005.

Zuckermann, M. J. and T. Heimburg (2001). Insertion and pore formation driven by adsorption of proteins onto lipid bilayer Membrane-Water interfaces. *Biophysical Journal 81*(5), 2458–2472.

Chapter 7

Conclusions and Outlook

As anyone working in interdisciplinary science knows, the combination of expertise from different realms of science tends to bring with it a wealth of opportunities. Laboratory techniques have to keep pace with this trend, and DIBs are a node at the interface between surface science, electrophysiology, lipid bilayer mechanics, force spectroscopy, and single molecule microscopy. We are only at the very beginning of exploiting their potential.

A better understanding of the process of lipid self assembly at the oil-water interfaces has to be one goal of further work to improve the reproducibility of stable DIBs in a wide range of experimental conditions. As the images in Figure 2.7 B have highlighted, the assumption of the existence of a pure monolayer of lipid encasing the droplet is a naïve one. It is most likely that multilamellar structures or cubic phase regions develop at the interface. Indeed, for the case of lecithin, the spontaneous growth of structures from a small aqueous phase into a surrounding alkane has been observed (Shchipunov and Schmiedel, 1996). It would be interesting to investigate the region at the edge of the bilayer further by other means, such as by cross-polarised or DIC microscopy, by incorporating fluorescent lipids, or even by freeze-fracture cryo-electron microscopy.

An intriguing effect is the change of bilayer area with an applied potential. The area change is relatively small for applied voltages of $< |100|$ mV. It is interesting that a very similar system to DIBs has been developed independently elsewhere (Guha et al., 2011) in efforts to create electrowetting on dielectric (EWOD) devices for the

actuation of aqueous volumes in microfluidic applications. Up to now, electrowetting systems have necessitated thick dielectric layers and actuation voltages typically exceeding 10 V (Mugele and Baret, 2005), but Guha et al. (2011) report large contact angle changes voltages < 1 V. This is due to the low surface tension of the oil-water interface in the presence of lipid.

Since the surface tension of the oil-water interface can be calculated by fitting the Lippmann equation to contact angle data, it is possible that DIBs represent a new method of measuring the surface tension of the oil-water interface in the presence of lipid. This quantity is difficult to determine, and existing methods require the determination of film area, which can lead to large errors. At present, the calculation employed here assumes that the specific capacitance of the dielectric is independent of the applied voltage. As was shown in Chapter 4, this is not necessarily the case where a compressible bilayer plays the role of the dielectric material, and further work will be necessary to determine the error of this effect on the surface tension measurement. Alternatively, the Lippmann-Equation will have to be modified to account for this effect.

Preliminary investigations of other means of manipulating bilayer area in this work show some promising results. The ability to induce membrane curvature by the simple means of incorporating beads into the substrate paves the way to the use of single-channel recording for the characterisation of the response of membrane channels to strain in the bilayer. As indicated in Chapter 5, total internal reflection microscopy is an effective method for the characterisation of membrane proteins reconstituted in DIBs. However, the Sephadex beads incorporated here are too large and would raise the bilayer beyond the reach of the evanescent field. An interesting development would be to create patterned substrates on a smaller scale, for example by the deposition of nanoparticles, guided self-assembly of polymers of different lengths, or nanolithography of a suitable substrate (Jung et al., 2011; Lee et al., 2009; Pum and Sleytr, 1999). The latter two are likely to represent a better approach, as nanoparticles and small beads have been shown to integrate into bilayers in a size-dependent manner, with the lipid membrane 'flowing' around the particle rather than curving over it (Jing and Zhu, 2011; Roiter et al., 2008, 2009).

The future potential of the optical tweezing of droplets that has been achieved here may appear to be limited by lack of electrical access to the droplet. However, if combined fluorescence microscopy and optical trapping can be implemented, optical patch clamping could, in theory, yield much the same information (Heron et al., 2009). Contrary to the current DIB setup, however, such a system would not be limited to a single droplet, but could enable the parallel investigation of multiple aqueous volumes, which could also be fused with one another or connected and disconnected to form dynamic droplet networks (Bayley et al., 2008).

The experiments on specific capacitance have perhaps the most immediate impact on studies of membrane proteins in DIBs, if not in artificial bilayers in general. In particular, the findings that bilayer thickness changes in response to an applied potential, and that bilayers formed from the common mixture of POPE:POPG are highly variable, highlight that extreme care must be taken when attempting to interpret results of membrane protein functional studies in these systems. DIBs will be invaluable in the development of systems that either minimise such effects, or are able to monitor them with high precision.

Finally, the ability to concentrate membrane proteins has been demonstrated. Further work in this area can begin to investigate the effect of membrane crowding on processes such as, for example, oligomerisation. This would be particularly interesting – and accessible – in simple systems with unknown stoichiometry, such as many types of antimicrobial peptides. As for more challenging systems, a constant debate over the last few years has been the question of the oligomeric state of GPCRs, not least because many studies that find oligomers do so in non-native conditions, and because the functional significance of oligomerisation remains elusive (Rovira et al., 2010; Smith and Milligan, 2010). If these proteins can be successfully reconstituted in DIBs, a wealth of surface density-dependent data could be accessible by single molecule fluorescence and single channel recording.

Aside from such functional data, DIBs could also be of great interest to structural biologists. There has recently been a revival of two-dimensional electron microscopy, primarily due to the fact that 2D crystals are most representative of the native state of membrane proteins (Hite et al., 2007). The major limitation of this method is

the difficulty of growing crystals. It is not inconceivable that DIBs could be used to encourage the spontaneous crystallisation by corralling membrane proteins at high surface density for extended periods.

I shall conclude this thesis with a very first step towards this ambitious goal: Figure 7.1 A shows an electron microscopy (EM) grid that was placed on the surface of the substrate agarose in PMMA device adapted for this purpose. Two small DIBs have formed within the confines of two of the holes of the copper grid. In Figure 7.1 B, one of these bilayers is reduced in size by a factor of just under ten by moving droplet with the electrode that is visible in the background.

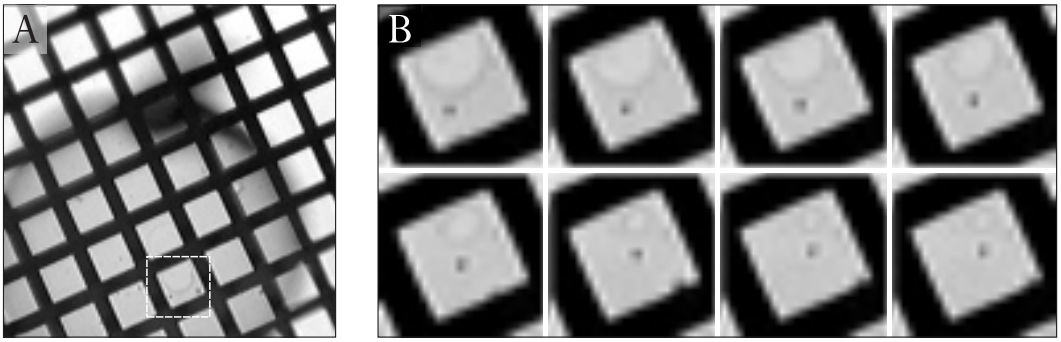

Figure 7.1: A first step towards 2D-membrane protein crystallisation in DIBs: **(A)** A DIB formed in a hole of a copper electron microscopy grid (mesh size: 100 μm). The white square indicates the region enlarged in B. **(B)** The bilayer is reduced in size by just under 10 $\times$by moving the electrode.

Bibliography

Bayley, H., B. Cronin, A. Heron, M. A. Holden, W. L. Hwang, R. Syeda, J. Thompson, and M. Wallace (2008). Droplet Interface Bilayers. *Molecular BioSystems 4*(12), 1191.

Guha, I. F., J. Kedzierski, and B. Abedian (2011). Low-voltage electrowetting on a lipid bilayer formed on hafnium oxide. *Applied Physics Letters 99*(2), 024105.

Heron, A. J., J. R. Thompson, B. Cronin, H. Bayley, and M. I. Wallace (2009). Simultaneous measurement of ionic current and fluorescence from single protein pores. *Journal of the American Chemical Society 131*(5), 1652–1653.

Hite, R. K., S. Raunser, and T. Walz (2007). Revival of electron crystallography. *Current Opinion in Structural Biology 17*(4), 389–395.

Jing, B. and Y. Zhu (2011). Disruption of supported lipid bilayers by semihydrophobic nanoparticles. *Journal of the American Chemical Society 133*(28), 10983–10989.

Jung, M., N. Vogel, and I. Köper (2011). Nanoscale patterning of solid-supported membranes by integrated diffusion barriers. *Langmuir 27*(11), 7008–7015.

Lee, B. K., H. Y. Lee, P. Kim, K. Y. Suh, and T. Kawai (2009). Nanoarrays of tethered lipid bilayer rafts on poly(vinyl alcohol) hydrogels. *Lab on a Chip 9*, 132.

Mugele, F. and J. Baret (2005). Electrowetting: from basics to applications. *Journal of Physics: Condensed Matter 17*(28), R705–R774.

Pum, D. and U. B. Sleytr (1999). The application of bacterial S-layers in molecular nanotechnology. *Trends in Biotechnology 17*(1), 8–12.

Roiter, Y., M. Ornatska, A. R. Rammohan, J. Balakrishnan, D. R. Heine, and S. Minko (2008). Interaction of nanoparticles with lipid membrane. *Nano Letters 8*(3), 941–944.

Roiter, Y., M. Ornatska, A. R. Rammohan, J. Balakrishnan, D. R. Heine, and S. Minko (2009). Interaction of lipid membrane with nanostructured surfaces. *Langmuir 25*(11), 6287–6299.

Rovira, X., J. Pin, and J. Giraldo (2010). The asymmetric/symmetric activation of GPCR dimers as a possible mechanistic rationale for multiple signalling pathways. *Trends in Pharmacological Sciences 31*(1), 15–21.

Shchipunov, Y. A. and P. Schmiedel (1996). Phase behavior of lecithin at the oil/water interface. *Langmuir 12*(26), 6443–6445.

Smith, N. J. and G. Milligan (2010). Allostery at G-protein-coupled receptor homo- and heteromers: Uncharted pharmacological landscapes. *Pharmacological Reviews 62*(4), 701 –725.

Appendix A

Publications

A.1 Journal Articles

Linda C. M. Gross, Oliver K. Castell, and Mark I. Wallace, 2011.
Dynamic and reversible control of 2D membrane protein concentration in a Droplet Interface Bilayer.
Nano Letters 11:3324–3328.

Linda C. M. Gross, Andrew J. Heron, Sylvan Baca, and M. I. Wallace, 2011.
Determining membrane capacitance by dynamic control of Droplet Interface Bilayer area.
Langmuir 27(23):14335–14342.

Appendix B

Code

B.1 Bilayer Area Fitting

B.1.1 ImageJ Macro for Image Pre-processing: getBilayerData.txt

The ImageJ macro shown on the next page takes a stack of bilayer images as an input and carries out the following image pre-processing (see section 3.3.5 and Figure 3.4):

1. bandpass filters to retain structures of dimensions between one and three pixels and auto-scales.
2. outputs a summed image of the filtered stack which shows a superposition of all bilayer edges in the stack
3. requests user input to select the region containing the data of interest:
   (a) a click on the approximate (average) centre of all bilayers
   (b) a click inside the minimum radius of all bilayers
   (c) a click outside the maximum radius of all bilayers
4. sets regions outside the area of interest to zero intensity
5. thresholds the image using ImageJ inbuilt setting "Intermodes" (for some datasets, this may have to be edited to "Minimum").

getBilayerData.txt

```
// Run this to obtain preprocessed stack to feed into IGOR for BilayerStackAreaFit.ipf.

// Outputs threshholded image stack containing bright points on the bilayer edge.

macro "getBilayerData" {

//Fundamentals
  dropletstack=getImageID();
  frames=nSlices;
  frame=0;

  run("Bandpass Filter...", "filter_large=3 filter_small=0 suppress=None tolerance=10 autoscale saturate process");
  run("Z Project...", "start=1 stop="+frames+" projection=[Max Intensity]");

  output=newArray(8);
  output=GetClicks();          // get max bounds of bilayer from Maxprojection
      close();                 // closes Maxprojection

  cc=newArray(2);
  ic=newArray(2);
  oc=newArray(2);

      cc[0]      = output[0];
      cc[1]      = output[1];
      ic[0] = output[2];
      ic[1] = output[3];
      oc[0]      = output[4];
      oc[1]      = output[5];
      ir     = output[6];
      or     = output[7];
      l      = or-ir;
            print ("vars imported");

selectImage(dropletstack);
            setAutoThreshold("Intermodes");
            run("Convert to Mask", " ");
            makeOval(cc[0]-or,cc[1]-or,or*2,or*2);          //Not sure if this can go outside of for loop
            setKeyDown("alt");
            makeOval(cc[0]-ir,cc[1]-ir,ir*2,ir*2);
            setKeyDown("none");
            getSelectionBounds(x,y,w,h);
            xcoords=newArray(h*w);                      // to hold the coordinates of bright points
            ycoords=newArray(h*w);

            //EXTRACT RELEVANT CIRCLE
      for (frame=1;frame<=frames; frame+=1) {

            setSlice(frame);                    // TO FILL IN IRRELEVANT AREAS IN Black
            run("Make Inverse");
            setColor(0,0,0);
            fill();
            run("Make Inverse");
```


getBilayerData.txt

```
            //  image into igor from here.

      } //endfor


      makeRectangle(x,y,w,h);
      run("Crop");
      path=getDirectory("");
      saveAs("Tiff", path+getTitle+"_thresh");
}

//GETTING CURSOR CLICK LOCATIONS FOR CENTER, INNER AND OUTER RADIUS

function GetClicks() {

      output=newArray(8);

      x2=-1;y2=-1;
      getCursorLoc(x,y,z,flags);                              // to initialise

      print("Click on center of bilayer:");
            while (flags&16==0 || (x==x2 && y==y2)){
                  getCursorLoc(x,y,z,flags);
            }
            x2=x;y2=y;                          // avoids next click in same location
            output[0]=x;output[1]=y;                        // saves values
            print("Center coordinates: "+x+" "+y+" "+z+" "+flags);

      print("Click inner radius limit:");
            while (flags&16==0 || (x==x2 && y==y2)){
                  getCursorLoc(x,y,z,flags);
            }
            x2=x;y2=y;
            output[2]=x;output[3]=y;
            print("Min radius: "+x+" "+y+" "+z+" "+flags);

      print("Click outer radius limit:");
            while (flags&16==0 || (x==x2 && y==y2)){
                  getCursorLoc(x,y,z,flags);
            }
            output[4]=x;output[5]=y;
            print("Max radius: "+x+" "+y+" "+z+" "+flags);

            print ("centerpoint coordinates: "+output[0]+","+output[1]);
            print ("inner radius coordinates: "+output[2]+","+output[3]);
            print ("outer radius coordinates: "+output[4]+","+output[5]);

            output[6] = sqrt(pow((output[2]-output[0]),2)+pow((output[3]-output[1]),2));
                                                            // inner radius, pythagoras
            output[7] = sqrt(pow((output[4]-output[0]),2)+pow((output[5]-output[1]),2));
                                                            // outer radius, pythagoras

            return output;
}
```

B.1.2 Igor Pro Procedure: BilayerStackAreaFit.ipf

The following pages reproduce the Igor Pro procedure used to fit bilayer areas of thresholded image stacks output by the ImageJ macro shown in section B.1.1. The algorithmic implementation of finding the circle defined by three arbitrary points using algebraic geometry is based on that detailed by Stephen R. Schmitt for the programming language zeno.
(http://mysite.verizon.net/res148h4j/zenosamples/zs_circle3pts.html).

BilayerStackAreaFit.ipf

```
#pragma rtGlobals=1        // Use modern global access method.
// pstack needs to be a binary (thresholded) stack, saved in
// datafolder root:stack. The function LoadStack sets up the
// required folder.
// Suggest running ImageJ Macro LCMG_getBilayerData.txt on raw
// data to create the thresholded stack.
// To run this procedure, execute the following:
//   - loadStack()
//   - fitStack(1000,root:stack:pstack)   (1000 = no. of iterations)

Function loadStack()
//eg: loadStack()
string path
      NewDataFolder /O root:stack
      SetDataFolder root:stack
      ImageLoad /O/N=pstack /T=tiff/S=0 /C=-1
      SetDataFolder root:
End

Function fitStack(iter,pstack)
// MainFunction:        eg:        fitStack(1000,root:stack:pstack)
      variable iter
      wave pstack
      Make/O/N=4 W_coef
      Make/O/N=4 W_sigma
      Make/O/N=4 whatiwant

      SetDataFolder root:
      Make/O /N=(dimsize(pstack,2)) areaspix
      areaspix=0
// making sparse matrix:
      SetDataFolder root:stack:
      Make/O /N=(dimsize(pstack,0)*dimsize(pstack,1),2) temp
// to hold sparse coordinates of brightpoints in each frame
      variable count, i, j, f
// cycle through all frames
      for (f=0; f<dimsize(pstack,2) ;f+=1)
            SetDataFolder root:stack
            temp=0
            count=0
            for (j=0; j<dimsize(pstack,1) ; j+=1)

                  for (i=0; i<dimsize(pstack,0) ; i+=1)
// this is for input images with inverted LUT, i.e brightpoints=0
                        if (pstack[i][j][f] == 0)
                              temp[count][0]=i
                              temp[count][1]=j
                              count+=1
                        endif
                  endfor
            endfor
```


BilayerStackAreaFit.ipf

```
            string brightpoints_f = "brightpoints_"+num2str(f)
            Duplicate/O/R=[0,count][] temp  $brightpoints_f

            SetDataFolder root:
// see function below
            whatiwant=findcircle(iter,root:stack:$brightpoints_f)
            areaspix[f]=whatiwant[1]

      CurveFit/L=2000  gauss  r_hist /D
      Make /O/N=(4) r_gauss_coef
      Make /O/N=(4) r_gauss_sigma
      r_gauss_coef=W_coef
      r_gauss_sigma =W_sigma

      string fit_f = "fit_"+num2str(f)
      string resultvals_f = "resultvals_"+num2str(f)
      string r_hist_f = "r_hist_"+num2str(f)
      string r_gauss_coef_f = "r_gauss_coef_"+num2str(f)
      string r_gauss_sigma_f = "r_gauss_sigma_"+num2str(f)
      string r_gauss_f = "r_gauss_"+num2str(f)

      Duplicate /O  fit root:stack:$fit_f
      Duplicate /O resultvals root:stack:$resultvals_f
      Duplicate /O r_hist root:stack:$r_hist_f
      Duplicate /O fit_r_hist root:stack:$r_gauss_f
      Duplicate /O r_gauss_coef root:stack:$r_gauss_coef_f
      Duplicate /O r_gauss_sigma root:stack:$r_gauss_sigma_f

      endfor
      Killwaves  fit, temp, resultvals, whatiwant
End

//supplementary function level 1
function findcircle(iter,brightpoints)

wave brightpoints
variable iter
variable i
wave params
wave threepoints
make/O/N=(iter) cx_wave
make/O/N=(iter) cy_wave
make/O/N=(iter) r_wave

Make/O/N=(360,2) fit


for (i=0;i<iter;i+=1)
// see function below - extracts three random points
      threepts(brightpoints)
// see function below - fits circle
      circle(threepoints)
```


BilayerStackAreaFit.ipf

```
      cx_wave[i]=params[0]
      cy_wave[i]=params[1]
      r_wave[i]=params[2]
endfor

Duplicate/O cx_wave cx_hist, cy_hist, r_hist
Histogram/B={0,1,500} cx_wave cx_hist
Histogram/B={0,1,500} cy_wave cy_hist
Histogram/B={0,1,500} r_wave r_hist


Wavestats/Q cx_hist
variable cx=V_maxloc

Wavestats/Q cy_hist
variable cy=V_maxloc

Wavestats/Q r_hist
variable r=V_maxloc

// see function below. creates fits.
drawcircle(fit, r,cy,cx )

Make/O/N=4 resultvals
      resultvals[0]=r
      resultvals[1]=PI*r*r
      resultvals[2]=cx
      resultvals[3]=cy

return resultvals

End


//supplementary function level 2
// coordinates of bright points in image
function threepts(brightpoints)
wave brightpoints
Make/O /N=(3,2) threepoints
Make/O /N=3 pick
variable i
variable num=dimsize(brightpoints,0)/2


for (i=0; i<3; i+=1)
      pick[i]=round(enoise(num)+num)
      threepoints[i][0]=brightpoints[pick[i]][0]
      threepoints[i][1]=brightpoints[pick[i]][1]
endfor
// Have matrix with three points. Now to fit circle.

Killwaves pick
```

BilayerStackAreaFit.ipf

```
End

// supplementary fiunction level 2
function circle(points)

wave points
Make/O/N=3 params
// (this is a matrix containing p (three points))
// (centrepointx centerpointy and radius)
variable i
variable m11, m12, m13, m14
Make/O/N=(3,3) a

    for (i=0; i<3; i+=1)        //find minor 11
        a[i][0]=points[i][0]
        a[i][1]=points[i][1]
        a[i][2]=1
    endfor
    m11 = matrixdet(a)
    //print(m11)

    for (i=0; i<3; i+=1)        //find minor 12
        a[i][0]=points[i][0]^2 + points[i][1]^2     // x^2+y^2
        a[i][1]=points[i][1]                        // y
        a[i][2]=1
    endfor
    m12 = matrixdet(a)


    for (i=0; i<3; i+=1)        //find minor 13
        a[i][0]=points[i][0]^2 + points[i][1]^2     // x^2+y^2
        a[i][1]=points[i][0]                        // x
        a[i][2]=1
    endfor
    m13 = matrixdet(a)

    for (i=0; i<3; i+=1)        //find minor 14
        a[i][0]=points[i][0]^2 + points[i][1]^2     // x^2+y^2
        a[i][1]=points[i][0]                        // x
        a[i][2]=points[i][1]                        // y
    endfor
    m14 = matrixdet(a)          // not a circle

        params[0] = 0.5 * m12 / m11                 // the centrepoint
        params[1] = -0.5 * m13 / m11
        params[2] = sqrt( params[0]^2+params[1]^2 + m14/m11)
                                                    // the radius

    Killwaves a
```


BilayerStackAreaFit.ipf

```
End

//supplementary function level 2
function drawcircle (coordinates, r,xoffset, yoffset)
wave coordinates
variable xoffset,yoffset
variable r
variable i

variable npoints=dimsize(coordinates,0)

for (i=0; i<npoints; i+=1)
    coordinates[i][0]=((r*cos(360/npoints*i)+xoffset))
    coordinates[i][1]=((r*sin(360/npoints*i)+yoffset))
endfor

End
```

B.2 Capacitance Measurement

B.2.1 Igor Pro Procedure: Capacitance.ipf

A procedure containing a series of optional functions that:

- measure the capacitative current at a series of timepoints,
- create a wave of timepoints with regular intervals, if needed
- convert this to capacitance if model cell data is available
- calculate specific capacitance if bilayer area data is available
- take an intensity wave from the image of a graticule to calculate pixel size
- calculate the average capacitance, bilayer area and specific capacitance at each applied voltage offset if voltage data is available
- plot specific capacitance, area, and capacitance against voltage, and the specific capacitance against the square of the voltage
- fit quadratic or linear fits to the above.

(See also section 3.3.3).

```
#pragma rtGlobals=1        // Use modern global access method.
//v3.0 (beta version), written by Linda C M Gross
//
// A procedure containing a series of optional functions that
//     - measure the capacitative current at a series of timepoints,
//     - create a wave of timepoints with regular intervals, if needed
//     - convert this to capacitance if model cell data is available
//     - calculate specific capacitance if bilayer area data is available
//     - take an intensity wave from the image of a graticule to calculate
//       pixel size
//     - calculate the average capacitance, bilayer area and specific
//       capacitance at each applied voltage offset if voltage data is available
//     - plot specific capacitance, area, and capacitance against voltage, and
//       the specific capacitance against the square of the voltage
//     - fit quadratic or linear fits to the above.

// For square wave amplitude measurement *only* (GetTagData Function)
// ====================================================
// Function GetTagData:
// A 1s section of trace just before each tag time is analysed. Points
// immediatly before and after each instantaneous upward change
// (defined by variables a - b and c - d) are averaged to obtain the
// amplitude of the square wave. This is output as a wave `peaks' (positive values)
// and `antipeak' (negative values) at each tag, which are averaged to give
// the capacitive current at each tag.
//
//USAGE:
//GetTagData(useframes,tagtimes_sec, trace, corrections)
//     useframes:    if set to -1, all timepoints n in tagtimes_sec (which usually
//           would contain the time points n at which bilayer images were taken)
//           are analysed, otherwise, a wave named frames in the root directory
//           has to contain a list of n to be analysed.
//     tagtimes_sec: wave containing the timepoints in the trace to be analysed.
//           in seconds. (use MinSec(tagtimes_min) to convert minutes to seconds)
//           (If tags were placed into the recording in clampfit, this can be generated
//           by clampfit: Tools>Go to Tag> Clipboard. Alternatively a list of times at
//           regular intervals can be made by the function MakeTagTimes
//     trace: a full current trace (so that point number equals 1ms)
//           exported as text from clampfit or Win-EDR
//     corrections: if set to 0, ignored. This exists to manually correct erroneous
//           results after the first run of the function. If set to 1, requires a wave
//           called peakcorrections in root, or dimensions (n,2) where n is the number
//           of points to be corrected. each row takes the form:
//           [index of peak wave][corrected value]. If set to 2, requires a wave called
//           antipeakcorrections in root. If set to 3, requires both.

// To execute RunDefault (executes all functions described at the top of this file)
//=============================================================
// RunDefault executes multiple functions, it is best to comment these out as needed
// future implementation should have a GUI for this.
//
// the following additional waves are required to be present in root:
//           frames: framenumber of images corresponding to tagtimes_sec
//           areapix: bilayer areas in each image  measured manually or
//                              from BilayerStackAreaFit.ipf
//           applied_V: is loaded applied Voltage trace in ms
//           graticule: is pixel intensity across a graticule spacing of 50um
//           mc_trace: is a section of model cell trace
//
// USAGE:
// RunDefault(start,interval,capoffset,voltageoffset,corrections,draw,datasetlabel)
//     start: first image time point in seconds if tagtimes_sec is created by this function:
//     interval: Interval between images in seconds if regular interval tagtimes_sec
//           is to be created. Set to 0 if custom tagtimes_sec wave is present in root.
//           (in this case start is ignored).
//     capoffset: background capacitance in pF.
//     voltageoffset: usually 0. If it becomes clear after a first run that a voltage offset
//           is present, this can be used to compensate.
//     corrections: set to value as described above for function GetTagData
```



```
//     draw: set to 1 if graphs of fits are to be output.
//     datasetlabel: string
//
// The function QuickCal can be used if graticule and mc_trace are not available.
//          eg. QuickCal(1.1, 101.9, 12)     -> microns per pixel, model cell current
//                                              upon application of triangular potential,
//                                              and background capacitance in pF

Macro RunDefault(start,interval,capoffset,voltageoffset,corrections,draw,datasetlabel)
     variable start          // first tagtime
     variable interval   // interval is time between tags/images
     variable capoffset// capoffset is the background capacitance, usually about 12 pF
     variable voltageoffset
     variable corrections  // requires waves peakcorrections (option 1) or
                           // antipeakcorrections (option2) or both (3)
     variable draw           // outputs graphs if set to 1
     string datasetlabel // name of the dataset

     if (interval !=0)
          MakeTagTimes(trace,start,interval,-1)
                           // makes tagtimes_sec based on fixed interval in seconds.
                           // -1 means the number of tags is trace length/interval.
     endif
     Setup()
     GetTagData(useframes,tagtimes_sec, trace, corrections)
                           // measures I at tagtimes_sec (ouputs CT)
     Calibration(graticule, mc_trace,capoffset)          // e.g Calibration(1,1,12)
                           // carries out pixel and model cell calibration.
                           // If either graticule or mc_trace is set to =-1, skips pixel
                           // or model cell calibration, outputs root:calibrations:calib
                           // which contains capoffset, modelcellvalue and micronsperpix
     //QuickCal(-1,-1,capoffset) // microns per pixel, model cell value ,background capacitance:
                           // manual override of calibration - does nothing if -1
     Csp(CT, usedareapix, root:calibrations:calib)
                           // outputs Capacitance, areamicrons and specificcap
     Condense(applied_V,tagtimes_sec)
                           //outputs voltage at tagtimes (needs framecounter present)
     //Correctdrift(capacitance, areamicrons, specificcap)
                           // optional function: outputs Cap_N and Aum_N,
                           // subtracting an exponential fit to Capactiance to correct any drift
                           // keeps specific capactanc constant and uses this to calculate
                           // correction ot area. type of fit may have to be adjusted in function
                           //itself
     Errors(voltage,capacitance,areamicrons,specificcap,voltageoffset)
                           // outputs cap, area and specifc cap vs applied voltage with errors
     //Errors(voltage,Cap_N,Aum_N,specificcap,voltageoffset)
                           // optional if Correctdrift was used, as above
     Linearise(voltage,capacitance,areamicrons,specificcap,voltageoffset)
                           // outputs linear plots with errors, plotted against V^2
     //Linearise(voltage,Cap_N,Aum_N,specificcap,voltageoffset)
                           // optional if Correctdrift was used, as above
     Fits(SLy, VLx, Cy, Ay, Sy, Vx)

     //Graphs
     DoWindow/K tracedisplay
     result()
     DoWindow/K quadA; DoWindow/K quadC;
     DoWindow/K quadCm; DoWindow/K linearCm; DoWindow/K dataforexport
     Dataforexport()

     if (draw==1)
     Area_vs_voltagewitherrors(datasetlabel)
     Cap_vs_V_witherrors()
     Specificcap_vs_V_witherrors()
     straightline()
     endif
End

Macro Setup()
```



```
     Duplicate/O areapix usedareapix                // replace first wave with custom wave
     Duplicate/O tagtimes_sec tagtimes_sec_store
     if (!exists("peakcorrections"))
     Make /N=(1,2) peakcorrections
     endif
     if (!exists("antipeakcorrections"))
     Make /N=(1,2) antipeakcorrections
     endif
     if (!exists("frames"))
     duplicate/o tagtimes_sec frames
     Extract/O /INDX tagtimes_sec, frames, tagtimes_sec>0
     endif
     Duplicate/O frames usedframes

End

Macro startagain()

     Duplicate/O root:calibrations:mc_trace root:mc_trace
     Duplicate/O root:calibrations:graticule root:graticule
     Killdatafolder root:calibrations
     Newdatafolder/O root:safe
     Duplicate/O trace root:safe:trace
     Duplicate/O applied_V root:safe:applied_V
     Duplicate/O areaspix_man root:safe:areaspix
     Duplicate/O mc_trace root:safe:mc_trace
     Duplicate/O graticule root:safe:graticule
     Killwaves /A
     Duplicate/O root:safe:trace root:trace
     Duplicate/O root:safe:applied_V root:applied_V
     Duplicate/O root:safe:areaspix root:areaspix
     Duplicate/O root:safe:mc_trace root:mc_trace
     Duplicate/O root:safe:graticule root:graticule

End

Function MakeTagTimes(trace,start,interval,numberoftags)      // if there is no tagoutput
     wave trace
     variable start                                          //pass start and interval in seconds
     variable interval
     variable numberoftags
          if (numberoftags==-1)
               numberoftags=findnumberoftags(trace,interval)  // see suppl functionbelow.
          endif
     variable i=0
     Make /O/N=(numberoftags) tagtimes_sec
     for (i=0;i<numberoftags;i+=1)
          tagtimes_sec[i]=start+interval*i
     endfor
End

Function MinSec(tagtimes_min)            //optional: converts tagtimes in minutes to seconds
     wave tagtimes_min
     Duplicate tagtimes_min tagtimes_sec
     tagtimes_sec = tagtimes_min*60
End

Function findnumberoftags(trace,interval)
     wave trace
     variable interval                  // in seconds
     variable numberoftags
     interval=interval*1000             // in ms
     numberoftags=floor(dimsize(trace,0)/interval)

     return numberoftags
End

////////////main calibration
Function Calibration(do_pixelcal, do_mc, backgroundcapacitance)
```

```
	variable do_pixelcal
	variable do_mc
	variable backgroundcapacitance
	WAVE graticule
	WAVE mc_trace

		NewDataFolder/O root:calibrations

		Make /O/N=3 calib
		variable temp
	if (do_mc!=-1)
		temp=ModelCell(mc_trace)  //mc
		print ("model cell value ="+num2str(temp))
		calib[0]=temp
		Duplicate/O mc_trace root:calibrations:mc_trace
		Killwaves mc_trace
	endif
	if (do_pixelcal!=-1)
		temp=PixelCal(graticule,50,30) //micronsperpix
		print ("micronsperpix ="+num2str(temp))
		calib[1]=temp
		Duplicate/O graticule root:calibrations:graticule
		Killwaves graticule
	endif
		calib[2]=backgroundcapacitance // capoffset


		Duplicate/O calib root:calibrations:calib
		killwaves calib  // clear from root.

End


Function QuickCal(mpp, mc,bgcap)
	variable mpp		//micronsperpix
	variable mc		//model cell value
	variable bgcap	//capoffset
	//wave calib

	If (DataFolderExists("calibrations"))
		SetDataFolder root:calibrations
			If (!exists("calib"))
			Make /O/N=3 calib
			endif
	else
		NewDataFolder root:calibrations
		SetDatafolder root:calibrations
		Make /O/N=3 calib
	endif

	Make /O/N=2 test
	if (mc!=-1)
		calib[0]=mc
	endif

	if (mpp!=-1)
		calib[1]=mpp
	endif

	if (bgcap!=-1)
		calib[2]=bgcap
	endif

	SetDatafolder root:
End

////////////////////////////////////////// main Function
Function GetTagData(useframes,tagtimes_sec,trace,corrections)
			//use tagtimes from axopatch, or wave created with maketagtimes
```



```
variable useframes
wave tagtimes_sec				//changed from mins to secs 17/11/2009
wave trace
variable corrections
variable i=0
variable j=0
variable freq=50
variable threshold
WAVE peakcorrections
WAVE antipeakcorrections
WAVE frames
variable temp
Duplicate/O trace,ftrace
		// filtering out spikes recorded on WinEDR but not axopatch
Smooth 2, ftrace
		// using binomial 2 filter
ftrace=trace
		// temp hack to undo filter - not convinced it works better yet.

Duplicate/O frames framecounter
framecounter=frames-1

if (useframes==-1)
Make/O/N=(Dimsize(tagtimes_sec,0)) /D tagtimes
tagtimes=tagtimes_sec*1000					//work in msecs
endif
if (useframes!=-1)
duplicate/O framecounter ftimes
for (i=0;i<(dimsize(frames,0));i+=1)
temp=framecounter[i]
ftimes[i]=tagtimes_sec[temp]
endfor
Make/O/N=(Dimsize(ftimes,0)) /D tagtimes
tagtimes=ftimes*1000
endif

Make /O/N=(Dimsize(tagtimes,0)) peaks
Make /O/N=(Dimsize(tagtimes,0)) antipeaks
Make /O/N=(Dimsize(tagtimes,0)) CT

for (j=0;j<(Dimsize(tagtimes,0));j+=1)
	Make /O/N=1000 tagdata
	Make /O/N=1000 upstrokes

	for (i=0;i<1000;i+=1)
	tagdata[i]=ftrace[tagtimes[j]-1500+i]
	endfor

	Differentiate/DIM=0  tagdata/D=tagdata_DIF
	Wavestats/Q tagdata_DIF
	threshold=0.5*V_max

	for (i=0;i<(1000/freq);i+=1)
		Duplicate /O/R=[i*freq,i*freq+(freq*2.1)] tagdata_DIF frame
		wavestats /Q frame
			if (V_max>threshold)
				upstrokes[V_maxloc]=1
			endif
		Killwaves frame
	endfor

	Extract /Indx /O upstrokes, pinpoints, (upstrokes[p]!=0)

	GetSingleTagValues(pinpoints,tagdata)
	wavestats/Q negpoints
	antipeaks[j]=V_avg
	wavestats/Q pospoints
	peaks[j]=V_avg
```



```
		Clear()
	endfor

	if(corrections==1 || corrections==3)
	for (i=0;i<dimsize(peakcorrections,0);i+=1)
		peaks[peakcorrections[i][0]]=peakcorrections[i][1]
	endfor
	endif

	if(corrections==2 || corrections==3)
	for (i=0;i<dimsize(antipeakcorrections,0);i+=1)
		antipeaks[antipeakcorrections[i][0]]=antipeakcorrections[i][1]
	endfor
	endif

	CT=(peaks-antipeaks)/2

	Execute "result()"
	//Execute "ShowValues()"

End

Function Tidy()  // Have to run this before running a different size frames.

	DoWindow tracedisplay
	if (V_flag)
	Killwindow tracedisplay
	endif
	DoWindow CapArea
	if (V_flag)
	Killwindow CapArea
	endif
	if (exists("tagtimes"))
	Killwaves tagtimes
	endif
	if (exists("framecounter"))
	Killwaves framecounter
	endif
	if (exists("ftimes"))
	Killwaves ftimes
	endif
	if (exists("usedframes"))
	Killwaves usedframes
	endif
	if (exists("usedareapix"))
	Killwaves usedareapix
	endif
End

Function GetSingleTagValues(pinpoints,tagdata) // supplementary Function
	wave pinpoints
	wave tagdata
	variable i=0
	variable a, b, c, d
	Make /N=(Dimsize(pinpoints,0)) negpoints
	Make /N=(Dimsize(pinpoints,0)) pospoints
	for (i=0;i<Dimsize(pinpoints,0);i+=1)
		a=pinpoints[i]-8
		b=pinpoints[i]-4
		c=pinpoints[i]+8
		d=pinpoints[i]+12
		Duplicate /O/R=[a,b] tagdata temp
		wavestats/Q temp
		negpoints[i]=V_avg
		Killwaves temp
		Duplicate /O/R=[c,d] tagdata temp
		wavestats/Q temp
		pospoints[i]=V_avg
		Killwaves temp
```

```
    endfor
End

//use manually or auto measured areas to calculate specific capacitance
Function Csp(C, areaspix,calib)  //C= measured capacitance: (=CT from above)
    wave C
    wave areaspix
    wave calib                  // contains mc_meas, micronsperpix, capoffset.
    variable mc_meas
    variable micronsperpix
    variable capoffset

    mc_meas=calib[0]
    micronsperpix=calib[1]
    capoffset=calib[2]
    duplicate/O CT capacitance areamicrons specificcap

    //CT=(-antipeaks+peaks)/2
    capacitance = C-capoffset
    areamicrons=areaspix*(micronsperpix^2)
    specificcap = (capacitance/1e6)/(areamicrons/(1000^2*10^2))
    //variable mc=100/mc_meas
    //duplicate/O specificcap specificcap_mc
    //specificcap_mc=specificcap*mc
    specificcap=specificcap*100/mc_meas

    //Edit capacitance areamicrons specificcap
    CurveFit line  CT /X=areamicrons /D
    Duplicate/O W_coef  Cm_coef
    Duplicate/O W_sigma Cm_sigma
    Killwaves W_coef, W_sigma
    InsertPoints 2,1, Cm_coef
    Cm_coef[2]=V_Pr

    Execute "Caparea()"
End

Function Clear() // supplementary Function
    Killwaves pinpoints, upstrokes, tagdata_DIF, tagdata, negpoints, pospoints
End


// The following two functions find the applied voltage level at tagtimes from a full V trace.
// Method: average V around 1000 points around tag, then round to nearest 10.
// (Specific for ramps that use 10V steps.)
Function Condense(applied_V,tagtimes)
                    // condenses a voltage trace to the applied voltage at tagtimes
    wave applied_V
    wave tagtimes
    WAVE framecounter
    duplicate/O frames voltage
    variable i

    for (i=0; i<dimsize(tagtimes,0); i+=1)
    voltage[i]=avg((tagtimes[framecounter[i]]-500,1000,applied_V)   // see suppl function below.
    endfor

    voltage=voltage/10
    voltage=round(voltage)
    voltage=voltage*10

End

Function avg(tstart,range,applied_V)  // supplementary function to Condense().

    variable tstart
    variable range                  // points to average over. (using 1000 in Condense())
    wave applied_V
```



```
    variable total=0
    variable i=tstart

    do
        total=total+applied_V(i)
        i+=1
    while (i<(tstart+range))

    variable average
    average = total/range

    return average
End

/// NORMALISING FUNCTION

Function Correctdrift(capacitance, areamicrons, specificcap)
    wave capacitance
    wave areamicrons
    wave specificcap
    Duplicate/O capacitance capacitance_fit

    CurveFit exp capacitance /D=capacitance_fit
    duplicate/O capacitance Cap_N
    duplicate/O areamicrons Aum_N

    //wave capacitance_fit
    wavestats /Q capacitance_fit
    variable capfitmin
    capfitmin = V_min
    print ("minimum capacitance used for correction of drift =" +num2str(capfitmin))

    Cap_N=capacitance-capacitance_fit+capfitmin
    Aum_N=Cap_N*100/specificcap

End


Function Errors(V,C,A,S,voltageoffset)                  // new function 2010-01-13
    wave V              // voltage          // from condense
    wave C              // capacitance      // use Cap_N  (Normalised)
    wave A              // areamicrons      // use Aum_N
    wave S              // specificcap
    variable voltageoffset

    make /O/N=21 Vx, Cy,Ay,Sy, Ce, Ae, Se  // voltagerange -100 to 100: y=mean, e=error )
    variable i
    variable j

    Duplicate/O V offsetV
    offsetV=V+voltageoffset

    for (i=0; i<21; i+=1)
        Vx[i]=-100+(i*10)+voltageoffset

        Extract /Indx/O offsetV, Vtemp, (offsetV==Vx[i])
                                        // find the index of all values at voltage Vx[i]

        Make /O/N=(dimsize(Vtemp,0)) Ctemp Atemp Stemp
        for (j=0;j<dimsize(Vtemp,0);j+=1)
            Ctemp[j]=C[Vtemp[j]]
            Atemp[j]=A[Vtemp[j]]
            Stemp[j]=S[Vtemp[j]]
        endfor

        Wavestats /Q Ctemp
        Cy[i]=V_avg
        Ce[i]=V_sdev/(V_npnts^0.5)
```



```
        Wavestats /Q Atemp
        Ay[i]=V_avg
        Ae[i]=V_sdev/(V_npnts^0.5)

        Wavestats /Q Stemp
        Sy[i]=V_avg
        Se[i]=V_sdev/(V_npnts^0.5)

        Killwaves Vtemp, Ctemp, Atemp, Stemp
    endfor

End

Function Linearise(V,C,A,S, voltageoffset)                  // new function 2010-01-13
    wave V              // voltage          // from condense
    wave C              // capacitance      // use Cap_N  (Normalised)
    wave A              // areamicrons      // use Aum_N
    wave S              // specificcap
    variable voltageoffset


    duplicate/O V Vmv
    Vmv=((V+voltageoffset)^2)

    //Edit Vmv                                      // uncomment to debug

    make /O/N=21 VLx, CLy,ALy,SLy, CLe, ALe, SLe
                                        // voltagerange -100 to 100: y=mean, e=error )
    variable i
    variable j

    variable l
    string vtemp_i

    for (i=0; i<21; i+=1)
        VLx[i]=(-100+(i*10)+voltageoffset)^2        //mv^2
        //print VLx[i]

        vtemp_i = "Vtemp_"+num2str(i)       // name of the extracted wave

        Extract /Indx/O Vmv, $vtemp_i, Vmv==VLx[i]
                                        // find the index of all values at voltage VLx[i]
        //Appendtotable $vtemp_i            // uncomment to debug
        Duplicate/O $vtemp_i Vtemp

        Killwaves $vtemp_i                  // comment to debug

        l =dimsize(Vtemp,0)
        Make /O/N=(l) Ctemp Atemp Stemp
        //print l
        for (j=0;j<l;j+=1)
            Ctemp[j]=C[Vtemp[j]]
            Atemp[j]=A[Vtemp[j]]
            Stemp[j]=S[Vtemp[j]]
        endfor

        Killwaves  Vtemp

        Wavestats /Q Ctemp
        CLy[i]=V_avg
        CLe[i]=V_sdev/(V_npnts^0.5)         //calculating Standard Error: SE=SD/n^0.5

        Killwaves  Ctemp

        Wavestats /Q Atemp
        ALy[i]=V_avg
        ALe[i]=V_sdev/(V_npnts^0.5)

        Killwaves Atemp
```

```
        Wavestats /Q Stemp
        SLy[i]=V_avg
        SLe[i]=V_sdev/(V_npnts^0.5)

        Killwaves Stemp
    endfor
    VLx=VLx/10000

End


Function Fits(SLy, VLx, Cy, Ay, Sy, Vx)
    wave SLy
    wave VLx
    wave Cy
    wave Ay
    wave Sy
    wave Vx

    CurveFit line  SLy /X=VLx /D
    Duplicate/O W_coef  fit_SLy_coef
    Duplicate/O W_sigma fit_SLy_sigma
    fit_SLy_coef[0]=fit_Sly_coef[0]/100                    // Co
    fit_SLy_coef[1]=fit_Sly_coef[1]/1000000                // beta


    Wavestats/Q Ay
    Make/D/N=3/O W_coef
    W_coef[0] = {V_min, (V_max-V_min)/(100^2), 0}
    FuncFit quadratic W_coef  Ay /X=Vx /D
    Duplicate/O W_coef  fit_Ay_coef
    Duplicate/O W_sigma fit_Ay_sigma

    Wavestats/Q Cy
    Make/D/N=3/O W_coef
    W_coef[0] = {V_min, (V_max-V_min)/(100^2), 0}
    W_coef[0] = {395,0.005,0}
    FuncFit  quadratic W_coef  Cy /X=Vx /D
    Duplicate/O fit_Cy fit_Cy_simple_quadratic
    Duplicate/O W_coef  fit_Cy_simple_coef
    Duplicate/O W_sigma fit_Cy_simple_sigma

    Wavestats/Q Sy
    Make/D/N=3/O W_coef
    W_coef[0] = {V_min, (V_max-V_min)/(100^2), 0}
    FuncFit  quadratic W_coef  Sy /X=Vx /D
    Duplicate/O fit_Sy fit_Sy_simple_quadratic
    Duplicate/O W_coef  fit_Sy_simple_coef
    Duplicate/O W_sigma fit_Sy_simple_sigma


    //fitting Cy using fixed values from Ay fit, and suggestions from SLy fit
    Make/O/N=5 fit_Cy_Coefficients   // to take 0: Ao (H), 1: B (H), 2: V_offset,   3: Co  4: beta
    fit_Cy_Coefficients={fit_Ay_coef[0] , fit_Ay_coef[1] , fit_Ay_coef[2] , fit_SLy_coef[0] , fit_SLy_coe

    Duplicate/O fit_Cy_Coefficients fit_Cy_Coeff_lower
    Duplicate/O fit_Cy_Coefficients fit_Cy_Coeff_upper

    // sigma constraints
    //fit_Cy_Coeff_lower = fit_Cy_Coefficients - fit_Cy_Coefficients_sigma
    //fit_Cy_Coeff_upper = fit_Cy_Coefficients + fit_Cy_Coefficients_sigma

    //override constraints
    fit_Cy_Coeff_lower[2] = -10                            // voltage offset
    fit_Cy_Coeff_upper[2] = 10

    fit_Cy_Coeff_lower[3] = 0.95 * fit_Cy_Coefficients[3]  // Co: 5%
    fit_Cy_Coeff_upper[3] = 1.05 * fit_Cy_Coefficients[3]
```



```
    fit_Cy_Coeff_lower[4] = 0.95 * fit_Cy_Coefficients[4]  // beta: 10%
    fit_Cy_Coeff_upper[4] = 1.05 * fit_Cy_Coefficients[4]

    string K0_l, K0_u,K1_l, K1_u,      K2_l, K2_u,      K3_l, K3_u,      K4_l, K4_u

    //K0_l = num2str(fit_Cy_Coeff_lower[0])
    //K0_u = num2str(fit_Cy_Coeff_upper[0])
    //K1_l = num2str(fit_Cy_Coeff_lower[1])
    //K1_u = num2str(fit_Cy_Coeff_upper[1])
    K2_l = num2str(fit_Cy_Coeff_lower[2])
    K2_u = num2str(fit_Cy_Coeff_upper[2])
    K3_l = num2str(fit_Cy_Coeff_lower[3])
    K3_u = num2str(fit_Cy_Coeff_upper[3])
    K4_l = num2str(fit_Cy_Coeff_lower[4])
    K4_u = num2str(fit_Cy_Coeff_upper[4])

    Make/D/N=5/O W_coef
    W_coef = fit_Cy_Coefficients
    Make/O/T/N=6 T_Constraints
    T_Constraints[0] = {"K2 > "+K2_l,"K2 < "+K2_u,"K3 > "+K3_l,"K3 < "+K3_u,"K4 > "+K4_l,"K4 < "+
    FuncFit/H="11000" Doublequadratic W_coef  Cy /X=Vx /D /C=T_Constraints

    Duplicate/O W_coef  fit_Cy_coef_output
    Duplicate/O W_sigma fit_Cy_sigma_output

    K0 = fit_Cy_coef_output[3]*100;K2 = fit_Cy_coef_output[4]*100;          //Co and beta

    CurveFit/H="101" poly 3,  Sy /X=Vx /D

    Duplicate/O W_coef  fit_Sy_coef
    Duplicate/O W_sigma fit_Sy_sigma


End


// CALIBRATION FUNCTIONS

Function ModelCell(mc_trace) // this is the output from GetTagData run on mc_trace
    wave mc_trace

    SetDataFolder root:calibrations
    variable l=dimsize(mc_trace,0)/1000        // length of trace in seconds
    variable interval=1
    maketagtimes(mc_trace,(0.1*l),interval,(0.8*l/interval))
                                        //start in secs, interval in secs, numberoftags
    GetTagdata(-1,tagtimes_sec,mc_trace,0)

    variable mc
    Duplicate/O/R=[5,50]  CT mc_avgpeaks
    wavestats/Q mc_avgpeaks
    mc=V_avg
    Killwaves tagtimes_sec, tagtimes, peaks, antipeaks, CT, mc_avgpeaks
                                        //kills those in calibrations folder.


    SetDataFolder root:
    return mc
End

Function PixelcaI(graticule, windowsize,thresh)
                // e.g (wave of px intensities along line disecting the graticule,40,50)

    wave graticule
    variable windowsize
    variable thresh

    SetDatafolder calibrations
```



```
    wavestats/Q graticule
    duplicate/O graticule pixintens
    pixintens=(graticule*-1)+V_max
                        // turns negative spikes (black graticule lines)
                        // into positive peaks
    //pixintens=graticule

    variable w=windowsize/2
    variable i
    variable micronsperpix

    Wavestats /Q pixintens
    Make/O/N=(dimsize(pixintens,0)) gpeaks
    gpeaks=0

    // find local maximum:

    for (i=w; i<dimsize(pixintens,0)-w; i+=windowsize)
        Duplicate/O/R=[(i-w), (i+w)] pixintens temp
        Wavestats /Q temp
    // record local maximum
                                //for some reason, V_maxloc pulls
                                 //out the index in graticule, not temp
        gpeaks[V_maxloc]=(V_max>thresh)*-20
    endfor
    Killwaves temp

    Extract /O/INDX gpeaks, gvals, gpeaks !=0
    Make/O/N=(dimsize(gvals,0)-1) gdists
    for (i=1;i<dimsize(gvals,0); i+=1)
        gdists[i-1]=gvals[i]-gvals[i-1]
    endfor
    Wavestats /Q gdists
    micronsperpix=50/V_avg              // V_avg is the number of px in one 50 um
                                        //division of the graticule


    Display pixintens,gpeaks

    SetDataFolder root:
    return micronsperpix
End

// STORAGE FUNCTIONS

Macro makesafe()
    NewDataFolder root:safe

    duplicate trace          root:safe:trace
    duplicate applied_V      root:safe:applied_V
    //duplicate tagtimes     root:safe:tagtimes
    duplicate tagtimes_sec root:safe:tagtimes_sec
    //duplicate frames       root:safe:frames
    //duplicate areaspix root:safe:areapix
End

Macro dorecover()
    duplicate/O root:safe:trace          root:trace
    duplicate/O root:safe:applied_V      root:applied_V
    duplicate/O root:safe:tagtimes       root:tagtimes
    duplicate/O root:safe:tagtimes_sec       root:tagtimes_sec
    duplicate/O root:safe:frames         root:frames
    duplicate/O root:safe:areapix        root:areapix
End



// DISPLAY Functions and MACROS: see digital file.
```

Appendix C

Reference Material

C.1 Fluorescent Dye

Quest™ Fluo-8 Absorption and Emission Spectra

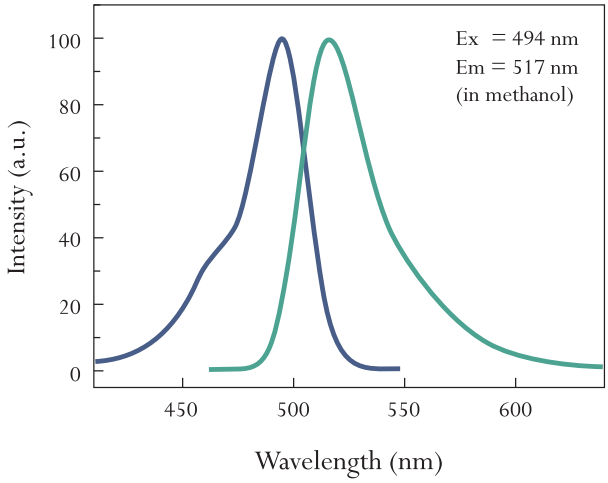

Figure C.1: Quest™ Fluo-8 absorption and emission spectra. *Source: www.aatbio.com*

C.2 Protein Sequence

Amino-acid sequence of long-linker H_6-tagged WT α-Hemolysin (WT-H_6 α-HL)

M A D S D I N I K T G T T D I G S N T T V K T G D L V T Y D K E N G M H
K K V F Y S F I D D K N H N K K L L V I R T K G T I A G Q Y R V Y S E E
G A N K S G L A W P S A F K V Q L Q L P D N E V A Q I S D Y Y P R N S I
D T K E Y M S T L T Y G F N G N V T G D D T G K I G G L I G A N V S I G
H T L K Y V Q P D F K T I L E S P T D K K V G W K V I F N N M V N Q N
W G P Y D R D S W N P V Y G N Q L F M K T R N G S M K A A D N F L D
P N K A S S L L S S G F S P D F A T V I T M D R K A S K Q Q T N I D V I Y
E R V R D D Y Q L H W T S T N W K G T N T K D K W T D R S S E R Y K I
D W E K E E M T N R G S G S S G G S S H H H H H H

C.3 Microbiology

C.3.1 Overexpression System

The genotype of the BL21(DE3)pLysS used in the overexpression of α-Hemolysin was as follows:

F-, ompT, *hsd*S_B (r_B-, m_B-), *dcm*, *gal*, λ(DE3), pLysS, Cam^r.